INTEGRATED MAGNETICS:

CONTRIBUTIONS TO IMPROVED PROCESSING AND INTERPRETATION OF MAGNETIC GRADIENT TENSOR DATA, NEW METHODS FOR SOURCE LOCATION AND ESTIMATION OF MAGNETISATION, AND PREDICTIVE MAGNETIC EXPLORATION MODELS

By

David Alan Clark
B.Sc.(Hons), M.Sc.

A thesis submitted for the degree of

DOCTOR OF PHILOSOPHY

at

MACQUARIE UNIVERSITY

NSW 2109, Australia

Department of Earth and Planetary Sciences

January, 2014

ABSTRACT

This thesis presents methods for processing and interpreting magnetic gradient tensor data, new approaches to estimation of source magnetisations from analysis of magnetic anomalies, and improved geological interpretation of magnetic surveys using magnetic petrological principles and predictive magnetic exploration models. The thesis emphasises the importance of an approach that integrates an understanding of the geological processes that create and destroy magnetic minerals with extra information obtained from magnetic gradient tensor data, and with petrophysical and palaeomagnetic information, to derive better geological models and to improve exploration success.

TABLE OF CONTENTS

PREAMBLE iii

CHAPTER 1: INTRODUCTION 1

CHAPTER 2: UTILITY OF MAGNETIC TENSOR GRADIOMETRY AND PROPERTIES OF THE MAGNETIC GRADIENT TENSOR 5

CHAPTER 3: NEW METHODS FOR INTERPRETATION OF MAGNETIC VECTOR AND GRADIENT TENSOR DATA I: EIGENVECTOR ANALYSIS AND THE NORMALISED SOURCE STRENGTH 35

CHAPTER 4: NEW METHODS FOR INTERPRETATION OF MAGNETIC VECTOR AND GRADIENT TENSOR DATA II: APPLICATION TO THE MOUNT LEYSHON ANOMALY, QUEENSLAND 85

CHAPTER 5: INTERPRETATION OF THE MAGNETIC GRADIENT TENSOR AND NORMALIZED SOURCE STRENGTH APPLIED TO THE TALLAWANG MAGNETITE SKARN DEPOSIT, NEW SOUTH WALES, AUSTRALIA 123

CHAPTER 6: CORRECTION OF ELECTRIC AND MAGNETIC FIELDS AND GRADIENTS MEASURED WITHIN AND AROUND AN INSULATING SENSOR CAPSULE IN SEAWATER 133

CHAPTER 7: NEW APPROACHES TO DEALING WITH REMANENCE: MAGNETIC MOMENT ANALYSIS USING TENSOR INVARIANTS AND REMOTE DETERMINATION OF *IN SITU* MAGNETISATION USING A STATIC TENSOR GRADIOMETER 155

CHAPTER 8: METHODS FOR DETERMINING REMANENT AND TOTAL MAGNETISATIONS OF MAGNETIC SOURCES - A REVIEW. 173

CHAPTER 9: MAGNETIC EFFECTS OF HYDROTHERMAL ALTERATION IN PORPHYRY COPPER AND IRON-OXIDE COPPER-GOLD SYSTEMS: A REVIEW 277

CHAPTER 10: CONCLUSIONS 341

PREAMBLE

This thesis comprises an introductory section dealing with the properties and utility of magnetic gradient tensor data, followed by a series of chapters, each of which represents a published paper, published extended abstract or, in the case of Chapter 8, an accepted manuscript. Chapter 3 presents new methods for interpretation of magnetic gradient tensor data, with emphasis on the utility of the normalised source strength. Chapters 4 and 5 apply these methods to analysis of magnetic gradient tensor data at the Mount Leyshon gold deposit, Queensland, and the Tallawang magnetite skarn in New South Wales.

Chapter 6 addresses the issue of relating electric and magnetic field and gradient measurements made in an insulating capsule within a conductive medium to the unperturbed quantities that prevailed before insertion of the capsule. The effects of water flow around the capsule are also analysed This has implications for marine controlled source electromagnetic surveys, magnetic gradient tensor measurements in the ocean, and marine magnetotellurics, as well as potential application to satellite measurements within the magnetosphere.

Chapter 7 describes two new methods for remote determination of magnetisation of isolated magnetic bodies, (i) Helbig analysis of rotational invariants of the gradient tensor and (ii) a combined vector magnetometer/gradiometer in base station mode that exploits local perturbation of natural geomagnetic variations by a magnetic source, which are particularly useful for remanence-dominated magnetic sources. Chapter 8 gives an extensive review of methods for estimation of total and remanent magnetisations of magnetic sources, incorporating some of the new approaches presented elsewhere in this thesis, and Chapter 9 reviews the effects of hydrothermal alteration on magnetic properties of rocks within mineralised systems, including implications for mineral exploration. A major emphasis in chapter 9 is on predictive magnetic exploration models for porphyry copper and iron oxide copper-gold deposits. Chapter 10 summarises the thesis and presents conclusions.

STATEMENT

I declare that all the work in this thesis is the author's own, except where otherwise acknowledged.

I hereby certify that no part of this thesis has been presented to any other University or Institution for the purpose of obtaining a higher degree

David Alan Clark

LIST OF PUBLICATIONS INCORPORATED INTO THIS THESIS

Clark, D.A., 2014. Methods for determining remanent and total magnetisations of magnetic sources - a review. Exploration Geophysics (accepted). (Chapter 8)

Clark, D.A.,2014. Magnetic effects of hydrothermal alteration in porphyry copper and iron-oxide copper–gold systems: A review, Tectonophysics (2014), http://dx.doi.org/10.1016/j.tecto.2013.12.011 (Chapter 9)

Clark, D.A., 2013. New approaches to dealing with remanence: magnetic moment analysis using tensor invariants and remote determination of *in situ* magnetisation using a static tensor gradiometer (Extended Abstract), 7p. ASEG-PESA Conference, Melbourne. http://dx.doi.org/10.1071/ASEG2013ab049 (Chapter 7)

Clark, D.A., 2013. New methods for interpretation of magnetic vector and gradient tensor data II: Application to the Mount Leyshon Anomaly, Queensland, Exploration Geophysics, 44, 114–127 (http://dx.doi.org/10.1071/EG12066). (Chapter 4)

Clark, D.A., 2012. New methods for interpretation of magnetic vector and gradient tensor data I: eigenvector analysis and the normalised source strength. Exploration Geophysics, 43, 267–282, http://dx.doi.org/10.1071/EG12020. (Chapter 3) [see also Errata submitted to Exploration Geophysics, May 2014]

Clark, D.A. 2012, Interpretation of the magnetic gradient tensor and normalized source strength applied to the Tallawang magnetite skarn deposit, New South Wales, Australia. Society of Exploration Geophysicists Annual Meeting Expanded Abstract, Las Vegas, 4p. http://dx.doi.org/10.1190/segam2012-0700.1 (Chapter 5)

Clark, D.A., 2010. Correction of Electric and Magnetic Fields and Gradients Measured Within and Around an Insulating Sensor Capsule in Seawater. OCEANS ’10 IEEE Conference, Sydney, 24-27 May 2010. 9p. doi: 10.1109/OCEANSSYD.2010.5603523 (https://wiki.csiro.au/confluence/download/attachments/457769088/CLARK+OCEANS10+paper+IEEE.pdf) (Chapter 6)

ACKNOWLEDGEMENTS

I thank my supervisors, Drs Mark Lackie and Richard Flood for their support, encouragement, and patience during the long slog of a part time Ph.D. candidacy. Through long years of association with the CSIRO, I have benefited greatly from interactions with many colleagues, some of whom I would like to mention here. Thanks go to my CMSE associates, especially Keith Leslie, Cathy Foley, Jeanne Young, David Tilbrook, Shane Keenan, Chris Lewis and Kyle Blay, and to my past CESRE colleagues, including Bruce Dickson, Silvana Geuna, and David French. I have enjoyed the interactions with current CESRE post-doctoral fellows, James Austin and Dean Hillan. Clive Foss was very helpful in providing data that was used in this thesis. I would like to particularly acknowledge my longstanding collaborator of 35 years, Phil Schmidt. Other acknowledgements specific to particular studies are given in the relevant chapters of the thesis.

CHAPTER 1: INTRODUCTION

Magnetic surveys rapidly provide cost-effective information on the magnetisation distribution of the Earth's crust, at all scales from local to global. In particular, aeromagnetics is the most widely used geophysical method in hard rock mineral exploration from prospect to province scales. Over time, improvements in acquisition, processing, display, and interpretation of magnetic survey data have led to new applications and greater acceptance by geologists, archaeologists and other non-specialists. New types of magnetic sensor, in particular tensor gradiometers, are being deployed or are under development. There is therefore a particular need to develop new methods that efficiently process gradient tensor data, exploit the extra information, and improve interpretability. All the methods presented in this thesis for interpretation of magnetic gradient tensor data can also be applied to tensor components calculated from conventional magnetic survey data of sufficiently high quality. This means that value can be added to existing high resolution surveys, by reprocessing them to exploit the latent, but cryptic, information that is present in single component data, although it can be shown that best results will be obtained from measured, rather than calculated, gradient tensor data. Regardless of new acquisition and processing techniques, it should be noted that better geophysical models are of limited use if they are not interpreted in terms of plausible geological models.

Chapter 3 presents new methods for interpretation of magnetic gradient tensor data, either measured directly or calculated from high quality conventional surveys, with emphasis on the utility of the normalised source strength (NSS). The NSS is a rotational invariant, calculated from the eigenvalues of the tensor, that has many attractive properties. In particular for dipole sources the NSS peaks directly over the source and is completely independent of the direction of magnetisation. This property extends to axially magnetised pipes (pole-type sources) and all 2D sources. Because the NSS is not a potential field, care must be exercised when calculating vertical derivatives or continuing it to a different level above the sources. Chapter 3 presents an algorithm for this purpose. Besides the geological applications, the algorithms for the dipole model are readily applicable to the detection, location and characterization (DLC) of magnetic objects, such as naval mines, unexploded ordnance, shipwrecks, archaeological artefacts and buried drums.

Chapter 4 applies the newly developed methods for source location and determination of magnetisation to analysis of the well-known remanence-dominated magnetic anomaly at the Mount Leyshon breccia-hosted, porphyry-related gold deposit in Queensland. Chapter 4 also discusses the merits of calculated, versus measured, magnetic vector and tensor data. Chapter 5 is a case study that analyses magnetic gradient tensor data over the Tallawang magnetite skarn in New South Wales.

Although considerable attention has been paid to magnetic gradient tensor data acquired in a non-conductive environment such as air, where the tensor is symmetric, there has been little analysis of measurements made in an electrically conductive medium, such as seawater. In the presence of electric current distributions, the gradient tensor is asymmetric. This raises the question of how the symmetric gradient tensor measured within an insulated capsule relates to the asymmetric tensor within the surrounding medium. Chapter 6 addresses the issue of relating electric and magnetic field and gradient measurements made in an insulating capsule to the unperturbed quantities that prevailed before insertion of the capsule. The effects of water flow around the capsule are also analysed. This has implications for marine controlled source electromagnetic surveys, magnetic gradient tensor measurements in the ocean, and marine magnetotellurics, as well as potential application to satellite measurements within the magnetosphere.

Chapter 7 describes two new methods for remote determination of magnetisation of isolated magnetic bodies, which are particularly useful for remanence-dominated magnetic sources. The first method estimates the magnetic moment and location of the source from integral moments of rotational invariants of the gradient tensor. This method was successfully applied to analysis of several remanently magnetised intrusions, hosted by weakly magnetic sediments, in northern New South Wales, yielding results that agreed well with detailed inversions of the magnetic survey data. Chapter 7 also gives the theory behind a second proposed method to determine magnetic properties, which exploits local perturbation of natural geomagnetic variations by a magnetic source. This method yields estimates of the resultant magnetisation direction, the direction of remanence, and the Koenigsberger ratio of the source, without making any assumptions about its geometry. Furthermore, if the source is compact, this method gives a direct indication of direction to source, which can be exploited for drill targetting.

Assuming without evidence that magnetic sources are magnetised parallel to the geomagnetic field can seriously mislead interpretation and can result in drill holes missing their targets. In Chapter 8 I review methods that are available for estimating, directly or indirectly, the natural remanent magnetisation (NRM) and total magnetisation of magnetic sources, noting the strengths and weaknesses of each approach. Characterising the total and remanent magnetisations of sources is important for several reasons:

1. knowledge of total magnetisation is often critical for accurate determination of source geometry and position,
2. knowledge of magnetic properties such as magnetisation intensity and Koenigsberger ratio constrains the likely magnetic mineralogy (composition and grain size) of a source, which gives an indication of its geological nature,
3. determining the direction of a stable ancient remanence gives an indication of the age of magnetisation, which provides useful information about the geological history of the source and its environs,
4. several methods exist for estimating the magnetic moment vector of a source, without any knowledge of its shape. This yields directions of the resultant magnetisation (remanent plus induced), which is crucial for accurate modelling, and gives an indication of the size of the source, when plausible magnetisation intensities are assumed.

Predictive magnetic exploration models for porphyry copper and iron oxide copper-gold (IOCG) deposits can be derived from standard geological models by integrating magnetic petrological principles with petrophysical data, deposit descriptions, and modelling of observed magnetic signatures of these deposits. Even within a particular geological province, the magnetic signatures of similar deposits may differ substantially, due to differences in the local geological setting. Searching for “look-alike” signatures of a known deposit is likely to be unrewarding unless pertinent geological factors are taken into account. These factors include the tectonic setting and magma type, composition and disposition of host rocks, depth of emplacement and post-emplacement erosion level, depth of burial beneath younger cover, post-emplacement faulting and tilting, remanence effects contingent on ages of intrusion and alteration, and metamorphism. Because the effects of these factors on magnetic signatures are reasonably well understood, theoretical magnetic signatures appropriate for the local geological environment can qualitatively guide exploration and make semiquantitative predictions of anomaly amplitudes and patterns.

The predictive models also allow detectability of deposit signatures to be assessed, for example when deposits are buried beneath a considerable thickness of nonmagnetic overburden, are covered by highly magnetic heterogeneous volcanic rocks, or there is a strong regional magnetic gradient.

Chapter 9 provides a review of the effects of hydrothermal alteration on magnetic properties within mineralised systems, including implications for mineral exploration. In particular, Chapter 9 discusses magnetic signatures of porphyry copper and iron oxide copper-gold (IOCG) systems and presents examples of magnetic exploration models, and their predicted signatures, in various geological settings, including circumstances in which remanence may make an important contribution to their magnetic signatures.

The theme of this thesis is that maximum benefit can be obtained from future developments in magnetics by adopting an *integrated* approach, whereby new technologies that generate information-rich, but complex multicomponent data, are efficiently processed to produce more interpretable parameters, which are used to generate source locations and inferred magnetisations that can then be interpreted geologically. Information on total magnetisation and remanence that is derived from analyses of these information-rich data sets can be used to constrain geometry, probable lithology, and geological history of sources. A final geological interpretation that is used to define exploration targets should incorporate insights from magnetic petrological principles and predictive exploration models.

Because the majority of the chapters in this thesis are in the form of published or accepted papers, each chapter has its own reference list at the end.

CHAPTER 2: UTILITY OF MAGNETIC TENSOR GRADIOMETRY AND PROPERTIES OF THE MAGNETIC GRADIENT TENSOR

Introduction

Airborne, ground and marine magnetic surveys have improved dramatically over the past three decades with advances in data acquisition, image processing, potential theory-based signal processing, and automated interpretation techniques (Nabighian et al., 2005a). Magnetic surveys form an integral part of exploration programs and are now routinely undertaken before geological mapping programs. The availability of mature, affordable sensing technologies, particularly optical pumping magnetometers, that can measure the absolute magnitude of the geomagnetic field, generally called the total magnetic intensity (TMI), at a high sampling rate has revolutionised data acquisition. TMI measurements with these sensors can be made with great precision, to sub nanoTesla (nT) levels, at sampling rates of 10 Hz or greater. The precision and accuracy of modern TMI surveys is generally limited by the quality of compensation for magnetic effects of the sensor platform (e.g. the aircraft for airborne surveys), the ability to remove geomagnetic variations during the survey, and practical constraints on line spacing, rather than by instrumental noise. For these reasons the overwhelming majority of modern magnetic surveys, on the ground as well as in the air, use TMI sensors.

These advances have been made despite relying only on scalar information and, in many processing methods, by treating the measured anomalous TMI as a potential field, which is strictly true only as a first order approximation. For anomalous fields that are much smaller than the background geomagnetic field, the first order approximation is quite accurate and the anomalous TMI is essentially equivalent to a single vector component, namely the projection of the anomalous field vector onto the regional geomagnetic field direction (Hughes and Pondrom, 1947). If accurate full three-component vector information could be retrieved, either by direct measurement or by mathematical manipulation, magnetic surveys could be improved even further. The extra information provided by the two additional vector components could help to constrain source geometries. Furthermore, for strong anomalies vector data could be used to correct the measured TMI, so it represents a true potential field.

Vector surveys, where the direct measurement of vector components has been attempted, have met with mixed success. An example of a successful airborne vector magnetic survey, in which useful extra information about remanently magnetised banded iron-formations

(BIFs) was provided by vector measurements, is given by Dransfield et al. (2003). In this case, very large anomalies due to BIFs, accurate measurements of aircraft attitude, and careful aircraft compensation gave an acceptable signal-to-noise ratio for the orientation-corrected vector magnetic data. The accuracy of direct measurement of the field vector is largely governed by orientation errors, which for mobile platforms are generally so large that the theoretical derivation of the components from densely sampled TMI is usually preferable. For example, an orientation error of 0.1° produces an error of up to ~100 nT in an unfavourably oriented vector component. For this reason, and others listed below, it is desirable to measure the field gradient(s), rather than the field vector.

Gradient measurements are much less sensitive to sensor orientation than vector measurements. This is because gradients arise largely from relatively near anomalous sources, which are the targets of interest, whereas the background (core field) geomagnetic gradient is relatively low (typically 0.01 – 0.03 nT/m). This contrasts with the field vector, which is dominated almost everywhere by the background field that arises from the Earth's core and has a typical magnitude of ~50,000 nT. Gradient measurements are therefore most appropriate for mobile applications.

Another advantage of gradient measurements is that they suppress, through common mode rejection, time-varying background fields such as diurnal variations, geomagnetic pulsations and magnetic storms, which arise from distant electric currents in the ionosphere and magnetosphere,. This obviates the need for base stations. They also greatly reduce the need for regional corrections, which are required for interpretation of TMI surveys because regional fields arise from deeper crustal sources that are normally not of exploration interest, or from the normal (quasi-) latitudinal intensity variation of the global field.

Gradient measurements also provide valuable additional information, compared to conventional total field measurements, when the field is undersampled. Undersampling is common perpendicular to flight lines in airborne surveys, is usual in ground surveys, and always pertains in down-hole surveys. Conditions under which calculation of vectors and gradient tensors from sufficiently densely and accurately sampled TMI data is actually preferable to direct measurement of these quantities have hitherto not been characterised by modelling and case studies. Chapters 3 and 5 present a case study from the Tallawang magnetite deposit, in central NSW, that compares measured gradient tensor data with calculated gradient tensors, derived from a detailed TMI survey. Criteria for the maximum

permissible sample spacing for which vector components and gradient tensors can be reliably calculated are developed in Appendix II of Chapter 4. Synergistic interpretation of calculated vectors and measured gradients may allow significantly more information to be extracted from airborne surveys.

General advantages of gradient measurements

The advantages of magnetic gradient surveys for mineral exploration and detailed geological mapping are well known and have been discussed by a number of authors, including Hood (1965, 1981) and Hood and Teskey (1981), who emphasise vertical gradient of TMI measurements, Harrison and Southam (1991), who discuss applications to marine magnetic anomalies, and Hardwick (1996, 1999) and Reford (2006), who emphasise transverse horizontal gradient of TMI measurements. These advantages include:

1. Gradiometry gives better resolution of shallow features, and closely spaced sources and structural features, compared to TMI or vector measurements
2. Gradiometry suppresses regional anomalies due to deep sources
3. Gradiometry is particularly useful as a subvertical contact mapper
4. Gradient anomalies are tighter around compact sources than field anomalies
5. Gradiometry aids detection and delineation of pipe-like sources
6. Gradiometry along widely spaced lines constrains local strike direction*
7. Gradiometry determines on which side of a profile the source lies*
8. Gradiometry provides common mode rejection of geomagnetic variations
9. Gradiometry is relatively insensitive to rotation noise
10. Gradiometry constrains interpolation between profiles* (important as all airborne surveys are aliased to some extent across flight lines; similarly marine surveys and some ground surveys are aliased across profiles)
11. IGRF corrections are less important for gradiometry (usually unnecessary)
12. Gradiometry provides direct indication of Euler structural index when combined with measurements of field
13. Higher resolution of gradiometric surveys compared to conventional TMI surveys can be offset against survey height, allowing somewhat higher, therefore considerably safer, flying.

*not vertical TMI gradients

Nobukazo et al. (1993) discussed the extra information obtainable from vector, as opposed to scalar, measurements for marine magnetic surveys with typically wide line spacing. In particular, the location and strike direction of boundaries between crustal units of contrasting magnetisation are better constrained by vector data. As mentioned above, vector measurements are afflicted by orientation noise and are generally not practical for airborne or ground surveys. However the theoretical advantages of vector measurements also apply to three-axis TMI gradient surveys and *a fortiori* to gradient tensor measurements.

Regarding point 9 above, consider a simple numerical example. Directly above a vertically magnetised dipole source of moment 5×10^5 Am², 100 m below the sensor, in a vertical geomagnetic field of 60,000 nT, the anomalous field components are $b_x = b_y = 0$, $b_z = 100$ nT, so the resultant vertical field is 60,100 nT. The corresponding nonzero anomalous gradient tensor elements are $B_{xx} = B_{yy} = -1.5$ nT/m, $B_{zz} = 3$ nT/m and the IGRF gradients are $G_{xx} = G_{yy} = -0.015$ nT/m, $G_{zz} = 0.03$ nT/m. As the tensor is diagonal in the geographic reference frame, the diagonal components are also the eigenvalues of the tensor. A 1° error in sensor orientation produces apparent anomalous vector components, after subtraction of the IGRF field, of 90.85 nT (vertical) and 1049 nT (horizontal). The apparent magnitude of the anomalous field vector is overestimated by a factor of ten and the apparent direction to the source is off by 85°. On the other hand, the apparent gradient tensor components are $B_{xx} = B_{yy} = -1.515$ nT/m, $B_{zz} = 3.03$ nT/m, with an off-diagonal component of 0.079 nT/m. The apparent tensor magnitude is only in error by ~1% if the regional gradient is ignored, and 0.02% if the regional gradient is subtracted. The apparent direction to source, given by the major eigenvector, is 1° off vertical, simply reflecting the misorientation of the sensor. The effect on the estimated source direction of ignoring the regional gradient is only 0.01°.

Total field gradient surveys, using two, three or four total field sensors, are common. An array of four TMI sensors provides an approximation to the vector gradient of the TMI, which represents a comparable amount of information to a three vector component survey, but with much less dramatic sensitivity to orientation. While TMI gradiometer surveys share many of the advantages of tensor gradients, such as obviating or ameliorating the need for base stations and regional corrections, total field gradients are not true potential

fields (Schmidt and Clark, 2006) and do not provide as much information as the full gradient tensor, which has five independent components.

Properties of the magnetic gradient tensor

The magnetic gradient tensor **B** is defined as the vector gradient of the magnetic field vector **b**:

$$\mathbf{B} = \nabla \mathbf{b}. \tag{1}$$

For static fields in the absence of conduction currents,

$$\nabla \times \mathbf{b} = 0, \tag{2}$$

which implies that **b** can be expressed as the gradient of a scalar potential:

$$\mathbf{b} = -\nabla \Omega, \tag{3}$$

where Ω is the magnetic scalar potential.

With respect to Cartesian axes **B** has nine components, B_{ij} (i, j = x, y, z), which may displayed as a matrix:

$$\mathbf{B} = \begin{bmatrix} B_{xx} & B_{xy} & B_{xz} \\ B_{yx} & B_{yy} & B_{yz} \\ B_{zx} & B_{zy} & B_{zz} \end{bmatrix} = \begin{bmatrix} \frac{\partial b_x}{\partial x} & \frac{\partial b_y}{\partial x} & \frac{\partial b_z}{\partial x} \\ \frac{\partial b_x}{\partial y} & \frac{\partial b_y}{\partial y} & \frac{\partial b_z}{\partial y} \\ \frac{\partial b_x}{\partial z} & \frac{\partial b_y}{\partial z} & \frac{\partial b_z}{\partial z} \end{bmatrix} = -\begin{bmatrix} \frac{\partial^2 \Omega}{\partial x^2} & \frac{\partial^2 \Omega}{\partial x \partial y} & \frac{\partial^2 \Omega}{\partial x \partial z} \\ \frac{\partial^2 \Omega}{\partial y \partial x} & \frac{\partial^2 \Omega}{\partial y^2} & \frac{\partial^2 \Omega}{\partial y \partial z} \\ \frac{\partial^2 \Omega}{\partial z \partial x} & \frac{\partial^2 \Omega}{\partial z \partial y} & \frac{\partial^2 \Omega}{\partial z^2} \end{bmatrix}. \tag{4}$$

In a source free region Ω and its derivatives of all orders are continuously differentiable functions, so the order of differentiation on the RHS of (4) can be reversed. This implies that the tensor is symmetric:

$$B_{ij} = B_{ji}, \forall i, j, \tag{5}$$

a conclusion which also follows directly from (2).

Furthermore, since

$$\nabla.\mathbf{b} = \frac{\partial b_x}{\partial x} + \frac{\partial b_y}{\partial y} + \frac{\partial b_z}{\partial z} = 0, \tag{6}$$

it follows that the tensor is traceless:

$$B_{xx} + B_{yy} + B_{zz} = 0. \tag{7}$$

The symmetry and tracelessness of the tensor imply that, of the nine tensor components, only five are independent.

Equations (3) and (6) also imply that Ω obeys Laplace's equation in the source free region:

$$\nabla^2 \Omega = \frac{\partial^2 \Omega}{\partial x^2} + \frac{\partial^2 \Omega}{\partial y^2} + \frac{\partial^2 \Omega}{\partial z^2} = 0. \tag{8}$$

Differentiation of eqn (8) shows that each of the field and gradient tensor components also obeys Laplace's equation:

$$\nabla^2 b_i = -\nabla^2 \left(\frac{\partial \Omega}{\partial i} \right) = -\frac{\partial}{\partial i} \left(\nabla^2 \Omega \right) = 0, \tag{9}$$

$$\nabla^2 B_{ij} = -\nabla^2 \left(\frac{\partial^2 \Omega}{\partial i \partial j} \right) = -\frac{\partial^2}{\partial i \partial j} \left(\nabla^2 \Omega \right) = 0. \tag{10}$$

Equations (9) and (10) have important implications for analytic continuation of field and tensor components and for interrelationships between different components in the space and spatial frequency domains.

Advantages of gradient tensor data

Pedersen and Rasmussen (1990) discuss in some detail the practical problems encountered in the collection and processing of gradient tensor data and the benefits obtainable from acquisition of tensor data. For instance, these workers point out that resolution is enhanced compared to conventional magnetic surveys and that rotational invariants calculated from tensor data have attractive properties for interpretation. Christensen and Rajagopalan (2000) suggested that the next breakthrough in magnetic exploration is likely to be the measurement of the gradient tensor and demonstrated the utility of analytic signal

amplitudes (total gradients) of vector components, which can be derived directly from gradient tensor components, for locating boundaries and interpreting source geometries in the presence of remanence.

The recent development of full tensor gravity gradiometry and derived, highly refined, systems such as FALCON^{TM} have revolutionised marine, and particularly airborne, gravity surveys (Nabighian et al., 2005b). This renewed interest in the gravity gradient tensor has stimulated interest in interpretation methods for magnetic gradient tensor data, as there are many mathematical similarities between the two types of data.

Schmidt and Clark (2006) have summarised benefits of gradiometry in general and tensor gradiometry in particular. Benefits that are specific to gradient tensor surveys include:

1. Gradient tensor surveys retain benefits of vector surveys, without disadvantage of extreme orientation sensitivity.
2. Tensor elements are true potential fields, with desirable mathematical properties (important in areas with strong anomalies), which allows rigorous continuation, RTP, magnetisation mapping, etc.
3. Very rapid sampling rate of SQUID sensors allows unaliased detection of high frequency aircraft noise and efficient removal by filtering, whereas total field magnetometers have much slower sampling, causing compensation problems.
4. Redundancy of tensor components gives inherent error correction and noise estimates.
5. A wide range of new types of processed data is possible with full tensor data: invariants, directional filters, depth slicing, source moments and dipole location unaffected by sensor misorientation.
6. Rotational invariants, which are inherently robust against sensor misorientation, are readily calculated from the tensor elements.
7. Invariant quantities, with higher resolving power than the analytic signal, can be derived from tensor data.
8. Gradient tensor surveys allow direct determination of the 3D analytic signal (defines source outlines; width/depth determinations that are only weakly sensitive to remanent magnetisation).
9. Each tensor component represents a directional filter, emphasising structures in particular orientations.

10. Measurement of the tensor allows calculation of parameters unaffected by aliasing across flight lines.
11. Superior Euler deconvolution solutions can be obtained using true measured gradients along and across lines.
12. Tensor elements are independent of skewing caused by the geomagnetic field direction, which improves interpretability.
13. Combinations of tensor components give information on magnetisation directions.
14. Measurement of the full tensor allows rotation of co-ordinate system, yielding transformed tensor components that emphasise specified structural orientations.
15. Full tensor data defines the direction to a compact (dipole) source and its magnetic moment directly from as few as two station measurements.
16. Full tensor data gives improved resolution of pipe-like bodies and sources subparallel to the flight path.
17. Full tensor data improves delineation of N-S elongated sources in low latitudes.
18. Development of full tensor sensors should have spin-off applications to down-hole magnetics and remote determination of source magnetic properties *in situ*.

Barnes et al. (2008) showed very clearly the advantages of gravity gradient tensor measurements over single component measurements for locating sources between survey lines and for determining orientations of contacts, even for compact sources, when survey lines are too widely spaced to completely define the field between the lines. In these circumstances, robust and accurate solutions for source parameters such as source density contrast, location and orientation can be obtained by inverting single lines of gradient tensor data, whereas inversion of single component data for the same sources produces inaccurate and misleading solutions. Those authors also showed that the same principle applies to the regional-residual separation problem, which is much more clear-cut when gradient tensor data are available. These advantages of gravity gradient tensor measurements apply *a fortiori* to magnetic gradient tensor data, because magnetic anomalies have additional complexity due to possible variations in magnetisation directions. Inverting for source magnetisation directions, as well as intensities, requires extra information that is best supplied by full magnetic gradient tensor data.

Apart from their uses in systematic magnetic surveys, gradient tensor measurements have a specific application to manoeuvrable search platforms that home onto compact magnetic targets, such as buried land mines, naval mines and unexploded ordnance (UXO). For

example, Wiegert and Oeschger (2006) and Wiegert et al. (2007) describe the application of sensor platforms with multiple tensor gradiometers for guidance towards a magnetic target and real time detection, localisation and classification (DLC) of targets.

Calculation of gradient tensors from TMI surveys

Vestine and Davids (1945) showed that three orthogonal components of a potential field vector could be derived from knowledge of a single component, along a fixed direction, over a horizontal plane that lies above all the sources. Hughes and Pondrom (1947) presented a method for deriving vertical and horizontal components of the anomalous magnetic field from TMI data, which was just becoming available due to the introduction of the proton precession magnetometer, so that newer surveys could be compared to older data sets acquired with fluxgate magnetometers. Baranov (1975) gives a comprehensive treatment of relationships in the space and wavenumber domains between field components, including TMI, their continuations and derivatives. Purucker (1990) described and evaluated the strengths and weaknesses of the available methods (Fourier filtering, convolution filtering, and equivalent source techniques) for calculating vector components from TMI, and Lima and Weiss (2009) give a detailed treatment of the underlying mathematical assumptions and numerical stability of algorithms for calculating all field components from a single measured component.

Schmidt and Clark (1998) discussed the calculation of vector components from the TMI, drawing on the Fourier domain method of Lourenço and Morrison (1973), then used integral moments of these components to calculate magnetic moments of isolated sources according to a modification of the method originally proposed by Helbig (1963), and finally compared the theoretical derivations with laboratory measurements to demonstrate the validity of the approach. Helbig's approach is attractive because it does not make any assumptions about source geometry, apart from a prohibition on the body extending to infinity in any direction. Phillips (2005) has since taken these ideas further by using a moving window to generalise the technique to tackle larger areas, and also to search for sources with specified directions of magnetization. Recently, Caratori Tontini and Pedersen (2008) have extended Helbig's method to calculation of second order integral moments of gridded magnetic component data to estimate the depth and horizontal location of the centres of magnetisation of extended, but finite, sources. Helbig's method

can also be applied to gradient tensor data. Phillips et al. (2007) show that second moments of the tensor elements provide information about the magnetic moment.

Over local and small regional scales, computation of magnetic vector components from gridded TMI data on a horizontal plane can be performed efficiently using the Fast Fourier Transform (FFT) algorithm. The 2D Fourier transform of a function $f(x, y)$ is given by:

$$F(k_x, k_y) = \Im[f(x,y)] = \int_{-\infty}^{\infty}\int_{-\infty}^{\infty} f(x,y)\exp(-i[k_x x + k_y y])dxdy, \tag{11}$$

which has inverse

$$f(x,y) = \Im^{-1}[F(k_x, k_y)] = \frac{1}{4\pi^2}\int_{-\infty}^{\infty}\int_{-\infty}^{\infty} F(k_x, k_y)\exp(i[k_x x + k_y y])dk_x dk_y. \tag{12}$$

where k_x and k_y are the wavenumbers along the horizontal x and y axes respectively, and the radial wavenumber $|k| = \sqrt{(k_x^2 + k_y^2)}$.

In the wavenumber domain the grid north, grid east and vertical down components (b_x, b_y, b_z) of the anomalous field vector **b** are related to the anomalous TMI, ΔT, by (Blakely, 1996, p.329, 342-343)

$$\Im[b_x] = \frac{ik_x\Im[\Delta T]}{|k|n + i(k_x\ell + k_y m)}, \quad |k| \neq 0, \tag{13}$$

$$\Im[b_y] = \frac{ik_y\Im[\Delta T]}{|k|n + i(k_x\ell + k_y m)}, \quad |k| \neq 0 \tag{14}$$

$$\Im[b_z] = \frac{|k|\Im[\Delta T]}{|k|n + i(k_x\ell + k_y m)}, \quad |k| \neq 0, \tag{15}$$

where (ℓ, m, n) are the direction cosines of the regional geomagnetic field **F** = $F(\ell, m, n)$ = (F_x, F_y, F_z) with respect to x, y, z, and ΔT is given by the projection of the anomalous field vector onto the regional field direction:

$$\Delta T = \frac{\mathbf{b}.\mathbf{F}}{F} = b_x \ell + b_y m + b_z n. \tag{16}$$

Equation (16) implies that ΔT is harmonic, i.e. it obeys Laplace's equation, because it is a linear combination of field components, each of which is harmonic by eqn (9).

It should be noted, however, that calculation of vector components from measured TMI surveys requires high quality, well levelled data, densely sampled to avoid aliasing. This applies even more strongly to calculation of gradient tensor components from TMI, because of the amplification of high frequencies, including noise, associated with differentiation of the field components. Furthermore, this processing becomes unstable close to the geomagnetic equator (Blakely, 1996, p.342-343). When the regional field inclination is zero, small to moderate anomalous field components in the magnetic E-W vertical plane have negligible effect on the measured TMI. In the presence of remanently magnetised elongated structures parallel to the magnetic meridian, which can produce substantial vertical and east components, these components cannot be reliably recovered from the TMI when the field inclination is too low.

These considerations also apply to calculation of gradient tensor elements from measured TMI surveys, which can in principle be accomplished by Fourier domain filtering of high quality TMI surveys by applying derivative filters to calculated vector components. The relationships in the Fourier domain between elements B_{ij} of the anomalous gradient tensor $\mathbf{B} = \nabla\mathbf{b}$ and anomalous TMI can be derived from relationships between a potential field and its directional derivatives. The DC ($|k| = 0$) components of the spectra are set to zero for all anomalous field and tensor components, as these components average to zero over the horizontal plane, for sources of finite horizontal and vertical extent. In practice with real data, after removal of regional trends the average value of each component is subtracted from its gridded values, to comply with this constraint. Applying relationships given by Blakely (1996, p.324-326) yields for $|k| > 0$ and $n \neq 0$:

$$\Im[B_{xx}] = \Im\left[\frac{\partial b_x}{\partial x}\right] = ik_x \Im[b_x] = \frac{-k_x^2 \Im[\Delta T]}{|k|n + i(k_x \ell + k_y m)}, \tag{17}$$

$$\Im[B_{xy}] = \Im\left[\frac{\partial b_y}{\partial x}\right] = ik_x \Im[b_y] = \frac{-k_x k_y \Im[\Delta T]}{|k|n + i(k_x \ell + k_y m)}, \tag{18}$$

$$\Im[B_{xz}] = \Im\left[\frac{\partial b_z}{\partial x}\right] = ik_x \Im[b_z] = \frac{ik_x |k| \Im[\Delta T]}{|k| n + i(k_x \ell + k_y m)}, \tag{19}$$

$$\Im[B_{yy}] = \Im\left[\frac{\partial b_y}{\partial y}\right] = ik_y \Im[b_y] = \frac{-k_y^2 \Im[\Delta T]}{|k| n + i(k_x \ell + k_y m)}, \tag{20}$$

$$\Im[B_{yz}] = \Im\left[\frac{\partial b_z}{\partial y}\right] = ik_y \Im[b_z] = \frac{ik_y |k| \Im[\Delta T]}{|k| n + i(k_x \ell + k_y m)}, \tag{21}$$

$$\Im[B_{zz}] = \Im\left[\frac{\partial b_z}{\partial z}\right] = |k| \Im[b_z] = \frac{|k|^2 \Im[\Delta T]}{|k| n + i(k_x \ell + k_y m)}, \tag{22}$$

Equations (17)-(22) show that the gradient tensor elements measured on a plane above the sources are interrelated. For $|k| > 0$:

$$\Im[B_{xx}] = \frac{ik_x}{|k|^2} \Im[B_{xz}] = -\frac{k_x^2}{|k|^2} \Im[B_{zz}], \tag{23}$$

$$\Im[B_{xy}] = \frac{ik_x}{|k|} \Im[B_{yz}] = \frac{ik_y}{|k|} \Im[B_{xz}] = \frac{-k_x k_y}{|k|^2} \Im[B_{zz}], \tag{24}$$

$$\Im[B_{xz}] = \frac{ik_x}{|k|} \Im[B_{zz}] = -\frac{i}{|k|} \left(k_x \Im[B_{xx}] + k_y \Im[B_{xy}]\right), \tag{25}$$

$$\Im[B_{yy}] = \frac{ik_y}{|k|} \Im[B_{yz}] = -\frac{k_y^2}{|k|^2} \Im[B_{zz}], \tag{26}$$

$$\Im[B_{yz}] = \frac{ik_y}{|k|} \Im[B_{zz}] = -\frac{i}{|k|} \left(k_x \Im[B_{xy}] + k_y \Im[B_{yy}]\right), \tag{27}$$

$$\Im[B_{zz}] = -\Im[B_{xx}] - \Im[B_{yy}] = -\frac{i}{|k|} \left(k_x \Im[B_{xz}] + k_y \Im[B_{yz}]\right), \tag{28}$$

Nelson (1988) derived relationships (23)-(28), from which it follows that, at least in principle, knowledge of B_{zz} everywhere on a horizontal plane determines all other tensor

elements on that plane, and hence everywhere in the source free region above and below the plane. For example,

$$B_{xy}(x,y)=\Im^{-1}\left(\Im\left[B_{xy}(k_x,k_y)\right]\right)=\Im^{-1}\left[\frac{-k_xk_y}{|k|^2}\Im\left[B_{zz}\right]\right],\quad |k|\neq 0. \tag{29}$$

The other tensor components can be determined similarly from the Fourier transform of B_{zz}. However knowledge of the vertical derivatives of both horizontal field components (i.e. of B_{xz} and B_{yz}), or alternatively knowledge of B_{xx} and B_{yy}, is required to determine the other tensor components.

In a similar vein, Nelson (1988) showed how TMI *gradient* data can be processed in the frequency domain to calculate grids of gradient tensor elements. For example:

$$\Im\left[B_{zz}\right]=\frac{|k|}{|k|n+i\left(k_x\ell+k_ym\right)}\Im\left[\frac{\partial\Delta T}{\partial z}\right]=\frac{-i}{|k|n+i\left(k_x\ell+k_ym\right)}\left(k_x\Im\left[\frac{\partial\Delta T}{\partial x}\right]+k_y\Im\left[\frac{\partial\Delta T}{\partial y}\right]\right), \tag{30}$$

from which all other tensor elements can be calculated by using (17)-(21). Equations (13)-(15), (23)-(28) and (30) yield the following expressions for the field components in terms of the TMI gradients:

$$\Im\left[b_x\right]=\frac{ik_x/|k|}{|k|n+i\left(k_x\ell+k_ym\right)}\Im\left[\frac{\partial\Delta T}{\partial z}\right]=\frac{k_x/|k|^2}{|k|n+i\left(k_x\ell+k_ym\right)}\left(k_x\Im\left[\frac{\partial\Delta T}{\partial x}\right]+k_y\Im\left[\frac{\partial\Delta T}{\partial y}\right]\right), \tag{31}$$

$$\Im\left[b_y\right]=\frac{ik_y/|k|}{|k|n+i\left(k_x\ell+k_ym\right)}\Im\left[\frac{\partial\Delta T}{\partial z}\right]=\frac{k_y/|k|^2}{|k|n+i\left(k_x\ell+k_ym\right)}\left(k_x\Im\left[\frac{\partial\Delta T}{\partial x}\right]+k_y\Im\left[\frac{\partial\Delta T}{\partial y}\right]\right), \tag{32}$$

$$\Im\left[b_z\right]=\frac{1}{|k|n+i\left(k_x\ell+k_ym\right)}\Im\left[\frac{\partial\Delta T}{\partial z}\right]=\frac{-i/|k|}{|k|n+i\left(k_x\ell+k_ym\right)}\left(k_x\Im\left[\frac{\partial\Delta T}{\partial x}\right]+k_y\Im\left[\frac{\partial\Delta T}{\partial y}\right]\right). \tag{33}$$

Either the vertical gradient of the TMI, or both horizontal gradients, is sufficient to calculate all vector and tensor components.

As usual, some caveats must be placed on Fourier domain processing of potential fields. Sampling must be sufficiently dense to reduce aliasing to negligible levels and precautions, such as removal of regional trends and judicious windowing of the data, must be taken to

minimise Gibbs phenomenon "ringing" and spectral leakage due to mismatches between opposite grid boundaries. A detailed discussion of the sampling density required to calculate vector and gradient tensor components accurately is given in the next section.

Another, fundamentally different, problem with calculation of vector components and gradient tensor elements from TMI survey data arises when very intense anomalies are present, so that the TMI locally departs significantly from a potential field. Schmidt and Clark (2006) give expressions for the departures of the Laplacian of the measured TMI from zero. In this case an iterative method can be employed to calculate the vector components correctly, as outlined by Schmidt and Clark (1998) and presented in detail by Clark (2013).

Denote the local field vector by $\mathbf{F}' = \mathbf{F}+\mathbf{b}$. Then the measured total field anomaly is given by:

$$\Delta B_m = |\mathbf{F}'| - |\mathbf{F}| = \sqrt{(F_x + b_x)^2 + (F_y + b_y)^2 + (F_z + b_z)^2} - F = |\mathbf{F} + \mathbf{b}| - F, \tag{34}$$

$$\therefore (\Delta B_m + F)^2 = \Delta B_m^2 + 2\Delta B_m F + F^2 = |\mathbf{F} + \mathbf{b}|^2 = F^2 + 2\mathbf{F}.\mathbf{b} + b^2. \tag{35}$$

Rearranging and using eqn (16):

$$\Delta B_m^2 + 2F\Delta B_m + F^2 = F^2 + 2F\Delta T + b^2, \tag{36}$$

which gives

$$\Delta B_m = \Delta T + \frac{b^2 - \Delta B_m^2}{2F}. \tag{37}$$

It can be seen from eqn (37) that the measured total field anomaly is only equal to ΔT to first order in $|\mathbf{b}|/F$. When anomalies are strong (thousands of nanoteslas) the difference between the two "total field" anomalies becomes significant. It can also be seen from (37) that the maximum error, for a given magnitude of the anomalous field vector $\boldsymbol{b}$, occurs when the anomalous field is oriented such that $\mathbf{F}'$ and $\mathbf{F}$ form an isosceles triangle, with base $\mathbf{b}$, in which case $\Delta B_\mathrm{m} = 0$. For example, the difference between the two types of total field anomaly can be as large as 1000 nT for a 10,000 nT anomaly in a 50,000 nT regional field.

Clark (2000) discussed the case of the magnetite-rich Osborne iron-oxide Cu-Au deposit in the Clocurry belt of NW Queensland, which is associated with a TMI anomaly of ~12,000 nT. The regional geomagnetic field in the vicinity of the deposit is locally deflected by the anomalous field, producing a significant difference between ΔB_{m} and ΔT. Figure 1(a) shows this difference for a profile across the deposit. Figure 1(b),(c) illustrate how this discrepancy is in fact fortuitously small for this deposit, due to a favourable geometry that partially suppresses the anomaly through self-demagnetisation. If the dip of the magnetite-rich body were vertical, or to the SW, rather than approximately perpendicular to the effective inducing field, the anomaly would be much larger and the deflection of the geomagnetic field, particularly on the SW flank of the anomaly, would be much greater. In these cases, the discrepancy between ΔB_{m} and ΔT would produce modelled dips that depart significantly from the true dip, if the modelling software calculated ΔT, according to the usual practice, and matched it to the measured TMI anomaly. This error is in addition to the very substantial error in interpreted dip if self-demagnetisation is neglected.

For this reason, it is recommended that magnetic modelling software should calculate ΔB_{m} rather than, or in addition to, ΔT for comparison with measured TMI data. This requires a simple modification of most programs, which calculate anomalous vector components as an intermediate step, then calculate ΔT using (16). Alternatively, ΔB_{m} can be calculated from the components using (34).

The gridded measured TMI, ΔB_m, is converted to the projection of the anomalous field vector onto the regional geomagnetic field direction, ΔT, which is a true potential field, from which the three orthogonal field components can then be reliably calculated. An initial estimate of the vector components on a regular grid is obtained by assuming that $\Delta B_m = \Delta T$. These approximate components are then used to estimate the difference between ΔB_m and ΔT, which is then used to obtain a better estimate of ΔT. The components are recalculated and the process is repeated, generally converging rapidly, until further improvement is negligible. The explicit correction procedure is given in Appendix I of Chapter 3.

Another useful attribute of ΔT anomalies is that contributions from multiple sources obey linear superposition (provided magnetostatic interactions between the sources can be neglected), whereas the ΔB_m anomaly due to multiple strongly magnetic sources is not

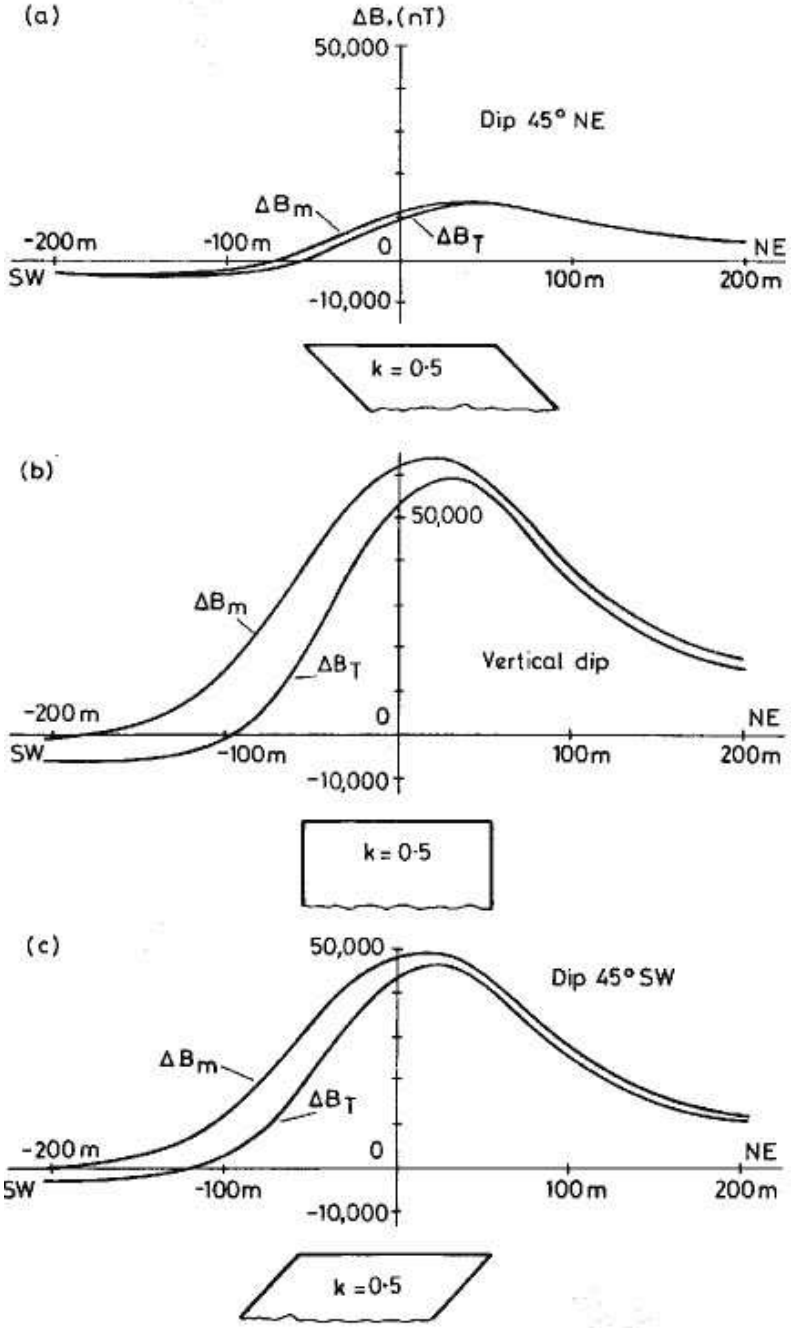

Fig.1. Modelled ΔB_m and ΔT profiles for a sheet-like source representing the main ironstone body (the original drill target) of the Osborne IOCG deposit (Clark, 2000). The assumed susceptibility, based on drill core measurements, is 0.5 G/Oe = 6.3 SI. (a) Geometry and anomalies that approximate the actual deposit, dipping NE. (b) Anomalies for the same body if it had vertical dip. (c) Anomalies for a SW dip.

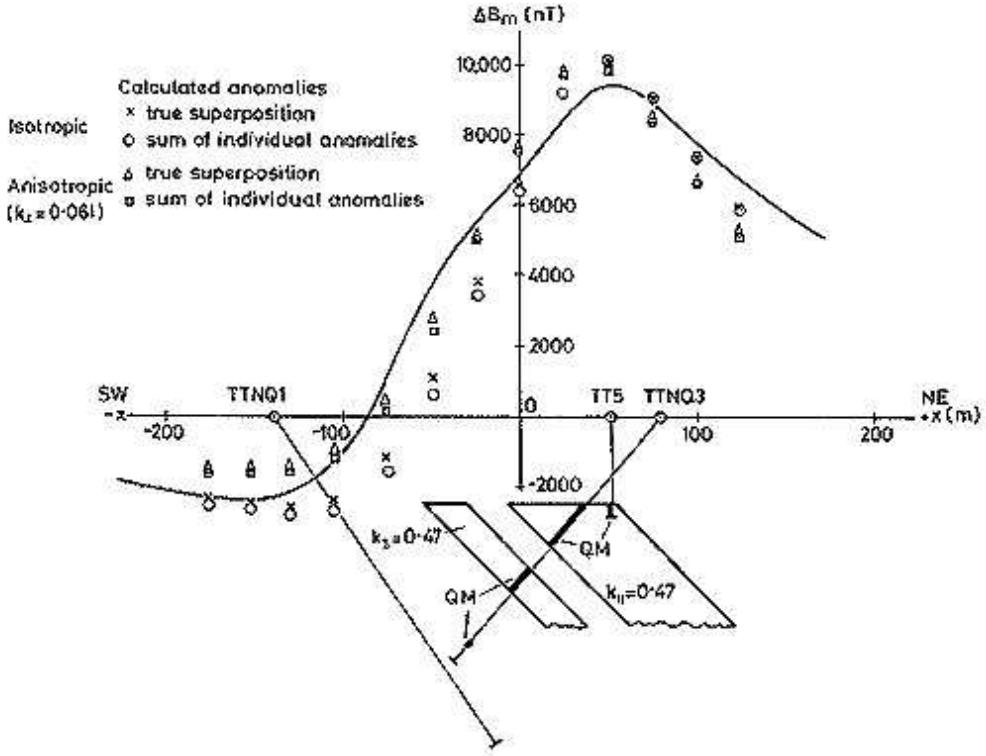

Fig.2. Observed (solid line) and calculated ground magnetic anomalies along line 1770N (Keel grid) over the Osborne deposit, showing a twin dipping sheet model, constrained by drill intersections. The first diamond drill hole (TTNQ1) was sited to intersect an interpreted SW dipping target and failed to intersect ironstone. TTNQ3 was the first hole based on incorporation of self-demagnetisation into modelling, which indicated a NE dip. About 5° of the error in interpreted dip is attributable to neglecting the difference between ΔB_m and ΔT. Note that the ΔB_m anomalies of the individual sheets do not strictly obey linear superposition. The convergent solution for ΔT represents a true potential field, from which field and gradient tensor components can be more reliably calculated.

exactly the sum of their individual anomalies. For direct comparison of modelled TMI anomalies from multiple sources with measured TMI, vector component anomalies from each body should be combined first, then the ΔB_m anomaly calculated from the components using eqn (34). Using the Osborne deposit again as an example, Fig.2 illustrates the differences between correctly combined ΔB_m anomalies from two magnetite-rich sheets and the anomaly obtained by simply adding the contributions from each sheet.

Although Fourier domain processing is very efficient, the computational advantages of Fourier filtering over space domain convolution filtering have become less significant as computer power has increased. Moreover, Fourier-based filters are somewhat inflexible, as they must be applied to a regular grid on a plane. Convolution filters are more flexible and, in some circumstances, can be more accurate than Fourier-based filters (Wang et al., 2008). It is therefore useful to give the space domain equivalents of the Fourier-based transformations given above.

The magnetic scalar potential at a height h above a horizontal plane can be calculated from the TMI on the plane $z = 0$ (Hughes and Pondrom, 1947; Robinson, 1970):

$$\Omega(x, y, z = -h) = \frac{1}{2\pi} \int_{-\infty}^{\infty}\int_{-\infty}^{\infty} \frac{(R\sin I + h)\Delta T(\xi,\eta,0)}{R[R + h\sin I + (x-\xi)\cos I]} d\xi d\eta, \quad (h > 0), \tag{43}$$

where $R = \sqrt{[(x-\xi)^2+(y-\eta)^2+h^2]}$ and I is the geomagnetic inclination.

Differentiating (43) with respect to h gives for the vertical field component on the plane $z = -h$:

$$b_z(x, y, z = -h) = -\left.\frac{\partial\Omega(x, y)}{\partial z}\right|_{z=-h} = \left.\frac{\partial\Omega(x, y)}{\partial h}\right|_{z=-h} \tag{44}$$

$$\therefore b_z(x, y, z = -h) = \frac{-1}{2\pi} \int_{-\infty}^{\infty}\int_{-\infty}^{\infty} \Delta T(\xi,\eta,0) K(x-\xi, y-\eta)\, d\xi d\eta, \tag{45}$$

where the convolution kernel K is given by:

$$K(x-\xi, y-\eta) = \frac{-\cos I\left(R\cos I + x - \xi\right) + h\sin I}{R\left[R + h\sin I + (x-\xi)\cos I\right]^2} + \frac{h^2\left[2R + h\sin I + (x-\xi)\cos I\right]}{R^3\left[R + h\sin I + (x-\xi)\cos I\right]^2}. \quad (46)$$

The convolution integral (45) is the space domain equivalent of eqn (15). Robinson (1970) also gives analogous expressions for the horizontal field components on the plane $z = -h$. These components can also be calculated by numerical differentiation of the scalar potential, calculated using (43), or from the following convolution integrals (Nabighian, 1984; Nelson, 1988):

$$b_x(x, y, z = -h) = \frac{-1}{2\pi} \int_{-\infty}^{\infty}\int_{-\infty}^{\infty} b_z(\xi, \eta, -h) \frac{(x-\xi)}{\left[(x-\xi)^2 + (\mathrm{y}-\eta)^2\right]^{3/2}} d\xi d\eta, \quad (47)$$

$$b_y(x, y, z = -h) = \frac{-1}{2\pi} \int_{-\infty}^{\infty}\int_{-\infty}^{\infty} b_z(\xi, \eta, -h) \frac{(\mathrm{y}-\eta)}{\left[(x-\xi)^2 + (\mathrm{y}-\eta)^2\right]^{3/2}} d\xi d\eta. \quad (48)$$

The five independent tensor elements B_{xx}, B_{xy}, B_{yy}, B_{xz}, B_{yz} on the plane $z = -h$ can be calculated from (45), (47), (48) by numerical differentiation. B_{zz} is, of course, determined once B_{xx} and B_{yy} are known, but it can also be calculated directly from knowledge of b_z on the same plane, using the following relationship (Baranov, 1975, p.73):

$$B_{zz}(x, y) = \int_0^{\infty} \frac{b_z(0) - \bar{b}_z(\rho)}{\rho^2} d\rho, \quad (49)$$

where $\rho = \sqrt{[(x-\xi)^2+(y-\eta)]^2}$ and

$$\bar{b}_z(\rho) = \frac{1}{2\pi}\int_0^{2\pi} b_z(\rho, \theta) d\theta, \quad (50)$$

is the average value of $b_z(\rho)$ on a circle of radius ρ centred on (x,y). The term $b_z(0)$ in the numerator of the integrand is required to remove the singularity at $\rho = 0$. In Cartesian co-ordinates eqn (50) becomes:

$$B_{zz}(x, y) = \frac{1}{2\pi} \int_{-\infty}^{\infty}\int_{-\infty}^{\infty} \frac{b_z(x, y) - b_z(\xi, \eta)}{\left[(x-\xi)^2 + (y-\eta)^2\right]^{3/2}} d\xi d\eta, \quad (51)$$

The reverse procedure is also straightforward. If the tensor element B_{zz} is measured on a horizontal plane, then b_z at a height h above the same plane can be derived using a convolution filter:

$$b_z(x, y, -h) = \frac{1}{2\pi} \int_{-\infty}^{\infty}\int_{-\infty}^{\infty} \frac{B_{zz}(\xi,\eta,0)d\xi d\eta}{\sqrt{(x-\xi)^2 + (y-\eta)^2 + h^2}}, \quad (h > 0). \tag{52}$$

Equation (52) represents the solution to the Neumann problem of potential theory (Baranov, 1975) and is similar to the relationship between the TMI anomaly above a horizontal plane and its vertical derivative on the plane (Henderson, 1970).

As $h \to 0$, the relationship between the vertical field and its azimuthally averaged vertical derivative on the same plane can be expressed as:

$$b_z(x, y) = \int_0^{\infty} \overline{B}_{zz}(\rho) d\rho. \tag{53}$$

Equation (53) is analogous to an expression, due to Ackerman and Dix (1955), that relates the first and second vertical derivatives of a gravity anomaly.

Knowledge of B_{zz} over a plane can determine all other gradient tensor elements, using the following convolution relationships (Nelson, 1988):

$$B_{xz}(x, y) = \frac{-1}{2\pi} \int_{-\infty}^{\infty}\int_{-\infty}^{\infty} B_{zz}(\xi,\eta) \frac{(x-\xi)}{\left[(x-\xi)^2 + (\mathrm{y}-\eta)^2\right]^{3/2}} d\xi d\eta, \tag{54}$$

$$B_{yz}(x, y) = \frac{-1}{2\pi} \int_{-\infty}^{\infty}\int_{-\infty}^{\infty} B_{zz}(\xi,\eta) \frac{(\mathrm{y}-\eta)}{\left[(x-\xi)^2 + (\mathrm{y}-\eta)^2\right]^{3/2}} d\xi d\eta, \tag{55}$$

$$B_{xx}(x, y) = \frac{-1}{2\pi} \int_{-\infty}^{\infty}\int_{-\infty}^{\infty} B_{xz}(\xi,\eta) \frac{(x-\xi)}{\left[(x-\xi)^2 + (\mathrm{y}-\eta)^2\right]^{3/2}} d\xi d\eta, \tag{56}$$

$$B_{yy}(x, y) = \frac{-1}{2\pi} \int_{-\infty}^{\infty}\int_{-\infty}^{\infty} B_{yz}(\xi,\eta) \frac{(\mathrm{y}-\eta)}{\left[(x-\xi)^2 + (\mathrm{y}-\eta)^2\right]^{3/2}} d\xi d\eta, \tag{57}$$

$$B_{xy}(x,y) = \frac{-1}{2\pi} \int_{-\infty}^{\infty}\int_{-\infty}^{\infty} B_{yz}(\xi,\eta) \frac{(\mathrm{x}-\xi)}{\left[(x-\xi)^2 + (\mathrm{y}-\eta)^2\right]^{3/2}} d\xi d\eta, \tag{58}$$

$$B_{xy}(x,y) = \frac{-1}{2\pi} \int_{-\infty}^{\infty}\int_{-\infty}^{\infty} B_{xz}(\xi,\eta) \frac{(\mathrm{y}-\eta)}{\left[(x-\xi)^2 + (\mathrm{y}-\eta)^2\right]^{3/2}} d\xi d\eta. \tag{59}$$

In practice, convolution integrals of the type given above can be calculated efficiently and with good precision using cubic B splines (Wang et al., 2008). For the case h = 0, knots of the splines must not coincide with sample points, to avoid singularities.

A detailed TMI survey over the Tallawang magnetite skarn deposit afforded an opportunity for comparison of Fourier-based processing of TMI data with measured full gradient tensor data (Schmidt et al., 2004), acquired with a prototype rotating axial gradiometer (GETMAG). Figure 3(a) presents an image of the TMI, gridded from closely sampled (< 1 m spacing) measurements along profiles, perpendicular to strike, with a 10 m line spacing. Since the geological structure is approximately 2D and the depth to top of the magnetic bodies is essentially the depth of weathering, which is typically greater than 10 m, this sampling density is clearly adequate to sample the magnetic signature of the main geological sources, which are strongly magnetic magnetite skarn bodies within weakly magnetic sedimentary rocks, adjacent to a relatively weakly magnetic granite.

TMI measurements were made in a vertical gradient configuration, with Caesium vapour magnetometers at 0.5 m and 1.5 m above the ground. Grids of tensor elements were calculated using eqns (17)-(22) applied to the gridded TMI, which was recalculated from mean of the two independent TMI grids, each continued to 1 m height to correspond with the height of the GETMAG tensor gradiometer. These calculated tensor elements exhibit coherent, smoothly varying, but somewhat sharper images of the geological structures (Figures 3(b)-(d)). The calculated values could be checked against direct measurements of the gradient tensor that were made by GETMAG along three profiles.

Direct comparison of calculated and measured gradient tensor elements along these profiles showed excellent quantitative agreement between the measured values and those calculated from the TMI survey. Figure 4 shows the comparison between measured and calculated gradient tensors along a profile that passed over the mid-section of the major skarn body. The overall agreement between the measured and calculated gradient tensors

confirmed the ability of the Fourier-based processing to accurately calculate gradient tensors from TMI surveys of sufficiently high quality, and also verified the accuracy of calibration of the tensor gradiometer.

The advantages of measured gradient tensor data for relatively widely separated lines are well known (see Chapters 3-5). For example, the location and magnetic moments of compact sources can be uniquely determined from measurements along a single profile that passes within the detection range, or even from a few isolated measurements within an anomaly. On the other hand, obtaining equivalent information from total magnetic intensity (TMI) or TMI gradient data requires closely spaced lines to allow accurate characterisation of the field between the lines. If the field or its gradient in a fixed direction is accurately defined over the whole extent of the anomaly, the gradient tensor can be calculated, at least in principle, as shown above. Appendix II of Chapter 3 discusses the criteria for reliable estimation of gradient tensor elements from TMI or TMI gradient data.

In 1981 the SEG published a collection of excellent papers on applications of superconducting quantum interference devices (SQUIDs) to geophysics (Weinstock and Overton, 1981), which emphasised the potential for exploitation of the extreme sensitivity and high bandwidth of low temperature (liquid He-cooled) SQUID magnetometers and gradiometers. Until recently, practical difficulties such as cost of He, size of liquid He dewars, and logistical problems with obtaining liquid He in remote areas have limited use of low T SQUIDs for routine geophysical applications. Slow but steady progress has been made with low T SQUID magnetometer/gradiometer systems (Wynn et al., 1975; Wilson et al., 1994; Clem, 1995; Clem et al., 1997, 2001), particularly for military applications such as naval mine detection and unexploded ordnance detection. Over the last decade the first practical low T SQUID-based system for geophysical gradient tensor surveys has been developed by the Jena (Germany) group (Stolz et al., 1999, 2006a,b; Chwala et al., 2012). Chapter 3 reviews recent developments of magnetic tensor gradiometry, including high T and low T SQUID-based systems.

References

Ackermann, H.A. and Dix, C.H., 1955. The first vertical derivative of gravity. Geophysics, 20, 148-154.

Baranov, W., 1975. Potential Fields and Their Transformations in Applied Geophysics. Geoexploration Monographs Series 1- Number 6. Gebrüder Borntraeger, Berlin, 121p.

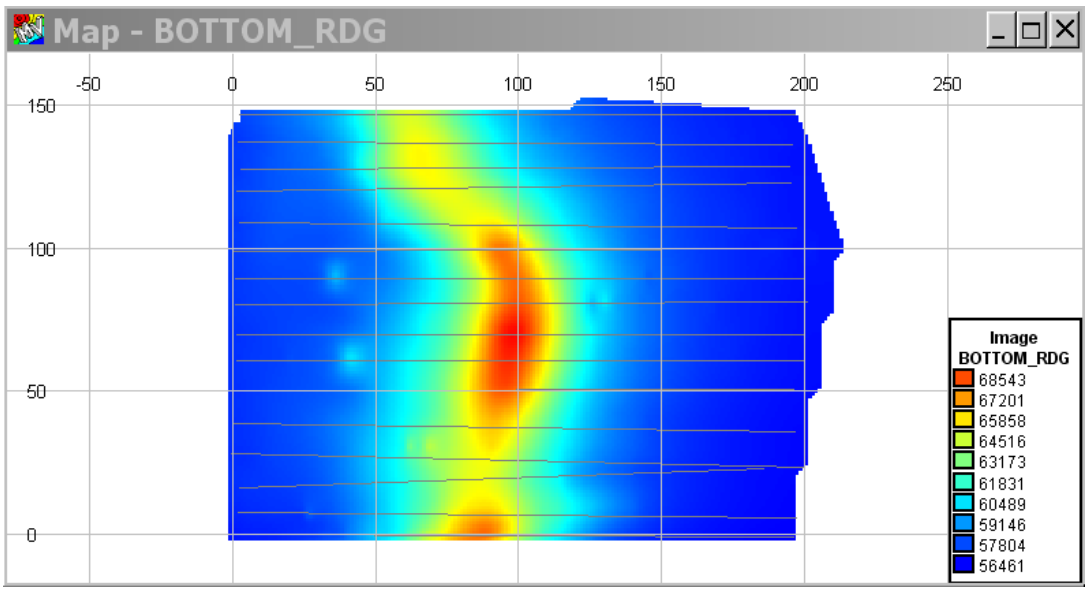

Fig.3(a). Image of measured TMI data over the Tallawang South magnetite skarn deposit, central N.S.W, with survey lines superimposed. Grid north is 340°TN/329°MN. TMI values are given in nT.

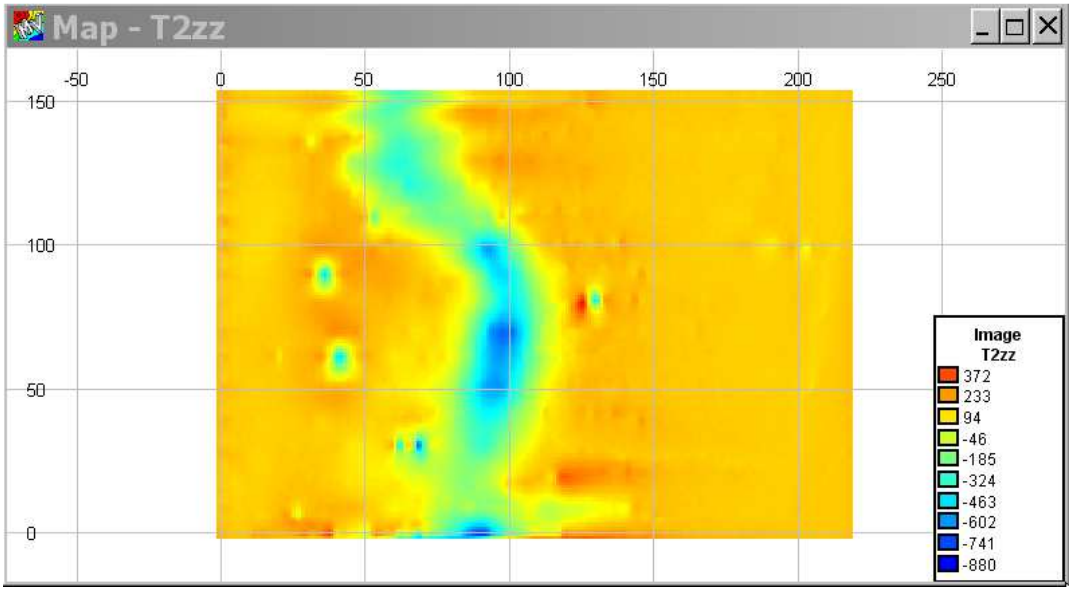

Fig.3(b). Image of B_{zz} (downward derivative of the vertical down feld component) over the Tallawang South deposit, calculated from the measured TMI using Fourier methods (eqn(22)). Gradient values are in nT/m.

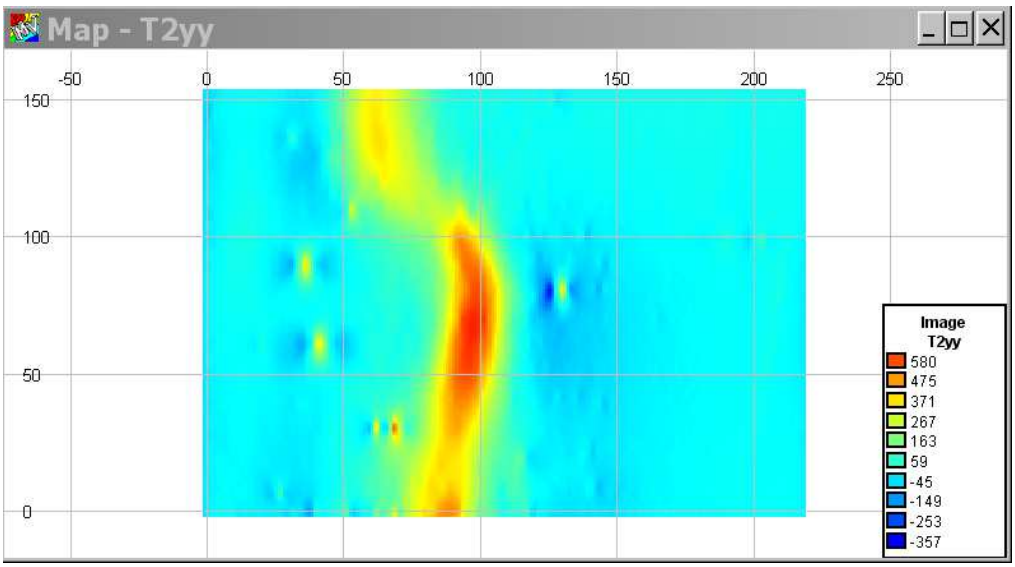

Fig.3(c). Image of B_{yy} (grid east derivative of the grid east field component) over the Tallawang South deposit, calculated from the measured TMI using Fourier methods. Gradient values are in nT/m.

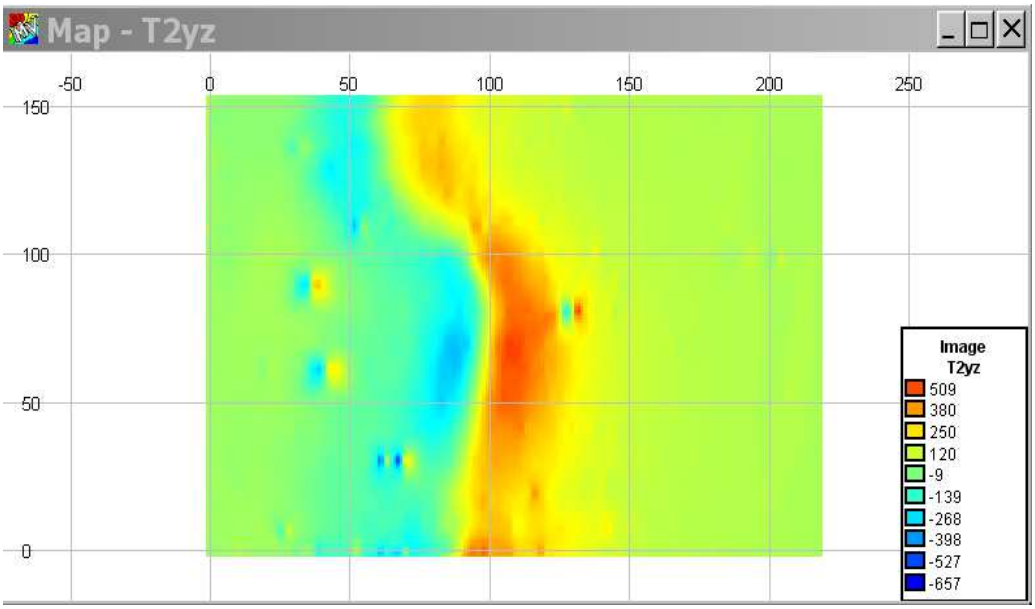

Fig.3(d). Image of B_{yz} (grid east derivative of the vertical down field component) over the Tallawang South deposit, calculated from the measured TMI using Fourier methods. Gradient values are in nT/m.

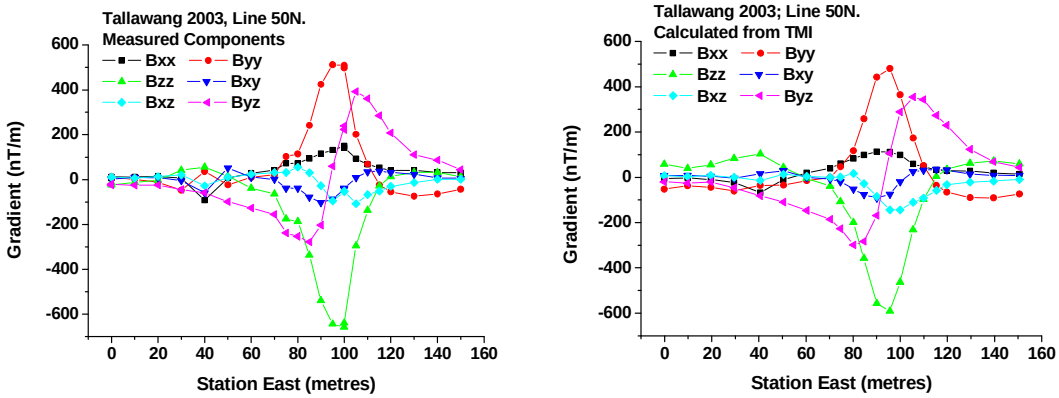

Fig.4(a). Comparison of gradient tensor elements, measured along a profile approximately perpendicular to the strike of the Tallawang magnetite skarn, with those calculated from the TMI grid. Note the good agreement between the two data sets.

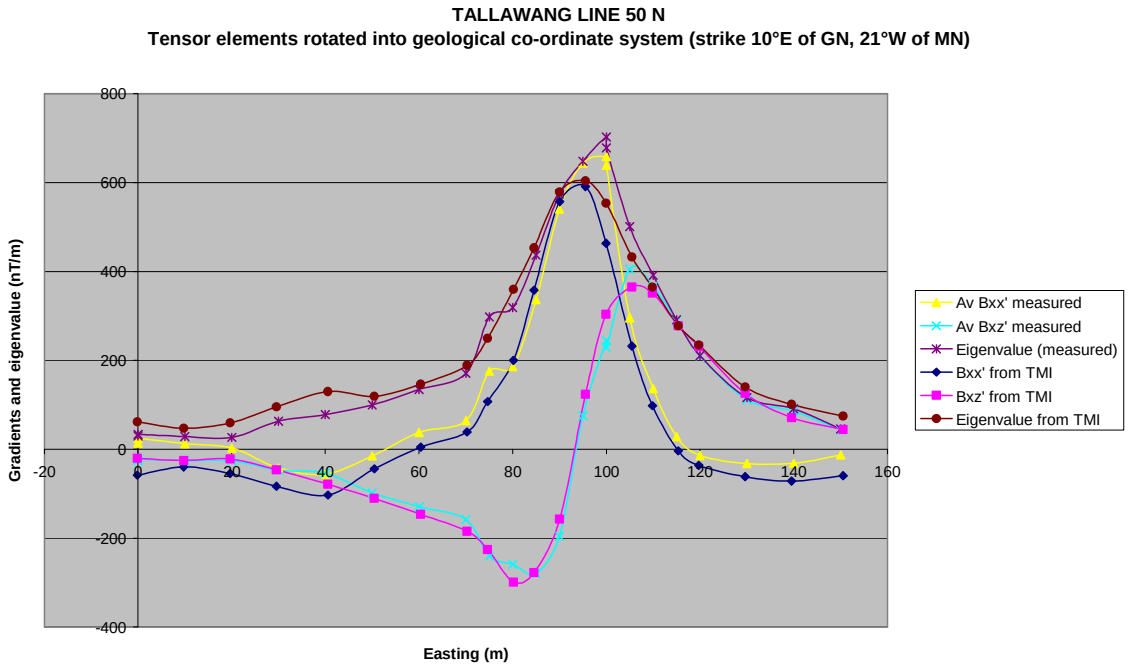

Fig.4(b). Comparison of gradient tensor elements, measured along a profile perpendicular to the strike of the Tallawang magnetite skarn, with those calculated from the TMI grid. Both sets of tensor elements have been rotated into a co-ordinate system with the *x* axis across strike and *y* along strike, such that B_{yy} and B_{yz} are minimised. Two dimensional structure is assumed for calculation of the eigenvalue of the tensor, which then has magnitude $\sqrt{(B_{xx}^2 + B_{xz}^2)}$. Note the excellent quantitative agreement between the two data sets.

Barnes, G., Barraud, J., Lumley, J. and Davies, M., 2008. Advantages of multi-tensor, high resolution gravity gradient data. Society of Exploration Geophysicists 74th Annual Meeting, Expanded Abstracts 27, 3587-3590.

Blakely, R.J., 1996. Potential Theory in Gravity and Magnetic Applications. Cambridge University Press, 441p.

Caratori Tontini, F. and Pedersen, L.B., 2008. Interpreting magnetic data by integral moments. Geophys. J. Int., 174, 815-824.

Christensen, A. and Rajagopalan, Shanti, 2000. The magnetic vector and gradient tensor in mineral and oil exploration. Preview, 84, p.77.

Chwala, A., Stolz, R., IJsselsteijn, R., Schultze, V., Ukhansky, N., Meyer, H.-G. and Schüler, T., 2001. SQUID gradiometers for archaeometry: Superconductor Science and Technology, **14**, 1111–1114.

Chwala, A., Stolz, R., Zakosarenko, V., Fritzsch, L., Shulz, M., Rompel, A., Polome, L., Meyer, M., and Meyer, H.G., 2012, Full tensor SQUID gradiometer for airborne exploration, Australian Society of Exploration Geophysicists, 22nd International Geophysical Conference and Exhibition, 26-29 February 2012 - Brisbane, Australia, CD-ROM, 4p.

Clark, D.A., 2000. Self-demagnetisation in practice: the Osborne Cu-Au deposit. Preview, 85, 31-36.

Clark, D.A., 2013. New methods for interpretation of magnetic vector and gradient tensor data II: Application to the Mount Leyshon Anomaly, Queensland, Exploration Geophysics, 44, 114–127 (http://dx.doi.org/10.1071/EG12066).

Clem, T.R., 1995. Superconducting magnetic sensors operating from a moving platform. IEEE Trans. Appl. Supercond., 5, 2124-2128..

Clem, T.R., Froelich, M.C., Overway, D.J., Purpura, J.W., Wiegert, R.F., Koch, R.H., Lathrop, D.K., Rozen, J., Eraker, J.H., Schmidt, J.M., 1997. Advances in sensor development and demonstration of superconducting gradiometers for mobile operation. IEEE Trans. Appl. Supercond., 7, 3287-3293.

Clem, T.R., Overway, D.J., Purpura, J.W., Bono, J.T., Koch, R.H., Rozen, J., Keeefe, G.A., Willen, S. and Mohling, R.A., 2001. High-Tc SQUID gradiometer for mobile magnetic anomaly detection. IEEE Trans. Appl. Supercond., 11, 871-875.

Dransfield, M., A. Christensen, and G. Liu, 2003, Airborne vector magnetics mapping of remanently magnetized banded iron formations at Rocklea, Western Australia: Exploration Geophysics, Exploration Geophysics, **34** , no.1/2, 93-96.

Foley, C.P., Tilbrook, D.L., Leslie, K.E., Binks, R.A., Donaldson, G.B., Du, J., Lam, S., G.J., Lam, S., Schmidt, P.W. and Clark, D.A., 2001. Geophysical exploration using magnetic gradiometry based on HTS SQUIDs. IEEE Trans. Appl. Supercond., 11(1), 1375-1378.

Hardwick, C., 1996, Aeromagnetic gradiometry in 1995. Exploration Geophysics, 27, 1-11.

Hardwick, C., 1999, Gradient-enhanced total field gridding: 69th Annual International Meeting, SEG, Expanded Abstracts , 381-384.

Harrison, C.G.A. and Southam, J.R., 1991. Magnetic field gradients and their uses in the study of the Earth's magnetic field. J. Geomagn. Geoelectr., 43, 585-599.

Helbig, K., 1963, Some integrals of magnetic anomalies and their relation to the parameters of the disturbing body: *Zeitschrift für Geophysik*, **29**, 83-96.

Henderson, 1970. On the validity of the use of the upward continuation integral for total magnetic intensity data. Geophysics, 35, 916-919.

Hood, P., 1965. Gradient measurements in aeromagnetic surveying. Geophysics, 30, 891-902.

Hood, P., 1981. Aeromagnetic gradiometry: a superior geological mapping tool for mineral exploration programs, In: (Ed. H. Weinstock and W.C. Overton) *SQUID Applications to Geophysics*, Proceedings of the Workshop held 2-4 June 1980, Los Alamos, Soc. Expl. Geophys., Tulsa, Oklahoma, 72-76.

Hood, P. and Teskey, D. J., 1981. Aeromagnetic gradiometer program of the Geological Survey of Canada. Geophysics, 54, 1012-1022.

Hughes, D.S. and Pondrom, W.L., 1947. Computation of vertical magnetic anomalies from total field measurements. Transactions of the American Geophysical Union, 28, 193-197.

Lima, E. A. and Weiss, B. P., 2009. Obtaining vector magnetic field maps from single-component measurements of geological samples. Journal of Geophysical Research: Solid Earth, 114(B6). doi:10.1029/2008JB006006

Lourenço, J. S., and H. F. Morrison, 1973, Vector magnetic anomalies derived from measurements of a single component of the field: Geophysics, **38** , no.2, 359-368.

Nabighian, M. N., V.J.S. Grauch, R. O. Hansen, T. R. LaFehr, Y. Li, J. W. Peirce, J. D. Phillips, and M.E. Ruder, 2005a, The historical development of the magnetic method in exploration: Geophysics, **70**, no.6, 33ND-61ND.

Nabighian, M. N., 1984. Toward a three-dimensional automatic intepretation of potential field data via generalized Hilbert transforms: Fundamental relations. Geophysics, 49, 780-786.

Nabighian, M. N., Ander, M.E., V.J.S. Grauch, R. O. Hansen, T. R. LaFehr, Y. Li, Pearson, W.C., Peirce, J. W., Phillips, J. D., and M.E. Ruder, 2005b, Historical development of the gravity method in exploration: Geophysics, **70**, no.6, 63ND-89ND.

Nelson, J.B., 1988. Calculation of the magnetic gradient tensor from total field gradient measurements and its application to geophysical interpretation. Geophysics 53, 957-966.

Nobukazo, S., Nogi, Y. and Isezaki, N., 1993. A new method for determination of the position and strike of magnetic boundaries using vector data of the geomagnetic anomaly field. Geophys. J. Int., 113, 155-164.

Pedersen, L.B. and Rasmussen, T.M., 1990. The gradient tensor of potential field anomalies: Some implications on data collection and data processing of maps. Geophysics, 55, 1558-1566.

Phillips, J.D., 2005. Can we estimate total magnetization directions from aeromagnetic data using Helbig's integrals? Earth Planets Space, Vol. 57 (No. 8), 681-689.

Phillips, J.D., Nabighian, M.N., Smith, D.V. and Li, Y., 2007. Estimating locations and total magnetization vectors of compact magnetic sources through combined Helbig and Euler analysis. SEG Expanded Abstracts, 26, 770-774.

Purucker, M. E., 1990. The computation of vector magnetic anomalies: A comparison of techniques and errors. Physics of the Earth and Planetary Interiors, 62(3), 231-245.

Reford, S., 2006. Gradient enhancement of the total field. The Leading Edge, 25 (1), 59-66.

Robinson, E.S. 1970. Upward continuation of total intensity magnetic fields. Geophysics, 35, 920-926.

Schmidt, P.W. and Clark, D.A., 1998. The calculation of magnetic components and moments from TMI: A case study from the Tuckers igneous complex, Queensland. Exploration Geophysics, 29, 609-614.

Schmidt, P., Clark, D., Leslie, K., Bick, M., Tilbrook, D. and Foley, C., 2004. GETMAG – A SQUID magnetic tensor gradiometer for mineral and oil exploration. Exploration Geophysics, 35, 297-305.

Schmidt, P.W. and Clark, D.A., 2006. The magnetic gradient tensor: Its properties and uses in source characterization. The Leading Edge, 25 (1), 75-78.

Stolz, R., L. Fritzsch, and H.-G. Meyer, 1999. LTS SQUID sensor with a new configuration: Superconductor Science and Technology, 12, 806.

Stolz, R., Zakosarenko, V. , Schulz, M., Chwala, A., Fritzsch, L., Meyer, H.-G. and Köstlin, E. O., 2006a. Magnetic full-tensor SQUID gradiometer system for geophysical applications. The Leading Edge, 25 (2), 178-180.

R. Stolz, A. Chwala, V. Zakosarenko, M. Schulz, L. Fritzsch, and H.-G. Meyer, 2006b. SQUID technology for geophysical exploration. SEG Expanded Abstracts 25, 894-898;

Veryaskin, A.V., 2001. Magnetic gradiometry: a new method for magnetic gradient measurement. Sensors and Actuators A, 91, 233-235.

Vestine, E.H. and Davids, N. 1945. Analysis and interpretation of geomagnetic anomalies. Terrestrial Magnetism and Atmospheric Electricity, 50, 1-36.

Wang, B., Krebes, E.S. and Ravat, D., 2008. High-precision potential-field and gradient-component transformations and derivative computations using cubic B-splines. Geophysics, 73, 135-142.

Weinstock, H., Overton, W.C., 1981 (Eds.). SQUID Applications to Geophysics. SEG, Tulsa (Oklahoma).

Wiegert, R. and Oeschger, J., 2005. Generalized magnetic gradient contraction based method for detection, localization and discrimination of underwater mines and unexploded ordnance. Proceedings of MTS/IEEE Oceans 2005, Vol.2, 1325-1332, DOI 10.1109/OCEANS.2005.1639938.

Wiegert, R. and Oeschger, J., 2006. Portable Magnetic Gradiometer for Real-Time Localization and Classification of Unexploded Ordnance. Proceedings of MTS/IEEE Oceans 2006, pp.1-6, 18-21 Sept. 2006, DOI 10.1109/OCEANS.2006.306805.

Wiegert, R., Oeschger, J., and Tuovila, E., 2007. Demonstration of a novel man-portable magnetic STAR technology for real time localization of unexploded ordnance. Proceedings of MTS/IEEE Oceans 2007, DOI 10.1109/OCEANS.2007.4449229.

Wilson, H., Hopkin, B., Dunstan, B. and Nelson, J.B., 1994. Flight test of a cylindrical tow-body for an airborne SQUID gradiometer, DREP Technical Memorandum 94-16, Defence Research Establishment Pacific, Vancouver.

Wynn, W.M., Frahm, C.P., Carroll, P.J., Clark, R.H., Wellhoner, J. and M.J. Wynn, 1975, Advanced super-conducting gradiometer/magnetometer arrays and a novel signal processing technique, IEEE Trans. Magn., MAG-11, 701-707.

CHAPTER 3: NEW METHODS FOR INTERPRETATION OF MAGNETIC VECTOR AND GRADIENT TENSOR DATA I: EIGENVECTOR ANALYSIS AND THE NORMALISED SOURCE STRENGTH

Clark, D.A., 2012. New methods for interpretation of magnetic vector and gradient tensor data I: eigenvector analysis and the normalised source strength. Exploration Geophysics, 43, 267–282, http://dx.doi.org/10.1071/EG12020.
[See also Errata, submitted to Exploration Geophysics, May 2014].

ABSTRACT

Acquisition of magnetic gradient tensor data is likely to become routine in the near future. New methods for inverting gradient tensor surveys to obtain source parameters have been developed for a number of elementary, but useful, models. These include point dipole (sphere), vertical line of dipoles (narrow vertical pipe), line of dipoles (horizontal cylinder), thin dipping sheet, and contact models. A key simplification is the use of eigenvalues and associated eigenvectors of the tensor. The normalised source strength (NSS), calculated from the eigenvalues, is a particularly useful rotational invariant that peaks directly over 3D compact sources, 2D compact sources, thin sheets and contacts, and is independent of magnetization direction. In combination the NSS and its vector gradient determine source locations uniquely. NSS analysis can be extended to other useful models, such as vertical pipes, by calculating eigenvalues of the vertical derivative of the gradient tensor. Inversion based on the vector gradient of the NSS over the Tallawang magnetite deposit obtained good agreement between the inferred geometry of the tabular magnetite skarn body and drill hole intersections**.** Besides the geological applications, the algorithms for the dipole model are readily applicable to the detection, location and characterization (DLC) of magnetic objects, such as naval mines, unexploded ordnance, shipwrecks, archaeological artefacts and buried drums.

Key words: Magnetic gradient tensor, magnetic field vector, eigenvalues, eigenvectors, normalised source strength, dipole localization, magnetization.

INTRODUCTION

This paper presents theory underlying some novel methods for interpretation of magnetic vector component and gradient tensor data. It is accompanied by a second paper (Clark, 2012, submitted to Exploration Geophysics), hereafter referred to as paper II, which applies some of these methods to analysis of the well-known magnetic anomaly at Mount Leyshon, Queensland.

The magnetic gradient tensor **B** is defined as the vector gradient of the magnetic field vector **b.** Pedersen and Rasmussen (1990) and Schmidt and Clark (2006) have reviewed the basic theory of the magnetic gradient tensor and discussed its applications.

With respect to Cartesian axes **B** has nine components, B_{ij} ($i, j = x, y, z$), which may be represented by a 3×3 matrix. Maxwell's equations imply that the gradient tensor is symmetric (in the absence of electric currents) and traceless. These constraints reduce the number of independent components to five, e.g. B_{xx}, B_{xy}, B_{xz}, B_{yy}, B_{yz}. Since derivatives of the magnetic scalar potential Ω of all orders are potential fields, vector and tensor components measured over a plane can be continued to different levels and vertical derivatives can be calculated using standard techniques (see Blakely, 1996, Chapter 12).

Advantages of gradient tensor measurements

A number of authors (e.g. Pedersen and Rasmussen, 1990; Christensen and Rajagopalan, 2000; Schmidt and Clark, 2006; Foss, 2006) have discussed theoretical advantages of magnetic gradient tensor measurements over conventional magnetic surveys. The overwhelming majority of modern magnetic surveys measure the total magnetic intensity (TMI). In most circumstances, for which the anomalous magnetic fields are small relative to the background geomagnetic field, the anomalous TMI is well approximated by the projection of the anomalous field vector onto the regional geomagnetic field direction (e.g. Emerson et al., 1985). To this approximation, the anomalous TMI represents a single magnetic field component that obeys Laplace's equation and is therefore a potential field. Unlike the TMI, all Cartesian vector and tensor components are true potential fields, irrespective of the anomaly magnitude. The anomalous field vector comprises three independent components and the gradient tensor has five independent components. In principle therefore, for a given number of observations the gradient tensor contains more

information about the magnetic sources than the vector, and considerably more than the TMI.

In addition to the extra information provided by the gradient tensor, gradient measurements suppress geomagnetic noise from the ionosphere and magnetosphere through common mode rejection and they largely remove long wavelength regional fields, while providing higher resolution by emphasising shallow sources and local structures.

The advantages of gradient tensor measurements are particularly apparent in low latitudes, where TMI surveys are insensitive to vertical and easterly components of the anomalous field. These components arise from compact sources, whether or not they are magnetized parallel to the geomagnetic field. In bodies that are elongated approximately along the magnetic meridian, vertical and easterly components of the anomalous field arise predominantly from magnetization components that are perpendicular to the geomagnetic field. These components, which are generally present to some extent due to remanence and anisotropy, contain valuable information about such sources, to which TMI surveys are almost blind. In areas of rugged topography, where TMI surveys struggle to produce reliable interpolated data on either constant elevation or draped surfaces, even relatively sparse, irregularly spaced measurements of the gradient tensor on an uneven surface are sufficient to locate sources and provide information on their magnetization.

Recent developments in magnetic tensor gradiometer systems

Recently there has been growing interest in developing new high sensitivity full tensor magnetic gradiometer systems. Slow but steady progress has been made with SQUID magnetometer/ gradiometer systems, both low T SQUID-based (LTS) liquid He-cooled (e.g. Clem *et al*., 1997) and high T liquid nitrogen-cooled (Clem *et al*., 2001; Young *et al*., 2010; Leslie et al., 2007), particularly for military applications such as naval mine detection and unexploded ordnance detection. Over the last decade the first practical low T SQUID-based system for geophysical gradient tensor surveys has been developed by the Jena (Germany) group (Stolz et al., 1999, 2006a,b; Chwala et al., 2012). The intrinsic noise of the LTS planar gradiometers developed by this group is 0.2 pT/m (integrated between 0.01 Hz and 10 Hz). Noise spectral density of the full tensor gradiometer system in motion is about 1-10 pT/m/√Hz over a frequency range of 0.1-2 Hz in a bird towed beneath a helicopter. A survey carried out in 2006 using a fixed wing aircraft achieved rms noise levels of 5-10 pT/m in a bandwidth of 4.5 Hz (Chwala et al., 2012).

The discovery of high T (liquid nitrogen temperatures and above) superconducting materials in the late 1980s has created opportunities for cheaper, smaller devices that can be readily transported and refilled, but retain very high sensitivities. Liquid nitrogen cooled SQUIDs and gradiometers are very sensitive, with noise levels that are about an order of magnitude higher than those of low T SQUIDs. Clark et al. (1998) suggested the use of combined vector field and gradient tensor measurements, using high T superconducting devices, for separating contributions of induced and remanent magnetization to magnetic anomalies and for inferring source properties, such as total magnetization direction, remanence direction and Koenigsberger ratio.

Humphrey et al. (2005) have demonstrated a high T SQUID-based gradiometer, designed for use on a mobile platform, with correction for common mode signals provided by vector sensors, combined with active compensation of ambient fields. This system attained white noise levels, above ~3 Hz, of 1 pT/m/√Hz while undergoing roll/pitch/yaw motions of ±5°. At 1 Hz the noise level was 80 pT/m/√Hz.

The availability of flexible high T superconducting tapes has allowed development of an intrinsic axial gradiometer (Tilbrook, 2004). Substantial improvements in common mode rejection of ambient magnetic fields and reduction in noise are achieved by spinning the gradiometer and detecting the second harmonic of the rotation frequency (Leslie et al., 2005; Tilbrook et al., 2006). This concept was the basis for a prototype manually rotated full tensor gradiometer for ground measurements, which was successfully demonstrated over the Tallawang deposit , central NSW (Schmidt et al., 2004). Further development has seen a successful helicopter-borne trial of a spinning gradiometer system (Leslie et al., 2007), which measured gradient tensor components with sensitivities down to 50 pT/m at a sampling rate of 10 Hz. A target intrinsic sensitivity of 1 pT/m is believed to be ultimately achievable with this system. The CSIRO-developed rotating axial gradiometer concept has also been applied to a downhole magnetic tensor gradiometer system that uses AMR sensors operating at ambient temperatures (K. Leslie, pers. comm., 2012).

Although the inherent sensitivity of fluxgate magnetometers is far inferior to that of superconducting devices, a practical fluxgate-based tensor gradiometer, capable of mapping anomalies greater than about 10 nT/m in mobile operation, has been developed (Bracken and Brown, 2006). Wiegert et al. (2007) describe a multiple tensor gradiometer

system, comprising an array of eight triaxial low noise fluxgate magnetometers, that has a sensitivity of about 0.25 nT/m in hand-carried mobile operation.

Other proposed technologies include a stiff metallic string carrying an AC current tuned to the second eigenmode of mechanical vibration, which is sensitive to an off-diagonal term of the gradient tensor (Veryaskin, 2001; McRae et al., 2004; Sunderland et al., 2009). Although this technique only measures a single tensor component, the full gradient tensor could in principle be obtained from an array of differently oriented string sensors. The noise spectrum of this instrument is very flat over the frequency range of interest, with the $1/f$ corner at ~ 2.5 mHz. The current white noise floor, measured in the geomagnetic field, obtained with this method is 0.4 nT/m/√Hz from 0.01-0.625 Hz (Sunderland et al., 2009), which corresponds to a rms noise level of 0.3 nT/m over this bandwidth. The target sensitivity for static measurements is 0.01 nT/m.

The developments discussed above suggest that we may be at the dawn of a new era in applied magnetic surveys, where magnetic gradient tensor surveys will become routine. Efficient use of the extra information provided by gradient tensor surveys will require creative new processing and interpretation. The seminal paper by Pedersen and Rasmussen (1990) demonstrated applications of eigenvalues, eigenvectors and rotational invariants to analysis of gravity and magnetic gradient tensor data. Other contributors to this effort include Schmidt *et al*. (2004) and Schmidt (2006), who extended the Euler deconvolution method to magnetic gradient tensor data and demonstrated its utility for mapping depth to sources and structural index variations over the Tallawang magnetite deposit ; Fitzgerald and Holstein (2006) and Fitzgerald *et al*., (2009, 2010), who developed improved methods for gridding and levelling of gradient tensor data; and Heath (2007) who derived expressions for magnetic gradient tensor component anomalies produced by simple geological models and multipole sources. More recently Clark *et al*. (2009) and Clark (2010) presented new methods for dipole detection, localization and characterization (DLC) ; Holstein *et al*. (2011) developed efficient interpretation methods for gradient tensor data over dykes; Beiki *et al*. (2011) gave methods for estimation of source depths and strike directions from eigenvector analysis of the pseudo-gravity gradient tensor, calculated from TMI data; Clark (2012a,b) presented methods for interpreting vector and tensor data, using components calculated from high quality TMI data over the Mount Leyshon gold-mineralized system and the Tallawang magnetite skarn deposit as

illustrations; and Beiki *et al*. (2012) developed an algorithm for depth estimation using Euler deconvolution of the NSS and applied it to analysis of gradient tensor data calculated from a TMI survey.

New methods developed for analysis of magnetic gradient tensor data can also be applied to high quality conventional TMI surveys that have been processed using Fourier filtering techniques, or otherwise, to calculate magnetic vector and tensor components (see paper II). This approach is, in fact, the only practical way at present to analyse vector component data, as measurements of vector components are seriously afflicted by motion noise, which is not as serious a problem for gradient components. In many circumstances, an optimal approach to extracting maximum information from magnetic surveys would be to combine analysis of measured gradient tensor data with vector components calculated from TMI measurements. In paper II, I apply some of the methods presented in this paper to the analysis of vector and tensor components calculated from a TMI survey over the Mount Leyshon area, Queensland.

Eigenvector analysis of the tensor

Eigenvalues and eigenvectors are discussed in many textbooks on linear algebra, e.g. Anton and Rorres (2000). Eigenvectors, **v**, of the magnetic gradient tensor, **B,** satisfy by definition the relationship **Bv** = λ**v**, for some scalar λ, which is the eigenvalue corresponding to **v**. The eigenvalues are found by solving the characteristic equation det(**B** – λ**I**). Expanding the determinant gives a cubic equation in λ:

$$\lambda^3 + I_1\lambda - I_2 = 0, \tag{1}$$

where

$$I_1 = B_{yy}B_{zz} + B_{xx}B_{yy} + B_{zz}B_{xx} - B_{xy}^2 - B_{xz}^2 - B_{yz}^2, \tag{2}$$

$$I_2 = \det(\mathbf{B}) = B_{xx}B_{yy}B_{zz} - B_{xx}B_{yz}^2 - B_{zz}B_{xy}^2 - B_{yy}B_{xz}^2 + 2B_{xy}B_{xz}B_{yz}. \tag{3}$$

The coefficient of λ^2 in the cubic equation for λ vanishes because the tensor is traceless. It can be shown that the quantities I_1 and I_2 are unchanged by rotation of the coordinate axes, i.e they are rotational invariants of the tensor. They have the property that they can be simply expressed directly in terms of the tensor components with respect to any Cartesian reference frame. In their seminal paper Pedersen and Rasmussen (1990) introduced these canonical invariants to the geophysical literature and discussed applications to interpretation of potential field surveys. Like all rotational invariants, I_1 and I_2 have the useful property that they are independent of sensor orientation and are therefore much less sensitive to orientation errors than the individual tensor components.

Each distinct root of the cubic equation defines an eigenvalue of the tensor. For each eigenvalue λ_i, the corresponding eigenvectors can be found as non-zero vectors $\mathbf{v}_i$ that satisfy $\mathbf{B}\mathbf{v}_i = \lambda_i \mathbf{v}_i$, which can then be normalised to define unit eigenvectors $\hat{\mathbf{v}}_i = \mathbf{v}_i / |\mathbf{v}_i|$. Since **B** is a symmetric real 3×3 matrix, all its eigenvalues are real, eigenvectors corresponding to distinct eigenvalues are orthogonal, and an orthonormal set of three eigenvectors can always be found, including the case of degenerate (i.e two equal) eigenvalues (Anton and Rorres, 2000, p.357-358). The matrix **R** that has these three unit eigenvectors as its columns is a rotation matrix that diagonalises **B** (Anton and Rorres, 2000, p.349). That is, with respect to Cartesian axes along the eigenvectors the rotated tensor $\mathbf{B}'$, is given by

$$\mathbf{B}' = \mathbf{R}^{-1}\mathbf{B}\mathbf{R} = \mathbf{R}^T\mathbf{B}\mathbf{R};\ \mathbf{R} = [\hat{\mathbf{v}}_1, \hat{\mathbf{v}}_2, \hat{\mathbf{v}}_3]. \tag{4}$$

Hereafter, the eigenvalues will be labelled in non-increasing order: $\lambda_1 \geq \lambda_2 \geq \lambda_3$. Since the tensor is traceless, the sum of the eigenvalues is zero. Thus only two of the eigenvalues are independent. It also follows that λ_2 is always the eigenvalue with the smallest absolute value.

It is easily shown that the eigenvalues of **B** are rotational invariants of the tensor. Evidently, any combination of the eigenvalues is also a rotational invariant. Conversely, any rotational invariant $f(B_{xx}, B_{xy}, B_{xz}, B_{yy}, B_{yz}, B_{zz})$ can be expressed as a combination of eigenvalues since, by definition, this function of the tensor elements is unchanged by

rotation into the principal axis frame, where it is equal to $f(\lambda_1, 0, 0, \lambda_2, 0, 0, \lambda_3)$. For example the canonical invariants are given by

$$I_1 = \lambda_1\lambda_2 + \lambda_2\lambda_3 + \lambda_3\lambda_1 = -(\lambda_1^2 + \lambda_2^2 + \lambda_3^2)/2 \leq 0, \tag{5}$$

$$I_2 = \lambda_1\lambda_2\lambda_3. \tag{6}$$

As will be shown in the following section, a particularly useful rotational invariant is the normalised source strength, which can be expressed as the following combination of eigenvalues:

$$\mu = \sqrt{-\lambda_2^2 - \lambda_1\lambda_3}. \tag{7}$$

For a dipole source, Wilson (1985) showed that equation (7) equals the normalised dipole moment, which is a particularly useful parameter for interpretation that is proportional to the magnitude of the dipole moment, but independent of the magnetization direction.

For 2D sources the gradients parallel to the strike direction are zero. If we choose axes such that y is parallel to the strike, the gradient tensor takes the form

$$\mathbf{B} = \begin{bmatrix} B_{xx} & 0 & B_{xz} \\ 0 & 0 & 0 \\ B_{xz} & 0 & -B_{xx} \end{bmatrix}, \tag{8}$$

which has only two independent components, B_{xx} and B_{xz}, since $B_{zz} = -B_{xx}$ by the tracelessness property.

The characteristic equation is

$$\det(\mathbf{B} - \lambda\mathbf{I}) = \begin{vmatrix} B_{xx} - \lambda & 0 & B_{xz} \\ 0 & -\lambda & 0 \\ B_{xz} & 0 & -B_{xx} - \lambda \end{vmatrix} = \lambda(B_{xx}^2 + B_{xz}^2 - \lambda^2) = 0, \tag{9}$$

for which the three roots are:

$$\lambda_1 = \sqrt{B_{xx}^2 + B_{xz}^2},\ \lambda_2 = 0,\ \lambda_3 = -\sqrt{B_{xx}^2 + B_{xz}^2} = -\lambda_1. \tag{10}$$

From (2), (3) and (10), the canonical invariants of the full 3×3 tensor are:

$$\begin{aligned} (I_1)_{2D} &= \lambda_2\lambda_3 - \lambda_1^2 = -\lambda_1^2 = -\left(B_{xx}^2 + B_{xz}^2\right) = -\left(B_{zz}^2 + B_{xz}^2\right), \\ (I_2)_{2D} &= \lambda_1\lambda_2\lambda_3 = 0. \end{aligned} \tag{11}$$

Thus the determinant of the full tensor is zero everywhere for a 2D source. The invariant I_1 is equal to the determinant of the 2 × 2 minor matrix of B_{yy}. Hereafter, the 2 × 2 matrix that contains the only nonzero gradient tensor elements when the geology is two-dimensional will be denoted $\mathbf{B}_{2D}$, i.e.

$$\mathbf{B}_{2D} = \begin{bmatrix} B_{xx} & B_{xz} \\ B_{xz} & -B_{xx} \end{bmatrix}. \tag{12}$$

From (7) and (10), in the 2D case the normalised source strength reduces to

$$\mu_{2D} = \lambda_1 = -\lambda_3 = \sqrt{B_{xx}^2 + B_{xz}^2} = \sqrt{\left(\frac{\partial b_x}{\partial x}\right)^2 + \left(\frac{\partial b_x}{\partial z}\right)^2} = \sqrt{B_{xz}^2 + B_{zz}^2} = \sqrt{\left(\frac{\partial b_z}{\partial x}\right)^2 + \left(\frac{\partial b_z}{\partial z}\right)^2}.$$

(13)

Thus the 2D normalised source strength is equal to the total gradient, or the analytic signal amplitude (ASA) of Nabighian (1972), of either the vertical field component, b_z, or of the strike-perpendicular horizontal component, b_x. Since, in the 2D case, the total gradient of TMI is independent of magnetization direction (Li, 2006), the normalised source strength also has this desirable property.

Denote the along-profile, across-profile (i.e. along-strike) and vertical direction cosines of the geomagnetic field by ℓ_1, ℓ_2, ℓ_3. In the weak anomaly approximation, the conventional

TMI anomaly is given by $T = b_x\ell_1 + b_y\ell_2 + b_z\ell_3 = b_x\ell_1 + b_z\ell_3$, since the along-strike field component, b_y, is zero .

Then

$$\begin{bmatrix} \ell_1 & \ell_3 \\ \ell_3 & -\ell_1 \end{bmatrix} \begin{bmatrix} B_{xx} \\ B_{xz} \end{bmatrix} = \begin{bmatrix} \partial T/\partial x \\ \partial T/\partial z \end{bmatrix}, \tag{14}$$

so for 2D sources, the ASA of TMI, $A(T)$, is given by

$$A(T) = \sqrt{\left(\frac{\partial T}{\partial x}\right)^2 + \left(\frac{\partial T}{\partial z}\right)^2} = (\ell_1^2 + \ell_3^2)A(b_i) = (1-\ell_2^2)A(b_i) = (1-\ell_2^2)\mu_{2D}, \quad (i = x, z). \tag{15}$$

Conversely, gradient tensor elements for the 2D case can be calculated from total field gradients by:

$$\begin{bmatrix} B_{xx} \\ B_{xz} \end{bmatrix} = \frac{1}{\ell_1^2 + \ell_3^2} \begin{bmatrix} \ell_1 & -\ell_3 \\ \ell_3 & \ell_1 \end{bmatrix} \begin{bmatrix} \partial T/\partial x \\ \partial T/\partial z \end{bmatrix}. \tag{16}$$

The analytic signal amplitude of the total field anomaly is proportional to $A(b_i)$, where b_i is any field component perpendicular to strike, including b_x and b_z. If the strike is magnetic E-W, so that the profile is along the magnetic meridian, then $\ell_2 = \pm 1$ and $A(T) = A(b_i)$. Otherwise the $A(T)$ profile has the same shape as $A(b_i)$, but smaller magnitude by a factor of $(1 - \ell_2^2) = (1-\cos^2\beta\cos^2 I)$, where β is the angle between the strike direction and magnetic north and I is the field inclination. For approximately N-S striking structures at low latitudes, where the inclination is small, $A(T)$ becomes much smaller than the normalised source strength μ_{2D}, which is equivalent to $A(b_i)$.

Since

$$\begin{bmatrix} B_{xx} & 0 & B_{xz} \\ 0 & 0 & 0 \\ B_{xz} & 0 & -B_{xx} \end{bmatrix} \begin{bmatrix} 0 \\ 1 \\ 0 \end{bmatrix} = \begin{bmatrix} 0 \\ 0 \\ 0 \end{bmatrix} = 0 \begin{bmatrix} 0 \\ 1 \\ 0 \end{bmatrix}, \tag{17}$$

an eigenvector corresponding to the zero eigenvalue is $(0,1,0)^T$, i.e. along strike, parallel to the y axis. In practice, when $|\lambda_2| << |\lambda_1|,|\lambda_3|$ and the eigenvector $\mathbf{v}_2$ is subhorizontal, its azimuth can be taken to represent the local strike direction. When the geology is approximately two dimensional, rotating the coordinate system so that the y axis aligns with the local strike direction greatly simplifies analysis, as essentially only two independent gradient components are significant. Pedersen and Rasmussen (1990) illustrated the utility of eigenvector analysis in determining local strike directions of elongated structures.

Analysis of dipole sources

The point dipole model is applicable to any sufficiently compact magnetized body. Outside a spherical surface that completely encloses an arbitrary magnetized body, the field can be expressed as a sum of multipole contributions, with a $1/r^3$ fall-off for the dipole term, $1/r^4$ fall-off for the quadrupole, $1/r^5$ fall-off for the octupole term, and so on. Thus for any compact body with a non-zero dipole moment the far field is always dominated by the dipole term. More specifically, the external fields and gradients due to a uniformly magnetized sphere are identical to that of a point dipole, because the quadrupole and all higher multipole moments vanish identically. As well as its importance in a geological context, the point dipole model is widely used in other applications. These include detection, location and classification of magnetic objects, such as naval mines, unexploded ordnance, shipwrecks, archaeological artefacts, and buried drums.

The magnetic field vector at observation point **r** produced by a point dipole of magnetic moment **m** is (Blakely, 1996, p.75)

$$\mathbf{b}(\mathbf{r}) = \frac{C}{r^3}\left[3(\mathbf{m}.\hat{\mathbf{r}})\hat{\mathbf{r}} - \mathbf{m}\right], \tag{18}$$

where for convenience the origin is placed at the dipole location. In equation (18) and thereafter, C has a numerical value of 100 if distances are in metres, field components are in nT (so gradients are in nT/m), and magnetisations are in A/m.

The gradient tensor elements are obtained by differentiating the Cartesian components of **b** with respect to x, y, z. Note that the dipole field falls off as $1/r^3$, so the gradient tensor falls off as $1/r^4$. Wilson (1985) gave the following expression for the tensor elements

$$B_{ij} = n_i\mu_j + n_j\mu_i + (\boldsymbol{\mu}\cdot\hat{\mathbf{r}})\delta_{ij} - 5(\boldsymbol{\mu}\cdot\hat{\mathbf{r}})n_i n_j, \quad (i, j = x, y, z) \tag{19}$$

where $\hat{\mathbf{r}} = \mathbf{r}/|\mathbf{r}|$ is the unit displacement vector, directed from source to observation point, with components (n_1, n_2, n_3), δ_{ij} is the Kronecker delta, and

$$\boldsymbol{\mu} = \frac{3C\mathbf{m}}{r^4} = \mu\frac{\mathbf{m}}{m} = \mu\hat{\mathbf{m}}, \tag{20}$$

is called the normalised magnetic moment vector (Wilson, 1985) or the scaled moment vector (Wynn, 1999). Its magnitude μ is simply called the normalised magnetic moment and has the same units as the gradient tensor elements. It is a natural scalar parameter of the dipole DLC application that characterizes the strength of the gradient at a given range (Wynn et al., 1975; Wilson, 1985).

If we choose the Cartesian coordinate system shown in Figure 1, with $(\hat{\mathbf{x}}_1 = \hat{\mathbf{r}}$, $\hat{\mathbf{x}}_2 = \hat{\mathbf{m}}\times\hat{\mathbf{r}}/|\hat{\mathbf{m}}\times\hat{\mathbf{r}}|$, $\hat{\mathbf{x}}_3 = \hat{\mathbf{x}}_1\times\hat{\mathbf{x}}_2)$, so that the observation point has coordinates $x_1 = r$, $x_2 = x_3 = 0$, $m_1 = m\cos\phi$, $m_2 = 0$, and $m_3 = m\sin\phi$, the gradient tensor takes a simple form

$$\mathbf{B} = \begin{bmatrix} B_{11} & 0 & B_{13} \\ 0 & B_{22} & 0 \\ B_{13} & 0 & B_{33} \end{bmatrix} = \mu\begin{bmatrix} -2\cos\phi & 0 & \sin\phi \\ 0 & \cos\phi & 0 \\ \sin\phi & 0 & \cos\phi \end{bmatrix}. \tag{21}$$

which has characteristic equation

$$\det(\mathbf{B} - \lambda\mathbf{I}) = -(\mu\cos\phi - \lambda)[(2\mu\cos\phi + \lambda)(\mu\cos\phi - \lambda) + \mu^2\sin^2\phi] = 0. \tag{22}$$

It is immediately apparent from equation (21) that $\hat{\mathbf{x}}_2 = \hat{\mathbf{m}}\times\hat{\mathbf{r}} = [0,1,0]^T$ is an eigenvector of **B**, with eigenvalue $\lambda_2 = \mu\cos\phi$. Then from equation (22), the remaining eigenvalues are found by solving the quadratic equation

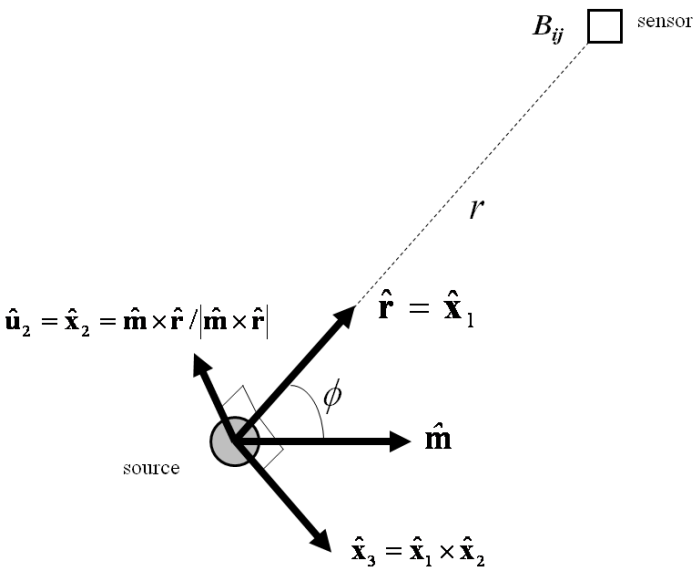

Figure 1. Canonical co-ordinate system for a dipole source.

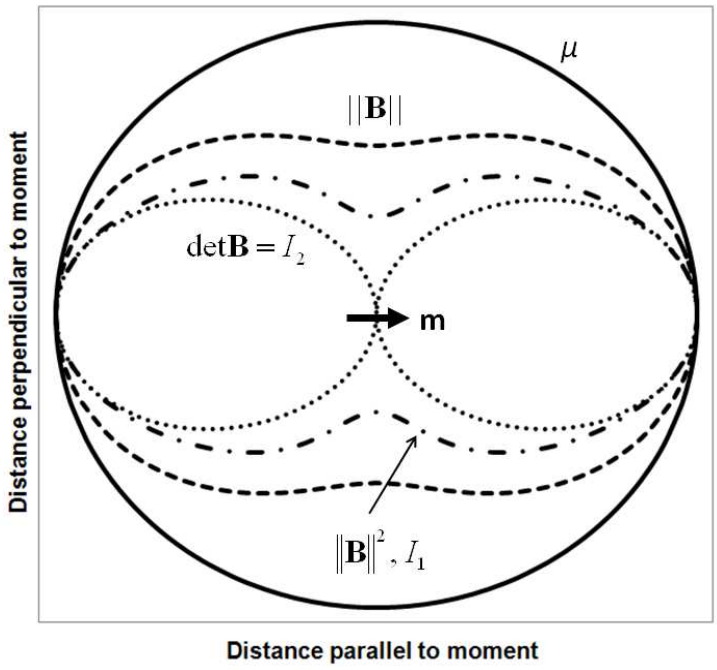

Figure 2. Angular dependence of tensor invariants μ, $||\mathbf{B}|| = [\mathrm{Trace}(\mathbf{B}^T\mathbf{B})]^{½}$, $I_1 = -||\mathbf{B}||^2/2$, and $\det\mathbf{B} = I_2$ around a dipole source. The dipole is horizontal and located at the origin. The polar plots show the magnitude of each invariant as a function of the angle ϕ between the dipole moment and the source-sensor displacement vector. Only the normalised moment μ is isotropic around the dipole.

$$\lambda^2 + (\mu\cos\phi)\lambda - \mu^2(2\cos^2\phi + \sin^2\phi) = 0, \tag{23}$$

Therefore in terms of the scaled moment μ and the angle ϕ, the three eigenvalues in non-increasing order are

$$\left.\begin{aligned} \lambda_1 &= \frac{\mu}{2}\left(-\cos\phi + \sqrt{4+5\cos^2\phi}\right) \geq 0\,, \\ \lambda_2 &= \mu\cos\phi, \\ \lambda_3 &= \frac{\mu}{2}\left(-\cos\phi - \sqrt{4+5\cos^2\phi}\right) \leq 0 \end{aligned}\right\}, \tag{24}$$

where $\lambda_1 \geq \lambda_2 \geq \lambda_3$ and λ_2 is always the eigenvalue with the smallest absolute value. This is the form given by Wilson (1985).

Note that the eigenvalues are functions of ϕ, so they depend on the direction of the magnetic moment. Rotational invariants can always be expressed in terms of eigenvalues, by referring the tensor to its principal axes, so they can be also be expressed in terms of μ and ϕ, by using equation (24). Thus in most cases rotational invariants are sensitive to the orientation of the moment, via their dependence on ϕ. For example the canonical invariants I_1, I_2, and the dimensionless ratio $I = -27\, I_2^2/4I_1^3$, which were introduced by Pedersen and Rasmussen (1990), are given by

$$I_1 = -\mu^2(2\cos^2\phi + 1) \tag{25}$$

$$I_2 = -\mu^3\cos\phi(\cos^2\phi + 1) \tag{26}$$

$$I = \frac{27}{4}\frac{\cos^2\phi(\cos^2\phi+1)^2}{(2\cos^2\phi+1)^3}\,. \tag{27}$$

However, if follows from equation (24) that the particular combination of eigenvalues on the RHS of equation (7), first introduced by Wilson (1985), equates to the normalised magnetic moment μ, is independent of ϕ and does not depend on the orientation of the dipole. Figure 2 compares the angular dependences of μ and other invariants, which have been more commonly used, around a dipole source. Unlike the tensor magnitude

(Frobenius norm) $||\mathbf{B}||$, I_1 and I_2; μ is completely isotropic around the dipole. This makes it an ideal parameter for homing applications (guidance towards a target) such as underwater mine-hunting, since increasing values of μ unambiguously indicate closer approach to a target.

The angle between the source-sensor displacement vector and the magnetic moment is constrained by

$$\cos\phi = \lambda_2 / \mu. \tag{28}$$

At a given observation point, the magnitude, but not the sign of $\sin\phi$, is determined by equation (28), which is the fundamental reason for the ambiguity of the single point inversion of the gradient tensor, along with the fact that reversing both **r** and **m** in equation (19) leaves the tensor elements unchanged.

A number of eigenvector-based methods have been developed for locating dipole targets from magnetic gradient tensor data (e.g. Wynn et al. 1975; Wilson, 1985). Wynn (1999) gives an excellent summary of dipole DLC methods. An accessible summary of Wilson's (1985) inversion algorithm can be found in Schmidt et al. (2004). There is an inherent four-fold ambiguity in obtaining solutions for dipole location and orientation of its moment from point-by-point analysis of gradient tensors (Wynn et al., 1975; Wilson, 1985; Wynn, 1995, 1997, 1999), which must be resolved by comparing solutions from different sensor locations, rejecting those that are not consistent (the so-called "ghost" solutions) and retaining the solutions that exhibit the best clustering. In addition to this geometric ambiguity, the range and the magnitude of the moment cannot be determined independently from a point measurement of the gradient tensor, but only as the combination m/r^4, unless there is an extra constraint.

Figure 3 illustrates the two types of ambiguity. In practice, this ambiguity can be fairly easily resolved in a number of ways:

1. Some or all of the false solutions can often be ruled out *a priori*. For example, if the source is known to lie below the sensor, the two "ghosts" that are above the sensor can be eliminated from consideration. If in addition there is information about which side of the sensor the source lies, the true solution is identifiable.

2. Gradient tensor measurements at more than one location produce four possible solutions for each measurement site, but only the solutions that correspond to the true location of the source are consistent, whereas the false solutions are scattered (see Figure 4). Once the location of the dipole is known, determination of the magnetic moment is straightforward.
3. If the magnetic field components are measured, even crudely, in addition to the gradient tensor, the extra information resolves the ambiguity. In fact, the sign of the field components is sufficient to eliminate the ghosts and confirm the true solution. Accurate values of the anomalous field vector allow the range ambiguity to be eliminated, due to the inverse cube fall-off, as opposed to the inverse fourth power fall-off of the gradients. The magnitude of the moment is then unambiguous.
4. Similarly, if some second order gradients of the magnetic field, in addition to the gradient tensor, are known at a given point, this extra information can resolve the ambiguity.

In practice, noise in the data results in estimated directions-to-source that do not quite intersect, so the source position must be estimated from the "near misses". Beiki and Pedersen (2010) give a method for least-squares estimation of source location, using estimated directions-to-source from several locations.

Methods based on point-by-point analysis of the eigenvectors of the tensor, or combining point vector and tensor measurements, tend to be adversely affected by noise in individual measurements of the components, and they are also not robust to the contamination of the measured signal by background gradients, interfering anomalies, instrument drift or departures of the target from a pure dipole source. Clark (2010) developed a method that analyses gradient tensor data collected along a profile passing near a dipole target. Unlike most other gradient tensor inversion techniques, this method can correct for contamination of the dipole signature by effects such as those given above. This method also reduces noise by incorporating a number of successive tensor values in the solutions. Clark's (2010) method separates the scalar and vector aspects of the inversion, by first deriving scalar parameters from an invariant quantity that is independent of moment orientation, then incorporating the inverted scalar parameters into inversion of the tensor elements to obtain vector parameters. An invariant that is independent of the dipole orientation is given by

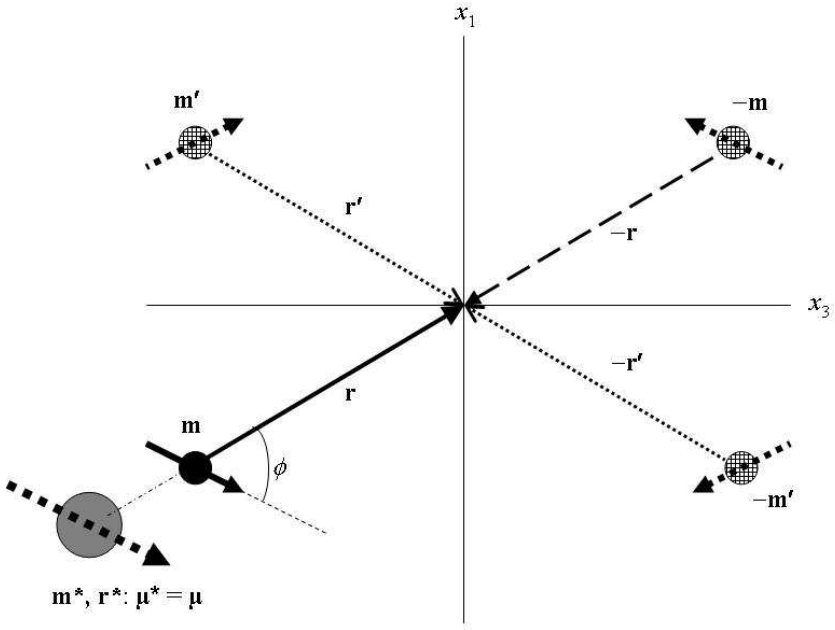

Figure 3. Intrinsic ambiguity of the inverse solution of the gradient tensor due to a point dipole source, measured at a single point (taken as the origin). The true source with magnetic moment **m** is indicated by the solid circle. The displacement vector from the source to the observation point is **r**. An equivalent source with moment **m***, parallel to **m**, and displacement vector **r***, parallel to **r**, such that $\mu^* = \mu$, is shown. Three ghost solutions, symmetrically disposed with respect to the principal axes within the plane containing **m** and **r**, are indicated by hatched circles.

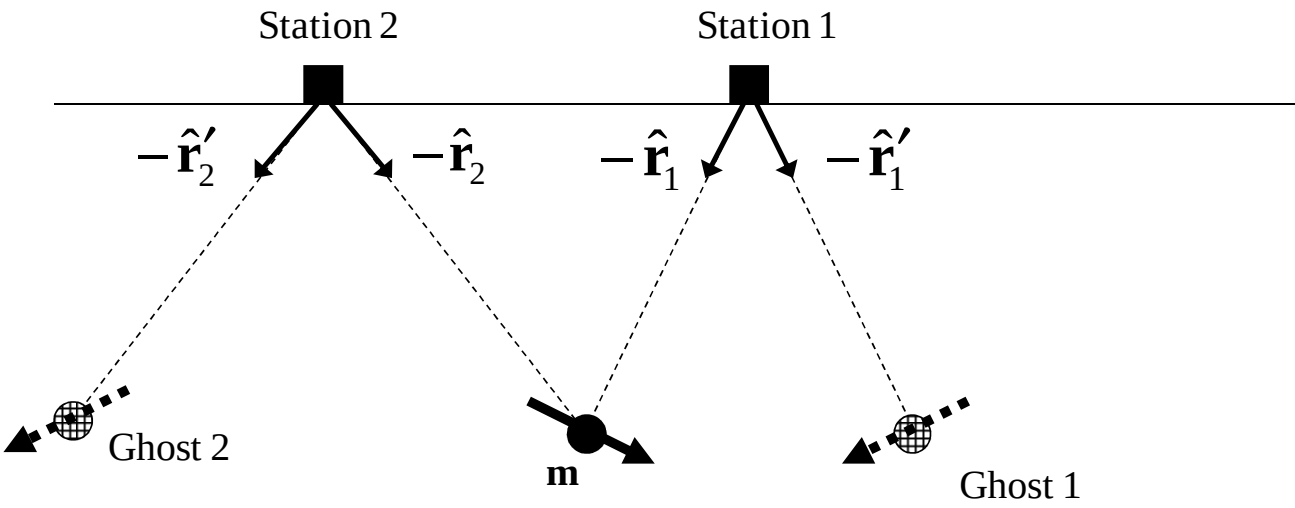

Figure 4. Disambiguation of gradient tensor inversion by elimination of ghost solutions. Gradient tensor measurements at stations 1 and 2 each produce two potential solutions in the subsurface for the direction to a dipole source and for its reduced moment vector. The ghost solutions are inconsistent, whereas the consistent solutions for the two stations correspond to the true source. Intersection of vectors to source determines the dipole location, hence the range from each station, which allows the magnetic moment to be calculated from the scaled moment.

$$\nu = \sqrt{(\mu/3)} = \{[\sqrt{(-\lambda_2^2 - \lambda_1\lambda_3)}]/3\}^{1/2}. \quad (29)$$

For a pure dipole signature ν is proportional to $\sqrt{m}/r^2$. Then at any point around an isolated dipole source ν can be estimated from the measured eigenvalues. In the presence of background gradients or interference from neighbouring bodies, at successive points $x = x_i$ (i = 1, 2,..., n) along a straight and level path, defined by $y - y_0$ = Y, ν determined from the measured data can be modelled as:

$$\nu_i = \frac{\sqrt{Cm}}{(x_i - x_0)^2 + S^2} + a + bx_i + cx_i^2. \quad (30)$$

where $S = \sqrt{(Y^2 + h^2)}$ is the slant distance from the point of closest approach to the dipole, $x = x_0$ is the point of closest approach, h is the depth of the dipole, a is the base level, and b, c are linear and quadratic terms that represent interference from other anomalies. The scalar inversion problem is to solve for the unknown parameters x_0, S, m, a, b, c. This is equivalent to conventional Werner deconvolution (e.g. Ku and Sharp, 1983) of the TMI anomaly of a thin sheet, although in this case the source is 3D.

Once the origin of x and slant distance are determined and the scaled moment, μ_i, and distance to source, r_i, at successive points are known, the measured gradient tensor elements can be modelled by:

$$B_{xx}^{(i)} = -\frac{\mu_i}{r_i^3}\left[2Lx_i^3 + 4M'Sx_i^2 - 3LS^2x_i - M'S^3\right] + \mathrm{a}_{xx} + \mathrm{b}_{xx}x_i + \mathrm{c}_{xx}x_i^2, \quad (31)$$

with similar terms for the other four independent tensor elements, where the distances along the profile, x_i, are now with respect to an origin at the point of closest approach, $M' = MY - Nh$ is the direction cosine of the slant component of magnetization and a quadratic interference term is assumed for each component. The vector inversion problem is to solve for the unknown parameters L, M, N, (direction cosines of the magnetization direction) Y, h and the interference terms a_{ij}, b_{ij}, c_{ij}. This is carried out in a similar way to the deconvolution of the invariant ν (Clark, 2010). At this stage it is recommended to remove the interference terms from the measured tensor elements and recalculate the eigenvalues

and ν. Using the new estimates of x_0, S, m the deconvolution of the tensor elements can be repeated. The process is generally rapidly convergent, the revised interference terms become small and the source parameters become more precisely determined.

Properties of the normalised source strength

Equation (7), which expresses normalised moment μ of a dipole source in terms of the eigenvalues of the tensor, can be interpreted more generally as a normalised source strength (NSS), which has a simple physical interpretation for a number of elementary source types and has generally desirable properties. For simple narrow sources, for spheres, and for horizontal cylinders, μ peaks directly above the centre of the source and for wide sheet-like bodies and prisms it peaks directly above the edges. For all 2D sources, for spheres, for compact 3D bodies that can be represented by a dipole, and for narrow, axially magnetized pipe-like bodies (pole-type sources) μ is completely independent of the magnetization direction. Beiki et al. (2012) show that for more complex 3D sources μ is only weakly dependent on magnetization direction, substantially less so than the 3D total gradient (which is the usual generalization of the ASA to 3D).

For several useful 2D and 3D models (e.g. the point pole, point dipole, line of dipoles (horizontal cylinder), thin dipping sheet, and contact models) the NSS is a homogeneous function with a simple $1/r^n$ fall-off, suitable for Euler deconvolution, and the width of the μ anomaly is simply related to the source depth. Beiki et al. (2012) and Clark (2012b) expressed the NSS of some simple sources as

$$\mu = \frac{Cq}{r^n}, \tag{32}$$

where q is a geometry-dependent source term and n is the structural index (SI) pertaining to gradient anomalies. Using this formulation, Beiki et al. (2012) demonstrated the efficacy of Euler deconvolution of the NSS for simultaneous estimation of structural indices, locations of geological boundaries, and source depths in an area that exhibits strong remanent magnetization. Clark (2012b) showed the utility of the NSS for interpreting the gradient tensor anomaly over a tabular magnetite skarn.

The NSS is not harmonic in general. For example μ for a dipole source is proportional to $1/r^4$, so $\nabla^2\mu$ is proportional to $\nabla^2(1/r^4) = 12/r^6$, and does not satisfy Laplace's equation. The definitions and properties of the NSS for simple source types are summarized in Table 1.

Generalization of the Nara and modified Nara methods to other source types

For the source types listed in Table 1, the anomalous vector and tensor components obey Euler's homogeneity equation. This fact can be exploited to generalize the Nara et al. (2006) inversion method for dipole sources, and the Clark et al. (2009) modification of it, to these other sources. The Appendix gives expressions for the vector and tensor components for these models, as a basis for the following general treatment.

Figure 5 illustrates the physical basis for the inversions. Along a fixed direction $\hat{\mathbf{r}}$, the field vector $\mathbf{b}$ is equal to a geometric factor, depending only on the magnitude and orientation of magnetization, divided by r^s, where $s = n - 1$ is the SI of the field components, i.e.

$$\mathbf{b} = \frac{\mathbf{c}(\hat{\mathbf{r}})}{r^s}. \tag{33}$$

where $\mathbf{c}$ is a constant vector for specified $\hat{\mathbf{r}}$. Therefore the directional derivative of $\mathbf{b}$ along $\hat{\mathbf{r}}$ is:

$$\frac{\partial \mathbf{b}}{\partial r} = \nabla \mathbf{b}.\hat{\mathbf{r}} = \mathbf{B}.\hat{\mathbf{r}} = \frac{-s\mathbf{c}(\hat{\mathbf{r}})}{r^{s+1}} = \frac{-s\mathbf{b}}{r}. \tag{34}$$

It follows that $\mathbf{r}$ obeys the matrix equation

$$\mathbf{Br} = -s\mathbf{b}, \tag{35}$$

which has solution

$$\mathbf{r} = r\hat{\mathbf{r}} = r\begin{bmatrix} n_1 \\ n_2 \\ n_3 \end{bmatrix} = -s\mathbf{B}^{-1}\mathbf{b}, \tag{36}$$

which, provided det**B** = I_2 is nonzero, gives the displacement vector from the source to the measurement point *independent* of the magnetization direction, even though each tensor element and vector component on the RHS of this expression depends on the direction of **J**. For 2D sources, equation (36) reduces to

$$\mathbf{r}_{2D} = r\begin{bmatrix} n_1 \\ n_3 \end{bmatrix} = -s\mathbf{B}_{2D}^{-1}\mathbf{b}_{2D}. \tag{37}$$

Once the location of the source is known, determination of the magnetization direction and source strength becomes a straight-forward linear inversion problem. For example, for a dipole source the moment **m** = $m(L, M, N) = (m_x, m_y, m_z)$ can be calculated as (Lima et al., 2006):

$$\mathbf{m} = \frac{r^3}{C}\left[\frac{3\mathbf{b}.\mathbf{r}}{2r^2}\mathbf{r} - \mathbf{b}\right]. \tag{38}$$

The dipole inversion method of Clark et al. (2009) and Clark (2012a,b) can be generalized similarly. Along a fixed direction $\hat{\mathbf{r}}$, the gradient tensor **B** is equal to a geometric factor, depending only on the magnitude and orientation of magnetization, divided by r^n, where n is the SI of the gradient components, i.e.

$$\mathbf{B} = \frac{\mathbf{G}(\hat{\mathbf{r}})}{r^n}. \tag{39}$$

where **G** is a constant tensor for specified $\hat{\mathbf{r}}$. For example, in the dipole case n = 4 and the explicit form of **G** can be obtained from (19)-(20). The directional derivative of **B** along $\hat{\mathbf{r}}$ is

$$\frac{\partial \mathbf{B}}{\partial r} = (\hat{\mathbf{r}}.\nabla)\mathbf{B} = \frac{-n\mathbf{G}(\hat{\mathbf{r}})}{r^{n+1}} = \frac{-n\mathbf{B}}{r}, \tag{40}$$

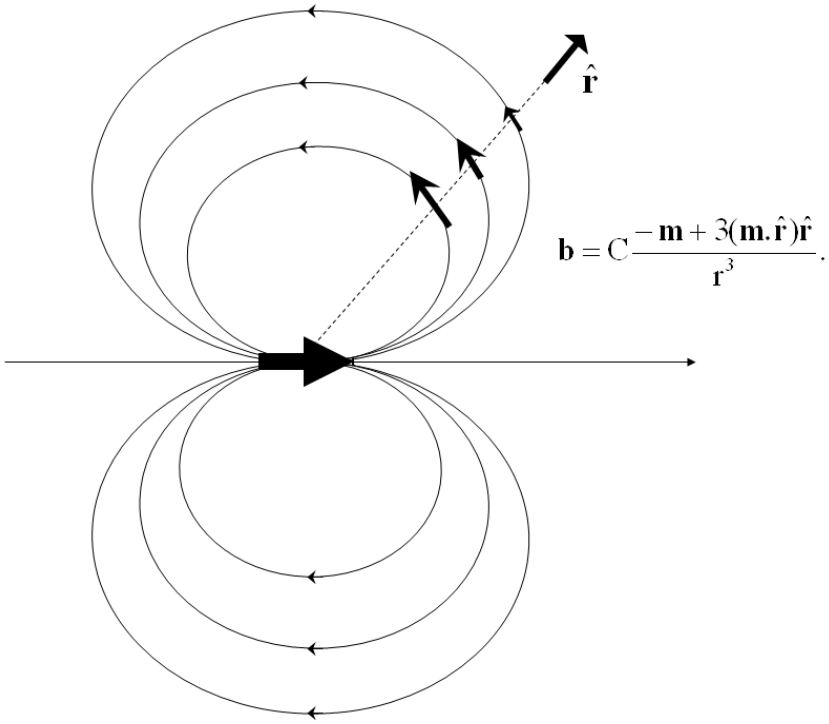

Figure 5. Physical basis of the Nara (2006) and Clark et al. (2009) methods for dipole DLC. Along a fixed direction $\hat{\mathbf{r}}$, the field vector **b** is equal to a geometric factor, depending only on the magnitude and orientation of **m**, divided by r^3. Similarly, the gradient tensor maintains the same structure, and falls off as $1/r^4$, while the second order gradients fall off as $1/r^5$. Measurements at a single location $\mathbf{r} = r\hat{\mathbf{r}}$ of the vector and first order gradient tensor, or of a subset of the first order and second order gradient components, provide enough information to uniquely determine the source-sensor vector **r**. Given **r**, the moment vector **m** can be determined from either **b** or **B**.

$$\therefore (\mathbf{r}.\nabla)\mathbf{B} = -n\mathbf{B}. \tag{41}$$

Equation (41) provides an overdetermined set of linear equations relating the components of **r** to tensor components and their spatial derivatives. Only a subset of the second order gradients is needed to obtain a unique location. If the gradient tensor is measured along a profile segment, parallel to the *x* axis, the source location can be calculated directly from the tensor and its along-profile derivative, which can be calculated by numerical differentiation:

$$\mathbf{r} = \begin{bmatrix} x - x_0 \\ y - y_0 \\ -h \end{bmatrix} = -n \begin{bmatrix} \frac{\partial B_{xx}}{\partial x} & \frac{\partial B_{xy}}{\partial x} & \frac{\partial B_{xz}}{\partial x} \\ \frac{\partial B_{xy}}{\partial x} & \frac{\partial B_{yy}}{\partial x} & \frac{\partial B_{yz}}{\partial x} \\ \frac{\partial B_{xz}}{\partial x} & \frac{\partial B_{yz}}{\partial x} & \frac{\partial B_{zz}}{\partial x} \end{bmatrix}^{-1} \begin{bmatrix} B_{xx} \\ B_{xy} \\ B_{xz} \end{bmatrix}. \tag{42}$$

Thus measurements of the gradient tensor along a short profile segment are sufficient to uniquely determine the source location. If the gradient tensor is known over a portion of a horizontal plane, so that *y* as well as *x* derivatives can be calculated, all tensor elements can be incorporated into a column vector on the RHS and the overdetermined system can be solved in a least squares sense using the generalized inverse.

Once the source location is determined, the source strength and magnetization direction can be determined from the gradient tensor through linear inversion. Clark et al. (2009) and Clark (2012a,b) give an explicit solution for the dipole moment vector. This can be generalized by noting that, for any source type, the geometric factor **G** can be rewritten as a 5×1 matrix (column vector) and expressed as the product of a 5×3 matrix **K** of terms that involve only direction cosines of **r** and a column vector $\mathbf{Q} = q[J_x, J_y, J_z]^T$, which represents a source strength. Then (39) takes the form

$$\begin{bmatrix} B_{xx} \\ B_{xy} \\ B_{xz} \\ B_{yy} \\ B_{yz} \end{bmatrix} = \frac{\mathbf{K}(\hat{\mathbf{r}})}{r^n} \begin{bmatrix} qJ_x \\ qJ_y \\ qJ_z \end{bmatrix}, \tag{43}$$

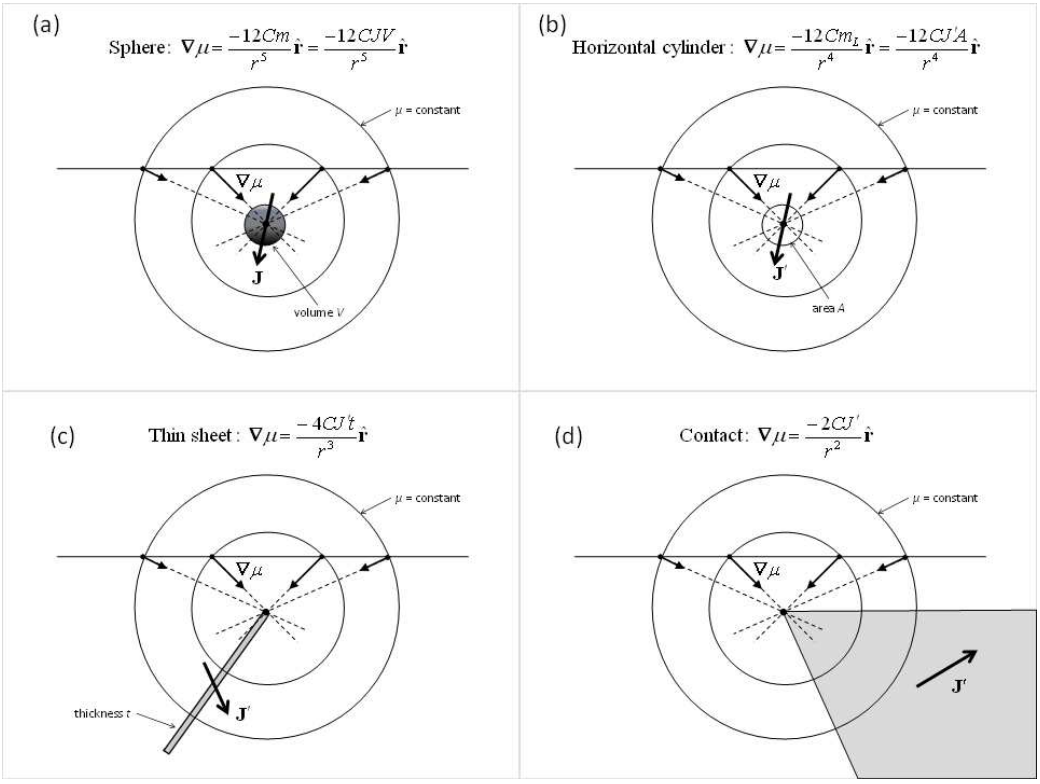

Figure 6. Determination of source location using the vector gradient of the NSS μ, for (a) sphere (point dipole), (b) 2D cylinder (horizontal line of dipoles), (c) semi-infinite thin sheet, and (d) contact models. Directions to source are defined by $\nabla\mu$. The displacement vector from observation point to source is proportional to $\mu/\nabla\mu$.

which implies that

$$\mathbf{Q} = \begin{bmatrix} qJ_x \\ qJ_y \\ qJ_z \end{bmatrix} = qJ \begin{bmatrix} L \\ M \\ N \end{bmatrix} = r^n \mathbf{K}^* \mathbf{B} = r^n \left(\mathbf{K}^T \mathbf{K}\right)^{-1} \mathbf{K}^T \mathbf{B}, \tag{44}$$

where **K*** denotes the pseudoinverse of the non-square matrix **K**. Equation (44) determines the source strength qJ and the direction (L, M, N) of magnetization.

Vector gradient of the normalised source strength

Consider a densely sampled grid of magnetic gradient tensor elements. The data are assumed to be of sufficient quality to allow accurate calculation of horizontal derivatives of tensor components by numerical differentiation or Fourier domain processing and calculation of vertical derivatives by Fourier domain filtering or convolution filtering. The scaled moment μ can be calculated at each grid point from the tensor elements and its horizontal derivatives can then be obtained by numerical differentiation. Because μ does not obey Laplace's equation, however, its vertical derivative cannot be obtained using standard Fourier filters that perform this task for potential fields. In principle, the vertical derivative of μ can be estimated by numerical differentiation of its values, evaluated at slightly different levels, calculated from the continuations of the tensor elements.

An alternative approach, which is generally more accurate, is to calculate the vertical derivative from the tensor elements and their vertical derivatives, by repeatedly using the product rule of differentiation. Since the canonical invariants I_1 and I_2 can be simply expressed in terms of the tensor elements, using equations (2) and (3), their vertical derivatives can be written in terms of tensor elements and their vertical derivatives

$$\frac{\partial I_1}{\partial z} = \frac{\partial}{\partial z}\left(B_{yy}B_{zz} + B_{xx}B_{yy} + B_{zz}B_{xx} - B_{xy}^2 - B_{xz}^2 - B_{yz}^2\right) = \frac{\partial}{\partial z}\left(-B_{yy}^2 - B_{xx}^2 - B_{xx}B_{yy} - B_{xy}^2 - B_{xz}^2 - B_{yz}^2\right),$$

which gives

$$\frac{\partial I_1}{\partial z} = -2B_{xx}\frac{\partial B_{xx}}{\partial z} - 2B_{xy}\frac{\partial B_{xy}}{\partial z} - 2B_{xz}\frac{\partial B_{xz}}{\partial z} - 2B_{yy}\frac{\partial B_{yy}}{\partial z} - 2B_{yz}\frac{\partial B_{yz}}{\partial z} - B_{xx}\frac{\partial B_{yy}}{\partial z} - B_{yy}\frac{\partial B_{xx}}{\partial z}. \tag{45}$$

The vertical derivatives of tensor elements can be obtained by standard Fourier processing techniques, because the tensor elements are harmonic. However, the vertical derivatives can also expressed in terms of horizontal derivatives of tensor elements, by swapping the order of differentiation:

$$\frac{\partial I_1}{\partial z} = -2B_{xx}\frac{\partial B_{xz}}{\partial x} - 2B_{xy}\frac{\partial B_{xz}}{\partial y} - 2B_{xz}\frac{\partial B_{zz}}{\partial x} - 2B_{yy}\frac{\partial B_{yz}}{\partial y} - 2B_{yz}\frac{\partial B_{zz}}{\partial y} - B_{xx}\frac{\partial B_{yz}}{\partial y} - B_{yy}\frac{\partial B_{xz}}{\partial x}. \quad (46)$$

Thus the vertical derivative of I_1 can be obtained directly from the tensor elements measured on a plane, using horizontal derivatives calculated by numerical differentiation.

Similarly,

$$\frac{\partial I_2}{\partial z} = \frac{\partial}{\partial z}\left(B_{xx}B_{yy}B_{zz} - B_{xx}B_{yz}^2 - B_{zz}B_{xy}^2 - B_{yy}B_{xz}^2 + 2B_{xy}B_{xz}B_{yz}\right),$$

$$\begin{aligned}
\therefore \frac{\partial I_2}{\partial z} &= \left(B_{xx}B_{yy} - B_{xy}^2\right)\frac{\partial B_{zz}}{\partial z} + \left(B_{xx}B_{zz} - B_{xz}^2\right)\frac{\partial B_{yy}}{\partial z} \\
&\quad + \left(B_{yy}B_{zz} - B_{yz}^2\right)\frac{\partial B_{xx}}{\partial z} + 2\left(B_{xy}B_{xz} - B_{xx}B_{yz}\right)\frac{\partial B_{yz}}{\partial z} \\
&\quad + 2\left(B_{yz}B_{xz} - B_{xy}B_{zz}\right)\frac{\partial B_{xy}}{\partial z} + 2\left(B_{xy}B_{yz} - B_{xz}B_{yy}\right)\frac{\partial B_{xz}}{\partial z} \\
&= -\left(B_{xx}B_{yy} - B_{xy}^2\right)\left(\frac{\partial B_{xz}}{\partial x} + \frac{\partial B_{yz}}{\partial y}\right) + \left(B_{xx}B_{zz} - B_{xz}^2\right)\frac{\partial B_{yz}}{\partial y} \\
&\quad + \left(B_{yy}B_{zz} - B_{yz}^2\right)\frac{\partial B_{xz}}{\partial x} + 2\left(B_{xy}B_{xz} - B_{xx}B_{yz}\right)\frac{\partial B_{zz}}{\partial y} \\
&\quad + 2\left(B_{yz}B_{xz} - B_{xy}B_{zz}\right)\frac{\partial B_{yz}}{\partial x} + 2\left(B_{xy}B_{yz} - B_{xz}B_{yy}\right)\frac{\partial B_{zz}}{\partial x}.
\end{aligned} \quad (47)$$

Expressions for vertical derivatives of the eigenvalues can be derived by differentiating the characteristic equation of the tensor, equation (1), and rearranging:

$$\frac{\partial}{\partial z}\left[\lambda_i^3 + I_1\lambda_i - I_2\right] = 3\lambda_i^2\frac{\partial \lambda_i}{\partial z} + I_1\frac{\partial \lambda_i}{\partial z} + \lambda_i\frac{\partial I_1}{\partial z} - \frac{\partial I_2}{\partial z} = 0,$$

$$\therefore \frac{\partial \lambda_i}{\partial z} = \frac{\frac{\partial I_2}{\partial z} - \lambda_i \frac{\partial I_1}{\partial z}}{3\lambda_i^2 + I_1}, \quad (3\lambda_2^2 + I_1 \neq 0). \tag{48}$$

This expression becomes indeterminate in the case of degenerate eigenvalues, for which $\lambda_2 = \lambda_3 = -\lambda_1/2$. This applies, for example, everywhere for the point pole model (representing a long, narrow, axially magnetized pipe) and everywhere along the magnetization axis for a dipole source. When the eigenvalues are degenerate in a neighbourhood of a measurement point for the gradient tensor, $I_1 = -3\lambda_2^2 = -3\lambda_3^2$, so their vertical derivatives are given by:

$$\begin{aligned} \frac{\partial \lambda_2}{\partial z} &= \frac{\partial \lambda_3}{\partial z} = -\frac{1}{6\lambda_2}\frac{\partial I_1}{\partial z}, \quad (3\lambda_2^2 + I_1 = 0), \\ \frac{\partial \lambda_1}{\partial z} &= \frac{1}{6\lambda_1}\frac{\partial I_1}{\partial z}, \quad (3\lambda_2^2 + I_1 = 0). \end{aligned} \tag{49}$$

The vertical derivative of the scaled moment can then be calculated from

$$\begin{aligned} \frac{\partial \mu}{\partial z} &= \frac{\partial}{\partial z}\sqrt{-I_1 - 2\lambda_2^2} = \frac{-\frac{\partial I_1}{\partial z} - 4\lambda_2 \frac{\partial \lambda_2}{\partial z}}{2\sqrt{-I_1 - 2\lambda_2^2}} \\ &= \begin{cases} -\dfrac{(I_1 - \lambda_2^2)\frac{\partial I_1}{\partial z} + 4\lambda_2 \frac{\partial I_2}{\partial z}}{2\mu(3\lambda_2^2 + I_1)}, & (3\lambda_2^2 + I_1 \neq 0), \\ -\dfrac{1}{6\mu}\dfrac{\partial I_1}{\partial z}, & (3\lambda_2^2 + I_1 = 0). \end{cases} \end{aligned} \tag{50}$$

Horizontal derivatives of μ can be calculated directly from measurements on a plane, by numerical differentiation, or by using analogous expressions to eqn (50), simply replacing z by x and y. Equation (50) breaks down at isolated points where the gradient disappears, in which case $\mu = 0$. This can occur, for example, where neighbouring sources fortuitously produce precise cancellation of the gradient tensor elements at a point. It is also possible in principle for regional trends in the gradient tensor, superimposed on a local anomaly, to produce cusps in eigenvalue profiles at points of degeneracy, so that the derivative is

discontinuous at those points. Such cases are easily recognised and should be excluded from analysis of the vector gradient of the NSS.

Since the isosurfaces of the scaled moment around a dipole are spheres centred on the dipole source and the magnitude falls off with distance, the vector gradient of μ points directly towards the dipole, as shown in Figure 6a. Specifically

$$\nabla\mu = \frac{\partial\mu}{\partial x}\hat{\mathbf{x}} + \frac{\partial\mu}{\partial y}\hat{\mathbf{y}} + \frac{\partial\mu}{\partial z}\hat{\mathbf{z}} = \nabla\left(\frac{3Cm}{r^4}\right) = -\frac{12Cm}{r^6}\mathbf{r} = -\frac{12Cm}{r^5}\hat{\mathbf{r}}. \tag{51}$$

Therefore the direction from the observation point to the source is

$$-\hat{\mathbf{r}} = \frac{\nabla\mu}{|\nabla\mu|}, \tag{52}$$

and the distance from the observation point to the source is

$$r = \frac{4\mu}{|\nabla\mu|}. \tag{53}$$

These two relations are sufficient to locate the dipole with respect to the grid point. This approach may be generalized to other simple models, as shown in Figure 6 and listed in Table 1. For sources for which the NSS conforms to eqn (32), the location of the source with respect to an observation point, $-\mathbf{r}$, is given by

$$-\mathbf{r} = \frac{n\mu}{|\nabla\mu|^2}\nabla\mu. \tag{54}$$

Note that this allows estimation of source location directly, without triangulation based on estimated directions to source. In this context, source location refers to the centre of the source for the sphere, horizontal cylinder and horizontal line current models, to the top of a narrow, axially magnetized pipe that can be represented by a point pole, to the top of a thin dipping sheet, and to the top corner of a contact. When the source type is uncertain, the appropriate structural index can be estimated as the value of n for which the clustering of

location solutions is tightest. For n too small the converging vectors to source fail to meet, for n too large they overshoot.

Estimation of source location and magnetization direction for a vertical pipe

The bottomless narrow vertical pipe model provides a useful representation of many igneous plugs, diatremes and pipe-like magnetite- or pyrrhotite bearing orebodies. Exploration for potentially diamond-bearing kimberlite and lamproite pipes is a major economic application. Kimberlites and lamproites tend to be vertically emplaced into stable cratonic areas, so post-emplacement tilting is unlikely, and their geometry is typically pipe-like. Remanent magnetization is often important in these intrusions, so their magnetization directions may depart significantly from the present geomagnetic field direction.

The magnetic gradient tensor elements for a narrow vertical pipe with arbitrary magnetization direction can be calculated by integrating the tensor elements, due to a dipole with the same magnetization direction, with respect to depth from the top of the pipe to infinity. If the cross-section area of the pipe is A and the magnetization vector is $\mathbf{J}$, this is equivalent to summing the effects of discs of area A and thickness dz, each with dipole moment $d\mathbf{m} = \mathbf{J}Adz$, from $z = h$ to $z = \infty$. The resulting expressions for the tensor elements are not as simple as those for the other simple models discussed in this paper, and will not be given here. Furthermore, the expressions for the eigenvalues and the NSS derived from them are much more complicated and difficult to interpret, unless the magnetization is vertical, in which case the model reduces to a point pole with pole strength $p = -J_zA$, where J_z is the vertical component of magnetization (Emerson et al., 1985). When a horizontal component of magnetization is present, μ does not peak perfectly above the pipe.

This difficulty can be resolved, however, by considering the vertical derivative of the gradient tensor over the pipe. The process of differentiation undoes the vertical integration and produces tensor elements that are equivalent to those of a thin disc of small diameter at the top of the pipe (see Figure 7). Therefore, provided the height of the sensor above the top of the pipe is large compared to the pipe diameter, the components of $\partial\mathbf{B}/\partial z$ correspond to those of a point dipole with magnetic moment parallel to the pipe

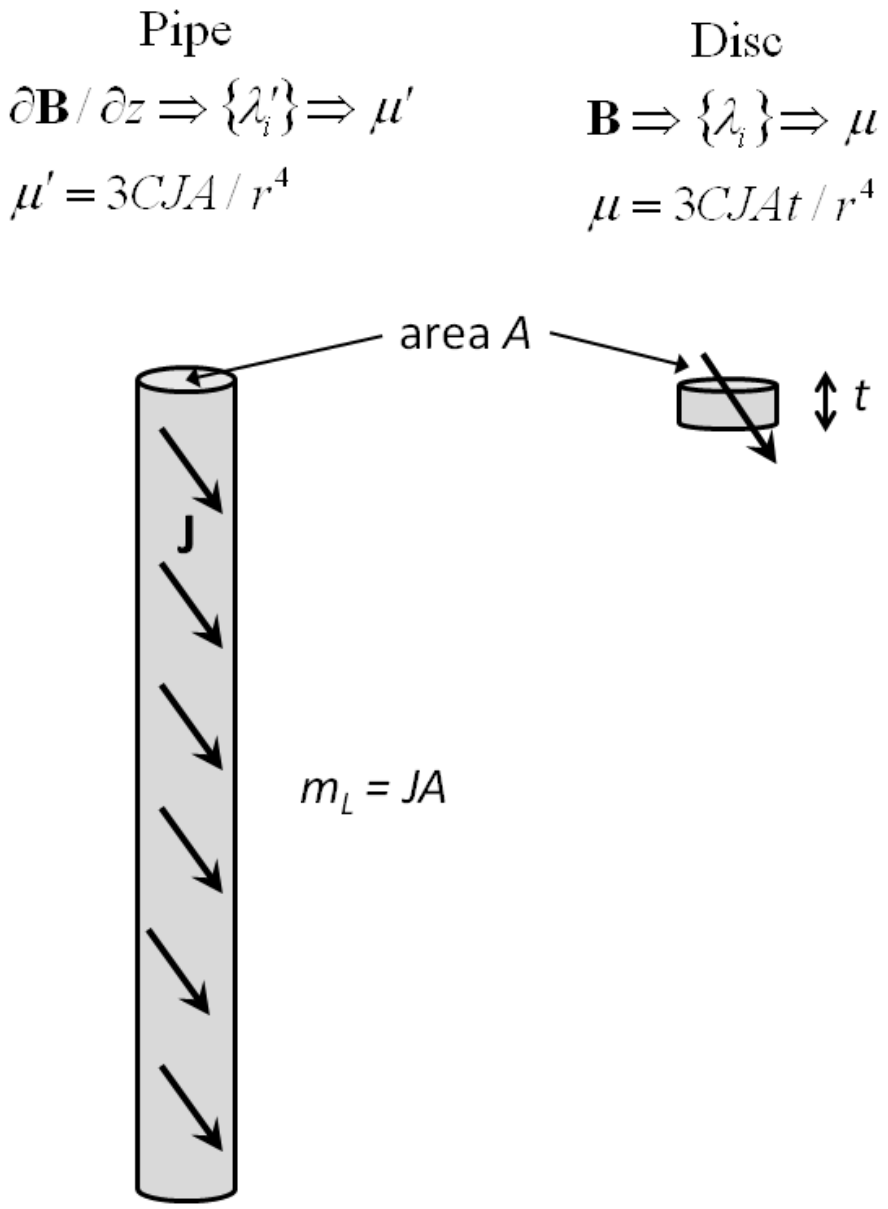

Figure 7. Relationship between ∂**B**/∂*z*, and its associated eigenvalues and modified NSS μ', for a vertical pipe; and the gradient tensor **B**, its eigenvalues and NSS, for a thin disc with identical magnetization direction, located at the top of the pipe.

magnetization. The eigenvalues of the matrix [$\partial B_{ij}/\partial z$], denoted by λ'_i, can be calculated and used to construct the modified NSS parameter given by

$$\mu' = \sqrt{-(\lambda'_2)^2 - \lambda'_1\lambda'_3} = \frac{3CJA}{r^4}, \tag{55}$$

which forms a symmetric anomaly, peaking directly over the top of the pipe, and can be used to locate it using the methods developed for dipole sources. If the elements of **B** are in nT/m, the units of μ' are nT/m². The magnetization direction of the pipe can be found from the elements of $\partial\mathbf{B}/\partial z$, using the methods applicable to dipole sources. Note that μ' is not equal to the vertical derivative of the usual NSS μ, because eigenvalues and their combinations are not linear functions of the tensor elements. This means that, although tensor elements from composite sources are simply the sum of contributions of all the elements that comprise the sources, eigenvalues do not exhibit linear superposition in the same way. If the pipe has non-vertical plunge, the radial symmetry of μ' about the pipe is distorted, particularly if the depth extent is limited. This provides an indication of plunge direction. Analysis of plunging and depth limited pipes will be the subject of a separate paper.

Example of source inversion for a horizontal cylinder source

Figure 8 shows theoretical vector and tensor components over a buried horizontal cylinder, calculated using equations (A7) and (A8). The components are contaminated by white Gaussian noise (WGN) with standard deviation equal to 10% of the respective rms anomaly magnitudes (|**b**| for the vector, μ for the tensor). The cross-section radius of the cylinder is 50 m, the depth to centre is 100 m, the centre of the cylinder lies beneath x = 70 m, the magnetization inclination is 55°, measured downwards from the +x axis, and the magnetization intensity is 1 A/m. Figure 9 shows Nara-type solutions for the centre of the horizontal cylinder, obtained by inverting the vector and tensor data shown in Figure 8, using equation (37) with s = 2. The mean estimated location (± 1 SE) for solutions from data points between x = –50 m and +170 m is both precise and accurate: x_0 = 70.0 ± 1.9 m, h = 101.1 ± 1.4 m (N = 23). If different values of s that are inappropriate for the source geometry are used, the vector endpoints are more scattered (if s < 2 the converging vectors to source fail to meet, if s > 2, they overshoot). The standard errors become slightly smaller

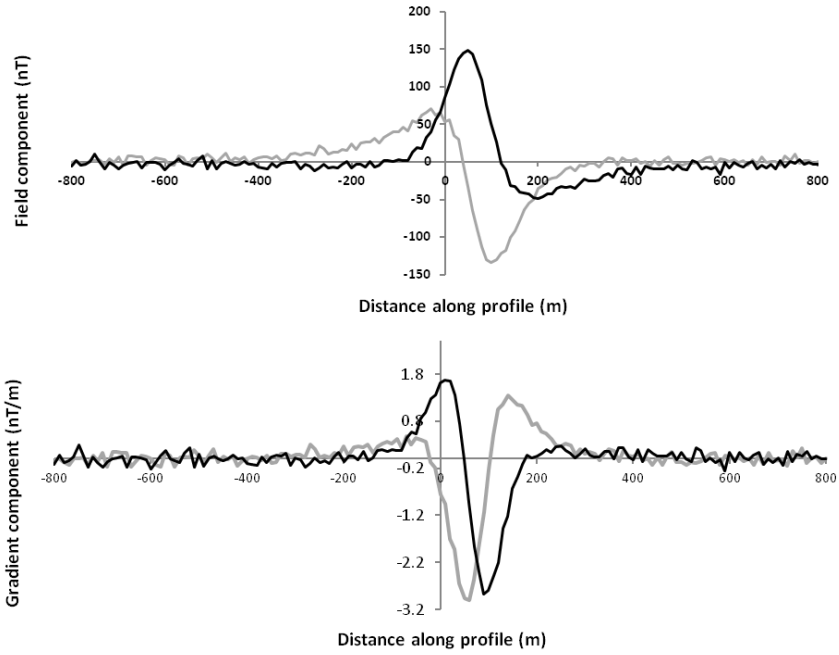

Figure 8. Theoretical vector (top) and tensor (bottom) components along a principal profile over a 2D horizontal cylinder, with 10% additive WGN. In the top plot, the grey line indicates b_x, black indicates b_z . In the bottom plot, grey = B_{xx}, black = B_{xz}.

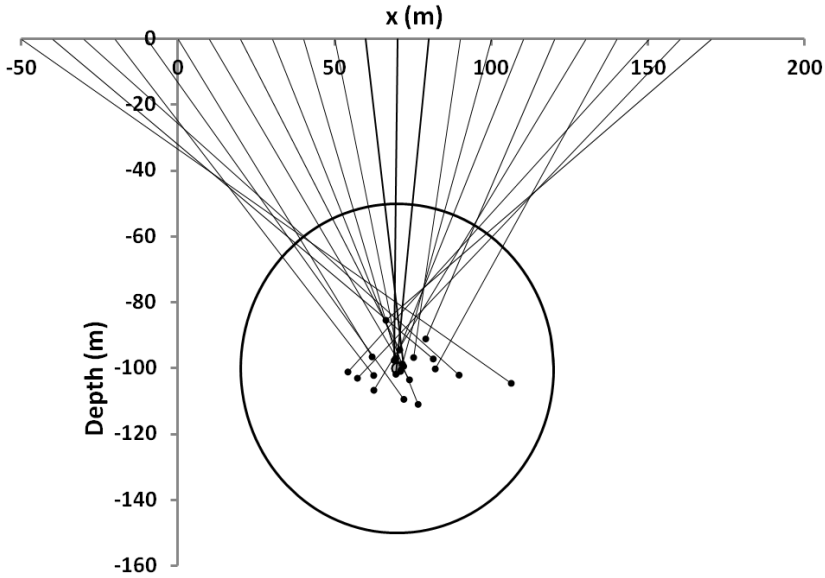

Figure 9. Inverted solutions for the centre of the horizontal cylinder that produces the anomalies shown in Figure 8, based on equation (37), the Nara-type method. Dots indicate estimated source locations, with lines connecting them to the corresponding observation point.

when the analysis is restricted to a range with higher signal-to-noise ratio. For data points that are more distant from the source, the solutions become much more scattered. Inversion based on the vector gradient of μ, using equation (54), gave a less precise mean estimated location for solutions from the same 23 data points: x_0 = 76 ± 10 m, h = 99 ± 6 m. This is to be expected, as numerical differentiation of the NSS amplifies the noise. By restricting the analysis to stations in the range x = 0-120 m, the estimated location becomes x_0 = 69 ± 5 m, h = 102 ± 3 m.

Given the inverted location, the source term for the horizontal cylinder (the linear dipole density) can be estimated by $m_L = J'A = \dfrac{\mu_{2D} r^3}{4C}$, (56)

and the direction of effective magnetization by

$$\begin{bmatrix} L' \\ N' \end{bmatrix} = \frac{1}{|\mathbf{b}|} \begin{bmatrix} n_1^2 - n_3^2 & 2n_1 n_3 \\ 2n_1 n_3 & n_3^2 - n_1^2 \end{bmatrix} \begin{bmatrix} b_x \\ b_z \end{bmatrix} = \frac{1}{\mu_{2D}} \begin{bmatrix} n_1(3n_3^2 - n_1^2) & n_3(3n_1^2 - n_3^2) \\ n_3(3n_1^2 - n_3^2) & -n_1(3n_3^2 - n_1^2) \end{bmatrix} \begin{bmatrix} B_{xx} \\ B_{xz} \end{bmatrix}. \qquad (57)$$

where $L' = J_x/J'$, $N' = J_z/J'$, $n_1 = (x - x_0)/r$, $n_3 = -h/r$.

To gain a better understanding of the robustness and reliability of the inversions for source location, they were repeated another 25 times in a Monte-Carlo simulation. For the Nara-type method, the resulting average inverted parameters, ± 1 sd with the true value in parentheses, are x_0 = 70.4 ± 1.6 (70) m, h = 100.3 ± 1.8 (100) m, m_L = 7690 ± 240 (7854) Am, Inc = 52.9° ± 2.0° (55°), when 23 solutions from x = –50 m to +170 m are used. If the profile segment is restricted to 13 solutions from the interval x = 0 to x =120 m, the corresponding results are: x_0 = 70.4 ± 1.2 m, h = 99.7 ± 1.3 m, m_L = 8100 ± 240 Am, Inc = 54.0° ± 2.1°.

For the vector gradient of NSS method the inverted location and source strength parameters are x_0 = 69.6 ± 5.4 m, h = 98.6 ± 5.4 m, m_L = 9460 ± 970 Am (x = –50 to 170 m; N = 23); and x_0 = 70.7 ± 2.8 m, h = 102.8 ± 2.3 m, m_L = 8900 ± 970 Am (x = 0 to 120 m; N = 13). Because the localization is less accurate for this method, although still quite acceptable, the inverted inclinations are also less accurate.

Analysis of the NSS over the Tallawang deposit

The Tallawang magnetite deposit, located 18 km north of Gulgong, NSW, is a tabular skarn body along the western margin of the Carboniferous Gulgong Granite, dipping steeply to grid west. Schmidt et al. (2004) described the geology of the deposit and analyzed three profiles of gradient tensor data acquired using the CSIRO GETMAG system along with a detailed conventional ground magnetic survey. Figure 10 shows profiles of the two dominant gradient tensor elements (B_{xx} and B_{xz}, with $+x$ along grid east) over the main portion of the southern extension of the Tallawang deposit. Gradient tensor elements calculated from the ground magnetic survey using Fourier filtering were in excellent quantitative agreement with the measured gradient tensors along the profiles.
Figure 11 shows solutions for the source location, derived using equation (54) with $n = 2$, which is appropriate for the thin sheet geometry of the skarn. The solutions cluster around the top of the fresh magnetite zone, with a mean location of 97.4 ± 0.7 mE, depth 19.9 ±1.1 m (1 SE, N = 15). As the observation point moves away from the skarn to the east, the solutions tend to deepen a little and dip slightly to the west. This is consistent with magnetization increasing somewhat down dip, as partial oxidation of magnetite to hematite decreases with increasing depth. The choice $n = 2$ is justified by the convergence of the vectors to source, confirming the appropriateness of the thin sheet model. This indicates that the source has considerable depth extent, because the SI should be greater than two if the depth extent is limited, approaching $n = 3$ for a body with depth extent comparable to the depth to top.

CONCLUSIONS

Eigenvector analysis; source inversions based on point-by-point combined vector and gradient tensor measurements such as the Nara (2006) method, or on tensor measurements along a profile segment (Clark et al., 2009; Clark, 2010); and new methods that exploit the properties of the normalised source strength parameter, calculated from eigenvalues of the tensor, provide powerful tools for exploiting the extra information provided by magnetic gradient tensor surveys. In the absence of gradient tensor measurements, Fourier processing of TMI data of sufficiently high quality can, in suitable circumstances, yield useful calculated estimates of anomalous magnetic field vectors and gradient tensors. The

methods that are being developed for vector and gradient tensor data are equally applicable to calculated data.

Therefore, new methods for analysing gradient tensor data can both assist interpretation of tensor gradiometer data from new systems that are under intense development and, in the meantime, add value to existing high quality TMI surveys by exploiting cryptic information that resides in single component data. Calculation is generally better than measurement for field vectors, whereas measurement is highly desirable for gradient tensors. In many cases the optimal scenario is to integrate measured tensor data with vector data derived from TMI.

Analysis of calculated vector and tensor data over Mount Leyshon, which is presented in paper II, demonstrates the utility of these data types for locating sources and defining magnetizations, even when the source does not match the assumed models perfectly. Plots of field vectors and major eigenvectors of the gradient tensor aid qualitative interpretation of the distribution of magnetic material at Mount Leyshon, including possible extensions of the mineralized system at depth, and the inversion methods discussed in this paper provide estimates of the centroid of magnetization and total moment of the magnetized zone that are consistent with the geological and petrophysical information.

Inversion based on the vector gradient of the NSS has also been successfully applied to analysis of gradient tensor data over the Tallawang magnetite deposit, obtaining good agreement between the inferred geometry of the tabular magnetite skarn body and drill hole intersections.

ACKNOWLEDGMENTS

This work comprises part of a Ph.D. project in the Department of Earth and Planetary Sciences at Macquarie University, under the supervision of Dr Mark Lackie.

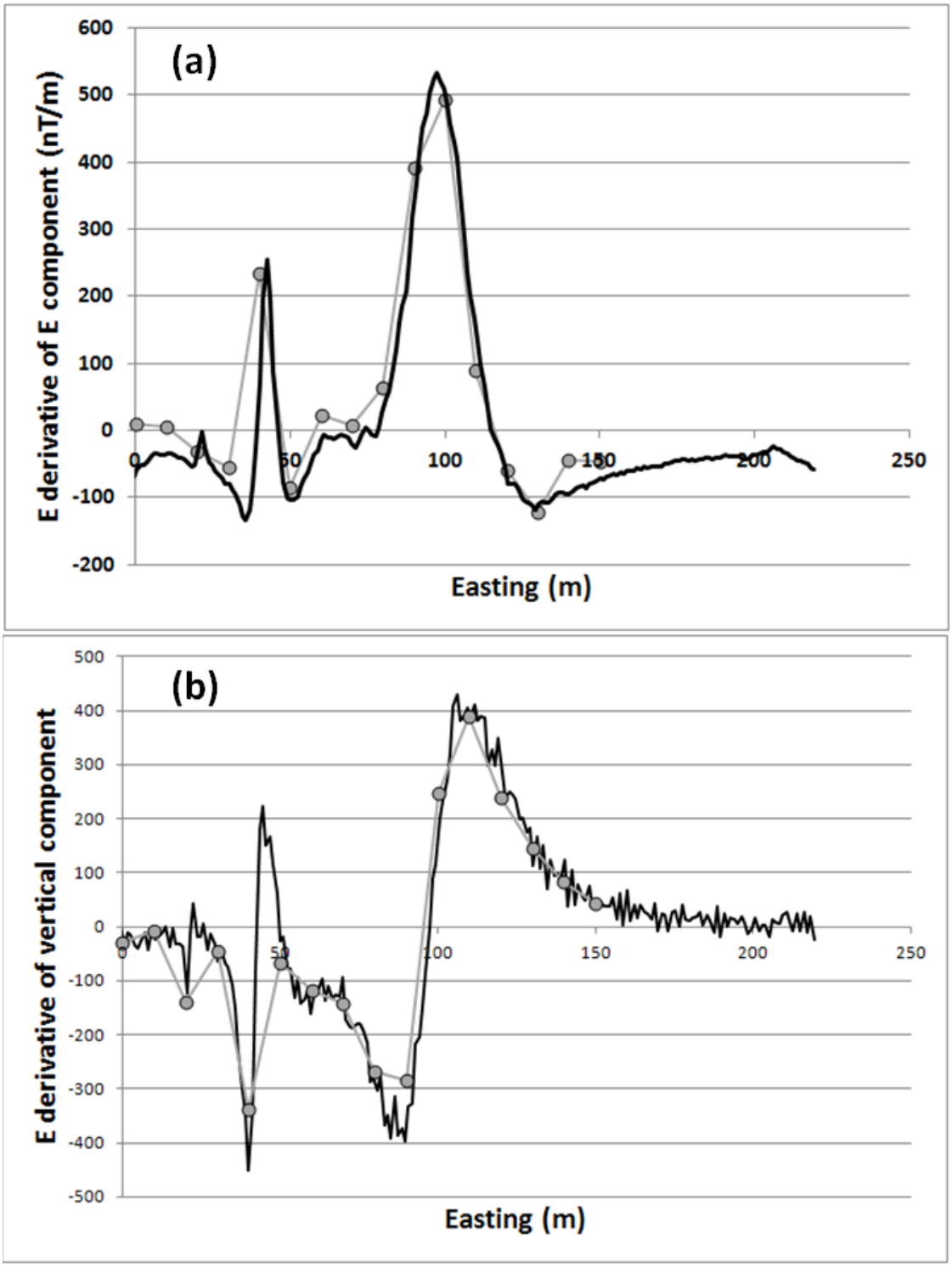

Figure 10. Gradient tensor element profiles, perpendicular to strike, along line 60 mN over the Tallawang magnetite skarn deposit, central NSW: (a) B_{xx}, (b) B_{xz}. Solid black lines indicate tensor elements calculated from a detailed TMI ground survey and grey lines and dots indicate measured gradient tensor data obtained using the CSIRO GETMAG system (Schmidt et al., 2004). The narrow anomaly to the west of the main skarn signature is caused by a steel drill collar.

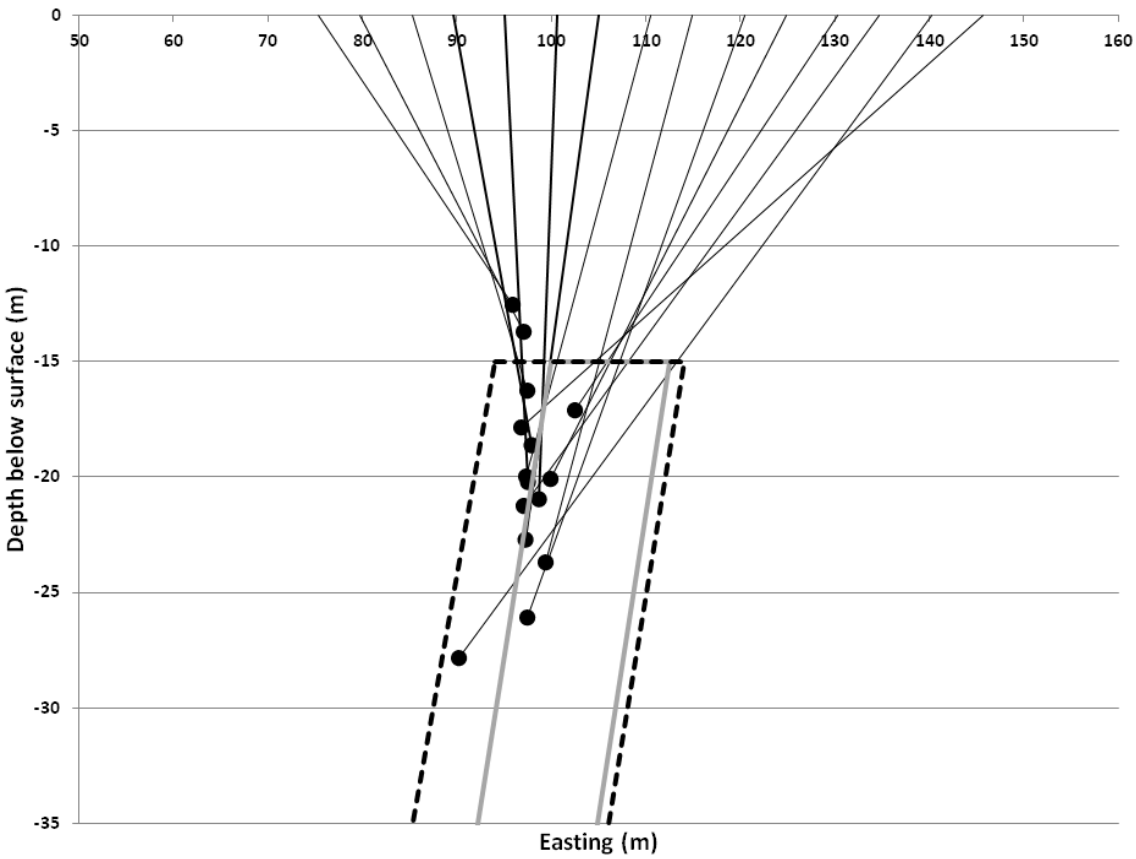

Figure 11. Solutions for the location of the top of the sheet-like skarn at Tallawang, derived using equation (54) with n = 2. The profile is along 60 mN. Solid black lines connect the solution with the station from which it was derived. The approximate outline of the skarn body is dashed, the high magnetite zone within the skarn is outlined in grey.

REFERENCES

Anton, H. and Rorres, C., 2000, Elementary Linear Algebra: Applications Version, Eighth Edition, Wiley, New York.

Beiki, M. and Pedersen, L. B., 2010, Eigenvector analysis of gravity gradient tensor to locate geologic bodies. Geophysics, 75(6): I37-I49.

Beiki, M., Pedersen, L.B. and Nazi, H., 2011, Interpretation of aeromagnetic data using eigenvector analysis of pseudogravity gradient tensor, Geophysics, 76(3), L1-L10, doi:10.1190/1.3555343.

Beiki, M., Clark, D.A., Austin, J.R. and Foss, C.A., 2012. Estimating source location using normalized magnetic source strength calculated from magnetic gradient tensor data. Geophysics (in press).

Blakely, R.J., 1996, Potential Theory in Gravity and Magnetic Applications, Cambridge University Press.

Bracken, R.E. and Brown, P.J., 2006, Concepts and Procedures Required for Successful Reduction of Tensor Magnetic Gradiometer Data Obtained from an Unexploded Ordnance Detection Demonstration at Yuma Proving Grounds, Arizona, US Geological Survey Open-File Report 2006-1027.

Christensen, A. and Rajagopalan, S., 2000. The magnetic vector and gradient tensor in mineral and oil exploration, Preview, 84, p.77.

Chwala, A., Stolz, R., Zakosarenko, V., Fritzsch, L., Shulz, M., Rompel, A., Polome, L., Meyer, M., and Meyer, H.G., 2012, Full tensor SQUID gradiometer for airborne exploration, Australian Society of Exploration Geophysicists, 22nd International Geophysical Conference and Exhibition, 26-29 February 2012 - Brisbane, Australia, CD-ROM, 4p.

Clark, D.A., Schmidt, P.W., Coward, D.A. and Huddleston, M.P., 1998, Remote determination of magnetic properties and improved drill targeting of magnetic anomaly sources by Differential Vector Magnetometry (DVM), Exploration Geophysics, 29, 312-319.

Clark, D.A., Young, J.A. and Schmidt, P.W., 2009, Magnetic Tensor Gradiometry in the Marine Environment: Correction of Electric And Magnetic Field And Gradient Measurements in a Conductive Medium and Improved Methods for Magnetic Target Location Using the Magnetic Gradient Tensor, MARELEC (Marine Electromagnetics) Conference, Stockholm, July, 2009, 10pp. CD-ROM.

Clark, D.A., 2010, Method and apparatus for detection using magnetic gradient tensor. U.S. Patent Application Pub. No.: US 2010/0211337 Al, Pub. Date: Aug. 19, 2010.

Clark, D.A. 2012a, New methods for interpretation of magnetic gradient tensor data. Australian Society of Exploration Geophysicists, 22nd International Geophysical Conference and Exhibition, 26-29 February 2012 - Brisbane, Australia, CD-ROM, 11p.

Clark, D.A. 2012b, Interpretation of the magnetic gradient tensor and normalized source strength applied to the Tallawang magnetite skarn deposit, New South Wales, Australia. Society of Exploration Geophysicists Annual Meeting, Las Vegas.

Clem, T.R., Froelich, M.C., Overway, D.J., Purpura, J.W., Wiegert, R.F., Koch, R.H., Lathrop, D.K., Rozen, J., Eraker, J.H., Schmidt, J.M., 1997, Advances in sensor development and demonstration of superconducting gradiometers for mobile operation, IEEE Transactions on Applied Super-conductivity, 7, 3287-3293.

Clem, T.R., Overway, D.J., Purpura, J.W., Bono, J.T., Koch, R.H., Rozen, J., Keeefe, G.A., Willen, S. and Mohling, R.A., 2001, High-Tc SQUID gradiometer for mobile magnetic anomaly detection, IEEE Transactions on Applied Superconductivity, 11, 871-875.

Emerson, D.W., Clark, D.A. and Saul, S.J., 1985. Magnetic exploration models incorporating remanence, demagnetization and anisotropy: HP 41C handheld computer algorithms, Explor. Geophys., 16, 1-122.

Fitzgerald, D. and Holstein, H., 2006, Innovative data processing methods for gradient airborne geophysical data sets. The Leading Edge, 25(1), 87-94.

Fitzgerald, D., Argast, D., Paterson, R. and Holstein, H., 2009, Full tensor magnetic gradiometery processing and interpretation developments, 11th SAGA Technical Meeting and Exhibition, Swaziland, 16-18 September, 2009, 265-272.

Fitzgerald, D., Argast, D., Paterson, R. and Holstein, H., 2010, Progress on interpreting dykes from full tensor magnetic gradiometry, SEG Expanded Abstracts, 29, 1162, doi:10.1190/1.3513050

Foss, C., 2006, The improvements in source resolution that can be expected from inversion of magnetic field tensor data, The Leading Edge, 25(1), 81-84.

Heath, P., 2007, Analysis of potential field gradient data: forward modelling, inversion and near-surface exploration, Ph.D. thesis, University of Adelaide.

Holstein, H., Fitzgerald, D., Willis, C.P. and Foss, C., 2011, Magnetic gradient tensor eigenanalysis for dyke location, 73rd EAGE Conference and Exhibition, Vienna, May 23-27, 2011, Vienna.

Humphrey, K.P. , Horton, T.J. and Keene, M.N. , 2005, Detection of mobile targets from a moving platform using an actively shielded, adaptively balanced SQUID gradiometer, IEEE Transactions on Applied Superconductivity, 15 (2), 753- 756.

Ku, C.C. and Sharp, J.A., 1983, Werner deconvolution for automated magnetic interpretation and its refinement using Marquardt's inverse modeling, Geophysics, 48, 754-774.

Leslie, K.E., Bick, M., Binks, R.A., Tilbrook, D.L., Clark, D.A., Schmidt, P.W., Cusack, P.J., Thorn, R.G., Blay, K. R. And Sullivan, P.R., 2005, Performance issues for a spinning

gradiometer, 10th International Superconductive Electronics Conference (ISEC 2005); Noordwijkerhout, The Netherlands. 2005: OO-01.

Leslie, K.E., Blay, K., Clark, D., Schmidt, P., Tilbrook, D., Bick, M. and Foley, C., 2007, Helicopter trial of magnetic tensor gradiometer. ASEG 19th International Conference, December 2007, Perth, Western Australia, 4 pp., CD ROM.

Li, X., 2006. Understanding the 3D analytic signal amplitude. Geophysics, 71(2), L13-L16.

Lima, E.A., Irimia, A. and Wikswo, J.P., 2006, The magnetic inverse problem, *In* J. Clarke and A.I. Braginski (Eds.), The SQUID Handbook, Vol. II Applications of SQUIDs and SQUID Systems, Wiley-VCH, Weinheim, pp.139-267.

McRae, W., Veryaskin, A.V., Greager, D., Ju, L., Blair, D., Chin, E-J, Dumas, J-C and Lee, B., 2004, String magnetic gradiometer system: recent airborne trials, Society of Exploration Geophysicists 74th Annual Meeting, Expanded Abstracts 23, 790-793.

Nabighian, M. N., 1972. The analytic signal of two-dimensional magnetic bodies with polygonal cross-section: its properties and use for automated anomaly intterpretation. Geophysics, 37, 501-517.

Nara, T., Suzuki, S., and Ando, S., 2006**,** A Closed-Form Formula for Magnetic Dipole Localization by Measurement of Its Magnetic Field and Spatial Gradients, IEEE Transactions on Magnetics. 42, 3291-3293.

Pedersen, L.B. and Rasmussen, T.M., 1990, The gradient tensor of potential field anomalies: Some implications on data collection and data processing of maps, Geophysics, 55, 1558-1566.

Schmidt, P.W., 2006, Inversion using Euler deconvolution of the magnetic gradient tensor, Australian Earth Sciences Congress, Melbourne, Extended Abstracts, 3pp.

Schmidt, P., Clark, D., Leslie, K., Bick, M., Tilbrook, D. and Foley, C., 2004, GETMAG – A SQUID magnetic tensor gradiometer for mineral and oil exploration, Exploration Geophysics, 35, 297-305.

Schmidt, P.W. and Clark, D.A., 2006, The magnetic gradient tensor: Its properties and uses in source characterization, The Leading Edge, 25(1), 75-78.

Stolz, R., L. Fritzsch, and H.-G. Meyer, 1999, LTS SQUID sensor with a new configuration, Superconductor Science and Technology, 12, 806.

Stolz, R., Zakosarenko, V. , Schulz, M., Chwala, A., Fritzsch, L., Meyer, H.-G. and Köstlin, E. O., 2006a, Magnetic full-tensor SQUID gradiometer system for geophysical applications, The Leading Edge, 25 (2), 178-180.

R. Stolz, A. Chwala, V. Zakosarenko, M. Schulz, L. Fritzsch, and H.-G. Meyer, 2006b, SQUID technology for geophysical exploration. SEG Expanded Abstracts 25, 894-898; DOI:10.1190/1.2370400.

Sunderland, A., Golden, H., McRae, W., Veryaskin, A., Ju, L. and Blair, D., 2009, Results from a novel direct magnetic gradiometer, Exploration Geophysics, 40, 222-226.

Tilbrook, D.L., 2004, The design of a new concept HTSC axial gradiometer, Physica C, 407, 1–9.

Tilbrook, D.L., Clark, D.A. and Blay, K.R., 2006, Data Extraction and Calibration of a Superconducting Rotating Magnetic Tensor Gradiometer, Applied Superconductivity Conference, Seattle, August 27 – September 1, 2006.

Veryaskin, A.V., 2001, Magnetic gradiometry: a new method for magnetic gradient measurement, Sensors and Actuators A, 91, 233-235.

Wiegert, R., Oeschger, J., and Tuovila, E., 2007, Demonstration of a novel man-portable magnetic STAR technology for real time localization of unexploded ordnance, Proceedings of MTS/IEEE Oceans 2007, DOI 10.1109/OCEANS.2007.4449229.

Wilson, H., 1985. Analysis of the Magnetic Gradient Tensor. Defence Research Establishment Pacific, Canada, Technical Memorandum, 85-13, 47.

Wynn, W.M., Frahm, C.P., Carroll, P.J., Clark, R.H., Wellhoner, J. and M.J. Wynn, 1975, Advanced super-conducting gradiometer/magnetometer arrays and a novel signal processing technique, IEEE Trans. Magn., MAG-11, 701-707.

Wynn, W.M., 1995, Magnetic dipole localization using the gradient rate tensor measured by a five-axis magnetic gradiometer with known velocity, Proc. SPIE, 2496, 357-367.

Wynn, W.M., 1997, Magnetic dipole localization with a gradiometer: obtaining unique solutions, IGARSS '97. Remote Sensing – A Scientific Vision for Sustainable Development, Geoscience and Remote Sensing, IEEE International, Vol. 4, 1483-1485.

Wynn, W.M., 1999, Detection, localization, and characterization of static magnetic-dipole sources, *In* C.E. Baum (Ed.), Detection and Identification of Visually Obscured Targets, Taylor & Francis, Philadelphia, pp. 337-374.

Young, J.A., S.T. Keenan, D.A. Clark, K.E. Leslie, P. Sullivan, P. Fairman, C. Williams, C.P. Foley and S.D. Billings, 2010, A Superconducting Magnetic Tensor Gradiometer for Underwater UXO Detection. 21st International Geophysical Conference & Exhibition (ASEG-PESA 2010); Sydney [extended abstract]. 4 pp. CD ROM.

Table 1. Properties of the Normalised Source Strength for Simple Sources

Model type	λ_1	λ_2	λ_3	NSS μ	Source term	HWHM of NSS	Location wrt observ. point	Harmonic NSS?
Sphere	$(\mu/2)[-\cos\phi + \sqrt{(4+5\cos^2\phi)}]$	$\mu\cos\phi$	$(\mu/2)[-\cos\phi - \sqrt{(4+5\cos^2\phi)}]$	$3Cm/r^4$	$q = 3m = 3JV$	$0.64h$	$4\mu\nabla\mu/\lvert\nabla\mu\rvert^2$	anharmonic
Point pole	$2Cp/r^3$ $(p > 0)$ $-Cp/r^3$ $(p < 0)$	$-Cp/r^3$	$-Cp/r^3$ $(p > 0)$ $2Cp/r^3$ $(p < 0)$	$C\lvert J_z\rvert A/r^3$	$q = \lvert p\rvert = \lvert J_z\rvert A$	$0.77h$	$3\mu\nabla\mu/\lvert\nabla\mu\rvert^2$	anharmonic
Horizontal cylinder	$4CJ'A/r^3$	0	$-4CJ'A/r^3$	$4CJ'A/r^3$	$q = 4m_L = 4J'A$	$0.77h$	$3\mu\nabla\mu/\lvert\nabla\mu\rvert^2$	anharmonic
Thin sheet	$2CJ't/r^2$	0	$-2CJ't/r^2$	$2CJ't/r^2$	$q = 2J't$	h	$2\mu\nabla\mu/\lvert\nabla\mu\rvert^2$	anharmonic
Contact	$2CJ'/r$	0	$2CJ'/r$	$2CJ'/r$	$q = 2J'$	$1.73h$	$\mu\nabla\mu/\lvert\nabla\mu\rvert^2$	harmonic
Horiz. line current	$2C\lvert i\rvert/r^2$	0	$-2C\lvert i\rvert/r^2$	$2C\lvert i\rvert/r^2$	$q = 2\lvert i\rvert$	h	$2\mu\nabla\mu/\lvert\nabla\mu\rvert^2$	anharmonic

The parameters μ and ϕ for a dipole are defined in Figure1. For gradients in nT/m, magnetizations in A/m, distances in m, C = 100 nTm/A or nH/m. Units of the geometry-dependent source term q are Am² for the sphere model, Am for the point pole and horizontal cylinder (2D line of dipoles) models, A for the thin sheet and line current models, and A/m for the contact model. J_z is the vertical component of magnetization in A/m; V is the volume of the sphere; A is the area of the flat top of the narrow pipe represented by a point pole, or the cross-section area of the horizontal cylinder; p is the pole strength in Am; $J' = \sqrt{(J_x^2 + J_z^2)}$ is the magnitude of the effective magnetization (the component normal to strike); $m_L = J'A$ is the linear density of effective dipole moment for the horizontal cylinder model; h (m) is the height of the sensor above the source location (centre for sphere, horizontal cylinder and line current models, top of the pipe for the point pole model, top of the sheet for the thin sheet model, top corner for the contact model); r (m) is the distance between the source location and the observation point.

Appendix. Vector and tensor components of simple models

Expressions for the anomalous vector components due to commonly used models, with the exception of the horizontal line current, are based on Emerson et al. (1985), and largely follow the notation of that publication. Expressions for gradient tensor elements are obtained by differentiation of the vector components and eigenvalues are calculated by solving the characteristic equation for 3D models, or by using eqn (13) in the 2D case. Equation (7) then gives expressions for the NSS.

Sphere

Vector and tensor components are given by equations (25) and (26) respectively. The eigenvalues are given by (32) and the NSS is

$$\mu = \sqrt{-\lambda_2^2 - \lambda_1\lambda_3} = \frac{3Cm}{r^4} = \frac{3CJV}{r^4}, \tag{A1}$$

where m is the magnetic moment, J is the magnetization intensity and V is the volume of the sphere.

Point pole

The point pole approximation represents a long narrow pipe-like body with nearly axial magnetization. The anomalous magnetic vector points directly away from a positive pole source and towards a negative pole. Its components at an observation point (x, y, 0) due to a point pole of strength p at (x_0,y_0,h) are given by

$$\begin{aligned} b_x &= \frac{Cp(x-x_0)}{[(x-x_0)^2+(y-y_0)^2+h^2]^{3/2}} = C\frac{p(x-x_0)}{r^3}, \\ b_y &= \frac{Cp(y-y_0)}{[(x-x_0)^2+(y-y_0)^2+h^2]^{3/2}} = C\frac{p(y-y_0)}{r^3}, \\ b_z &= \frac{-Cph}{[(x-x_0)^2+(y-y_0)^2+h^2]^{3/2}} = -C\frac{ph}{r^3}, \end{aligned} \tag{A2}$$

where

$$r = \sqrt{(x-x_0)^2+(y-y_0)^2+h^2}, \tag{A3}$$

is the distance from the source to the measurement point. The pole strength p is given by the product of the area of the top face of the pipe, multiplied by the outward normal component of magnetization. The tensor components are

$$
\begin{aligned}
B_{xx} &= \frac{-Cp[2(x-x_0)^2-(y-y_0)^2-h^2]}{r^5}, \\
B_{xy} &= \frac{-3Cp(x-x_0)(y-y_0)}{r^5}, \\
B_{xz} &= \frac{3Cph(x-x_0)}{r^5}, \\
B_{yy} &= \frac{-Cp[2(y-y_0)^2-(x-x_0)^2-h^2]}{r^5}, \\
B_{yz} &= \frac{3Cph(y-y_0)}{r^5}, \\
B_{zz} &= \frac{-Cp[2h^2-(y-y_0)^2-(x-x_0)^2]}{r^5}.
\end{aligned}
\tag{A4}
$$

The eigenvectors are radial, analogous to the eigenvectors of the gravity gradient tensor of a point mass (Pedersen and Rasmussen, 1990). Eigenvalues in non-increasing order of absolute value are

$$\lambda_1 = -C\frac{2p}{r^3}, \lambda_2 = C\frac{p}{r^3}, \lambda_3 = C\frac{p}{r^3}. \tag{A5}$$

Note that, at every observation point the eigenvalues are proportional to the vertical component of the anomalous field. The NSS is

$$\mu = |\lambda_2| = C\frac{|p|}{r^3}. \tag{A6}$$

Horizontal cylinder (2D line of dipoles)

The vector and tensor components are

$$
\begin{aligned}
b_x &= \frac{2CA\left(J_x[(x-x_0)^2-h^2]-2J_z(x-x_0)h\right)}{r^4}, \\
b_z &= \frac{2CA\left(J_z[h^2-(x-x_0)^2]-2J_x(x-x_0)h\right)}{r^4},
\end{aligned}
\tag{A7}
$$

$$B_{xx} = \left(4CA/r^6\right)\left(J_x\left(x - x_0\right)[3h^2 - \left(x - x_0\right)^2] + J_z h[3\left(x - x_0\right)^2 - h^2]\right),$$
$$B_{xz} = -\left(4CA/r^6\right)\left(J_x h[h^2 - 3\left(x - x_0\right)^2] + J_z\left(x - x_0\right)[3h^2 - \left(x - x_0\right)^2]\right), \tag{A8}$$

where J_x and J_z are the along-profile (normal to strike) and vertical down components of magnetization respectively. The nonzero eigenvalues and NSS are given by

$$\mu_{2D} = \lambda_1 = -\lambda_3 = \sqrt{B_{xx}^2 + B_{xz}^2} = \frac{4CJ'A}{r^3} = \frac{4Cm_L}{r^3}. \tag{A9}$$

Thin sheet

It is a consequence of the well-known dip ambiguity of infinite depth-extent sheet models (see e.g. Blakely, 1996, p.246-248) that the apparent magnetization direction of a vertical sheet can be converted into the effective magnetization direction of an equivalent dipping sheet by rotating the magnetization vector and the plane of the sheet together about the strike. Equivalent sheets have identical magnetization-thickness products, $J't$, where J' is the intensity of the effective magnetization in the vertical plane perpendicular to strike and t is the perpendicular thickness of the sheet.

For a vertical sheet of thickness $t << h$, the anomalous magnetic field components are given by:

$$b_x = -\frac{2Ct\left[J_z x + J_x h\right]}{r^2},\ b_z = \frac{2Ct\left[J_z h - J_x x\right]}{r^2}. \tag{A10}$$

The independent nonzero tensor elements are:

$$B_{xx} = \frac{2Ct}{r^4}[2J_x xh + J_z(x^2 - h^2)],\ B_{xz} = \frac{2Ct}{r^4}[J_x(x^2 - h^2) - 2J_z xh]. \tag{A11}$$

The nonzero eigenvalues and the NSS tensor are

$$\mu_{2D} = \lambda_1 = -\lambda_3 = \sqrt{B_{xx}^2 + B_{xz}^2} = \frac{2CJ't}{r^2}. \tag{A12}$$

Contact

Sloping contacts exhibit dip ambiguity analogous to that of a dipping sheet. The vector components become infinite as the depth to bottom goes to infinity. The tensor components of an infinite depth-extent vertical contact with top corner at $x = x_0$, $z = h$ can be calculated by differentiating vector components of a finite thickness contact (sloping step) model and taking the limit as the bottom goes to infinity. This gives

$$B_{xx} = \frac{2C}{r^2}\left[J_z(x - x_0) \; - \; J_x h\right], \; B_{xz} = \frac{2C}{r^2}\left[J_x(x - x_0) \; + \; J_z h\right]. \tag{A13}$$

which has nonzero eigenvalues and NSS given by

$$\mu_{2D} = \lambda_1 = -\lambda_3 = \sqrt{B_{xx}^2 + B_{xz}^2} = \frac{2J'}{\sqrt{(x - x_0)^2 + h^2}} = \frac{2J'}{r}. \tag{A14}$$

Horizontal line current

The vector components (in nT) due to a quasistatic horizontal line current at a horizontal displacement x, perpendicular to the conductor, and height h above the conductor, with current i amperes along $+y$ are

$$b_x = -\frac{200ih}{r^2}, b_y = 0, b_z = -\frac{200ix}{r^2}. \tag{A15}$$

The nonzero independent tensor elements are

$$B_{xx} = \frac{400ixh}{r^4}, B_{xz} = \frac{200i(x^2 - h^2)}{r^4}, \tag{A16}$$

and the nonzero eigenvalues and the NSS are given by

$$\mu_{2D} = \lambda_1 = -\lambda_3 = \frac{200\,|\,i\,|}{r^2}. \tag{A17}$$

CHAPTER 4: NEW METHODS FOR INTERPRETATION OF MAGNETIC VECTOR AND GRADIENT TENSOR DATA II: APPLICATION TO THE MOUNT LEYSHON ANOMALY, QUEENSLAND

Clark, D.A., 2013. New methods for interpretation of magnetic vector and gradient tensor data II: Application to the Mount Leyshon Anomaly, Queensland, Exploration Geophysics, 44, 114–127
(http://dx.doi.org/10.1071/EG12066).

Abstract

Acquisition of magnetic gradient tensor data is anticipated to become routine in the near future. In the meantime, modern ultrahigh resolution conventional magnetic data can be used, with certain important caveats, to calculate magnetic vector components and gradient tensor elements from total magnetic intensity (TMI) or TMI gradient surveys. An accompanying paper presented new methods for inverting gradient tensor data to obtain source parameters for a number of elementary, but useful, models. These include point dipole (sphere), vertical line of dipoles (narrow vertical pipe), line of dipoles (horizontal cylinder), thin dipping sheet, and contact models. A key simplification is the use of eigenvalues and associated eigenvectors of the tensor. The normalised source strength (NSS), calculated from the eigenvalues, is a particularly useful rotational invariant that peaks directly over 3D compact sources, 2D compact sources, thin sheets and contacts, independent of magnetisation direction. Source locations can be inverted directly from the NSS and its vector gradient.

Some of these new methods have been applied to analysis of the magnetic signature of the Early Permian Mount Leyshon gold-mineralised system, Queensland. The Mount Leyshon magnetic anomaly is a prominent TMI low that is produced by rock units with strong reversed remanence acquired during the Late Palaeozoic Reverse Superchron. The inferred magnetic moment for the source zone of the Mount Leyshon magnetic anomaly is ~ 10^{10} Am^2. Its direction is consistent with petrophysical measurements. Given estimated magnetisation from samples and geological information, this suggests a volume of ~1.5 km × 1.5 km × 2 km (vertical). The inferred depth of the centre of magnetisation is about 900 m below surface, suggesting that the depth extent of the magnetic zone is ~1800 m. Some of the deeper, undrilled portion of the magnetic zone could be a mafic intrusion similar to the nearby coeval Fenian Diorite, representing part of the parent magma chamber beneath the Mount Leyshon Intrusive Complex.

Key words: Magnetic gradient tensor, magnetic field vector, eigenvalues, eigenvectors, normalised source strength, dipole localisation, magnetic moments, Mount Leyshon

Introduction

An accompanying paper (Clark, 2012a), hereafter referred to as Paper I, presented theoretical background regarding the magnetic gradient tensor **B**, which is defined as the vector gradient of the magnetic field vector $\mathbf{b} = [b_x, b_y, b_z]^T$, i.e.

$$\mathbf{B} = \nabla \mathbf{b}. \tag{1}$$

Outside magnetic sources and in the absence of conduction currents, **B** is a symmetric and traceless tensor whose elements can be expressed as second derivatives of a scalar potential Ω

$$\mathbf{B} = \begin{bmatrix} B_{xx} & B_{xy} & B_{xz} \\ B_{yx} & B_{yy} & B_{yz} \\ B_{zx} & B_{zy} & B_{zz} \end{bmatrix} = \begin{bmatrix} \frac{\partial b_x}{\partial x} & \frac{\partial b_y}{\partial x} & \frac{\partial b_z}{\partial x} \\ \frac{\partial b_x}{\partial y} & \frac{\partial b_y}{\partial y} & \frac{\partial b_z}{\partial y} \\ \frac{\partial b_x}{\partial z} & \frac{\partial b_y}{\partial z} & \frac{\partial b_z}{\partial z} \end{bmatrix} = -\begin{bmatrix} \frac{\partial^2 \Omega}{\partial x^2} & \frac{\partial^2 \Omega}{\partial x \partial y} & \frac{\partial^2 \Omega}{\partial x \partial z} \\ \frac{\partial^2 \Omega}{\partial y \partial x} & \frac{\partial^2 \Omega}{\partial y^2} & \frac{\partial^2 \Omega}{\partial y \partial z} \\ \frac{\partial^2 \Omega}{\partial z \partial x} & \frac{\partial^2 \Omega}{\partial z \partial y} & \frac{\partial^2 \Omega}{\partial z^2} \end{bmatrix}. \tag{2}$$

The symmetry and tracelessness of the tensor imply that, of the nine tensor components, only five are independent. The magnetic potential Ω and its derivatives of all orders obey Laplace's equation (Blakely, 1996, p.117), i.e. they are potential fields that can be continued analytically in source-free space. Therefore vector and tensor components measured over a plane can be continued to different levels and vertical derivatives can be calculated using standard techniques (Blakely, 1996, Chapter 12).

A number of authors (e.g. Pedersen and Rasmussen, 1990; Christensen and Rajagopalan, 2000; Schmidt and Clark, 2006; Foss, 2006) have discussed theoretical advantages of magnetic gradient tensor measurements over conventional magnetic surveys (see paper I for a summary). However, the overwhelming majority of modern magnetic surveys measure the total magnetic intensity (TMI). In most circumstances, for which the

anomalous magnetic fields are small relative to the background geomagnetic field, the anomalous TMI (i.e. the residual obtained after subtracting the regional total field from the measured TMI) is well approximated by the projection of the anomalous field vector onto the regional geomagnetic field direction (see e.g. Emerson et al., 1985). To this approximation, the anomalous TMI represents a single magnetic field component that obeys Laplace's equation and is therefore a potential field. Unlike the TMI, all Cartesian vector and tensor components are true potential fields, irrespective of the anomaly magnitude. The anomalous field vector comprises three independent components and the gradient tensor has five independent components.

In theory therefore, for a given number of observations, the gradient tensor contains more information about the magnetic sources than the vector, and considerably more than the TMI. However potential field theory shows that, given perfect knowledge and complete coverage of a single field component over a horizontal plane, in principle the potential and all other field and gradient components of all orders can be calculated at all levels above the magnetic sources (Blakely, 1996, chapter 12). In practice, deficiencies in TMI surveys limit the accuracy with which vector and tensor components can be calculated from TMI measurements.

In this paper, I analyse the well-known Mount Leyshon anomaly in the Charters Towers area, Queensland, using some of the new approaches to interpretation of calculated vector and gradient tensor data that were presented in paper I.

Calculation versus Measurement for Magnetic Vectors and Gradient Tensors

In paper I, I reviewed recent developments in emerging technologies, which should see routine deployment of magnetic tensor gradiometer systems in the near future. In the meantime, new methods developed for analysis of magnetic gradient tensor data can also be applied to high quality conventional TMI surveys that have been processed using Fourier filtering techniques, or otherwise, to calculate magnetic vector and tensor components. This approach is, in fact, the only practical way at present to analyse vector component data, as measurements of vector components are seriously afflicted by motion noise, which is not as serious a problem for measurement of gradient components.

Vestine and Davids (1945) showed that, in principle, three orthogonal components of a potential field vector could be derived from knowledge of a single component, along a fixed direction, over a horizontal plane that lies above all the sources. Hughes and Pondrom (1947) presented a method, based on convolution filtering, for deriving vertical and horizontal components of the anomalous magnetic field from TMI data (which was just becoming available due to the introduction of the proton precession magnetometer), so that newer surveys could be compared to older data sets acquired with fluxgate magnetometers. Baranov (1975) gives a comprehensive treatment of relationships in the space and wavenumber domains between field components, including TMI, their continuations and derivatives. Nelson (1988) gave expressions for calculation of gradient tensor elements, in either the space or Fourier domains, from total field gradient surveys. Pedersen et al. (1990) gave Fourier domain expressions for calculation of vector components from TMI and noted that, in practice, it is often necessary to reduce aliasing by applying upward continuation before calculating vector components. Blakely (1996, chapter 12) provides an accessible account of the necessary underlying theory. Appendix I outlines the Fourier filtering process that calculates magnetic potential, vector components and gradient tensor components from gridded TMI data.

Schmidt and Clark (1998) discussed the calculation of vector components from the TMI, drawing on the Fourier domain method of Lourenço and Morrison (1973), then used integral moments of these components to calculate magnetic moments of isolated sources according to a modification of the method originally proposed by Helbig (1963). Magnetic moments derived in this manner from a TMI survey over the Early Permian Tuckers Igneous Complex, Queensland, which exhibits strong remanence effects, were compared with laboratory measurements to demonstrate the validity of the approach (Schmidt and Clark, 1998).

While it should be stressed that direct measurement of the gradient tensor will provide superior results, useful gradient tensor data can be obtained by Fourier processing of TMI surveys, provided a number of caveats are addressed. These include: effective removal of regional trends and careful windowing of survey areas, to minimise artefacts such as Gibbs phenomenon “ringing”and spectral leakage; a density of sampling (particularly across lines) that is sufficient to effectively eliminate aliasing of high frequencies in the measured fields; reliable interpolation algorithms to provide accurate (not just visually gratifying)

gridded TMI data for Fourier domain calculation of gradient tensor elements; and accurate reduction of TMI data to a common level before Fourier processing, using equivalent source methods or otherwise, which is a very challenging requirement in areas of rugged topography.

It can be shown by an analysis similar to that of Reid (1980) that the grid spacing of TMI measurements can be no more than about half the depth to the sources, for accurate calculation of tensor components, with negligible aliasing, when there are isolated compact sources or complex 3D geology. Appendix II gives a theoretical analysis of aliasing when calculating vector and tensor components from gridded TMI data, and Table I summarises aliasing effects for a range of grid spacings relative to source depth.

Careful regularisation of the filtering process is essential when the geomagnetic inclination is low, because calculation of vector components from TMI surveys becomes unstable close to the geomagnetic equator (Blakely, 1996, p.342-343). This is true *a fortiori* for calculation of gradient tensor elements. When the regional field inclination is zero, small to moderate vertical or magnetic east anomalous field components have negligible effect on the measured TMI. In the presence of remanently magnetised elongated structures parallel to the magnetic meridian, which can produce substantial vertical and east components, these components cannot be reliably recovered from the TMI when the field inclination is too low.

Furthermore, if intense anomalies are present, measured TMI data must be corrected to a true potential field, as suggested by Lourenço and Morrison (1973), and elaborated by Schmidt and Clark (2006). Appendix I outlines the required correction procedure. Gordin et al. (2006) demonstrated an equivalent source algorithm that accomplishes the same purpose. This method inverts the observed data to a source distribution that can account for the measured TMI, then calculates the true field components from this source distribution. This approach is more computationally expensive than Fourier filtering. Importantly, Gordin et al. (2006) also provide a proof that, if the iterative corrections of the observed TMI converge to a stable solution, that solution for the true projection of the anomalous field vector onto the regional field direction (which represents a true potential field) is correct.

Eigenvalues, eigenvectors and the normalised source strength

Paper I discussed calculation of the eigenvalues and eigenvectors of the gradient tensor and their applications to interpretation. Since **B** is a symmetric real 3×3 matrix, all its eigenvalues are real, eigenvectors corresponding to distinct eigenvalues are orthogonal, and an orthonormal set of three eigenvectors can always be found, including the case of degenerate (i.e. two equal) eigenvalues. Rotational invariants can be calculated from the tensor and are often simpler to interpret than the tensor elements. Since they are independent of sensor orientation, they are more robust to measurement errors in sensor orientation. Invariants can always be expressed in terms of the eigenvalues. A particularly useful rotational invariant is the scaled or normalised source strength (NSS) (Clark, 2012a,b,c; Beiki et al., 2012a,b), which can be expressed as the following combination of eigenvalues of the tensor, labelled in nonincreasing order, $\lambda_1 \geq \lambda_2 \geq \lambda_3$:

$$\mu = \sqrt{-\lambda_2^2 - \lambda_1\lambda_3}. \qquad (3)$$

Note that the sum of the eigenvalues is always zero (the tracelessness property of the tensor), so that $\lambda_1 > 0$, $\lambda_3 < 0$, and λ_2 is always the eigenvalue with the smallest absolute value. These properties ensure that the expression under the square root sign in equation 3 is always positive, so that μ is a real, positive definite quantity.

For 2D sources $\lambda_2 = 0$ and $\lambda_1 = -\lambda_3$, so the NSS is simply equal to the absolute value of the nonzero eigenvalues, i.e. $\mu = \lambda_1 = -\lambda_3$. As shown in paper I, in this case the NSS is also equal to the total gradient (analytic signal amplitude) of the vertical field component or, equivalently, the total gradient of the strike-perpendicular horizontal component. It is proportional to, but always larger than, the total gradient of the TMI, particularly for meridionally striking structures at low latitudes. In the 2D case, therefore, μ has the desirable property, like the 2D total gradient, that it is independent of magnetisation direction. For approximately 2D sources the intermediate eigenvalue (with the smallest absolute value) is close to zero and the corresponding eigenvector indicates the strike. The NSS is also completely independent of magnetisation direction for uniformly magnetised spheres and for compact 3D sources that can be represented by a point dipole. For general 3D sources the NSS is only weakly dependent on magnetisation direction, significantly

less so than the 3D total gradient (Beiki et al., 2012a; Pilkington and Beiki, 2012), which simplifies determination of source location.

For several useful 2D and 3D models (e.g. the point pole, line of poles, point dipole (sphere), line of dipoles (horizontal cylinder), thin dipping sheet, and contact models), μ peaks directly above the source. Here the source location is defined as the centre for the sphere and horizontal cylinder models; as the top of the narrow, axially magnetised pipe for the point pole model; the top of the thin sheet model; and the top corner of the contact model. For these models the NSS calculated from the eigenvalues can be expressed as

$$\mu = \frac{Cq}{r^n}, \tag{4}$$

which is a homogeneous function with a simple $1/r^n$ fall-off, suitable for Euler deconvolution (Beiki et al., 2012a). In equation 4 C is a constant that depends on the system of units, q is a source strength term, and r is the source-sensor distance. The width of the μ anomaly is simply related to the source depth, as shown in paper I.

For a number of important magnetic model types, eigenvector analysis of the gradient tensor yields some simple direct solutions for model parameters. For point pole and line of pole models the major eigenvectors (associated with the largest magnitude eigenvalue) point directly toward the source, allowing its location to be obtained by triangulation (Pedersen and Rasmussen, 1990; Clark, 2012b). A gradient tensor anomaly for which, at all points within the main anomaly, two eigenvalues are approximately equal and the third is opposite in sign and double the magnitude, is diagnostic of a pole-like source. The magnetic anomaly vector **b** is radial, pointing directly away from the pole of strength p if p is positive and directly towards the pole if $p < 0$. At every observation point the eigenvalues are proportional to the vertical component of the anomalous field,
and the ratio of the vertical component over an eigenvalue provides an estimate of the depth of the source (Clark, 2012b). For a point pole, the scaled source strength is simply equal to the absolute value of the degenerate eigenvalues ($\mu = |\lambda_2|$).

The point dipole model is applicable to any sufficiently compact magnetised body, i.e. when the largest dimension of the body is small compared to the minimum source-sensor

separation. Outside a spherical surface that completely encloses an arbitrary magnetised body, the field can be expressed as a sum of multipole contributions, with a $1/r^3$ fall-off for the dipole term, $1/r^4$ fall-off for the quadrupole, $1/r^5$ fall-off for the octupole term, and so on. Thus for any compact body with a non-zero dipole moment the far field is always dominated by the dipole term. More specifically, the external fields and gradients due to a uniformly magnetised sphere are identical to that of a point dipole, because the quadrupole and all higher multipole moments vanish identically.

Nara et al. (2006) have presented a neat solution to the single point dipole location problem that uses measurements of the anomalous field vector and gradient tensor, if accurate values of both are available. They showed the displacement vector from the dipole to the measurement point, *independent* of the orientation of its moment **m**, is given by:

$$\mathbf{r} = -3\mathbf{B}^{-1}\mathbf{b}, \tag{5}$$

even though each tensor element and vector component on the right hand side of this expression depends on **m**. Equation 5 is applicable provided det**B** is nonzero, so that the matrix representation of the tensor is invertible. The special case where **B** is singular occurs when the measurement point lies within the plane orthogonal to the dipole axis, and is easily treatable separately.

Although Nara et al. (2006) did not treat this aspect, once the location of the dipole is known, determination of the moment becomes a straight-forward linear inversion problem. If the anomalous field vector **b** is known to sufficient accuracy, the moment **m** = $m_x\hat{\mathbf{x}} + m_y\hat{\mathbf{y}} + m_z\hat{\mathbf{z}}$ can be calculated as (Lima et al., 2006):

$$\mathbf{m} = \frac{r^3}{C}\left[\frac{3\mathbf{b}.\mathbf{r}}{2r^2}\mathbf{r} - \mathbf{b}\right]. \tag{6}$$

Clark et al. (2009) showed that this simple method could be extended to analysis of gradient tensor data along a short profile segment, without requiring vector data (see also paper I). Clark (2010) developed a more sophisticated method, which analyses gradient tensor data collected along a profile that passes near a dipole target. Unlike most other

gradient tensor inversion techniques, this method can correct for contamination of the dipole signature by geological gradients, interfering anomalies, or instrumental drifts.

Analysis of anomalous vector and tensor components at Mount Leyshon

The mineralised system associated with the former Mount Leyshon gold mine in Queensland produces a prominent TMI magnetic low due to strong remanent magnetisation, acquired in the Early Permian, of reverse polarity (Lackie et al., 1991; Sexton et al., 1995; Clark and Lackie, 2003). Sexton et al. (1995) showed that the magnetic anomaly is substantially attributable to early potassic (biotite-magnetite) alteration of Palaeozoic host rocks (dolerite and metasiltstones) and associated quartz-magnetite veins. This magnetic alteration zone is largely peripheral to the mineralised breccia and porphyry complex, which is dominated by felsic compositions that are strongly overprinted by magnetite-destructive phyllic alteration and is accordingly very weakly magnetic, so that the anomaly is slightly offset to the SW of the mine. The bottom of the magnetic potassic alteration zone has not been determined by drilling, but its depth extent in the centre of the Mount Leyshon anomaly is known to be at least 800 m (Sexton et al., 1995). The hydrothermal magnetite grains are generally quite fine-grained, with a substantial proportion within the pseudosingle domain size range (~1-20 μm), and retain a stable remanence that is directed south and steeply down.

Magnetic vector components and gradient tensor elements were derived from publicly available TMI data (flown by Fugro Airborne Surveys in 1987/88 and downloaded from Geoscience Australia's Geophysical Archive Data Delivery System) by Fourier filtering. Clark (2012b) presented a preliminary analysis of this data set. Figure 1 shows images over the Mount Leyshon area of the TMI and quantities derived from it (vector components; the total gradient of TMI, also known as the analytic signal amplitude; and the B_{zz} component of the gradient tensor). The most prominent magnetic anomalies in this area are the pronounced TMI lows associated with Mount Leyshon and, to the NE of Mount Leyshon in the Mathews Pinnacle area, with two lobes of a coeval mafic intrusion, the Fenian Diorite, which carries a strong remanence of reverse polarity. Figure 2 shows profiles of the vector components along line 423400 mE, which passes through the centre of the Mount Leyshon anomaly, over the potassic alteration zone. Figures 3-4 show gradient tensor component profiles along this line and Figure 5 plots a number of rotational invariants derived from the full tensor, including the normalised source strength.

The vertical component B_z is dominant within the anomaly, reflecting the subvertical down magnetisation, which produces negative poles on the upper surface of the subcropping source region, with much lower pole density on the sides of the steep-sided causative body. The field vector over the source is downward pointing, producing a B_z high, and opposing the geomagnetic field, so the corresponding TMI anomaly is a low. The north component B_x is approximately antisymmetric about the centre of the source, as expected for a pole-type anomaly, and the east component B_y is relatively weak. The asymmetry of the east component reflects the fact that the magnetic alteration zone is somewhat elongated SW-NE, so that the majority of the magnetised material lies west of the southern portion of the profile and east of the profile in the north.

Compared to the field components, the tensor element profiles show higher resolution of heterogeneity within the magnetic alteration zone, with emphasis on shallower sources. The double-humped form of the B_{zz} profile, in particular, highlights the presence of two lobes within the Mount Leyshon anomaly. The peaks in the NSS profile in Figure 5 provide a good indication of the northing of these strong magnetic zones.

The source region of the Mount Leyshon anomaly evidently does not conform closely to either a point pole or a sphere (point dipole) model, but it is nevertheless of interest to apply simple methods of analysis developed for these models, to test their robustness in less-than-ideal conditions. Such simple models would work better on magnetic data that has been continued upward to a level where the source zone can be considered compact, at least in lateral extent. However, upward continuation also tends to merge the anomaly of interest with those of surrounding sources. Figure 6 shows simplified models, representing two end members, each of which is consistent with drilling information about the depth extent of the magnetic zone. Given the steep down magnetisation of the magnetic lithologies at Mount Leyshon, if the magnetic zone extends to great depths, the source of the magnetic anomaly can be regarded as a distribution of negative magnetic poles at the top of the zone. If, on the other hand, the bottom of the magnetic zone lies just below the maximum depth of drilling, then the source has a dipolar character, with a steep down magnetic moment.

Along line 42300 mE the anomalous field vectors lie almost in the N-S vertical plane. Figure 7 shows projections of these vectors onto the vertical plane containing the profile.

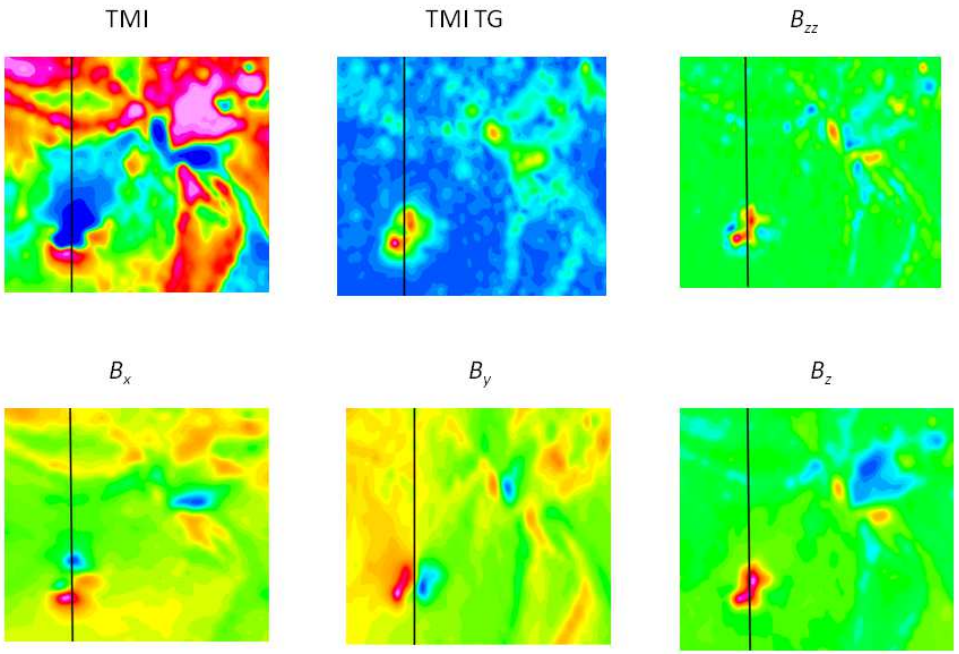

Figure 1. Magnetic anomalies over the Mount Leyshon – Mathews Pinnacle area. TMI = total magnetic intensity, B_x = calculated north component, B_y = calculated east component, B_z = calculated down component, TMI TG = total gradient (analytic signal amplitude) of TMI, B_{zz} = calculated vertical gradient of B_z. Note that the total gradient (like the NSS) is positive definite, so anomalies are always highs, i.e. they do not distinguish between sources with positive and negative magnetisation contrasts. The TMI image has a normalised stretch with a range of –1300 to +500 nT. All other images have linear stretches, with the following ranges (TMI TG: 0 to +6.05 nT/m; B_{zz}: –2.69 to +7.15 nT/m; B_x: –869 to +964 nT; ; B_y: –763 to +949 nT; B_z: –638 to +1797 nT. The Mount Leyshon anomaly is the prominent TMI low/vertical component high in the SW of the image. The prominent TMI lows in the NE quadrant of the image are associated with two outcropping lobes of the remanently magnetised Early Permian Fenian Diorite, which wrap around the SW side of the TMI high associated with Devonian granodiorite intrusions. The Fenian Diorite is coeval with the Mount Leyshon Complex and has a primary remanence direction that is indistinguishable from that found at Mount Leyshon (Clark and Lackie, 2003). The black vertical lines indicate line 43400 mE, corresponding to the profiles shown in Figures 2-5, 7-8.

For a narrow vertical pipe, of great depth extent, with steep downward magnetisation, the extensions of the field vectors should converge on the top of the pipe, which acts as a point south pole. However, the Mount Leyshon magnetic zone is wide compared to the depth below the sensor, so the top surface corresponds to a sheet of poles, rather than a point pole. Thus the lateral extent of the magnetic source zone produces subparallel, near-vertical vectors over the central portion of the anomaly. The steepness of the vectors either side of the source zone, which results in convergence well below the mapped top of the magnetic zone, indicates a "centre of pole density" that appears to lie well below the surface. This suggests that the magnetisation may be larger at depth than near the surface, which would produce a pole distribution within the magnetic zone as well at its upper surface.

Figure 8 shows the corresponding projections of major eigenvectors of the tensor, which should also point directly towards a pole-type source. The pattern is similar to that of Figure 7, lending support to the applicability of a pole-type model, and to the qualitative interpretation given above. For a point pole source, the ratio of the vertical field component, B_z, and the dominant eigenvalue (with absolute value double that of the other two, degenerate, eigenvalues), λ_m, is proportional to the depth of the source (Clark, 2012b). Depth estimates $h = 2B_z/\lambda_m$, calculated along profile 423400 mE over the Mount Leyshon anomaly between 7753500 mN and 7756000 mN, range from 200 m to 840 m beneath the surface, with an average of 500 m (N = 251) and a standard deviation of 185 m. The considerable width of the magnetic zone, contrary to the assumption of a narrow source, biases the calculated h to greater depths. Thus the true layer of strongest pole density, corresponding to maximum vertical gradient of magnetisation (or, in the limit, discontinuity in magnetisation at the top of the magnetic zone), is somewhat shallower than the apparent depths derived from the point pole assumption.

The method of Clark et al. (2009) (equations 5 and 6), extending the algorithm of Nara et al. (2006), calculates the location and magnetic moment of a dipole source. This method was applied to vector and tensor data over the main anomalous zone along line 423400 mE. This method can only be expected to produce meaningful results if the depth extent of the magnetic zone is limited, so that the anomaly reflects the bottom of the zone as well as its top. Figure 9 plots the solutions obtained for the location of the "centres of magnetisation", assuming a dipole source, and the corresponding magnetic moment.

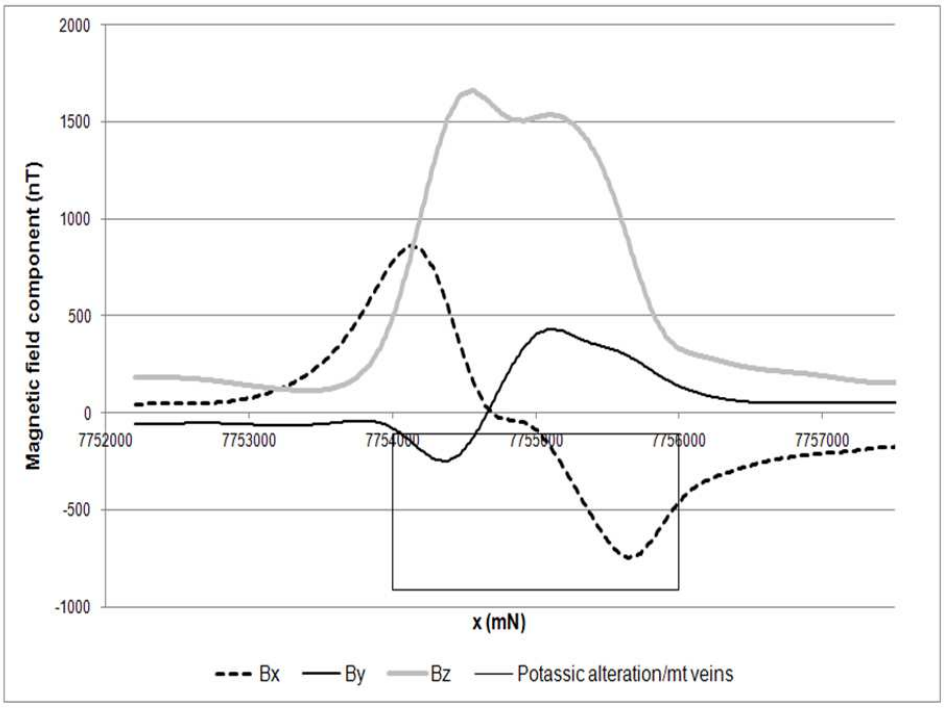

Figure 2. Magnetic vector component profiles along line 423400 mE over the Mount Leyshon anomaly, with approximate extent of the magnetic potassic alteration zone indicated. $B_{x,y,z}$ are the north, east, and down field components respectively. All grid coordinates given in this paper are Australian Map Grid (AMG84), zone 55.

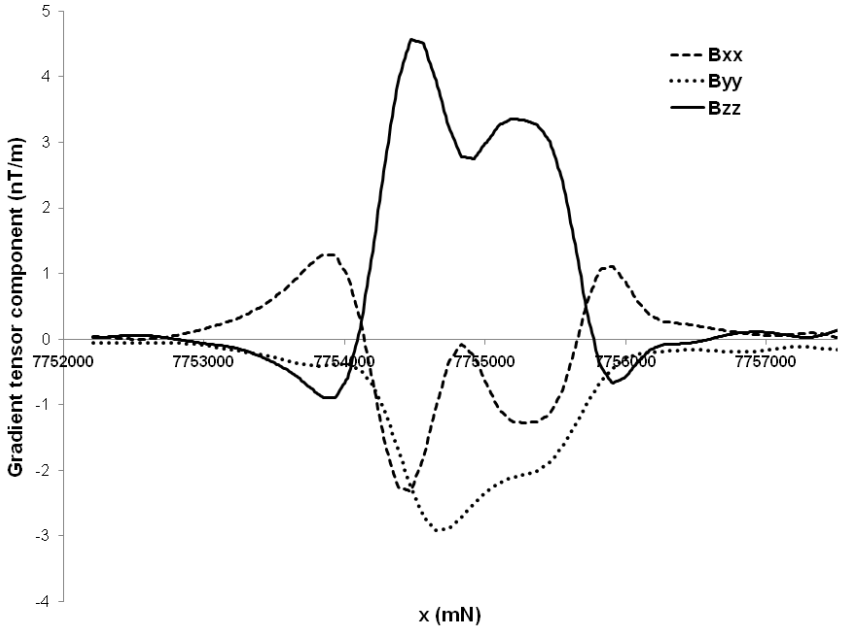

Figure 3. Diagonal elements of the calculated gradient tensor along line 423400 mE.

The average location for the three southernmost solutions is 423360 mE, 7754700 mN, depth below sensor (surface) 960 m (880 m), and for solutions from the four northernmost stations is 423820 mE, 7755420 mE, depth below sensor (surface) 1040 m (960 m). The corresponding inferred magnetic moments are 9.1×10^9 Am² (dec = 82°, inc = +81°) and 1.3×10^{10} Am² (dec = 55°, inc = +37°) for the southern and northern solution clusters respectively.

These clusters of solutions correspond to the two main lobes of the Mount Leyshon anomaly, with the southern lobe centred just west of the line and the northern lobe centred about 400 m east of the the line, consistent with the patterns exhibited by the full anomaly grid. This illustrates the power of full vector and tensor measurements along widely spaced lines, as sources that lie to one side of the lines can be defined. If we take the dipole solutions at face value, the depth estimates put the equivalent centre of depth-integrated magnetisation about 900 m below the surface, suggesting a total vertical extent of about 1800 m for the magnetic zone.

The resultant magnetisation direction at Mount Leyshon represents competition between a dominant south and steep down remanence and induced magnetisation, directed just east of north with moderate upward inclination. The inverted magnetic moments suggest that remanence is strongly dominant in the southern lobe, and less dominant over induction in the northern lobe. The overall magnetic moment of the magnetic zone appears to be about 10^{10} Am². A magnetic zone with dimensions of 1.5 km × 1.5 km × 2 km (vertical) has a volume of 4.5×10^9 m^3, which requires an average magnetisation of about 2 A/m to account for the moment. Reducing the available volume to $1 \times 1 \times 2$ km^3 increases the required magnetisation to 5 A/m.

Such magnetisations are well within the range of measured magnetic properties for the potassic zone at Mount Leyshon (Sexton et al., 1995; Clark and Lackie, 2003). The AMIRA P700 database (Clark *et al*., 2004) gives average remanent intensities of 7.5 A/m (SI susceptibility k = 0.06, Koenigsberger ratio Q = 3.1) for biotite-magnetite altered dolerite and 4.2 A/m (k = 0.048 SI, Q = 2.2) for biotite-magnetite altered Puddler Creek Formation. Resultant magnetisations in this case are approximately given by the remanence intensity multiplied by (1−1/Q), as the induced magnetisation is roughly antiparallel to the remanence.

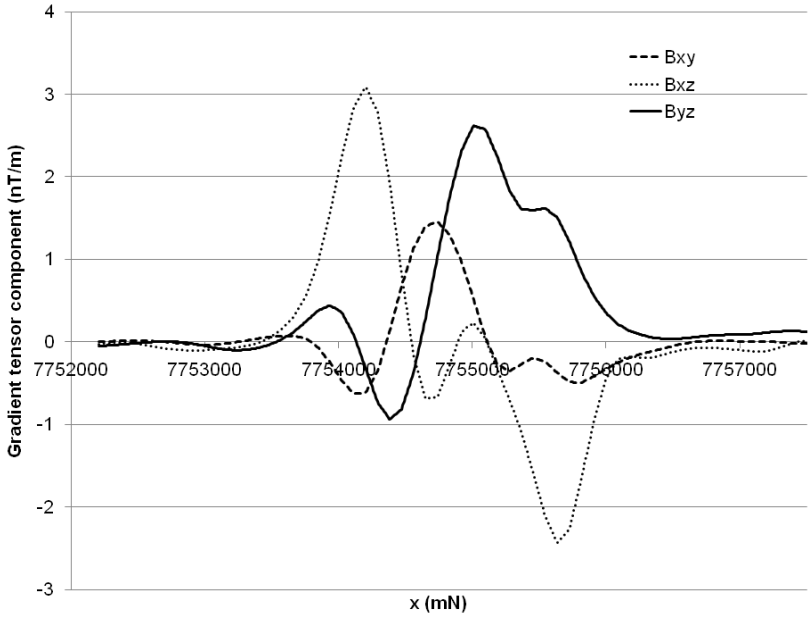

Figure 4. Off-diagonal elements of the calculated gradient tensor along line 423400 mE.

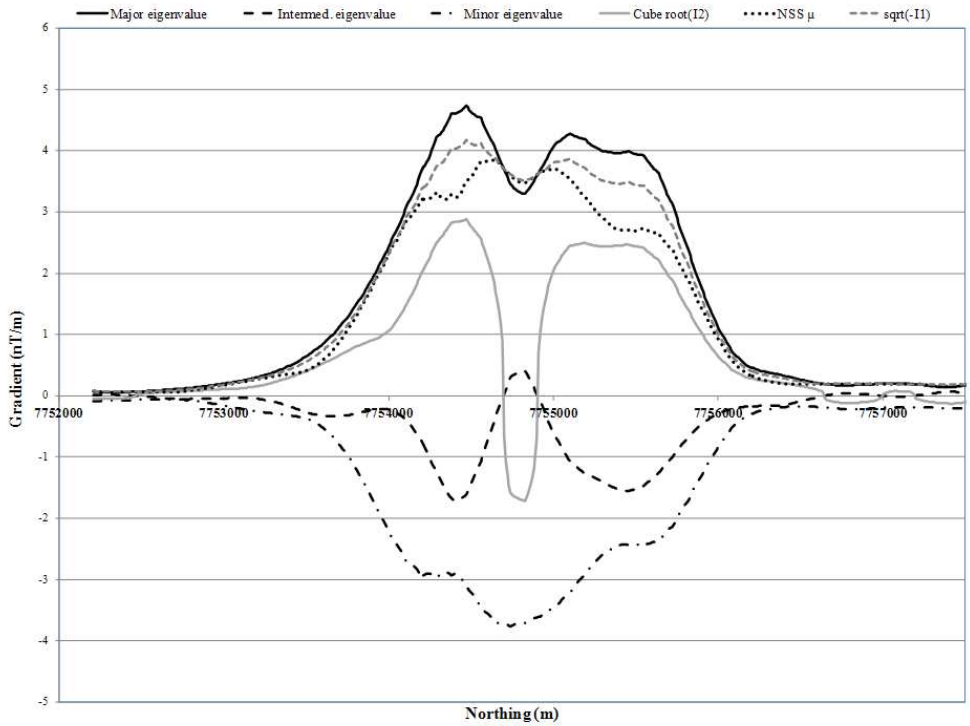

Figure 5. Rotational invariants of the calculated gradient tensor along line 423400 mE. I_1 and I_2 are the canonical invariants of Pedersen and Rasmussen (1990). The square root of I_1 and the cube root I_2 of have been taken so that all quantities are in the same units (nT/m) as the gradient tensor elements. The scaled source strength μ is the NSS, given by equation 3.

Confirmation that the inferred magnetic moment for the magnetic zone is reasonable comes from two other lines of evidence: (i) modelling of the Mount Leyshon TMI anomaly, and (ii) a Helbig-type analysis of the gradient tensor elements, using the method of Phillips et al. (2007). The 3D model of Lackie et al. (1991) fitted TMI profiles across the anomaly (see Figure 10), incorporating petrophysical data from outcrop and drill core samples. The model comprised multiple cylinders, with a large deep body of great depth extent overlain by a number of apophyses that extend to shallow depths. Originally it was thought that the modelled source probably represented a mafic intrusion, similar to the Fenian Diorite, assumed to be genetically related to the Mount Leyshon porphyries and associated mineralisation. However Sexton et al. (1995) subsequently showed that the upper 800 m, at least, of the magnetic zone consists of potassically (biotite-magnetite) altered host rocks. Therefore the "apophyses" of the model shown in Figure 10 represent pipe-like and sheet-like zones of intense alteration along structurally controlled fluid pathways. The igneous source of the high temperature fluids that produced this paragenetically early potassic alteration has not been intersected by drilling to 800 m depth.

Assuming that the deep body (top 560 m below surface) that accounts for most of the long wavelength signature extends to a depth of 2 km below the sensor, the total moment of the model (including the shallower bodies that account for the short wavelength features) is 1.3×10^{10} Am², with a total volume of 3.5×10^{9} m^{3}. The corresponding average magnetisation intensity of the model is 3.8 A/m, with a declination of 163°, inclination of +88°. The average susceptibility of the model is 0.037 SI and the NRM intensity is 4.9 A/m, (dec = 184°, inc = +77°), which corresponds to a Koenigsberger ratio of 3.3. The magnetic moment calculated from the resultant magnetisation and volume of the model is consistent with that obtained from the Nara-type solutions.

The second confirmatory analysis uses integral moments of gradient tensor elements, following the method of Phillips et al. (2007), to estimate the total magnetic moment of the source. This method has some limitations: in principle it requires estimation of integrals over the entire horizontal plane and assumes that interference from neighbouring sources is negligible. On the other hand, the magnetic moment vector can be estimated using this method, irrespective of the source geometry (provided it is finite in all directions). Estimation of magnetisation direction is quite robust when the integration area is limited,

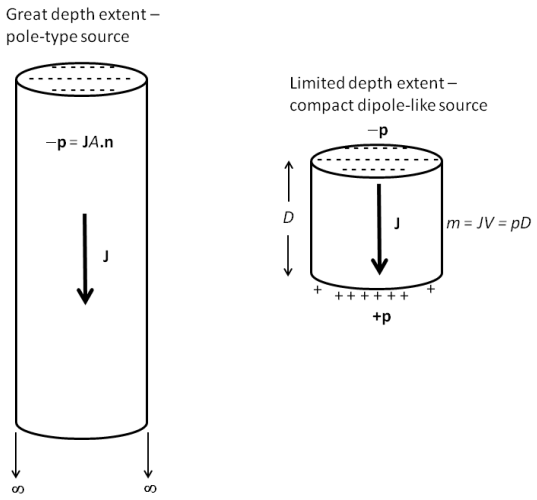

Figure 6. Idealised models that may approximate the gross features of the source of the Mount Leyshon anomaly. The LHS shows a bottomless vertically-downward magnetised cylinder, which is equivalent to a disc of negative poles at the top surface. The RHS shows an equidimensional truncated cylinder with discs of negative (positive) pole density at the top (bottom) surface. At distances several times the radius of the cylinder, or greater, the LHS model corresponds to a point pole source and the RHS model approximates a vertical point dipole.

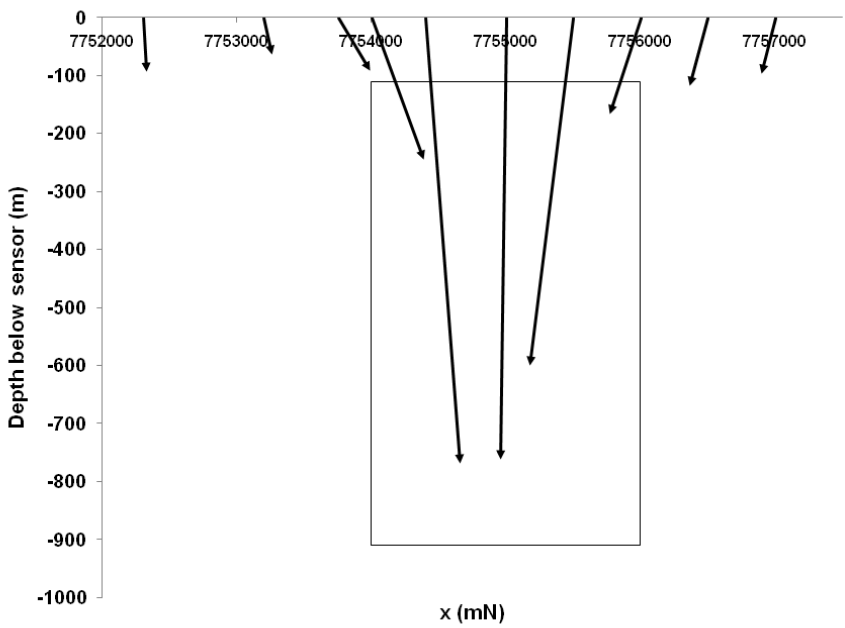

Figure 7. Projected magnetic field vectors along line 423400 mE, indicating directions to pole-type sources at the top of a reversely magnetised magnetic zone. The putative extent in cross-section of the potassic alteration zone is indicated by the box. The bottom of the zone has not been delineated by drilling.

however estimation of the magnetic moment magnitude requires a correction for the finite integration area (Schmidt and Clark, 1998; Caratori Tontini and Pedersen, 2008). Fortunately, the Mount Leyshon anomaly is large and relatively isolated, which allows correction for the missing tails of the truncated integrals.

The Helbig-type analysis of Phillips et al. (2007) yields a steep down estimated magnetisation direction for the Mount Leyshon anomaly source (dec = 213°, inc = +61°), which is quite compatible with the petrophysical data and with the Nara-type inversion and the 3D modelling. The estimated magnetic moment was corrected for the finite range of integration using a new algorithm that will be the subject of another paper [see Chapters 7 and 8 of this thesis]. The depth of the centre of magnetisation h is first estimated from integral moments of tensor invariants and the estimated components of magnetic moment are then corrected for the finite radius of integration R using a correction term that is a function of R/h. Using this method the depth to the centroid of the magnetic zone is estimated to be 880 m beneath the surface and the estimated magnetic moment is 8.3×10^9 Am², which is quite consistent with the estimates from Nara-type dipole inversion and 3D modelling. Note that the method based on integral moments is complementary to the point-by point dipole inversion, as it uses data over the whole anomaly. The agreement between these independent approaches is encouraging.

To supplement the analysis of line 423400 mE, which passes directly over the anomaly, data from line 422500 mE, which passes to the west of the main anomaly, were also analysed. Figures 11 and 12 show, respectively, field vectors and major eigenvectors in plan view. The vectors shown all have shallow plunges to the east and converge at moderate depths within the magnetic source region. This again illustrates the ability of vector and tensor data to aid interpretation of off-line sources. The data hint at an extension of the magnetic zone at depth to the north, passing beneath the Mount Leyshon pit, although some of the signature could result from a negative magnetisation contrast between the nonmagnetic porphyries and mineralised breccias of the mine area, which have been strongly overprinted by magnetite-destructive phyllic alteration, and the slightly magnetic Fenian Granite host rock .

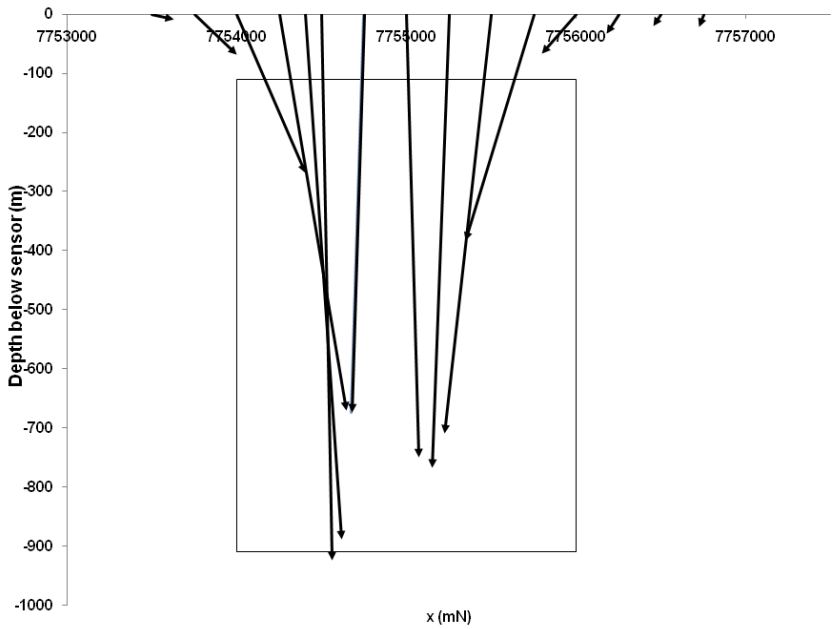

Figure 8. Projected major eigenvectors of the gradient tensor along line 423400 mE. The approximate extent of the potassic alteration zone is indicated by the box.

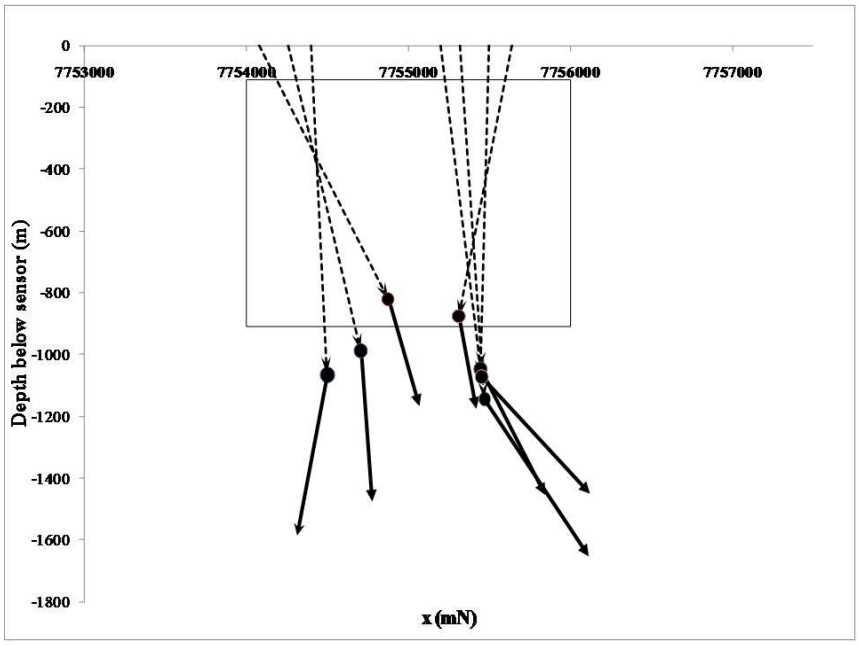

Figure 9. Locations of equivalent dipoles, inverted from anomalous field vectors and gradient tensors, shown as dots terminating inferred displacement vectors from measurement locations (dashed arrows). Solid arrows indicate projected magnetic moment vectors corresponding to each solution. The box shows the approximate outline of the potassic alteration zone, whose bottom has not been found by drilling.

Analysis of the normalised source strength over Mount Leyshon

The TMI survey from which the vector and tensor components, and derived quantities such as the NSS, over Mount Leyshon were calculated was flown at an altitude of 80 m above the surface and had a line spacing of 400 m. Contributions to the gradient anomalies from shallow, narrow sources are therefore aliased. However the gross features of the deeper portions of the magnetic zone should be well defined by the calculated tensor components. Aliasing is reduced compared to the worst case considered in Appendix II, a point dipole source, due to the width of the source region. The lateral dimensions of the Mount Leyshon magnetic zone ensure that the anomaly is intersected by about six north-south lines, which adequately define the general features of the near surface source region, as well as those of roughly east-west oriented shallow features, although fine detail of north-south oriented and equidimensional features is lost. On the other hand, the width of the magnetic zone implies that the point pole and point dipole models provide at best only a crude representation of the source region, so inverse solutions based on these models cannot be expected to be very accurate. It is nevertheless interesting to test the robustness of the simple inversion approach in the face of these problems. Aliasing of the signal could be ameliorated by calculating tensor components from upward continued TMI data, at the expense of losing all fine detail within the anomaly.

The profile of the NSS shown in Figure 5 exhibits a broad high over the Mount Leyshon magnetic zone, as expected, but also shows local peaks, troughs and inflections that are clear signs of the near-surface heterogeneity discussed above. A grid of the NSS calculated from a detailed gradient tensor survey would produce a high resolution map of the shallow magnetic zones and structural controls, with greater detail than that obtainable from a TMI survey with the same line spacing. NSS anomalies also would exhibit negligible offset from the source locations, whereas TMI anomalies are displaced due to geomagnetic inclination and source magnetisation effects.

An estimate of the horizontal location of the centroid of the magnetic zone $\bar{x}, \bar{y}$ can be obtained from first integral moments of the NSS grid over the whole Mount Leyshon anomaly, normalised by 2D integrals of the NSS:

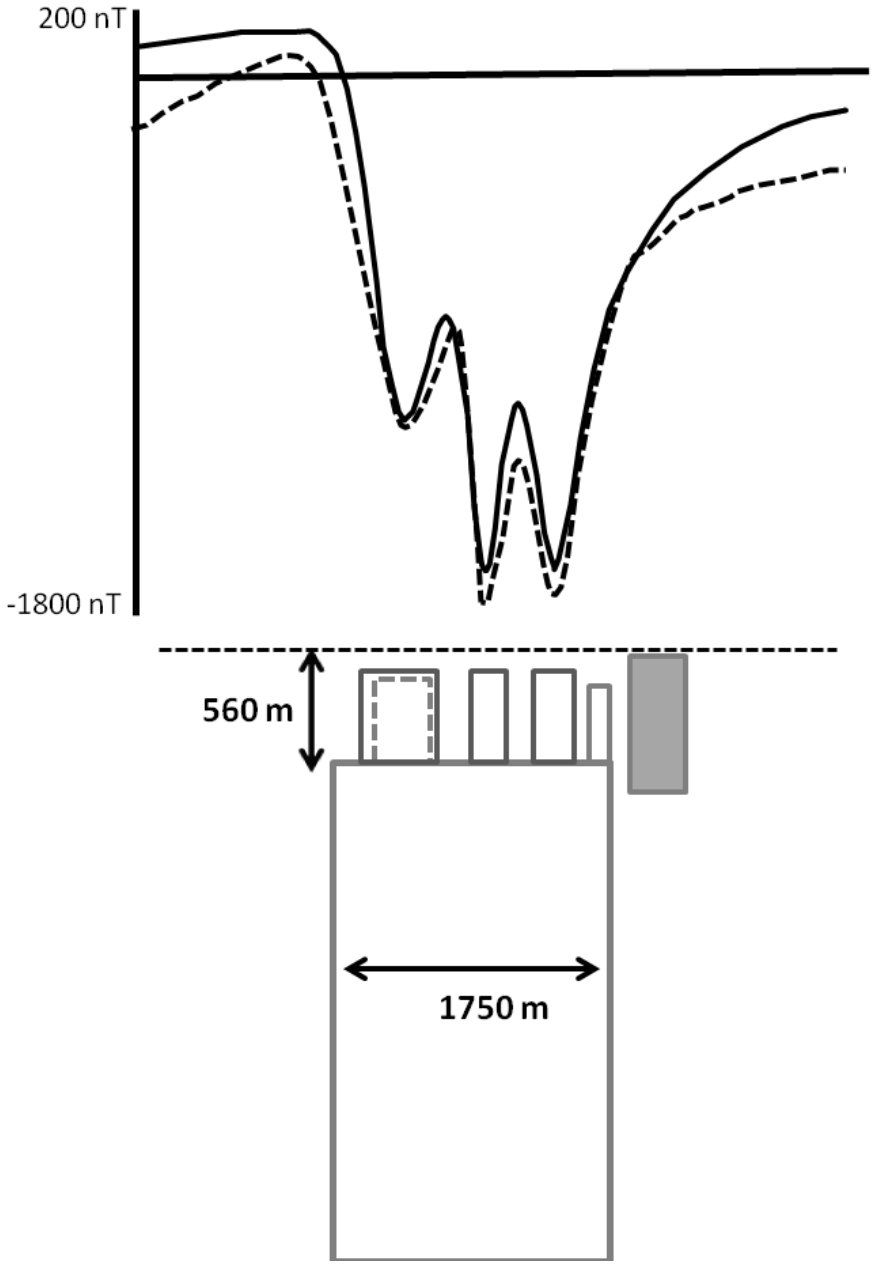

Figure 10. Top: TMI anomaly profiles along 423500 mE. Dashed line indicates the observed data, the solid line shows the calculated anomaly derived from the 3D model of Lackie et al. (1991). Bottom: projection of 3D model onto vertical section along TMI profile, shown at the same horizontal scale as the observed anomaly shown above. Horizontal and vertical scales are indicated by the arrows. The model comprises a large and deep vertical cylinder of great depth extent, centred on the profile, with pipe-like apophyses, offset slightly east and west of the profile, extending to shallow depths. The grey body to the north represents the Mount Leyshon mineralised zone, comprising weakly magnetic breccias and felsic porphyries with strong phyllic overprinting. The ground surface is indicated by the horizontal black dashed line.

$$\bar{x} = \frac{\iint x\mu dxdy}{\iint \mu dxdy}, \bar{y} = \frac{\iint y\mu dxdy}{\iint \mu dxdy}, \tag{7}$$

where the integrals are in principle over the entire horizontal plane. However both theory and numerical tests show that if a preliminary estimate of $\bar{x}, \bar{y}$ is obtained using a limited range of integration around the anomaly, recalculating the integrals over a new range symmetrically disposed about this approximate centroid greatly reduces the location errors. If necessary, this procedure can be iterated, although normally the first correction is sufficient.

Application of equation 7 to the Mount Leyshon anomaly gives an estimated centroid location of 423320 mE, 7754680 mN. As this incorporates all of the data over and around the anomaly, rather than relying on point-by-point inversions, effects of local heterogeneity within the magnetic zone tend to average out. The estimated "centre of magnetisation" is consistent with the known distribution of magnetisation within the Mount Leyshon magnetic zone, the horizontal coordinates of the dipole solutions in Figure 9 and the intersection points of directions to source shown in Figures 11 and 12.

In paper I it was shown that, for sources for which the NSS conforms to eqn (4), the location of the source with respect to an observation point, $-\mathbf{r}$, is given by

$$-\mathbf{r} = \frac{n\mu}{|\nabla\mu|^2}\nabla\mu. \tag{8}$$

Paper I gives an algorithm for calculating the vector gradient of the NSS μ, which is required to use equation 8. For the contact model, the appropriate value of the gradient structural index is n = 1. Figure 13 shows solutions with this value of n, obtained for observation points approaching the southern and northern margins of the magnetic zone. Given the simplified model, the depth and horizontal locations of the margins of the magnetic zone are quite well determined by this method. Note that the margins of the magnetic zone are gradational, because of weathering effects at shallow depths, gradually decreasing over tens of metres, and a broad zonation of the alteration from proximal magnetite-dominant to distal hematite-dominant (Clark and Lackie, 2003). The absence of a sharp margin may contribute to some of the spread of solutions.

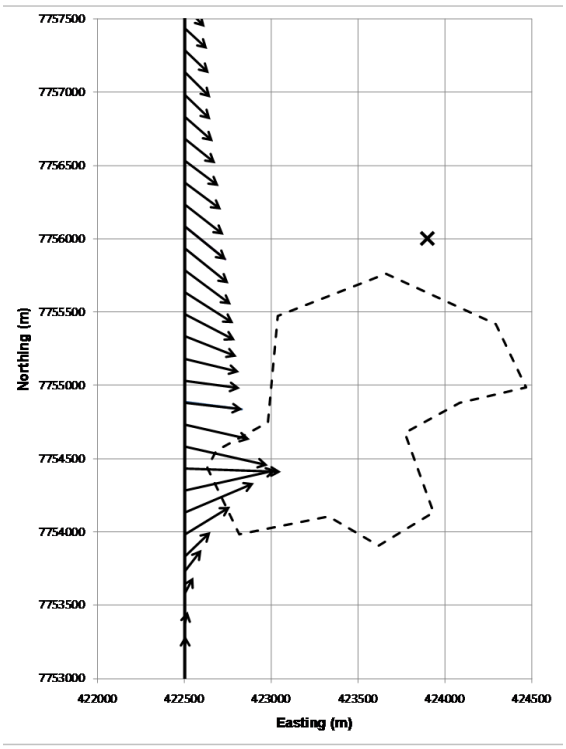

Figure 11. Plan view of magnetic field vectors along line 422500 mE. The potassic alteration zone in plan view is indicated by the dashed outline. The cross indicates the Mount Leyshon mine.

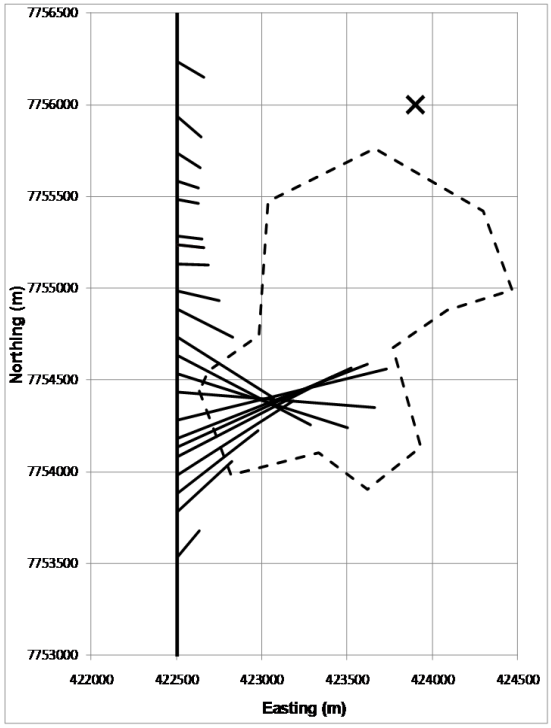

Figure 12. Plan view of major eigenvectors along line 422500 mE. The potassic alteration zone in plan view is indicated by the dashed outline. The cross indicates the Mount Leyshon mine.

Figure 14 shows solutions obtained across the magnetic zone using the gradient structural index applicable to a pole model, $n = 3$. The solutions tend to cluster around the top of the modelled deep body and within the inferred overlying pipe-like bodies. The solutions lie almost beneath the profile - the mean lateral offset is 57 ± 18 m east of the profile. The solutions can be reasonably interpreted as providing a crude map of excess magnetic pole density, representing discontinuities or strong vertical gradients in the steep magnetisation of the magnetic zone. The mean depth beneath the surface of the solutions for $n = 3$ is 371 ± 11 m (1 SE). This can be taken as a crude proxy for the top of the strongest magnetisation zone. If the gradient structural index appropriate to a dipole source, $n = 4$, is used the solutions are shifted deeper and are better clustered laterally, due to the overall convergence of the directions to source with increasing depth that is evident from Figure 14. If $n = 4$ is used, rather than $n = 3$, the rays from the measurement points to the inferred source locations in Figure 14 are simply extended by a factor of 4/3. In this case the average source location is 7754880 ± 45 mN, 4423475 ± 25 mE, at a depth of 520 ± 15 m. For a quasispherical source the $n = 4$ solutions should cluster around the centre of the source. For $n = 4$ solutions analogous to those shown in Figure 14, the still considerable north-south spread of solutions indicates that the source geometry departs significantly from the idealised model (a uniformly magnetised sphere). The gross geometry of the magnetic zone is in fact better represented by a steep sided prism, which biases solutions towards the edges; with depth extent greater than its width, which tends to shift solutions above the centroid of the prism. Thus the the mean depth of the solutions given above for $n = 4$ represents a minimum depth to the centre of magnetisation of the source zone.

The quality of this data set is inadequate for detailed analysis of the internal magnetisation distribution of the Mount Leyshon magnetic zone, using equation 8. However, it is encouraging that a first order analysis using equation 7 gives results that are broadly consistent with the known nature of the source of the Mount Leyshon anomaly When source geometry conforms more closely to a model that has a well-defined structural index, such as at the Tallwang magnetite deposit (Clark, 2012a,c), source location using the vector gradient of the NSS works well, as shown in paper I. Application of equation 7 to upward continued data should produce clustering of source location solutions for $n \approx 4$ near the centre of magnetisation of the Mount Leyshon magnetic zone. This would be at the expense of losing any indication of the extent of the upper surface.

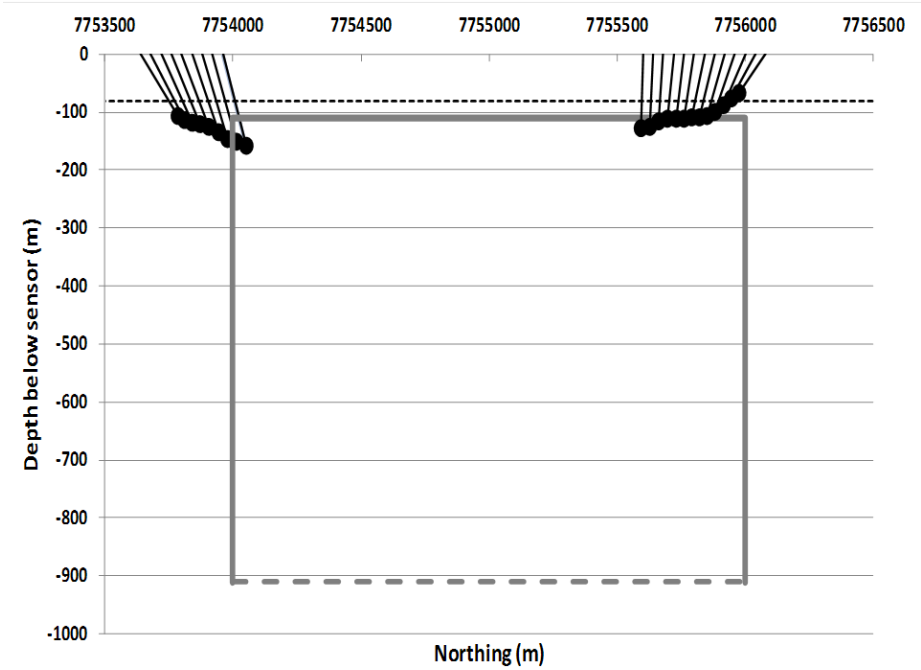

Figure 13. Inverted source locations from data points along 423400 mE near the southern and northern margins of the Mount Leyshon magnetic zone, using equation 8 with n = 1, which is appropriate for a contact model. The approximate extent of the magnetic zone, inferred from surface mapping of alteration and limited drilling information, is outlined in grey. The bottom of the zone is shown dashed, as the full depth extent has not been determined by drilling. The ground surface is indicated by the horizontal black dashed line.

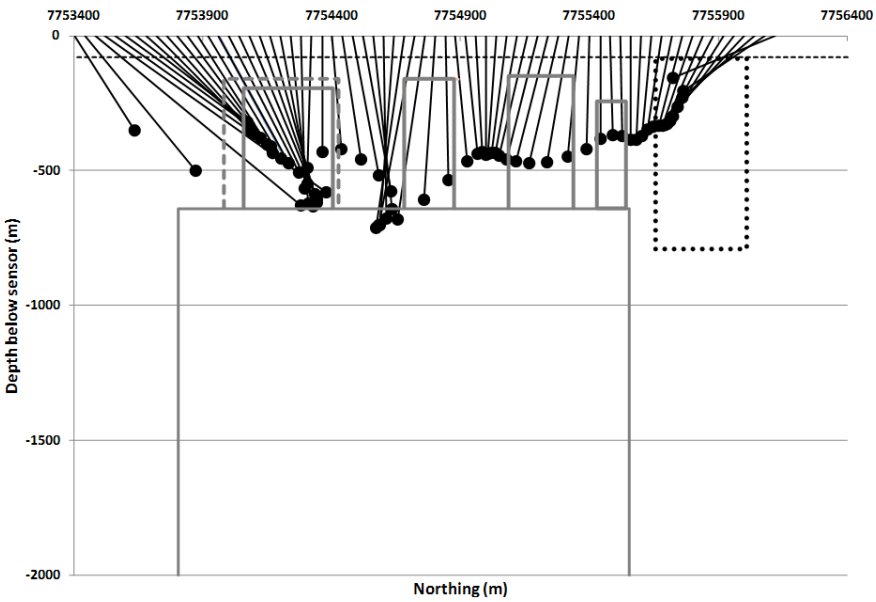

Figure 14. Inverted source locations from data points along 423400 mE over the the Mount Leyshon magnetic zone, using equation 8 with n = 3, which is the gradient structural index appropriate for a pole model. The projection of the detailed 3D multicylinder model of Lackie et al. (1991) is also shown. The dotted outline to the north represents the weakly magnetic Mount Leyshon mineralised zone, and the ground surface is indicated by the horizontal black dashed line.

CONCLUSIONS

Eigenvector analysis and other methods for interpretation of magnetic gradient tensor data, including those outlined in paper I, provide powerful tools for exploiting the extra information provided by gradient tensor surveys. In the absence of gradient tensor measurements and in suitable circumstances, Fourier processing of TMI data of sufficiently high quality can yield useful calculated estimates of anomalous magnetic field vectors and gradient tensors. The methods that are being developed for vector and gradient tensor data are equally applicable to calculated data. Processing of high quality TMI data can add value to existing surveys by exploiting cryptic information that resides in single component data. Calculation is generally more accurate than measurement for field vectors, but measurement is highly desirable for gradient tensors. An optimal scenario is to integrate measured tensor data with vector data derived from TMI.

Preliminary analysis of calculated vector and tensor data over the remanently magnetised Mount Leyshon system has demonstrated the utility of these data types for locating sources and defining magnetisations, even when the source does not match the assumed models perfectly. The analysis accords with petrophysical and geological information and constrains the depth extent, magnetic moment, total volume, and possible northward extensions at depth, of the magnetic zone.

The inferred magnetic moment for the source zone of the Mt Leyshon magnetic anomaly is ~ 10^{10} Am^2. Its direction is consistent with petrophysical measurements. Given estimated magnetisation from samples and geological information, this suggests a volume of ~1.5 km $\times$ 1.5 km $\times$ 2 km (vertical). The inferred depth of the centre of magnetisation is about 900 m below surface, suggesting that the depth extent of the magnetic zone is ~1800 m. Some of the deeper, undrilled portion of the magnetic zone could be a mafic intrusion with a composition similar to that of the Fenian Diorite, representing part of the parent magma chamber beneath the Mount Leyshon Intrusive Complex.

ACKNOWLEDGMENTS

I thank Clive Foss for providing grids of the field and tensor components over the Mount Leyshon area, and Phil Schmidt and James Austin for helpful comments on the manuscript. This work comprises part of a Ph.D. project in the Department of Earth and Planetary Sciences at Macquarie University, under the supervision of Dr Mark Lackie.

REFERENCES

Baranov, W., 1975, *Potential Fields and Their Transformations in Applied Geophysics*: Geoexploration Monographs Series 1- Number 6, Gebrüder Borntraeger.

Beiki, M., Clark, D.A., Austin, J.R. and Foss, C.A., 2012a, Estimating source location using normalized magnetic source strength calculated from magnetic gradient tensor data: *Geophysic*s, **77**(6), J23-J37.

Beiki, M., Keating, P. and Clark, D.A., 2012b, Depth estimation of magnetic and gravity sources using normalized source strength calculated from gradient tensor: *Society of Exploration Geophysicists Annual Meeting, Las Vegas, Expanded Abstracts*.

Blakely, R.J., 1996, *Potential Theory in Gravity and Magnetic Applications*: Cambridge University Press.

Caratori Tontini, F. and Pedersen, L.B., 2008, Interpreting magnetic data by integral moments: *Geophysical Journal International*, **174**, 815-824.

Christensen, A. and Rajagopalan, S., 2000, The magnetic vector and gradient tensor in mineral and oil exploration: *Preview*, **84**, p.77.

Clark, D.A., 2012a, New methods for interpretation of magnetic vector and gradient tensor data I: eigenvector analysis and the normalised source strength: *Exploration Geophysics*, **43**, 267-282, doi:10.1071/EG12020.

Clark, D.A., 2012b, New methods for interpretation of magnetic gradient tensor data: *ASEG 22nd International Geophysical Conference and Exhibition, 26-29 February 2012, Brisbane, Australia, Expanded Abstracts*, CD-ROM, 11p.

Clark, D.A., 2012c, Interpretation of the magnetic gradient tensor and normalized source strength applied to the Tallawang magnetite skarn deposit, New South Wales, Australia: *Society of Exploration Geophysicists Annual Meeting, Las Vegas, Expanded Abstracts*.

Clark, D.A. and Lackie, M.A., 2003, Palaeomagnetism of the Early Permian Mount Leyshon Intrusive Complex and Tuckers Igneous Complex, North Queensland, Australia: *Geophysical Journal International*, **153**, 523-547.

Clark, D.A., Geuna, S.E. and Schmidt, P.W., 2004, Predictive magnetic exploration models for porphyry, epithermal and iron oxide Cu-Au deposits: implications for exploration: CSIRO Exploration and Mining Report 1073R, 398 p. + CD Atlas of Geophysical Signatures + Relational Database of Porphyry, Epithermal and Iron Oxide Cu-Au Deposits (AMIRA International P700 Final Report CD ROM).

Clark, D.A., Young, J.A. and Schmidt, P.W., 2009, Magnetic Tensor Gradiometry in the Marine Environment: Correction of Electric And Magnetic Field And Gradient Measurements in a Conductive Medium and Improved Methods for Magnetic Target Location Using the Magnetic Gradient Tensor: MARELEC (Marine Electromagnetics) Conference, Stockholm, July, 2009, 10pp. CD-ROM.

Clark, D.A., 2010, Method and apparatus for detection using magnetic gradient tensor. U.S. Patent Application Pub. No.: US 2010/0211337 Al, Pub. Date: Aug. 19, 2010 (US patent 8,229,688 B2 granted July 24, 2012).

Emerson, D.W., Clark, D.A. and Saul, S.J., 1985, Magnetic exploration models incorporating remanence, demagnetization and anisotropy: HP 41C handheld computer algorithms: *Exploration Geophysics*, **16**, 1-122.

Foss, C., 2006, The improvements in source resolution that can be expected from inversion of magnetic field tensor data: *The Leading Ed*ge, **25**(1), 81-84.

Gordin, V.M., Tikhotskii, S.A. and Shur, D.Y., 2006, Reconstruction of the harmonic component of the magnetic field modulus anomalies: *Izvestiya, Physics of the Solid Earth*, **42**, no. 4, 334-343.

Helbig, K., 1963, Some integrals of magnetic anomalies and their relation to the parameters of the disturbing body: *Zeitschrift für Geophysik*, **29**, 83-96.

Hughes, D.S. and Pondrom, W.L., 1947, Computation of vertical magnetic anomalies from total field measurements: *Transactions of the American Geophysical Union*, **28**, 193-197.

Lackie, M.A., Clark, D.A. and French, D.H., 1991, Rock magnetism and palaeomagnetism of the Mount Leyshon gold mine in northeast Queensland. CSIRO Exploration Geoscience Report 217R, 108p.

Lima, E.A., Irimia, A. and Wikswo, J.P., 2006, The magnetic inverse problem, *in* J. Clarke and A.I. Braginski (Eds.), *The SQUID Handbook, Vol. II Applications of SQUIDs and SQUID Systems*, Wiley-VCH, pp.139-267.

Lourenço, J. S., and H. F. Morrison, 1973, Vector magnetic anomalies derived from measurements of a single component of the field: *Geophysics*, **38** , no.2, 359-368.

Munschy, M. and Fleury, S., 2011, Scalar, vector, tensor magnetic anomalies: Measurement or computation?: *Geophysical Prospecting*, **59**, 1035-1045.

Nara, T., Suzuki, S., and Ando, S., 2006**,** A Closed-Form Formula for Magnetic Dipole Localization by Measurement of Its Magnetic Field and Spatial Gradients: *IEEE Transactions on Magnetics*, 42, 3291-3293.

Nelson, J.B., 1988, Calculation of the magnetic gradient tensor from total field gradient measurements and its application to geophysical interpretation: *Geophysics*, **53**, 957-966.

Pedersen, L.B. and Rasmussen, T.M., 1990, The gradient tensor of potential field anomalies: Some implications on data collection and data processing of maps: *Geophysics*, **55**, 1558-1566.

Pedersen, L.B., Rasmussen, T.M., and Dyrelius, D., 1990, Construction of component maps from aeromagnetic total field anomaly maps: *Geophysical Prospecting*, **38**, 795-804.

Phillips, J.D., Nabighian, M.N., Smith, D.V. and Li, Y., 2007, Estimating locations and total magnetization vectors of compact magnetic sources through combined Helbig and

Euler analysis: *Society of Exploration Geophysicists Annual Meeting Expanded Abstracts*, **26**, 770-774.

Pilkington, M. and Beiki, M., 2012, Mitigating remanent magnetization effects in magnetic data using the normalized source strength: *Society of Exploration Geophysicists Annual Meeting, Las Vegas, Expanded Abstracts*.

Reid, A.B., 1980, Aeromagnetic Survey Design: *Geophysics*, **45**, 973-976.

Schmidt, P.W. and Clark, D.A., 1998, The calculation of magnetic components and moments from TMI: A case study from the Tuckers igneous complex, Queensland: *Exploration Geophysics*, **29**, 609-614.

Schmidt, P.W. and Clark, D.A., 2006, The magnetic gradient tensor: Its properties and uses in source characterization: *The Leading Edge*, **25**(1), 75-78.

Sexton, M.A., Morrison, G.W., Orr, T.O.H., Foley, A.M. and Wormald, P.J., 1995, The Mount Leyshon magnetic anomaly: *Exploration Geophysics*, **26**, 84-91.

Vestine, E.H. and Davids, N. 1945, Analysis and interpretation of geomagnetic anomalies: *Terrestrial Magnetism and Atmospheric Electricity*, **50**, 1-36.

Appendix I. Fourier domain processing of TMI to calculate magnetic potential, vector and tensor components

The relationships in the Fourier domain between elements B_{ij} of the anomalous gradient tensor $\mathbf{B} = \nabla\mathbf{b}$ and anomalous TMI can be derived from relationships between a potential field and its directional derivatives. The DC ($|k| = 0$) components of the spectra are set to zero for all anomalous field and tensor components, as these components average to zero over the horizontal plane, for sources of finite horizontal and vertical extent. In practice with real data, after removal of regional trends the average value of each component is subtracted from its gridded values, to comply with this constraint. Over local and small regional scales, computation of magnetic vector components from gridded TMI data on a horizontal plane can be performed efficiently using the Fast Fourier Transform (FFT) algorithm. The 2D Fourier transform of a function $f(x, y)$ is given by:

$$F(k_x, k_y) = \Im[f(x,y)] = \int_{-\infty}^{\infty}\int_{-\infty}^{\infty} f(x,y)\exp(-i[k_x x + k_y y])dxdy, \qquad \text{(A1)}$$

which has inverse

$$f(x,y) = \Im^{-1}[F(k_x, k_y)] = \frac{1}{4\pi^2}\int_{-\infty}^{\infty}\int_{-\infty}^{\infty} F(k_x, k_y)\exp(i[k_x x + k_y y])dk_x dk_y. \qquad \text{(A2)}$$

where k_x and k_y are the wavenumbers along the horizontal x and y axes respectively, and the radial wavenumber $|k| = \sqrt{(k_x^2 + k_y^2)}$.

In the wavenumber domain the magnetic potential Ω, and the grid north, grid east and vertical down components (b_x, b_y, b_z) of the anomalous field vector $\mathbf{b}$ are related to the anomalous TMI, ΔT, by (Blakely, 1996, p.328-329, 342-343)

$$\Im[\Omega] = \frac{\Im[\Delta T]}{|k|n + i(k_x \ell + k_y m)}, \quad |k| \neq 0, \qquad \text{(A3)}$$

$$\Im[b_x] = \frac{ik_x \Im[\Delta T]}{|k|n + i(k_x \ell + k_y m)}, \quad |k| \neq 0, \tag{A4}$$

$$\Im[b_y] = \frac{ik_y \Im[\Delta T]}{|k|n + i(k_x \ell + k_y m)}, \quad |k| \neq 0 \tag{A5}$$

$$\Im[b_z] = \frac{|k| \Im[\Delta T]}{|k|n + i(k_x \ell + k_y m)}, \quad |k| \neq 0, \tag{A6}$$

where (ℓ, m, n) are the direction cosines of the regional geomagnetic field $\mathbf{F} = F(\ell, m, n) = (F_x, F_y, F_z)$ with respect to x, y, z, and ΔT is given by the projection of the anomalous field vector onto the regional field direction:

$$\Delta T = \frac{\mathbf{b}.\mathbf{F}}{F} = b_x \ell + b_y m + b_z n. \tag{A7}$$

Equation (A7) implies that ΔT is harmonic, i.e. it obeys Laplace's equation, because it is a linear combination of field components, each of which is a derivative of the harmonic function Ω along a fixed direction in space. In fact, the measured TMI, ΔB_m, is only equal to ΔT to first order in $|\mathbf{b}|/F$ and is accordingly not a true potential field. In many cases, where the anomalous field is much smaller than F, the error is negligible, but when anomalies of thousands of nT occur, the measured TMI should be corrected to a true potential field (Lourenço and Morris, 1973; Schmidt and Clark, 2006, Gordin et al., 2006; Munschy and Fleury, 2011). Schmidt and Clark (2006) show that

$$\Delta B_m = \sqrt{(F_x + b_x)^2 + (F_y + b_y)^2 + (F_z + b_z)^2} - F = \Delta T + \frac{b^2 - \Delta B_m^2}{2F}. \tag{A8}$$

When anomalies are strong the difference between the two "total field" anomalies becomes significant. It can also be seen from (A8) that the maximum error, for a given magnitude of the anomalous field vector $\boldsymbol{b}$, occurs when the anomalous field is oriented such that $\mathbf{F}' = \mathbf{F}+\mathbf{b}$ and $\mathbf{F}$ form an isosceles triangle, with base $\mathbf{b}$, in which case $\Delta B_{\mathrm{m}} = 0$. For example, the difference between the two types of total field anomaly can be as large as 1000 nT for a 10,000 nT anomaly in a 50,000 nT regional field.

The gridded measured TMI, ΔB_m, is converted to the projection of the anomalous field vector onto the regional geomagnetic field direction, ΔT, which is a true potential field, from which the three orthogonal field components can then be reliably calculated. An initial estimate of the vector components on a regular grid is obtained by assuming that $\Delta B_m = \Delta T$. These approximate components are then used to estimate the difference between ΔB_m and ΔT, which is then used to obtain a better estimate of ΔT. The components are recalculated and the process is repeated, generally converging rapidly, until further improvement is negligible. The explicit correction procedure is:

1. Set the initial estimate of ΔT equal to the measured TMI, i.e.

$$\Delta T_1 = \Delta B_m. \tag{A9}$$

2. Calculate initial estimates of the field components from ΔT_1 using equations (A4)-(A6) and transforming back to the space domain:

$$b_x^{(1)} = \Im^{-1}\left[\frac{ik_x \Im[\Delta T_1]}{|k|n + i(k_x \ell + k_y m)}\right], \quad |k| \neq 0, \tag{A10}$$

$$b_y^{(1)} = \Im^{-1}\left[\frac{ik_y \Im[\Delta T_1]}{|k|n + i(k_x \ell + k_y m)}\right], \quad |k| \neq 0 \tag{A11}$$

$$b_z^{(1)} = \Im^{-1}\left[\frac{|k| \Im[\Delta T_1]}{|k|n + i(k_x \ell + k_y m)}\right], \quad |k| \neq 0. \tag{A12}$$

3. Rearrange eqn (A8) to calculate a corrected estimate of ΔT:

$$\Delta T_2 = \Delta B_m - \frac{(b_x^{(1)})^2 + (b_z^{(1)})^2 + (b_z^{(1)})^2 - \Delta B_m^2}{2F}. \tag{A13}$$

4. Repeat steps 2 and 3 with the updated estimate of ΔT.

At convergence, successive estimates of ΔT should differ by less than a threshold determined by the expected noise level. A further check on the solution is provided by comparison between the estimated ΔB_m calculated from equation (A8), using the final estimates of the anomalous components, and the measured ΔB_m.

Appendix II. Aliased power of calculated vector and tensor components

The maximum permissible line spacing to resolve isolated compact sources using TMI or TMI gradient data can be estimated using the approach of Reid (1980). Reid's analysis can also be extended to the vertical gradient of the reduced-to-pole (RTP) TMI, which can be regarded as equivalent to B_{zz}, as shown below. Total aliased power is defined as the ratio of the integrated power spectral density above the Nyquist frequency to the total power (i.e. power spectral density integrated from DC to infinite frequency). Reid's approach to the 2D integration of the power spectrum of the RTP TMI involves integrating the radial power spectrum $P(k)$ of a dipole source with respect to wavenumber k, i.e. along a single direction in 2D Fourier space. This is reasonable for estimating aliased power in the cross-line direction, assuming the along-line sampling interval is small enough that the along-line aliasing is negligible.

For an equidimensional grid, however, the 2D power spectrum must be integrated over the whole plane in Fourier space. In this case the differential area element $dk_x dk_y$ is equal to $kdkd\theta$ in polar co-ordinates, which increases the proportion of aliased power, due to the extra factor k in the integrand. Closely sampled data collected along lines is useful for detailed analysis of individual profiles. In practice, however, much of the detailed along-line data is effectively discarded when grid based analysis, such as calculating gradient tensor elements, is performed.

For a given source depth beneath the sensor, the sharpest anomaly that a survey is normally required to resolve is that of a point dipole. To simplify the discussion we consider the RTP TMI signature of a dipole. According to Blakely (1996), the spectrum of the RTP TMI signature due to a vertically magnetised dipole, at depth h below the sensor, is radially symmetric and is given by:

$$\Im[\Delta B_z] = \alpha |k| \exp[-h|k|], \qquad \text{(A14)}$$

where α is a constant. The power spectrum is therefore:

$$P(|k|) = |\Im[\Delta B_z]|^2 = \alpha^2 k^2 \exp[-2h|k|]. \tag{A15}$$

For a square grid of measurements at intervals of Δx, the aliased power for ΔB_z is:

$$\begin{aligned} f_{aliased} &= \frac{\int_{k_N}^{\infty}\int_{k_N}^{\infty} P(k_x,k_y)dk_x dk_y}{\int_0^{\infty}\int_0^{\infty} P(k_x,k_y)dk_x dk_y} = \frac{\int_0^{2\pi}\int_{k_N}^{\infty} P(k)kdkd\theta}{\int_0^{2\pi}\int_0^{\infty} P(k)kdkd\theta} \\ &= \frac{\int_{k_N}^{\infty} k^3 \exp[-2hk]dk}{\int_0^{\infty} k^3 \exp[-2hk]dk} = \frac{\left(3+6hk_N+6h^2k_N^2+4h^3k_N^3\right)}{3}\exp(-2hk_N) \end{aligned} \tag{A16}$$

$$\therefore\ f_{aliased}\left(\Delta B_z\right) = \left(1+\frac{2\pi h}{\Delta x}+\frac{2\pi^2 h^2}{(\Delta x)^2}+\frac{4\pi^3 h^3}{3(\Delta x)^3}\right)\exp\left(\frac{-2\pi h}{\Delta x}\right), \tag{A17}$$

where

$$k_N = \frac{\pi}{\Delta x}, \tag{A18}$$

is the Nyquist wavenumber. Pedersen and Rasmussen (1990) carried out a similar analysis, but used what amounts to a more liberal cutoff criterion for a square grid, with their radial cutoff wavenumber κ chosen to make the area of the disc $k \le \kappa$ equal to the square area defined by $|k_x|,|k_y| \le k_N$, i.e. $\pi\kappa^2 = 4(k_N)^2$. This criterion produces a cutoff wavenumber that is 1.13 k_N along the cardinal (x, y) directions and 1.6 times the effective Nyquist wavenumber ($k_N/\sqrt{2}$) along the diagonal directions. Accordingly, I prefer the more conservative criterion given above.

The spectrum of the vertical derivative of ΔB_z is obtained by simply multiplying by $|k|$ (Blakely, 1996, p.326), i.e.

$$\Im[\Delta B_{zz}] = \alpha k^2 \exp[-h|k|]. \tag{A19}$$

The power spectrum is therefore:

$$P(|k|) = \alpha^2 k^4 \exp[-2h|k|], \tag{A20}$$

and the aliased power fraction is:

$$\begin{aligned} f_{aliased} &= \frac{\int_{k_N}^{\infty} k^5 \exp[-2hk]dk}{\int_0^{\infty} k^5 \exp[-2hk]dk} \\ &= \frac{\left(15 + 30hk_N + 30h^2k_N^2 + 20h^3k_N^3 + 10h^4k_N^4 + 4h^5k_N^5\right)}{15}\exp(-2hk_N) \end{aligned} \tag{A21}$$

$$\therefore\ f_{aliased}\left(\Delta B_{zz}\right) = \left(1 + \frac{2\pi h}{\Delta x} + \frac{2\pi^2 h^2}{(\Delta x)^2} + \frac{4\pi^3 h^3}{3(\Delta x)^3} + \frac{2\pi^4 h^4}{3(\Delta x)^4} + \frac{4\pi^5 h^5}{15(\Delta x)^5}\right)\exp\left(\frac{-2\pi h}{\Delta x}\right). \tag{A22}$$

Figure 15 plots the proportion of aliased power relative to signal power for calculated magnetic components and gradient tensor elements over a dipole source, as a function of measured grid spacing Δx divided by depth h. It can be seen from Figure 15 that even a relatively liberal criterion of less than 10% aliased power in the measured signal requires a grid spacing less than ~ h for the TMI and less than ~0.7h for the TMI gradient or for calculation of gradient tensor elements from TMI data. Reid (1980) suggests that 5% aliased power is the maximum acceptable for reliable contouring of the data. The corresponding maximum allowable grid spacings are 0.8h for field components and 0.6h for gradients.

Table 1 summarises the aliased power for field and gradient components due to a point dipole source as a function of grid spacing. As Reid (1980) pointed out, detailed modelling of an anomaly source requires aliased power to be negligible, as most of the diagnostic information resides in the higher frequencies. It is clear from Table 1 that sampling at a grid interval greater than ~0.5 h produces unacceptable errors in calculated gradients. The tabulated values also apply to other elementary sources of practical interest. For example the aliasing of the gradient signal from a point pole source is comparable to the aliasing of the field components from a dipole. Similarly the frequency content of field components from a quadrupole source resembles the spectrum of gradient components

from a dipole. In geological applications a narrow pipe-like body can often be reasonably represented by a point pole model. Ferrous objects at shallow depths often exhibit strong quadrupole moments, particularly if they are irregular in shape. The quadrupole signature can therefore be important in near-surface geophysical applications.

This analysis shows that surveys using total field sensors require a very close line spacing, comparable to the survey altitude (plus depth to magnetic basement if there is nonmagnetic cover), to provide similar information to that given by relatively sparse lines of tensor data, even if the sensor noise levels are comparable. For reliable modelling of isolated compact sources or for accurate calculation of gradients from TMI data when the geology is heterogeneous, without a consistent trend, the sampling interval should be no more than about half the depth.

This very strict criterion can be relaxed if the sources are elongated along regional trends and are crossed by several survey lines. Reasonably accurate interpolation between lines is then possible, so the effective sample spacing becomes less than the line spacing and aliasing is reduced substantially. In the limit of perfectly 2D geology, a single line across strike contains all the information present in the measured field, the Nyquist wavenumber is determined by the sample interval along the line, and in most cases the aliasing becomes negligible.

It should be stressed that sufficiently close sampling is necessary, *but not sufficient*, for accurate determination of field and gradient tensor components from TMI surveys. If the stringent criteria for accurate calculation of gradient tensors from TMI or TMI gradient data are not fulfilled, the gradient tensor must be determined by measurement. The extra information provided by accurately measured gradient tensor data greatly reduces the need for close sampling, as sources that are offline can be located and characterised from just a few gradient tensor measurements within the anomalies produced by the sources.

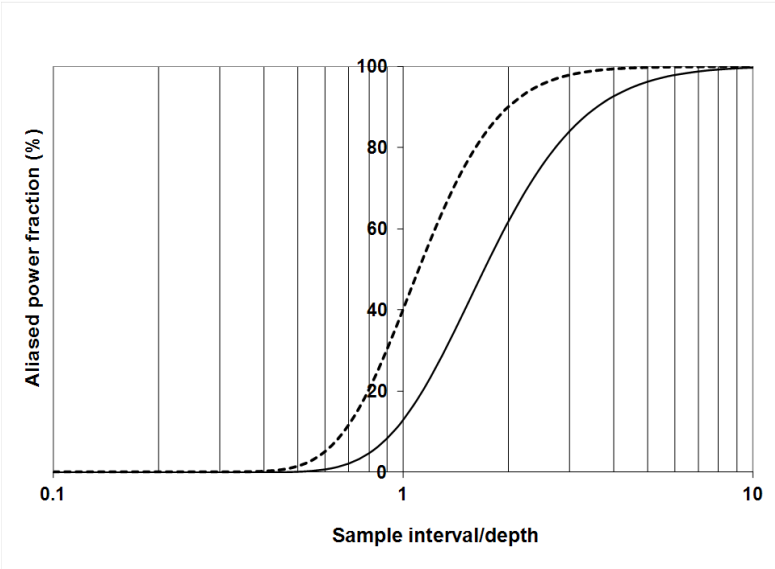

Figure 15. Proportion of aliased power relative to signal power for calculated magnetic components and gradient tensor elements over a dipole source, as a function of measured grid spacing Δx divided by depth h. The solid line pertains to vector components, the dashed line indicates aliased power for gradient components. For typical aeromagnetic and ground magnetic surveys over isolated compact sources, the effective measurement spacing Δx is the line spacing.

Table 1. Percentage aliased power in calculated components as a function of scaled grid spacing for elementary sources

Scaled grid spacing $\Delta x/h$	**Field of Point Dipole/ Gradient of Point Pole** % aliased power	**Gradient of Point Dipole/ Field of Point Quadrupole** % aliased power
4	92.5	99.4
3	84.0	98.0
2	61.6	90.1
1.5	39.7	75.5
1	12.8	40.1
0.75	3.3	15.9
0.5	0.15	1.4
0.25	4×10^{-6}	0.0001

CHAPTER 5: INTERPRETATION OF THE MAGNETIC GRADIENT TENSOR AND NORMALIZED SOURCE STRENGTH APPLIED TO THE TALLAWANG MAGNETITE SKARN DEPOSIT, NEW SOUTH WALES, AUSTRALIA

Clark, D.A. 2012, Interpretation of the magnetic gradient tensor and normalized source strength applied to the Tallawang magnetite skarn deposit, New South Wales, Australia. Society of Exploration Geophysicists Annual Meeting Expanded Abstract.
http://dx.doi.org/10.1190/segam2012-0700.1

Summary

Acquisition of magnetic gradient tensor data is likely to become routine in the near future. In the meantime, significant value can be added to conventional TMI surveys of sufficiently high quality by calculating vector and tensor components and applying newly developed methods to interpretation of these more complex data forms. New methods for inverting gradient tensor surveys to obtain source parameters have been developed for a number of elementary, but useful, models. These include point dipole (sphere), vertical line of dipoles (narrow vertical pipe), line of dipoles (horizontal cylinder), thin dipping sheet, and contact models. A key simplification is the use of eigenvalues and associated eigenvectors of the tensor. The normalized source strength (NNS), calculated from the eigenvalues, is a particularly useful rotational invariant that peaks directly over 3D compact sources, 2D compact sources, thin sheets and contacts, independent of magnetization direction. In combination the NSS and its vector gradient determine source locations uniquely.

Introduction

Pedersen and Rasmussen (1990) and Schmidt and Clark (2006) have strongly advocated the advantages of magnetic gradient tensor surveys for exploration applications. Magnetic tensor gradiometer systems, based on a variety of technologies, are under active development as discussed in a recent review by Clark (2012). In the near future magnetic gradient tensor surveys are likely to become routine. In the meantime, however, in favorable circumstances, high resolution total magnetic intensity (TMI) surveys can be reprocessed to produce grids of vector and tensor components (Lourenço and Morrison, 1973, Pedersen et al. (1990), Schmidt and Clark, 1998). New methods for interpretation of vector and tensor data, which have been developed in anticipation of new acquisition systems, can also be profitably applied to calculated component data.

Pedersen and Rasmussen (1990) and Schmidt and Clark (2006) *inter alia* have reviewed the properties of the magnetic gradient tensor and this background information will not be repeated here.

The normalized source strength

Use of gradient tensor data for detection, localization and characterization (DLC) of compact ferrous sources, which can be well represented by a point dipole source, is a topic of great practical importance and has been the subject of much research (Wynn, 1999). Algorithms for point-by-point inversion of the gradient tensor, to solve for dipole location and magnetic moment vector, have been developed by Wynn et al. (1975), Wilson (1985, Analysis of the magnetic gradient tensor, DREP Technical Memorandum 85-13, Defence Research Establishment Pacific, Canada), hereafter referred to as Wilson (1985), and a number of other workers.

A natural scalar parameter of the dipole inversion problem is known as the scaled moment or normalized moment, which has the same units as gradient tensor elements, is directed parallel to the dipole moment, is proportional to moment (i.e. the source strength), and falls off as the inverse fourth power of distance. Wilson (1985) recognized that the normalized moment could be calculated from the ordered eigenvalues of the gradient tensor, $\lambda_1 \geq \lambda_2 \geq \lambda_3$:

$$\mu = \sqrt{-\lambda_2^2 - \lambda_1\lambda_3} = \frac{3Cm}{r^4}, \qquad (1)$$

where m is moment magnitude in Am², r is the source-sensor separation in meters, and C = 100 nTm/A if μ is given in nT/m.

Note that the RHS of equation (1) represents a positive definite function that exhibits a unimodal peak directly above the dipole source, where r is a minimum, completely independent of the dipole orientation. Therefore if a grid of gradient tensor data is available over an isolated dipole source, the normalized moment can be calculated from the eigenvalues of the tensor and used to locate the dipole (horizontal location beneath the peak, depth equal to 1.55 times the half width at half maximum (HWHM)), irrespective of the source magnetization. Once the source is located, determination of the moment vector becomes a straightforward linear inversion problem.

In a geological context, equation (1) is applicable not only to quasispherical magnetic bodies, but to any sufficiently compact source, except possibly very close to the body. Furthermore, the relationships in equation (1) can be generalized to other simple source types that are often reasonable approximations to geological sources. Equation (1), which expresses normalized moment μ of a dipole source in terms of the eigenvalues of the tensor, can be interpreted more generally as a normalized source strength (NSS), which has a simple physical interpretation for a number of elementary source types and has generally desirable properties. For simple narrow sources, for spheres, and for horizontal cylinders, μ peaks directly above the centre of the source and for wide sheet-like bodies and prisms it peaks directly above the edges. For all 2D sources, for spheres, for compact 3D bodies that can be represented by a dipole, and for narrow, axially magnetized pipe-like bodies (pole-type sources) μ is completely independent of the magnetization direction. Beiki et al. (2012, submitted to Geophysics, under revision) show that for more complex 3D sources μ is only weakly dependent on magnetization direction, substantially less so than the 3D total gradient (also known as the analytic signal amplitude). For these sources, the generalization of (1) can be written

$$\mu = \sqrt{-\lambda_2^2 - \lambda_1\lambda_3} = \sqrt{-I_1 - 2\lambda_2^2} = \frac{Cq}{r^n}, \tag{2}$$

where $n = s + 1$ is the Euler structural index (SI) of magnetic gradients for the particular source type (s is the SI for field components) and q is a source term. I_1 is the first canonical invariant of Pedersen and Rasmussen (1990). The width of the μ anomaly is simply related to the source depth. For sources that obey equation (2), μ is clearly a homogeneous function that is suitable for Euler deconvolution. Beiki et al. (2012) have demonstrated the efficacy of Euler deconvolution of the NSS for simultaneous estimation of structural indices, locations of geological boundaries, and source depths in an area that exhibits strong remanent magnetization. Table 1 summarizes properties of the NSS.

For 2D sources, the intermediate eigenvalue λ_2 is zero and the NSS reduces to

$$\begin{aligned}\mu_{2D} &= \lambda_1 = -\lambda_3 = \sqrt{B_{xx}^2 + B_{xz}^2} = \sqrt{\left(\frac{\partial B_x}{\partial x}\right)^2 + \left(\frac{\partial B_x}{\partial z}\right)^2} \\ &= \sqrt{B_{xz}^2 + B_{zz}^2} = \sqrt{\left(\frac{\partial B_z}{\partial x}\right)^2 + \left(\frac{\partial B_z}{\partial z}\right)^2}.\end{aligned} \tag{3}$$

Thus the 2D normalized source strength is equal to the total gradient, or the analytic signal amplitude (ASA) of Nabhigian (1972), of either the vertical field component, B_z, or of the strike-perpendicular horizontal component, B_x. Since, in the 2D case, the total gradient of TMI is independent of magnetization direction (Li, 2006), the normalized source strength also has this desirable property. The analytic signal amplitude of the total field anomaly is proportional to $A(B_i)$, where B_i is any field component perpendicular to strike, including B_x and B_z. If the strike is magnetic E-W, so that the profile is along the magnetic meridian, $A(T) = A(B_i)$. Otherwise the $A(T)$ profile has the same shape as $A(B_i)$, but smaller magnitude by a factor of $(1-\cos^2\beta\cos^2 I)$, where β is the angle between the strike direction and magnetic north and I is the field inclination. For approximately N-S striking structures at low latitudes, where the inclination is small, $A(T)$ becomes much smaller than the normalized source strength μ_{2D}, which is equivalent to $A(B_i)$.

An eigenvector corresponding to the zero eigenvalue is $(0,1,0)^T$, i.e. along strike, parallel to the y axis. In practice, when $|\lambda_2| << |\lambda_1|,|\lambda_3|$ and the eigenvector $\mathbf{v}_2$ is sub-horizontal, its azimuth can be taken to represent the local strike direction. When the geology is approximately two dimensional, rotating the coordinate system so that the y axis aligns with the local strike direction greatly simplifies analysis, as essentially only two independent gradient components are significant. Pedersen and Rasmussen (1990) illustrated the utility of eigenvector analysis in determining local strike directions of elongated structures.

Source location from the vector gradient of the NSS

For simple sources that obey equation (2), it is evident that the isosurfaces of μ are spheres centered on the source point. Since μ falls off with distance, the vector gradient of μ points toward this source point, as shown in Fig.1. If $\nabla\mu$ is known at two or more observation points, the location of the source can therefore be estimated by triangulation. Furthermore, since the fall off rate for the gradient of μ is one power of r faster than the fall of for μ itself, the distance to the source can also be estimated. In combination, these two pieces of information allow the source location to be estimated from μ and $\nabla\mu$ at a single location. If gradient tensor data are available over a horizontal plane, the NSS can be calculated from the tensor and the horizontal derivatives obtained by numerical differentiation. Determination of the vertical derivative is not as straightforward. Because μ is not harmonic, except for the special case where $n = 1$ in equation (2), its vertical

derivative cannot be calculated by the normal Fourier filtering techniques that apply to potential fields.

The vertical derivative of the NSS can be calculated by continuation of the gradient tensor elements to a slightly higher level, calculating the NSS at this level from the eigenvalues, subtracting the NSS values at the two levels and dividing by the continuation distance. A generally more accurate method employs several steps. First the vertical derivatives of the canonical invariants I_1 and I_2 are calculated by applying the product rule of differentiation to the expressions given by Pedersen and Rasmussen (1990) for these invariants in terms of tensor elements. The resulting expressions involve vertical derivatives of tensor elements, which can be calculated by Fourier filtering. Alternatively, by interchanging the order of differentiation, the vertical derivatives of tensor elements can all be replaced by horizontal derivatives (e.g. $\partial B_{xx}/\partial z = \partial B_{xz}/\partial x$), which can calculated numerically without filtering. The results are

$$\begin{aligned}\frac{\partial I_1}{\partial z} &= -2B_{xx}\frac{\partial B_{xz}}{\partial x} - 2B_{xy}\frac{\partial B_{xz}}{\partial y} - 2B_{xz}\frac{\partial B_{zz}}{\partial x} \\ &- 2B_{yy}\frac{\partial B_{yz}}{\partial y} - 2B_{yz}\frac{\partial B_{zz}}{\partial y} - B_{xx}\frac{\partial B_{yz}}{\partial y} - B_{yy}\frac{\partial B_{xz}}{\partial x}.\end{aligned} \tag{4}$$

$$\begin{aligned}\frac{\partial I_2}{\partial z} &= -\left(B_{xx}B_{yy} - B_{xy}^2\right)\left(\frac{\partial B_{xz}}{\partial x} + \frac{\partial B_{yz}}{\partial y}\right) \\ &+ \left(B_{xx}B_{zz} - B_{xz}^2\right)\frac{\partial B_{yz}}{\partial y} + \left(B_{yy}B_{zz} - B_{yz}^2\right)\frac{\partial B_{xz}}{\partial x} \\ &+ 2\left(B_{xy}B_{xz} - B_{xx}B_{yz}\right)\frac{\partial B_{zz}}{\partial y} + 2\left(B_{yz}B_{xy} - B_{yy}B_{xz}\right) \\ &\times\frac{\partial B_{zz}}{\partial x} + 2\left(B_{xy}B_{yz} - B_{xz}B_{yy}\right)\frac{\partial B_{xz}}{\partial y}.\end{aligned} \tag{5}$$

Expressions for the vertical derivatives of the eigenvalues are obtained by differentiating the characteristic equation that defines them. The result is

$$\frac{\partial \lambda_i}{\partial z} = \frac{\frac{\partial I_2}{\partial z} - \lambda_i \frac{\partial I_1}{\partial z}}{3\lambda_i^2 + I_1}, \quad (3\lambda_2^2 + I_1 \neq 0). \tag{6}$$

Finally the vertical derivative of the NSS can be found by differentiating the first expression on the RHS of (2)

$$\frac{\partial \mu}{\partial z} = \frac{\partial}{\partial z}\sqrt{-I_1 - 2\lambda_2^2} = \frac{-\frac{\partial I_1}{\partial z} - 4\lambda_2 \frac{\partial \lambda_2}{\partial z}}{2\sqrt{-I_1 - 2\lambda_2^2}}$$

$$= \begin{cases} -\dfrac{(I_1 - \lambda_2^2)\dfrac{\partial I_1}{\partial z} + 4\lambda_2 \dfrac{\partial I_2}{\partial z}}{2\mu(3\lambda_2^2 + I_1)}, & (3\lambda_2^2 + I_1 \neq 0), \\ -\dfrac{1}{6\mu}\dfrac{\partial I_1}{\partial z}, & (3\lambda_2^2 + I_1 = 0). \end{cases} \tag{7}$$

Clearly, from (2), the vertical derivative of μ can also be expressed in terms of vertical derivatives of the eigenvalues (Beiki et al., 2012), but the formulation of (4)-(7) allows $\partial\mu/\partial z$ to be calculated without any Fourier filtering. Analogous expressions for the horizontal derivatives can be obtained by replacing z by x and y in (4)-(7).

For sources for which the NSS conforms to eqn (2), the location of the source with respect to an observation point, $-\mathbf{r}$, is given by

$$-\mathbf{r} = \frac{n\mu}{|\nabla\mu|^2}\nabla\mu. \tag{8}$$

Note that this allows estimation of source location directly, without triangulation based on estimated directions to source. In this context, source location refers to the center of the source for the sphere, horizontal cylinder and horizontal line current models, to the top of a narrow, axially magnetized pipe that can be represented by a point pole, to the top of a thin dipping sheet, and to the top corner of a contact. When the source type is uncertain, the appropriate structural index can be estimated as the value of n for which the clustering of location solutions is tightest. For n too small the vectors to source fail to meet, for n too large they overshoot.

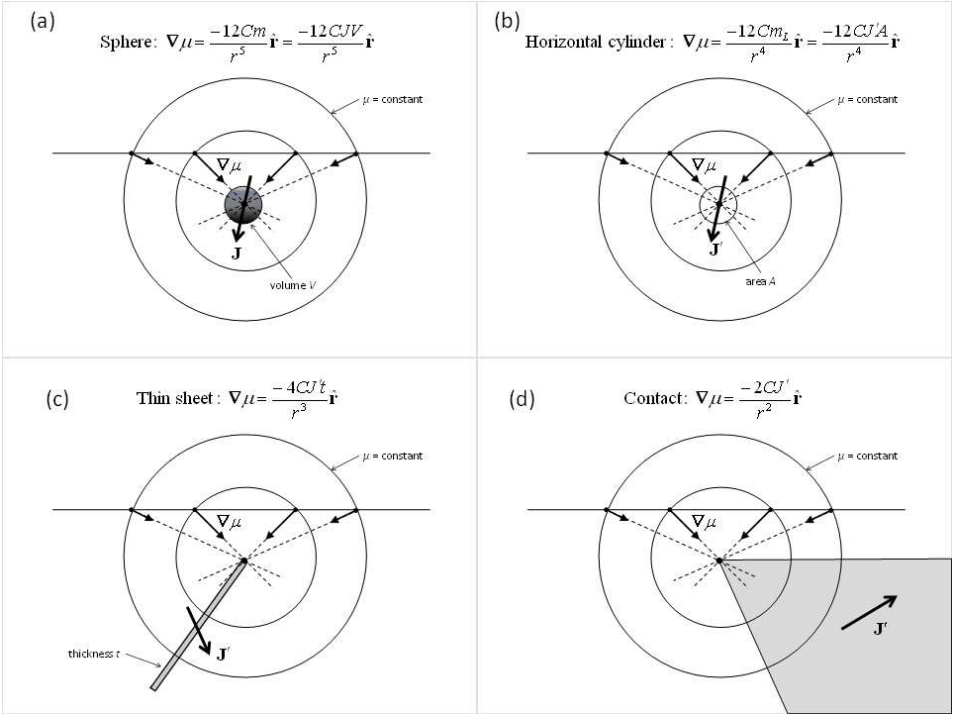

Figure 1: Determination of source location using the vector gradient of the NSS μ. Directions to source are defined by $\nabla\mu$. The displacement vector from observation point to source is proportional to $\mu/\nabla\mu$.

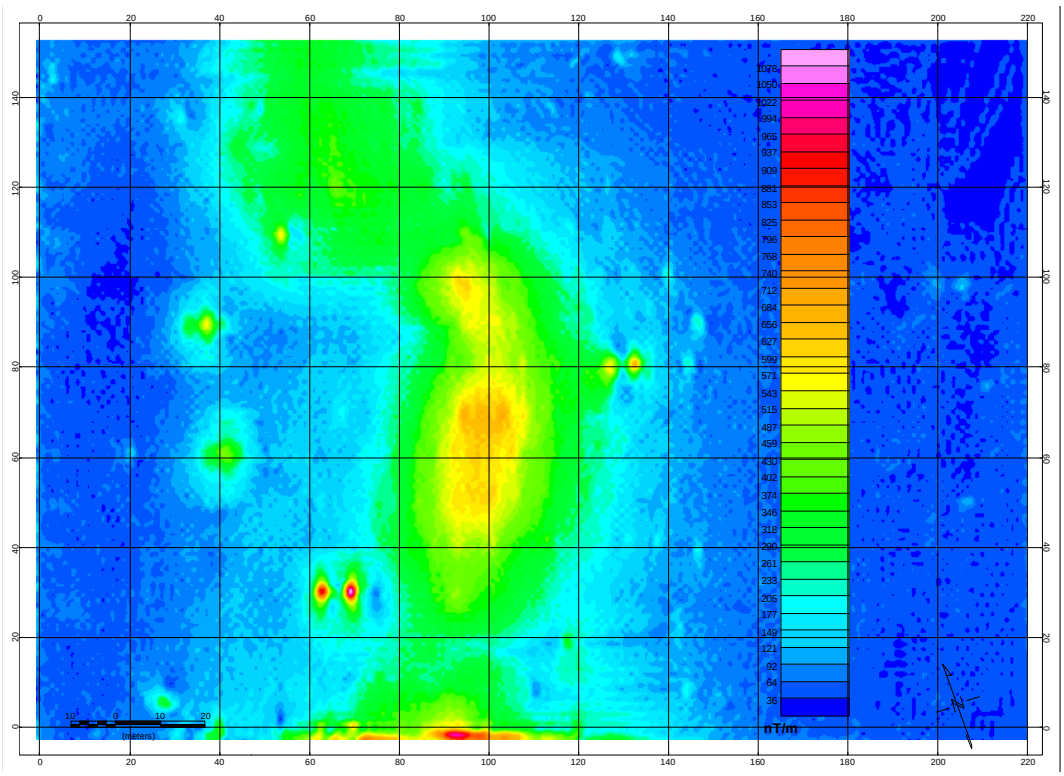

Figure 2: Normalized source strength over the Tallawang magnetite deposit.

Analysis of magnetic data over the Tallawang deposit

The Tallawang magnetite deposit, which is situated 18 km north of Gulgong, NSW, occurs as a skarn along the western margin of the Late Carboniferous Gulgong Granite. The deposit is roughly tabular, striking generally NNW and dipping steeply to the west. Schmidt et al. (2004) described the geology of the deposit and analyzed three profiles of gradient tensor data acquired using the CSIRO GETMAG system along with a detailed conventional ground magnetic survey. Gradient tensor elements calculated from the ground magnetic survey using Fourier filtering were in excellent quantitative agreement with the measured gradient tensors along the profiles. Figure 2 shows an image of the NSS, calculated from the eigenvalues of the gridded tensor data, over the Tallawang deposit. Apart from the main ridge of high values that overlies the skarn, several strong, very localized anomalies are seen. These correspond to steel drill collars.

Figure 3 shows solutions for the source location, derived using equation (8) with $n = 2$, which is appropriate for the thin sheet geometry of the skarn. The solutions cluster around the top of the fresh magnetite zone, with a mean location of 97.4 ± 0.7 mE, depth 19.9 ±1.1 m (1 SE, N = 15). As the observation point moves away from the skarn to the east, the solutions tend to deepen a little and dip slightly to the west. This is consistent with magnetization increasing somewhat down dip, as partial oxidation of magnetite to hematite decreases with increasing depth. The choice $n = 2$ is justified by the convergence of the vectors to source, confirming the appropriateness of the thin sheet model. This indicates that the source has considerable depth extent, because the SI should be greater than two if the depth extent is limited, approaching $n = 3$ for a body with depth extent comparable to the depth to top.

Conclusions

The normalized source strength is a parameter derived from the eigenvalues of the (measured or calculated) magnetic gradient tensor that is minimally sensitive to magnetization direction. It obeys Euler's homogeneity equation for a number of useful models. For these source types the NSS and its vector gradient can be combined to directly determine source locations. This concept has been demonstrated using gradient tensor data from the Tallawang magnetite deposit.

Acknowledgments

This work represents part of a PhD project at Macquarie University under the supervision of Dr Mark Lackie. I thank Phil Schmidt and Clive Foss for reviewing the paper.

Table 1. Properties of the NSS for Simple Sources

Model type	**NSS μ**	**Source term**	**Location wrt observ. point**
Sphere	$3Cm/r^4$	$q = 3JV$	$4\mu\nabla\mu/\lvert\nabla\mu\rvert^2$
Point pole	$C\lvert J_z\rvert A/r^3$	$q = \lvert p\rvert = \lvert J_z\rvert A$	$3\mu\nabla\mu/\lvert\nabla\mu\rvert^2$
Hor. cylinder	$4CJ'A/r^3$	$q = 4J'A$	$3\mu\nabla\mu/\lvert\nabla\mu\rvert^2$
Thin sheet	$2CJ't/r^2$	$q = 2J't$	$2\mu\nabla\mu/\lvert\nabla\mu\rvert^2$
Contact	$2CJ'/r$	$q = 2J'$	$\mu\nabla\mu/\lvert\nabla\mu\rvert^2$
Horizontal line current	$2C\lvert i\rvert/r^2$	$q = 2\lvert i\rvert$	$2\mu\nabla\mu/\lvert\nabla\mu\rvert^2$

J_z is the vertical component of magnetization in A/m; V is the volume of the sphere; A is the area of the flat top of the narrow vertical pipe represented by a point pole, or the cross-section area of the horizontal cylinder; p is the pole strength in Am; J' is the magnitude of the effective magnetization (the component normal to strike); I is the current in A; h is the height of the sensor above the source location (centre for sphere, horizontal cylinder and line current models, top of the pipe for the point pole model, top of the sheet for the thin sheet model, top corner for the contact model) in meters; r is the distance between the source location and the observation point in meters.

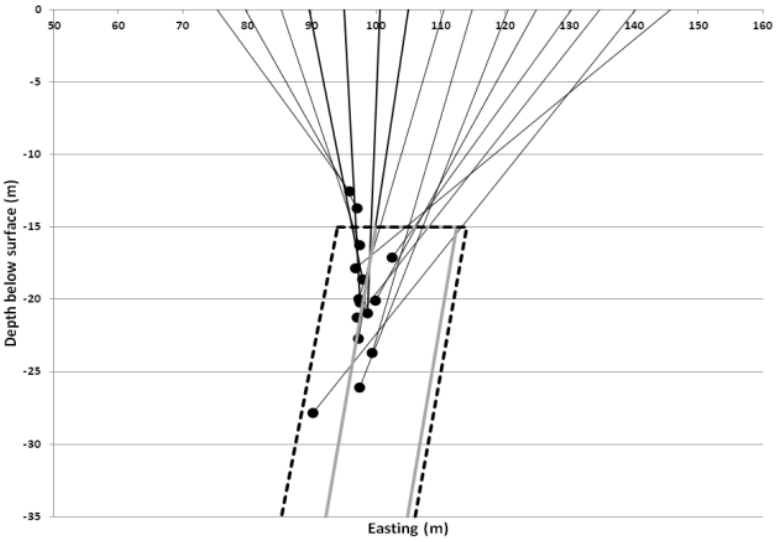

Figure 3. Solutions for the location of the top of the sheet-like skarn at Tallawang. The profile is along 60 mN. Solid black lines connect the solution with the station from which it was derived. The approximate outline of the skarn body is dashed, the high magnetite zone within the skarn is outlined in gray.

CHAPTER 6: CORRECTION OF ELECTRIC AND MAGNETIC FIELDS AND GRADIENTS MEASURED WITHIN AND AROUND AN INSULATING SENSOR CAPSULE IN SEAWATER

Clark, D.A., 2010. Correction of Electric and Magnetic Fields and Gradients Measured Within and Around an Insulating Sensor Capsule in Seawater. OCEANS '10 IEEE Conference, Sydney, 24-27 May 2010. 9p. doi: 10.1109/OCEANSSYD.2010.5603523 (https://wiki.csiro.au/confluence/download/attachments/457769088/CLARK+OCEANS10+paper+IEEE.pdf)

Abstract

The presence of a highly conductive medium around a measurement capsule influences electromagnetic measurements made in the ocean and fundamentally alters the structure of the magnetic gradient tensor. Additional effects arise if seawater is flowing past the sensor package. This paper presents a quantitative analysis of these effects and describes the corrections that need to be applied to obtain accurate absolute measurements of electromagnetic fields and gradients in the ocean. For example, for a small spherical cavity within a 1D horizontal quasistatic electric current distribution, the electric field within the cavity is parallel to the unperturbed applied field and larger by 50%, and the magnetic field at the centre of the cavity is equal to the unperturbed magnetic field that existed at the same point in the conductive medium, prior to insertion of the measurement capsule. The symmetric magnetic gradient tensor within the cavity is uniform. If the unperturbed electric current is parallel to the *x* axis, the only non-zero components of the magnetic gradient tensor within the cavity are $B_{yz} = B_{zy}$. These components are each equal to half the value of $\partial B_y/\partial z$ that is produced by the unperturbed current flow in the conductive medium. The external perturbation of the electric field around the cavity has the configuration of a dipole field and the external magnetic field due to the cavity is that of an elementary current dipole. An ellipsoidal cavity has an anisotropic response, except in the degenerate case where all axes are equal and the cavity is spherical. Unless the applied field lies along a principal axis of the ellipsoid, the internal field is not parallel to the applied field, but is deflected away from the major axis and towards the minor axis. An applied electric field is amplified within the cavity. For a disk-like cavity the amplification of the applied electric field normal to the disk can be very large within the cavity. The anomalous magnetic field within the ellipsoidal cavity due to electric current flow around the cavity is nonuniform, but has a uniform gradient. At the center of the ellipsoidal cavity the magnetic field is equal to the field that existed at that point before insertion of the cavity. The *resultant* internal magnetic gradient tensor is symmetric and traceless, as required. Seawater motion past a sensor package produces easily detectable effects that can represent an important source of electromagnetic noise. In the vicinity of a measurement capsule, water velocities of the order of 1 ms^{-1} produce perturbations of ~45 μVm^{-1} in electric field, ~75 pT in magnetic field, and produce magnetic gradients of ~150 pT/m.

INTRODUCTION

The CSIRO Division of Materials Science and Engineering is developing sensitive magnetic tensor gradiometers, based on high-temperature SQUID technology, for deployment in the marine environment. The applications include gradient measurements as an adjunct to electric and magnetic measurements in marine CSEM surveys, unexploded ordnance detection in shallow water, and exploration for seafloor mineralization.

Electric (**E**) and magnetic (**B**) fields within a conductive medium are perturbed by the measurement process. In particular, sensors located within or around an insulating measurement capsule measure fields that are modified by the diversion of conduction currents around the capsule. For quasistatic field measurements in air or free space, where conduction and convection currents are absent and displacement currents are negligible, the magnetic gradient tensor, which has elements $B_{ij} = \partial B_j/\partial x_i$ (i,j = 1,2,3), is symmetric, as well as traceless. In this case the tensor only has five independent components (e.g. B_{11}, B_{22}, B_{12}, B_{13}, B_{23}). On the other hand, in the presence of conduction currents the curl of **B** is non-zero and the gradient tensor is asymmetric, with eight independent components.

This raises the question of what is actually measured by magnetometers and gradiometers immersed in the electrically conductive ocean. In particular, how does the signal measured within a sealed capsule (within which the gradient tensor is symmetric) relate to the field components and the asymmetric gradient tensor that existed in the surrounding medium prior to insertion of the measurement package? The answer to this question depends on the configuration of the sensors, in particular whether conduction currents flow between individual sensors or the entire sensor package is contained within an insulating capsule. In the quasistatic limit, which applies to measurements made for magnetotelluric and typical marine controlled source EM surveys, and to oceanographic applications, the effects depend only on geometry and are independent of frequency.

This paper presents theoretical relationships between measured electric and magnetic fields and gradients and the corresponding quantities that would exist in the unperturbed medium, for a variety of geometries, including ellipsoidal measurement capsules. The effects of water flow around the capsule are also considered.

Consider an infinite ohmic medium of conductivity σ subject to a uniform applied electric field $\mathbf{E}_0$. Insertion of an insulating measurement capsule into the initially uniform electric current distribution, of density $\mathbf{j}_0 = \sigma\mathbf{E}_0$, distorts the current flow and the associated electric field. Ellipsoidal cavities can be used to model a wide variety of capsule shapes, whilst conveniently allowing analytic solutions. Let us represent the capsule by a triaxial ellipsoidal cavity, centered at the origin, with semiaxes $a > b > c$ along x_1, x_2, x_3 respectively. The ellipsoidal coordinates ξ, η, ζ are the roots, in descending order, of the cubic equation in λ

$$\frac{x_1^2}{a^2+\lambda}+\frac{x_2^2}{b^2+\lambda}+\frac{x_3^2}{c^2+\lambda}=1, \tag{1}$$

where $\xi > -c^2$, $-c^2 > \eta > -b^2$, $-b^2 > \zeta > -a^2$ ([1], [2]). The boundary of the ellipsoidal cavity is defined by $\xi = 0$. In terms of Cartesian coordinates, the potential V_0 associated with a uniform applied electric field $\mathbf{E}_0$ is

$$V_0 = -\mathbf{E}_0.\mathbf{r} = -(\mathbf{E}_0)_1 x_1 - (\mathbf{E}_0)_2 x_2 - (\mathbf{E}_0)_3 x_3. \tag{2}$$

In terms of ξ, η, ζ, the applied potential is given by

$$\begin{aligned} V_0 = &-(\mathbf{E}_0)_1\sqrt{\frac{(\xi+a^2)(\eta+a^2)(\zeta+a^2)}{(a^2-b^2)(a^2-c^2)}} \\ &-(\mathbf{E}_0)_2\sqrt{\frac{(\xi+b^2)(\eta+b^2)(\zeta+b^2)}{(c^2-b^2)(a^2-c^2)}} \\ &-(\mathbf{E}_0)_3\sqrt{\frac{(\xi+c^2)(\eta+c^2)(\zeta+c^2)}{(b^2-c^2)(a^2-c^2)}}. \end{aligned} \tag{3}$$

The electric potential V obeys Laplace's equation every-where, is continuous at the cavity boundary, asymptotically approaches V_0 at large distances ($\xi \sim r^2 >> a^2$), and is subject to the boundary condition $\partial V/\partial n \to 0$ as $\xi \to 0^+$, since the external electric field is

proportional to the electric current within the ohmic medium and no current crosses the cavity boundary. Solving the boundary value problem in ellipsoidal coordinates gives

$$V(\xi \le 0) = -\frac{(\mathbf{E}_0)_1}{1-D_1}x_1 - \frac{(\mathbf{E}_0)_2}{1-D_2}x_2 - \frac{(\mathbf{E}_0)_3}{1-D_3}x_3, \tag{4}$$

for the internal potential, and

$$V(\xi \ge 0) = V_1 + V_2 + V_3 \tag{5}$$

for the external potential, where

$$\begin{aligned} V_1(\xi \ge 0) &= -(\mathbf{E}_0)_1 x_1 \left[1 + \frac{abc/2}{1-D_1} \int_\xi^\infty \frac{ds}{(s+a^2)R_s} \right] \\ &= -(\mathbf{E}_0)_1 x_1 \left[1 + \frac{abc/2}{1-D_1} A(\xi) \right], \end{aligned} \tag{6}$$

$$\begin{aligned} V_2(\xi \ge 0) &= -(\mathbf{E}_0)_2 x_2 \left[1 + \frac{abc/2}{1-D_2} \int_\xi^\infty \frac{ds}{(s+b^2)R_s} \right] \\ &= -(\mathbf{E}_0)_2 x_2 \left[1 + \frac{abc/2}{1-D_2} B(\xi) \right], \end{aligned} \tag{7}$$

$$\begin{aligned} V_3(\xi \ge 0) &= -(\mathbf{E}_0)_3 x_3 \left[1 + \frac{abc/2}{1-D_3} \int_\xi^\infty \frac{ds}{(s+c^2)R_s} \right] \\ &= -(\mathbf{E}_0)_3 x_3 \left[1 + \frac{abc/2}{1-D_3} C(\xi) \right]. \end{aligned} \tag{8}$$

In (7)-(8) $R_s = \sqrt{(s+a^2)(s+b^2)(s+c^2)}$. The D_i (i = 1,2,3) are demagnetizing (or depolarizing) factors of the ellipsoid along its major, intermediate and minor axes respectively. Explicit expressions in terms of standard elliptic integrals for $D_1 = abcA(0)/2$, $D_2 = abcB(0)/2$, $D_3 = abcC(0)/2$, and for the functions $A(\xi)$, $B(\xi)$, $C(\xi)$ are given in [3]. If two or more axes are equal, or if an axis becomes infinite, the elliptic integrals reduce to elementary functions.

Equation (2) implies a uniform internal field given by:

$$\mathbf{E}(\xi \le 0) = -\nabla V = \left(\frac{1}{1-D_1}\right)(\mathbf{E}_0)_1 \hat{\mathbf{x}}_1 + \left(\frac{1}{1-D_2}\right)(\mathbf{E}_0)_2 \hat{\mathbf{x}}_2 + \left(\frac{1}{1-D_3}\right)(\mathbf{E}_0)_3 \hat{\mathbf{x}}_3. \tag{9}$$

The demagnetizing factors sum to unity. Since $D_1 \le D_2 \le D_3$, an ellipsoidal cavity has an anisotropic response, except in the degenerate case where all axes are equal and the cavity is spherical. In that case $D_1 = D_2 = D_3 = 1/3$. Unless the applied field lies along a principal axis of the ellipsoid, the internal field is not parallel to the applied field, but is deflected away from the major axis and towards the minor axis. It is obvious from (9) that an applied electric field is amplified within the cavity. For a disk-like cavity $D_3 \to 1$ as $c/a \to 0$, so the amplification of the applied electric field normal to the disc can be very large within the cavity.

The corresponding external field components are obtained from (5)-(8) by differentiation:

$$E_1(\xi \ge 0) = (\mathbf{E}_0)_1 \left\{ \left[1 + \frac{abc/2}{1-D_1} A(\xi) \right] + \frac{abcA'(\xi)x_1}{2(1-D_1)} \frac{\partial \xi}{\partial x_1} \right\} + \left[(\mathbf{E}_0)_2 \frac{abcB'(\xi)x_2}{2(1-D_2)} + (\mathbf{E}_0)_3 \frac{abcC'(\xi)x_3}{2(1-D_3)} \right] \frac{\partial \xi}{\partial x_1}, \tag{10}$$

$$E_2(\xi \ge 0) = (\mathbf{E}_0)_2 \left\{ \left[1 + \frac{abc/2}{1-D_2} B(\xi) \right] + \frac{abcB'(\xi)x_2}{2(1-D_2)} \frac{\partial \xi}{\partial x_2} \right\} + \left[(\mathbf{E}_0)_1 \frac{abcA'(\xi)x_1}{2(1-D_1)} + (\mathbf{E}_0)_3 \frac{abcC'(\xi)x_3}{2(1-D_3)} \right] \frac{\partial \xi}{\partial x_2}, \tag{11}$$

$$E_3(\xi \ge 0) = (\mathbf{E}_0)_3 \left\{ \left[1 + \frac{abc/2}{1-D_3} C(\xi) \right] + \frac{abcC'(\xi)x_3}{2(1-D_3)} \frac{\partial \xi}{\partial x_3} \right\} + \left[(\mathbf{E}_0)_2 \frac{abcB'(\xi)x_2}{2(1-D_2)} + (\mathbf{E}_0)_1 \frac{abcA'(\xi)x_1}{2(1-D_1)} \right] \frac{\partial \xi}{\partial x_3}. \tag{12}$$

Reference [3] gives explicit expressions for the demagnetizing factors, the functions $A(\xi)$, $B(\xi)$, $C(\xi)$ and their derivatives with respect to ξ, and the derivatives $\partial\xi/\partial x_i$. For a spherical cavity $D_i = 1/3$, so (9) implies that the internal electric field is parallel to the applied field, but amplified by a factor of 1.5. The *external* field around a spherical cavity

is identical to that of an elementary current dipole located at the center of the cavity, immersed in an infinite homogeneous conductive medium, in the limit as frequency goes to zero [4]. The moment **p** of this equivalent current dipole is

$$\mathbf{p} = I\Delta\mathbf{x} = -2\pi a^3\mathbf{j}_0 = -2\pi a^3\sigma\mathbf{E}_0. \tag{13}$$

where Δx (<< a) is the length and I is the current carried by the dipole.

Fig.1 shows the variation of the local electric field around a spherical cavity. Also shown is the average electric field over a finite baseline, which is what is measured by a standard marine electrometer that estimates the electric field from the potential difference between two electrodes, symmetrically disposed about an electronics capsule, divided by the electrode separation. For a long cylindrical cavity, oriented perpendicular to the applied field, the internal field is also parallel to the applied field, but in this case is approximately doubled in strength, because $D_2 = D_3 = 1/2$ for an infinite cylinder.

For a spherical cavity, the perturbation of the electric current corresponds to a ball of impressed current $\mathbf{j}' = -\mathbf{j}_0$, with a return flow that conforms to a dipole field. In this case the anomalous magnetic field $\mathbf{B}'$ due to the perturbation of the electric current distribution can be calculated by applying Ampere's circuital law to circular contours centered on an axis passing through the sphere, parallel to the applied electric field. In terms of spherical polar coordinates r, θ, φ with the polar axis along x_1, parallel to the applied electric field, the anomalous internal magnetic field is

$$B'_\varphi(r \le a) = \frac{-\mu_0 j_0 r \sin\theta}{2} = \frac{-\mu_0 j_0 \sqrt{x_2^2 + x_3^2}}{2}. \tag{14}$$

The nonzero Cartesian components are

$$B'_2(r \le a) = \frac{\mu_0 j_0 x_3}{2}, B'_3(r \le a) = -\frac{\mu_0 j_0 x_2}{2}, \tag{15}$$

and the nonzero anomalous gradient tensor elements are

$$B'_{23}(r \le a) = -\frac{\mu_0 j_0}{2}, B'_{32}(r \le a) = \frac{\mu_0 j_0}{2}. \tag{16}$$

The anomalous magnetic field $\mathbf{B}'$ and corresponding gradient tensor $\mathbf{G}'$ within a spherical cavity can also be written in coordinate-free form as

$$\mathbf{B}'(r \le a) = \frac{\mu_0(\mathbf{r} \times \mathbf{j}_0)}{2}, \tag{17}$$

and

$$\mathbf{G}'(r \le a) = \frac{\mu_0 \mathbf{I} \times \mathbf{j}_0}{2}, \tag{18}$$

where $\mathbf{I} = \hat{\mathbf{x}}_1\hat{\mathbf{x}}_1 + \hat{\mathbf{x}}_2\hat{\mathbf{x}}_2 + \hat{\mathbf{x}}_3\hat{\mathbf{x}}_3$ is the identity dyadic or idemfactor.

In vector form the anomalous external magnetic field is

$$\mathbf{B}'(r \ge a) = \frac{\mu_0 a^3(\mathbf{r} \times \mathbf{j}_0)}{2r^3}, \tag{19}$$

and the gradient tensor is

$$\mathbf{G}'(r > a) = \frac{\mu_0 a^3}{2}\left[\frac{1}{r^3}\mathbf{I} \times \mathbf{j}_0 - \frac{3\mathbf{r}}{r^5}(\mathbf{r} \times \mathbf{j}_0)\right]. \tag{20}$$

The magnetic field configuration given by (19) is identical to that of an infinitesimal current element, given by the Biot-Savart law, which is applicable in this case because the contributions of the return currents in the medium integrate to zero around the return paths [5].

Ampere's circuital law cannot be used in the same way for a nonspherical cavity, due to the lower symmetry of the problem. Consider initially an ellipsoidal cavity with major axis aligned with the applied electric field. The volume of the cavity $\tau = 4\pi abc/3$. The effect of the ellipsoidal cavity can be regarded as the superposition of an ellipsoidal distribution of impressed current $\mathbf{j}' = -\mathbf{j}_0$, together with its ohmic return currents in the surrounding medium, and the uniform applied current flow $\mathbf{j}_0$. The anomalous magnetic field $\mathbf{B}'$ arising from the perturbation $\mathbf{j}'$ of the current distribution is continuous at the

cavity surface and satisfies $\nabla\times \mathbf{B}' = \mu_0\mathbf{j}'$ and $\nabla.\ \mathbf{B}' = 0$ everywhere inside and outside the ellipsoid. Outside the ellipsoid $\mathbf{j}'$ is equal to $\sigma(\mathbf{E}-\mathbf{E}_0)$, where $\mathbf{E}$ is given by (10)-(12). The components of $\mathbf{B}'$ that satisfy these conditions are

$$B_1' = 0, \quad \forall\xi \tag{21}$$

$$\begin{aligned} B_2'(\xi<0) &= \frac{\mu_0 j_1 abcC(0)}{2(1-D_1)} x_3 \\ &= \frac{\mu_0 j_1 abcC(0)}{2(1-D_1)} \sqrt{\frac{(\xi+c^2)(\eta+c^2)(\zeta+c^2)}{(a^2-c^2)(b^2-c^2)}}, \end{aligned} \tag{22}$$

$$\begin{aligned} B_3'(\xi<0) &= -\frac{\mu_0 j_1 abcB(0)}{2(1-D_1)} x_2 \\ &= -\frac{\mu_0 j_1 abcB(0)}{2(1-D_1)} \sqrt{\frac{(\xi+b^2)(\eta+b^2)(\zeta+b^2)}{(a^2-c^2)(b^2-c^2)}}, \end{aligned} \tag{23}$$

$$\begin{aligned} B_2'(\xi\geq 0) &= \frac{\mu_0 j_1 abcC(\xi)}{2(1-D_1)} x_3 \\ &= \frac{\mu_0 j_1 abcC(\xi)}{2(1-D_1)} \sqrt{\frac{(\xi+c^2)(\eta+c^2)(\zeta+c^2)}{(a^2-c^2)(b^2-c^2)}}, \end{aligned} \tag{24}$$

$$\begin{aligned} B_3'(\xi\geq 0) &= -\frac{\mu_0 j_1 abcB(\xi)}{2(1-D_1)} x_2 \\ &= -\frac{\mu_0 j_1 abcB(\xi)}{2(1-D_1)} \sqrt{\frac{(\xi+b^2)(\eta+b^2)(\zeta+b^2)}{(a^2-c^2)(b^2-c^2)}}. \end{aligned} \tag{25}$$

The anomalous field given by (21)-(25) is solenoidal, has the correct curl everywhere and is continuous across the cavity boundary ($\xi = 0$), as required. It is therefore the unique solution to the boundary value problem. As confirmation, the anomalous magnetic field, given by (24)-(25), conforms to the field of a current dipole at large distances. Noting that for $r >> a$, $\xi \to r^2$ and $A(\xi)$, $B(\xi)$, $C(\xi)\to 2/3r^3$, asymptotic expressions for the field components are

$$B_2'(\xi >> a^2) \sim \frac{\mu_0 j_1 abc}{3(1-D_1)} \frac{x_3}{r^3} = \frac{\mu_0 j_1 \tau}{4\pi(1-D_1)} \frac{x_3}{r^3}, \tag{26}$$

$$B_3'(\xi >> a^2) \sim -\frac{\mu_0 j_1 abc}{3(1-D_1)} \frac{x_2}{r^3} = \frac{-\mu_0 j_1 \tau}{4\pi(1-D_1)} \frac{x_2}{r^3}. \tag{27}$$

It can be seen by comparison with (19) that the expressions on the RHS of (26) and (27) are consistent with the corresponding expressions for a spherical cavity of equal $\tau/(1-D_1)$, where $D_1 = 1/3$ for a sphere.

So far only a specific orientation of the ellipsoid has been considered. In general the ellipsoid may have arbitrary orientation with respect to the current flow. If the components of the unperturbed current flow with respect to the ellipsoid axes are j_1, j_2, j_3 then the resultant anomalous field represents the superposition of the effects that would be produced by currents along each of the ellipsoid axes. The result, obtained analogously to (21)-(25), is

$$\begin{aligned} B_1'(\xi<0) &= \frac{\mu_0 j_3 abcB(0)}{2(1-D_3)}x_2 - \frac{\mu_0 j_2 abcC(0)}{2(1-D_2)}x_3 \\ &= \mu_0\left(\frac{j_3 D_2 x_2}{(1-D_3)} - \frac{j_2 D_3 x_3}{(1-D_2)}\right), \end{aligned} \tag{28}$$

$$\begin{aligned} B_2'(\xi<0) &= \frac{\mu_0 j_1 abcC(0)}{2(1-D_1)}x_3 - \frac{\mu_0 j_3 abcA(0)}{2(1-D_3)}x_1 \\ &= \mu_0\left(\frac{j_1 D_3 x_3}{(1-D_1)} - \frac{j_3 D_1 x_1}{(1-D_3)}\right), \end{aligned} \tag{29}$$

$$\begin{aligned} B_3'(\xi<0) &= \frac{\mu_0 j_2 abcA(0)}{2(1-D_2)}x_1 - \frac{\mu_0 j_1 abcB(0)}{2(1-D_1)}x_2 \\ &= \mu_0\left(\frac{j_2 D_1 x_1}{(1-D_2)} - \frac{j_1 D_2 x_2}{(1-D_1)}\right), \end{aligned} \tag{30}$$

$$\begin{aligned} B_1'(\xi>0) &= \frac{\mu_0 j_3 abcB(\xi)}{2(1-D_3)}x_2 - \frac{\mu_0 j_2 abcC(\xi)}{2(1-D_2)}x_3 \\ &= \frac{3\mu_0\tau}{8\pi}\left(\frac{B(\xi) j_3 x_2}{(1-D_3)} - \frac{C(\xi) j_2 x_3}{(1-D_2)}\right), \end{aligned} \tag{31}$$

$$\begin{aligned} B_2'(\xi>0) &= \frac{\mu_0 j_1 abcC(\xi)}{2(1-D_1)}x_3 - \frac{\mu_0 j_3 abcA(\xi)}{2(1-D_3)}x_1 \\ &= \frac{3\mu_0\tau}{8\pi}\left(\frac{C(\xi) j_1 x_3}{(1-D_1)} - \frac{A(\xi) j_3 x_1}{(1-D_3)}\right), \end{aligned} \tag{32}$$

$$
\begin{aligned}
B_3'(\xi > 0) &= \frac{\mu_0 j_2 abcA(\xi)}{2(1-D_2)} x_1 - \frac{\mu_0 j_1 abcB(\xi)}{2(1-D_1)} x_2 \\
&= \frac{3\mu_0 \tau}{8\pi} \left(\frac{A(\xi) j_2 x_1}{(1-D_2)} - \frac{B(\xi) j_1 x_2}{(1-D_1)} \right).
\end{aligned}
\tag{33}
$$

The anomalous magnetic field within the ellipsoidal cavity is nonuniform, but has a uniform gradient. At the center of the ellipsoidal cavity ($x_1 = x_2 = x_3 = 0$) the magnetic field is equal to the field that existed at that point before insertion of the cavity. The *resultant* internal magnetic gradient tensor is symmetric and traceless, as required. Its components are given by

$$
\begin{aligned}
&G_{ii} = G_{ii}^0, (i = 1,2,3) \\
&G_{12} = G_{21} = G_{21}^0 + \mu_0 D_2 j_3 /(1-D_3) \\
&G_{13} = G_{31} = G_{13}^0 + \mu_0 D_1 j_2 /(1-D_2) \\
&G_{23} = G_{32} = G_{32}^0 + \mu_0 D_3 j_1 /(1-D_1)
\end{aligned}
\tag{34}
$$

where the unperturbed gradient tensor is $\mathbf{G}_0 = [\, G_{ij}^0 \,]$, which depends on the configuration of the unperturbed current flow, on geological anomalies and on other magnetic sources. As an example, Fig.2 shows magnetic gradient tensor components within and around a spherical cavity placed within a 1D current distribution in the ocean. These results allow measurements by sensors that have been calibrated in air to be corrected for the effect of a conductive medium. For a capsule adjacent to a conductivity interface, such as the sea surface or seafloor, the interaction effects can be approximately evaluated using the method of images.

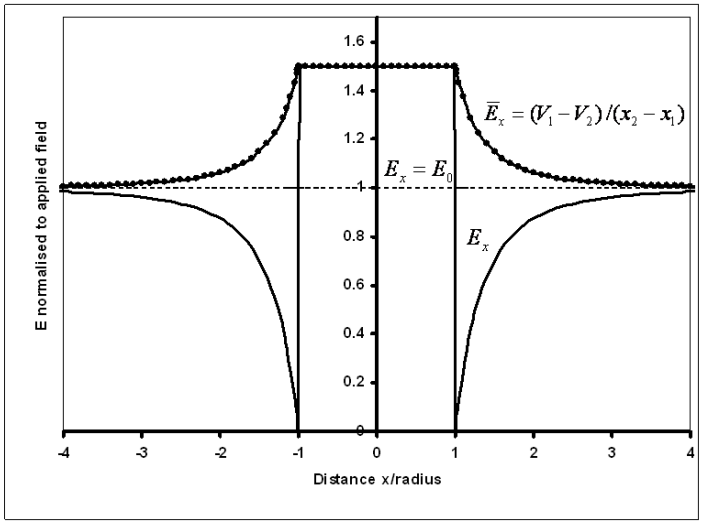

Fig.1. Normalized electric field (E) profile, parallel to the uniform applied field, passing through the centre of a spherical cavity. Solid line indicates the local field; the horizontal dashed line represents the unperturbed applied field; the line with dots shows the average field over a baseline defined by symmetrically placed potential electrodes.

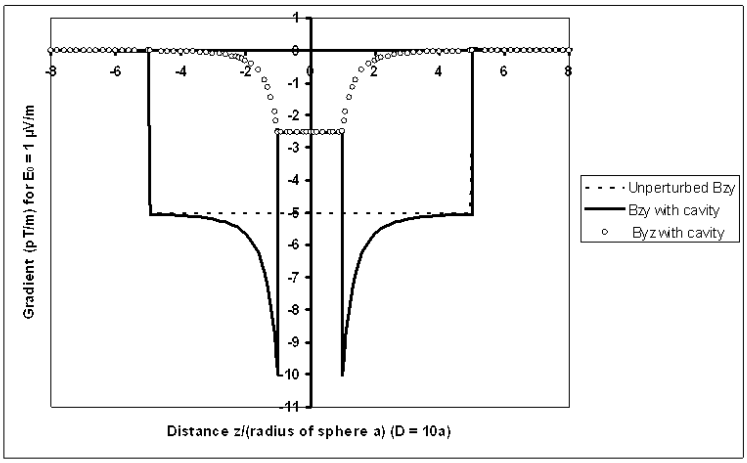

Fig.2. Magnetic gradient tensor elements along a vertical profile through the centre of a spherical cavity within a horizontal current flow distribution of limited depth extent. The assumed conductivity of the seawater is 4 Sm^{-1}. Magnetic gradients are normalized to an applied electric field of 1 μV/m. The current flow is confined to an infinite horizontal slab of thickness D equal to five times the diameter of the cavity. Within the current flow, but beyond the influence of the cavity, the only nonzero gradient tensor component is B_{zy} (solid line). The dashed horizontal line is the unperturbed value of B_{zy} within the 1D current distribution. The dots indicate B_{yz}. Within the cavity $B_{zy} = B_{yz}$. The influence of the cavity is significant out to $r \approx 3a$.

So far it has been assumed that the conductive medium is stationary. If the seawater is moving with respect to the sensor with velocity **v**, however, Maxwell's equations must be modified to take the Lorentz field into account. Scaling arguments show that the conduction current totally dominates other sources of magnetic field in the ocean and that the contribution of electromagnetic induction to the electric field is minor at low frequencies and for quasistatic water flow [6]. We consider steady state water flow and static fields and neglect transport of free charges, which can be shown to be effectively absent within the seawater. Maxwell's equations for moving media are then [7]

$$\nabla.(\varepsilon_0\mathbf{E}+\mathbf{P})=0, \tag{35}$$

$$\nabla\times\mathbf{E}=\mathbf{0}, \tag{36}$$

$$\nabla.\mathbf{B}=0, \tag{37}$$

$$\nabla\times\mathbf{B}=\mu_0[\mathbf{j}+\nabla\times(\mathbf{P}\times\mathbf{v})], \tag{38}$$

with constitutive equations

$$\mathbf{j}=\sigma(\mathbf{E}+\mathbf{v}\times\mathbf{F}), \tag{39}$$

$$\mathbf{P}=(\varepsilon-\varepsilon_0)(\mathbf{E}+\mathbf{v}\times\mathbf{F}), \tag{40}$$

where $\mathbf{E} = -\nabla V$ is the electric field in a stationary reference frame and **F** is the geomagnetic field. In principle **F** includes the local anomalous magnetic field due to electric current flow, but this contribution is orders of magnitude less than the geomagnetic field, so in practice this perturbation can be ignored and **F** can be taken to be the background geomagnetic field, assumed uniform. The magnetic body force $\mathbf{j}\times\mathbf{F}$ acting on the seawater can be safely ignored because it is minuscule compared to the pressure and buoyancy forces that drive the water motion.

Equation (38) includes the magnetic effect of the moving electrically polarized medium, which is equivalent to that of a magnetized material with magnetization $\mathbf{M} = \mathbf{P} \times \mathbf{v}$. However, the second term in the brackets on the RHS of (38) can be neglected because it is many orders of magnitude less than the conduction current. For example, taking $\sigma = 4$ Sm^{-1}, $\varepsilon = 80\varepsilon_0$, $v \leq 10\ \mathrm{ms}^{-1}$, and a characteristic length $L \sim 1\text{-}10$ m, implies that the ratio of the contribution to the curl of **B** from motion of the polarized medium to that of the conduction current is less than $(\varepsilon - \varepsilon_0)v/\sigma L \approx 10^{-9} - 10^{-10}$. Thus we may safely drop the term involving **P** from (38) when determining the electro-magnetic fields.

Incorporating seawater motion into the analysis is straightforward, provided the water is assumed to be incompressible (an excellent approximation) and its flow is irrotational, which is an idealization that is reasonable in many circumstances, provided the flow is not too rapid or turbulent. Incompressibility implies that

$$\nabla.\mathbf{v} = 0. \tag{41}$$

For irrotational flow

$$\nabla \times \mathbf{v} = 0, \tag{42}$$

which implies that

$$\mathbf{v} = \nabla\phi, \tag{43}$$

where ϕ is the velocity potential. For initially uniform water flow $\mathbf{v}_0$ the unperturbed velocity potential is $\phi_0 = \mathbf{r}.\ \mathbf{v}_0$. From (41) and (43), ϕ obeys Laplace's equation. For ideal fluid flow around an ellipsoid the boundary value problem for ϕ is identical in form to the problem for $-V$ around an ellipsoidal cavity in a stationary conductive medium. For example, the perturbed velocity potential and corresponding velocity around a spherical cavity are

$$\phi(\mathbf{r}) = \left(1 + \frac{a^3}{2r^3}\right)\mathbf{v}_0.\mathbf{r}, \quad (r \geq a) \tag{44}$$

$$\mathbf{v} = \left(1 + \frac{a^3}{2r^3}\right)\mathbf{v}_0 - \frac{3a^3(\mathbf{v}_0.\hat{\mathbf{r}})}{2r^3}\hat{\mathbf{r}} \quad (r \geq a). \tag{45}$$

The perturbation of the velocity field is given by:

$$\mathbf{v}' = \mathbf{v} - \mathbf{v}_0 = \frac{a^3}{2r^3}\mathbf{v}_0 - \frac{3a^3(\mathbf{v}_0.\hat{\mathbf{r}})}{2r^3}\hat{\mathbf{r}} \quad (r \geq a). \tag{46}$$

The electric potential associated with flow of a conductive medium is not necessarily harmonic. For this type of ideal fluid flow, however, the electric potential does obey Laplace's equation. From (35) and (40)

$$\begin{aligned}\nabla^2 V &= -\nabla.\mathbf{E} = (\varepsilon - \varepsilon_0)\nabla.(\mathbf{v}\times\mathbf{F})/\varepsilon \\ &= [(\varepsilon - \varepsilon_0)/\varepsilon][\mathbf{F}.(\nabla\times\mathbf{v}) - \mathbf{v}.(\nabla\times\mathbf{F})] = 0,\end{aligned}$$

because **v** is irrotational and **F** is uniform.

Assuming for the moment that there is no applied electric field in the stationary reference frame, from (39) the boundary condition that there is no electric current flow into the cavity implies

$$(\mathbf{j}.\hat{\mathbf{r}})_{r=a} = \sigma[\mathbf{E}'.\hat{\mathbf{r}} + (\mathbf{v}\times\mathbf{F}).\hat{\mathbf{r}}]_{r=a} = 0. \tag{47}$$

Therefore

$$-(\mathbf{E}'.\hat{\mathbf{r}})_{r=a} = \left(\frac{\partial V'}{\partial r}\right)_{r=a} = [(\mathbf{v}\times\mathbf{F}).\hat{\mathbf{r}}]_{r=a}, \tag{48}$$

where $\mathbf{E}' = -\nabla V'$ here is the electric field due to the charge distribution on the cavity wall that is established initially by the Lorentz field associated with the moving medium.

From (45) and (48), the boundary condition is

$$\left(\frac{\partial V'}{\partial r}\right)_{r=a} = \frac{3}{2}\hat{\mathbf{r}}.([\mathbf{v}_0 - (\mathbf{v}_0.\hat{\mathbf{r}})\hat{\mathbf{r}}]\times\mathbf{F}) = \frac{3}{2}\hat{\mathbf{r}}.[\mathbf{v}_0\times\mathbf{F}], \tag{49}$$

since $\hat{\mathbf{r}}.[\hat{\mathbf{r}}\times\mathbf{F}]=0.$

Equation (49) gives a Neumann boundary condition for the external potential. The solution is

$$V'(r \geq a) = -\frac{3a^3}{4r^2}\hat{\mathbf{r}}.(\mathbf{v}_0 \times \mathbf{F}) = -\frac{3a^3}{4r^3}\mathbf{r}.(\mathbf{v}_0 \times \mathbf{F}). \tag{50}$$

The electric potential given by (50) is that of an elementary current dipole in a homogeneous medium of conductivity σ with moment

$$\mathbf{p} = -3\pi\sigma a^3 \mathbf{v}_0 \times \mathbf{F} = -\frac{9\sigma\tau}{4}\mathbf{v}_0 \times \mathbf{F}. \tag{51}$$

The internal potential is determined by the Dirichlet boundary condition that matches the potential across the cavity boundary, yielding

$$V'(r \leq a) = -\frac{3}{4}\mathbf{r}.(\mathbf{v}_0 \times \mathbf{F}). \tag{52}$$

The corresponding internal electric field due to the water flow in the surrounding medium is therefore

$$\mathbf{E}'(r < a) = \frac{3}{4}(\mathbf{v}_0 \times \mathbf{F}). \tag{53}$$

Equation (53) implies that the internal electric field arising from the perturbed water flow is 0.75 times the Lorentz field that pertains to the unperturbed flowing medium.

Differentiating (50) gives the external electric field components due to the water flow around the cavity. Combining these, the anomalous external electric field vector is

$$\mathbf{E}'(r > a) = -\nabla V'(r > a) = \frac{3a^3[\mathbf{v}_0 \times \mathbf{F} - 3\hat{\mathbf{r}}.(\mathbf{v}_0 \times \mathbf{F})\hat{\mathbf{r}}]}{4r^3}. \tag{54}$$

It is obvious from (53)-(54) that only the component of the unperturbed water flow that is perpendicular to the geomagnetic field contributes to the anomalous electric field in and around the cavity.

The average electric field components between symmetrically placed potential electrodes, as measured by a triaxial electrometer, are

$$\overline{E}_x = \frac{V'(-x,0,0) - V'(x,0,0)}{2|x|} = \begin{cases} \dfrac{3a^3(v_y^0 F_z - v_z^0 F_y)}{4|x|^3}, & (|x| \geq a), \\ \dfrac{3(v_y^0 F_z - v_z^0 F_y)}{4}, & (|x| \leq a). \end{cases} \tag{55}$$

$$\overline{E}_y = \frac{V'(0,-y,0) - V'(0,y,0)}{2|y|} = \begin{cases} \dfrac{3a^3(v_z^0 F_x - v_x^0 F_z)}{4|y|^3}, & (|y| \geq a), \\ \dfrac{3(v_z^0 F_x - v_x^0 F_z)}{4}, & (|y| \leq a). \end{cases} \tag{56}$$

$$\overline{E}_z = \frac{V'(0,0,-z) - V'(0,0,z)}{2|z|} = \begin{cases} \dfrac{3a^3(v_x^0 F_y - v_y^0 F_x)}{4|z|^3}, & (|z| \geq a), \\ \dfrac{3(v_x^0 F_y - v_y^0 F_x)}{4}, & (|z| \leq a). \end{cases} \tag{57}$$

As an example, (55)-(57) show that a favorably oriented water flow speed of 1 ms^{-1} in a geomagnetic field of 60 μT produces a substantial internal electric field of up to 45 μVm^{-1}. As the potential electrodes are moved away from the cavity wall, the measured average field decreases from that value to ~5.7 μVm^{-1} at $r = 2a$, i.e. when the electrometer baseline is twice the cavity diameter, and to ~1.7 μVm^{-1} at $r = 3a$. In general an applied electric field is also present and the perturbation of this field by the cavity, which is discussed above, supplements the effects of water flow around the cavity.

There are two contributions to the magnetic effects of flow of a conductive fluid around a measurement capsule. The Lorentz field associated with water flow produces an electric current, which is diverted around the insulating capsule. A magnetic field and associated gradient are produced by this perturbed electric current flow. Additionally, the diversion of water flow around the capsule produces a local perturbation of the Lorentz field, with associated induced currents and a secondary magnetic field. The vortex sources of the magnetic field may be separated into contributions $\mathbf{B}'_E$ from the anomalous conduction current and $\mathbf{B}'_v$ from the perturbation of the water flow, with

$$\nabla \times \mathbf{B}'_E = \mu_0 \sigma \mathbf{E}', \tag{58}$$

$$\nabla \times \mathbf{B}'_v = \mu_0 \sigma \mathbf{v}' \times \mathbf{F}. \tag{59}$$

In (59) the contribution of moving polarized fluid has been neglected, as justified above. The external magnetic field associated with the equivalent current dipole (51) is given by the Biot-Savart law. The result is

$$\mathbf{B}'_E(r \geq a) = \frac{\mu_0(\mathbf{p} \times \mathbf{r})}{4\pi r^3} = \frac{-3\mu_0 \sigma a^3 [(\mathbf{v}_0 \times \mathbf{F}) \times \mathbf{r}]}{4r^3}. \tag{60}$$

The magnetic field lines *due to this effect alone* circulate around an axis of the sphere that is perpendicular to both $\mathbf{v}_0$ and $\mathbf{F}$. The Cartesian components of the magnetic field due to this current dipole are harmonic. The continuation of this field into the cavity is

$$\mathbf{B}'_E(r \leq a) = \frac{-3\mu_0 \sigma [(\mathbf{v}_0 \times \mathbf{F}) \times \mathbf{r}]}{4}. \tag{61}$$

There is an additional contribution to the anomalous magnetic field, however, from the electric current associated with the Lorentz field of the *perturbed* water flow. From (59) it can be seen that, unlike $\mathbf{B}'_E$, the Cartesian components of $\mathbf{B}'_v$ are not harmonic outside the cavity, since

$$\begin{aligned} \nabla \times \nabla \times \mathbf{B}'_v &= \nabla(\nabla.\mathbf{B}'_v) - \nabla^2 \mathbf{B}'_v = -\nabla^2 \mathbf{B}'_v = \mu_0 \sigma \nabla \times (\mathbf{v}' \times \mathbf{F}) \\ &= \mu_0 \sigma [(\mathbf{F}.\nabla)\mathbf{v}' - \mathbf{F}(\nabla.\mathbf{v}') - (\mathbf{v}'.\nabla)\mathbf{F} + \mathbf{v}'(\nabla.\mathbf{F})] \end{aligned} \tag{62}$$

The last three terms on the RHS drop out by (41) and the fact that **F** is uniform. Therefore

$$\nabla^2\mathbf{B}' = \nabla^2\mathbf{B}'_v = -\mu_0\sigma(\mathbf{F}.\nabla)\mathbf{v}'. \tag{63}$$

where $\mathbf{B}'$ is the total anomalous field arising from currents associated with the perturbed electric field and the Lorentz field of the perturbed water flow.

The general solutions of the Poisson equations (63) for the Cartesian components of $\mathbf{B}'$ comprise particular solutions supplemented by harmonic functions. It can be verified by calculating the Laplacian of each of the following equations, and the divergence and curl of the vector formed from all three components, that solutions of (63) that yield the correct divergence and curl everywhere for the total exterior field are

$$\begin{aligned} B'_x = \frac{\mu_0\sigma a^3 v_0}{4r^5}\Big[&F_x x\left(2x^2 - y^2 - z^2\right) \\ &+ \left(F_y y + F_z z\right)\left(5x^2 + 2y^2 + 2z^2\right)\Big], \end{aligned} \tag{64}$$

$$\begin{aligned} B'_y = \frac{\mu_0\sigma a^3 v_0}{4r^5}\Big[&F_x y\left(2x^2 - y^2 - z^2\right) \\ &+ F_y x\left(y^2 - 2x^2 - 2z^2\right) + 3F_z xyz\Big], \end{aligned} \tag{65}$$

$$\begin{aligned} B'_z = \frac{\mu_0\sigma a^3 v_0}{4r^5}\Big[&F_x z\left(2x^2 - y^2 - z^2\right) \\ &+ 3F_y xyz + F_z x\left(z^2 - 2x^2 - 2y^2\right)\Big], \end{aligned} \tag{66}$$

The radial component of $\mathbf{B}'$ is therefore

$$\begin{aligned} B'_r &= \frac{B'_x x + B'_y y + B'_z z}{r} \\ &= \frac{\mu_0\sigma a^3 v_0}{4r^4}\left[F_x\left(2x^2 - y^2 - z^2\right) + 3F_y xy + 3F_z xz\right] \end{aligned} \tag{67}$$

At the surface of the cavity this becomes

$$B_r'(r=a^+) = \frac{\mu_0 \sigma a v_0}{4}\Big[F_x\left(3\cos^2\theta - 1\right) + 3F_y\cos\varphi\sin\theta\cos\theta + 3F_z\sin\varphi\sin\theta\cos\theta\Big]. \tag{68}$$

Within the cavity there are no currents and $\mathbf{B}'$ is therefore derivable from a harmonic scalar potential Ω, i.e.

$$\mathbf{B}' = -\nabla\Omega, \tag{69}$$

where

$$\nabla^2\Omega = -\nabla.\mathbf{B}' = 0. \tag{70}$$

Matching the radial component of the field across the cavity wall gives the Neumann boundary condition:

$$B_r'(r=a^+) = -\left(\frac{\partial\Omega}{\partial r}\right)_{r=a^-}. \tag{71}$$

The solution of (70) subject to (71) is:

$$\begin{aligned}\Omega &= \frac{\mu_0\sigma v_0}{8} r^2\Big[F_x\left(3\cos^2\theta - 1\right) - 3F_y\cos\varphi\sin\theta\cos\theta - 3F_z\sin\varphi\sin\theta\cos\theta\Big] \\ &= \frac{\mu_0\sigma v_0}{8}\Big[F_x\left(2x^2 - y^2 - z^2\right) - 3F_y xy - 3F_z xz\Big].\end{aligned} \tag{72}$$

The internal field components, obtained by differentiation of (72), are therefore

$$\left.\begin{aligned} B_x' &= -\frac{\partial\Omega}{\partial x} = \frac{\mu_0\sigma v_0}{8}\left[-4F_x x + 3F_y y + 3F_z z\right] \\ B_y' &= -\frac{\partial\Omega}{\partial y} = \frac{\mu_0\sigma v_0}{8}\left[2F_x y + 3F_y x\right] \\ B_z' &= -\frac{\partial\Omega}{\partial z} = \frac{\mu_0\sigma v_0}{8}\left[2F_x z + 3F_z x\right] \end{aligned}\right\} \quad (r \le a). \tag{73}$$

and the gradient tensor elements are

$$\left.\begin{aligned}
B'_{xx} &= \frac{-\mu_0 \sigma v_0 F_x}{2} \\
B'_{xy} &= \frac{3\mu_0 \sigma v_0 F_y}{8} \\
B'_{xz} &= \frac{3\mu_0 \sigma v_0 F_z}{8} \\
B'_{yy} &= \frac{\mu_0 \sigma v_0 F_x}{4} \\
B'_{yz} &= 0 \\
B'_{zz} &= \frac{\mu_0 \sigma v_0 F_x}{4}
\end{aligned}\right\} \quad (r \le a). \tag{74}$$

Since $\mathbf{B}'$ as given by (64)-(66), (73) is continuous, has the correct divergence and curl everywhere, and is regular at the origin and at infinity, it represents the unique solution to the boundary value problem. Note that the internal field components vary linearly with the Cartesian co-ordinates and that the internal gradient is uniform.

The contributions of water flow parallel to the geomagnetic field (which produces no background Lorentz field) and perpendicular to the geomagnetic field produce different configurations of the anomalous electric and magnetic fields in and around the cavity. For water flow parallel to **F**, there is no anomalous electric field. The magnetic field arises solely from the diversion of water flow around the cavity, producing flow components that are not parallel to **F**. The electric currents induced by this flow circulate about the x_1 axis (parallel to $\mathbf{v}_0$ and **F**) and effectively simulate a gradient coil set, with coils in series opposition, wound around the cavity. The magnetic field is rotationally symmetric about $\mathbf{v}_0$ and **F**. Fig.3 shows the resulting magnetic field pattern.

For the component of water flow that is perpendicular to **F** the internal magnetic field lines are confined to planes perpendicular to $\mathbf{v}_0 \times \mathbf{F}$, and the only nonzero gradient tensor element is B_{xy}, if y is taken to be parallel to **F**. The internal magnetic field lines are hyperbolas given by $x^2 - y^2 = \pm C^2$ (see Fig.4). The external field configuration is more complex than for the case of $\mathbf{v}_0$ parallel to **F**, but the overall field fall-off is $1/r^2$ for all cases. From (64)-(66) and (73)-(74), the magnetic effects of seawater flow can be substantial. For example, for a geomagnetic field of 60 μT and a cavity of radius 0.5 m within a 1 ms^{-1} flow, the field perturbation adjacent to the cavity boundary is up to ~75 pT and the gradients are of the order of 150 pT/m.

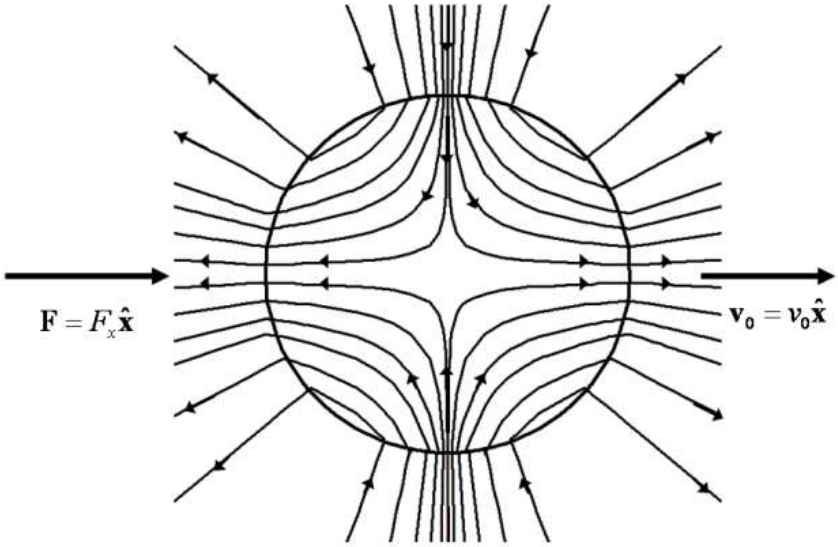

Fig.3. Lines of anomalous magnetic field within and around a spherical cavity due to the water flow component parallel to the geomagnetic field. The view is a section containing $\mathbf{v}_0$ and **F**, through the centre of the sphere. The field is rotationally symmetric about the *x* axis. Inside the cavity the gradient is uniform, with maximum gradient parallel to the *x* axis.

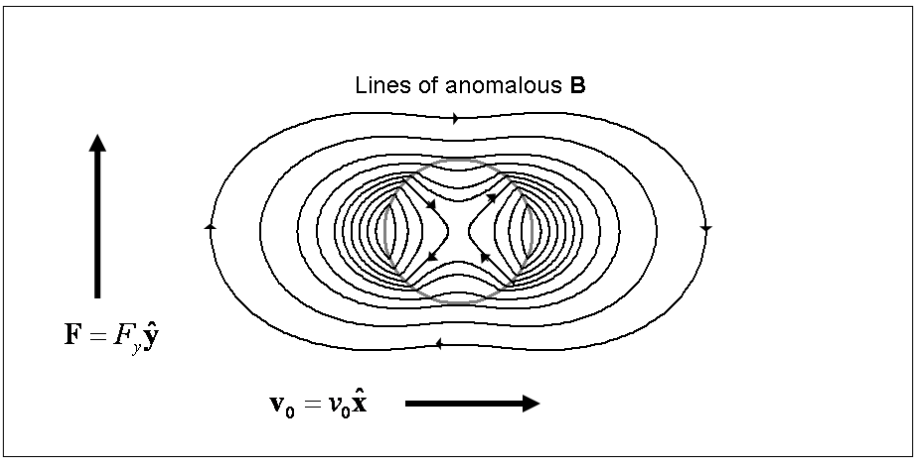

Fig.4. Lines of anomalous magnetic field within and around a spherical cavity due to the water flow component perpendicular to the geomagnetic field. The view is a section containing $\mathbf{v}_0$ and **F**, through the centre of the sphere. Inside the cavity the only nonzero gradient tensor element is B_{xy} , which is uniform, and gradients perpendicular to the section are zero.

CONCLUSIONS

This study has shown that perturbation of electric and magnetic fields and gradients by the measurement process is significant in the marine environment. Accurate measurements require corrections for diversion of electric currents and water flow around measurement capsules. This has implications for marine magnetotelluric and CSEM measurements and for magnetic tensor gradiometry surveys in the ocean.

ACKNOWLEDGMENTS

This study has been carried out for the CSIRO Wealth from Oceans Flagship. I thank my colleagues Jeanne Young and Peter Watterson for commenting on the manuscript. This work represents a contribution to a Ph.D. undertaken by the author at Macquarie University, under the supervision of Prof. Richard Flood and Dr Mark Lackie.

REFERENCES

[1] O.D. Kellog, *Foundations of Potential Theory*, New York: Dover, 1953, pp.184-188.

[2] J.A. Stratton, *Electromagnetic Theory*, New York: McGraw-Hill, 1941, pp. 58-59.

[3] D.A. Clark, D.W. Emerson, and S.J. Saul, "Magnetic and gravity anomalies of a triaxial ellipsoid", *Exploration Geophysics*, vol. 17, pp. 189-200, 1986.

[4] M.B. Kraichman, *Handbook of Electromagnetic Propagation in Conducting Media*, U.S. Headquarters Naval Material Command, NAVMAT P-2302, pp. 3-1,3-2, 1970.

[5] E.A. Lima, A. Irimia, and J.P. Wikswo, "The magnetic inverse problem", in *The SQUID Handbook*, Vol. II , J. Clarke and A.I. Braginski, Eds. Weinheim, Wiley-VCH, 2006, pp.139-267.

[6] T.B. Sanford, " Motionally induced electric and magnetic fields in the sea," *J. Geophys. Res.*, Vol. 76, pp. 3476-3492, 1971.

[7] W.K.H. Panofsky and M. Phillips, *Classical Electricity and Magnetism*, 2nd Edition. Reading, Massachusetts: Addison-Wesley, 1962, p. 164.

CHAPTER 7: NEW APPROACHES TO DEALING WITH REMANENCE: MAGNETIC MOMENT ANALYSIS USING TENSOR INVARIANTS AND REMOTE DETERMINATION OF *IN SITU* MAGNETISATION USING A STATIC TENSOR GRADIOMETER

Clark, D.A., 2013. New approaches to dealing with remanence: magnetic moment analysis using tensor invariants and remote determination of *in situ* magnetisation using a static tensor gradiometer (Extended Abstract), ASEG-PESA Conference, Melbourne.

SUMMARY

Assuming without evidence that magnetic sources are magnetised parallel to the geomagnetic field can seriously mislead interpretation and can result in drill holes missing their targets. I present two new methods for providing information about magnetisation of anomaly sources, independent of the geometry of the causative bodies. The first method is based on analysis of magnetic gradient tensor data. Integral moments of tensor invariants locate the horizontal and vertical centres of magnetisation and estimate the magnetisation direction. The depth estimate allows correction of the integral moments for the finite range of integration, which can accordingly be restricted to the main part of the anomaly. This reduces interference from neighbouring sources. This method provides information on location, total magnetic moment (magnetisation × volume), and magnetisation direction of a compact source, without making any assumptions about its shape.

The second method employs a single combined gradiometer/magnetometer, operating in base station mode within a magnetic anomaly of interest. The response to geomagnetic time variations allows the contributions of induced magnetisation and remanence to the anomaly to be separated. This method allows remote estimation, prior to drilling of (i) the total magnetisation direction of the source, which is a key to accurate modelling (ii) the remanence direction, which can provide geological information such as age of intrusion or alteration, (iii) the Koenigsberger ratio Q, which is indicative of the magnetic mineralogy of the source. If the source is compact, the method also provides a direct indication of the direction to its centroid.

Key words: magnetisation, remanence, tensor invariants, normalised source strength, geomagnetic variations

INTRODUCTION

A major source of ambiguity in interpretation of magnetic survey data lies in the fact that the physical property contrast that produces the observed magnetic anomalies is a vector, the magnetisation, which may in principle have any orientation. In the absence of independent information about source magnetisation, magnetic modelling usually proceeds on the assumption that the source is magnetised parallel to the local geomagnetic field. However, if the source magnetisation direction differs significantly from the present field direction, due to remanent magnetisation or strong anisotropy, models that fit the data may be grossly in error. For example, interpreted dips of sheet-like bodies and plunges and locations of pipes will be erroneous, with serious consequences for drill targeting. For highly magnetic sources, self-demagnetisation effects may cause similar problems.

This paper presents two methods for analysis of individual magnetic anomalies that allow remote estimation of source magnetisation, while making minimal assumptions about source geometry. The first method relies on integral moments, calculated over a measurement plane, of tensor invariants. These invariants are calculated from magnetic gradient tensor data, which can be either measured directly or derived from high quality conventional magnetic surveys through Fourier filtering or equivalent source techniques.

The integral moments yield estimates of the horizontal and vertical location of the source centroid, the total magnetic moment (magnetisation $\times$ volume), and the magnetisation direction. Although integral moment methods are based on integrals calculated over the entire horizontal plane, the centroid depth estimate can be corrected for the finite radius of integration. Once this depth is known, the integral moments of vector and tensor components, as used in Helbig (1963) analysis and its offshoots, can also be accurately corrected for the finite radius of integration, allowing numerical integrations to be confined to the main part of the anomaly, thereby reducing contamination of the integral moments by neighbouring sources and greatly improving parameter estimation.

Provided the area of integration extends well beyond the horizontal dimensions of the source, and the source can be assumed to be depth limited, with bottom depth comparable to the radius of integration or smaller, integral moment methods are in principle independent of source geometry. With the above caveats, estimated parameters are quite

robust and do not depend on assumptions about source shape and size. The method is sensitive, however, to erroneous base levels in the vector and tensor components, and to regional trends, which must be removed before applying the method.

The second method is a variant of the differential vector magnetometry (DVM) approach of Clark et al. (1998), which is only now becoming feasible due to improving sensor technology. The original DVM method employs two carefully aligned vector magnetometers, operating in base station mode, with one placed within a magnetic anomaly of interest and the other outside the anomaly to monitor unperturbed geomagnetic time variations. The new method replaces the two vector magnetometers with a single gradiometer plus magnetometer package, placed within an anomaly of interest. The response to geomagnetic time variations allows the contributions of induced magnetisation and remanence to the anomaly to be separated. This method allows remote estimation, prior to drilling of (i) the total magnetisation direction of the source, which is a key to accurate modelling (ii) the remanence direction, which can provide geological information such as age of intrusion or alteration, (iii) the Koenigsberger ratio Q, which is indicative of the magnetic mineralogy of the source. If the source is compact, the method also provides a direct indication of the direction to its centroid.

With current measurement capabilities the modified DVM method can be applied to anomalies for which contribution of induced magnetisation to the anomalous field and gradient is sufficiently large (>100 nT and > 1 pT/m respectively), by monitoring geomagnetic time variations (diurnal, pulsations, substorms etc.) of tens of nT. Given an adequate signal-to-noise ratio, the estimated magnetic properties are completely independent of any assumptions about source geometry, including bodies of effectively infinite depth extent. Thus this method can in principle resolve pathological cases of ambiguity associated with 2D dipping sheets and axially magnetised plunging pipes of great depth extent.

METHOD I: INTEGRAL MOMENTS OF TENSOR INVARIANTS AND COMPONENTS

Helbig (1963) showed that it was possible in principle to determine the magnetic moment vector of an arbitrary finite source by calculating various integral moments of magnetic

vector components over an entire horizontal plane above the source. This method was largely neglected over subsequent decades, probably because vector data were rarely available. Schmidt and Clark (1997, 1998) revived the method, with some modifications, by applying it to vector components calculated by Fourier processing of a conventional TMI survey. Since then, a number of researchers, including Phillips (2005), Li et al. (2004), Foss (2006), and Caratori Tontini and Pedersen (2008), have developed and applied this concept. Phillips et al. (2007) extended the analysis to integral moments of the magnetic gradient tensor.

Consider an isolated source with magnetisation **M**, which produces an anomalous field vector **b**. The anomalous magnetic gradient tensor **B** is a symmetric traceless second order tensor (Pedersen and Rasmussen, 1990) given by the vector gradient of **b**. Rotational invariants of the tensor, such as the canonical invariants I_1, I_2 of Pedersen and Rasmussen (1990), can always be expressed in terms of the eigenvalues of the tensor. The normalised source strength (NSS) μ is a particularly useful invariant, because it is completely independent of magnetisation direction for a number of simple, but useful source types: spheres, compact sources that can be represented by a dipole, axially magnetised thin pipes, and 2D sources of arbitrary shape (Beiki et al. 2012; Clark, 2012a,b,c), and is only weakly dependent on magnetisation direction for 3D sources in general (Pilkington and Beiki, 2012). The NSS is defined by

$$\mu = \sqrt{-\lambda_2^2 - \lambda_1\lambda_3}, \qquad (1)$$

where $\lambda_1 \geq \lambda_2 \geq \lambda_3$ are the eigenvalues of the tensor in nonincreasing order, which sum to zero due to the tracelessness of the tensor. For a dipole source at (x_0, y_0, h) the NSS takes the simple form

$$\mu = \frac{3Cm}{r^4} = \frac{3Cm}{[(x-x_0)^2 + (y-y_0)^2 + h^2]^2}, \qquad (2)$$

where $C = \mu_0/4\pi$, m is the magnitude of the magnetic moment **m** and r is the distance from the dipole to the measurement point (x,y,0). Clearly from equation 2, the NSS measured over a plane peaks directly over a dipole source (where r is a minimum) and is independent of orientation of **m**. The depth of the dipole is simply related to the halfwidth of the NSS

anomaly. This suggests that measurements of μ over a plane can provide robust estimates of dipole location, unaffected by magnetisation direction.

The intermediate eigenvalue λ_2 for a dipole source is given by Clark (2012b) as

$$\lambda_2 = \mu \cos\phi = \frac{3C\mathbf{m}.\hat{\mathbf{r}}}{r^4}, \tag{3}$$

where ϕ is the angle between the magnetic moment vector and the displacement vector **r** from the dipole to the observation point. Equation 3 shows that λ_2 depends on the orientation of the moment, and therefore can provide information about the magnetisation direction.

The horizontal location (x_0, y_0) of the centre of magnetisation can be estimated from first integral moments of μ or μ^2:

$$x_0 = \frac{\int_{-\infty}^{+\infty}\int_{-\infty}^{+\infty} x\mu dxdy}{\int_{-\infty}^{+\infty}\int_{-\infty}^{+\infty} \mu dxdy} = \frac{\int_{-\infty}^{+\infty}\int_{-\infty}^{+\infty} x\mu^2 dxdy}{\int_{-\infty}^{+\infty}\int_{-\infty}^{+\infty} \mu^2 dxdy}, \tag{4}$$

$$y_0 = \frac{\int_{-\infty}^{+\infty}\int_{-\infty}^{+\infty} y\mu dxdy}{\int_{-\infty}^{+\infty}\int_{-\infty}^{+\infty} \mu dxdy} = \frac{\int_{-\infty}^{+\infty}\int_{-\infty}^{+\infty} y\mu^2 dxdy}{\int_{-\infty}^{+\infty}\int_{-\infty}^{+\infty} \mu^2 dxdy}. \tag{5}$$

In practice the numerical integration is carried out over a finite area to obtain initial estimates of (x_0, y_0). The area of integration is then centred on this point and the integrals recalculated to make any necessary small corrections to the location, which is subsequently used as the origin of coordinates for calculation of all other integral moments. The depth of the centre of magnetisation, h, can be found from

$$h = \frac{\int_{-\infty}^{+\infty}\int_{-\infty}^{+\infty} \mu dxdy}{\left[3\pi \int_{-\infty}^{+\infty}\int_{-\infty}^{+\infty} \mu^2 dxdy\right]^{1/2}}, \tag{6}$$

The magnitude of the magnetic moment, m, is given by

$$m = \frac{\left[\int_{-\infty}^{+\infty}\int_{-\infty}^{+\infty} \mu dxdy\right]^3}{9\pi^2 C \int_{-\infty}^{+\infty}\int_{-\infty}^{+\infty} \mu^2 dxdy}. \tag{7}$$

Equations 4-7 are exact for a point dipole source, which is equivalent to a uniformly magnetised sphere, and are also very accurate for compact sources of arbitrary shape and for fairly equidimensional sources buried at moderate depths, for which the dipole contribution dominates the anomaly. The horizontal location of the centre of magnetisation is also well estimated, even for sources of complex geometry, due to the high centricity of the NSS over arbitrary 3D sources (Pilkington and Beiki, 2012). The depth of the centre of magnetisation can be expected to be reasonably accurate, provided the depth extent of the source is smaller than the radius of integration.

Corrections of the calculated integrals for the finite ranges of x and y are necessary to account for the tails of the anomaly, which are buried in noise, obscured by interfering anomalies or may lie outside the survey area. The first step is to correct the initial estimated depth of the centroid, h', obtained from equation 6 when the integration is perfomed over a disc of radius R:

$$h' = \frac{\iint_{\rho<R} \mu\rho d\rho d\vartheta}{\left[3\pi \iint_{\rho<R} \mu^2 \rho d\rho d\vartheta\right]^{1/2}} = R\sqrt{\frac{1+(R/h)^2}{3+3(R/h)^2+(R/h)^4}}. \tag{8}$$

In equation 8 ρ and ϑ are polar coordinates centred on (x_0, y_0). Solving equation 8 for the true depth h in terms of the known quantities R and h' gives

$$h = h'\sqrt{\frac{2}{1-3(h'/R)^2+\sqrt{1-2(h'/R)^2-3(h'/R)^4}}}. \tag{9}$$

Once the true depth of the centroid has been estimated, all other integral moments used in the subsequent analysis can be corrected for the finite area of integration using analytic integrals based on the theoretical fall-off rate of a point dipole anomaly, as done for conventional Helbig analysis by Schmidt and Clark (1998) and Caratori Tontini and Pedersen (2008).

While it is often more convenient to carry out 2D integrations over square or rectangular areas, rather than discs, it turns out that the corrections for finite discs and for squares of equivalent area (with side $X = R\sqrt{\pi}$) are almost identical for the integral moments of interest, differing by at most about 1% over a wide range of R/h. Therefore the corrections based on discs of integration, which are much easier to calculate, can be used, even though the integrations are performed using square windows.

The corrected magnitude of the magnetic moment, based on the initial estimate m' is

$$m = m'[1 + 3(h/R)^2 + 3(h/R)^4]. \tag{10}$$

The corrected components of the magnetic moment **m** = (m_x, m_y, m_z) are given by

$$m_x = \frac{h}{2\pi C}\int_{-\infty}^{+\infty}\int_{-\infty}^{+\infty}(x - x_0)\lambda_2 dxdy = \frac{h}{2\pi C}\frac{\int_0^{2\pi}\int_0^{R}(x - x_0)\lambda_2 \rho d\rho d\theta}{1 - \frac{1 + 3R^2/2h^2}{\left(1 + R^2/h^2\right)^{3/2}}}, \tag{11}$$

$$m_y = \frac{h}{2\pi C}\int_{-\infty}^{+\infty}\int_{-\infty}^{+\infty}(y - y_0)\lambda_2 dxdy = \frac{h}{2\pi C}\frac{\int_0^{2\pi}\int_0^{R}(y - y_0)\lambda_2 \rho d\rho d\theta}{1 - \frac{1 + 3R^2/2h^2}{\left(1 + R^2/h^2\right)^{3/2}}}, \tag{12}$$

$$m_z = -\frac{h^2}{2\pi C}\int_{-\infty}^{+\infty}\int_{-\infty}^{+\infty}\lambda_2 dxdy = -\frac{h^2}{2\pi C}\frac{\int_0^{2\pi}\int_0^{R}\lambda_2 \rho d\rho d\theta}{\left[1 - \frac{1}{\left(1 + R^2/h^2\right)^{3/2}}\right]} \tag{13}$$

Note that the declination of the magnetisation, given by dec = atan2(m_x,m_y), is independent of the radius of integration (provided the integral is centred correctly above the source). On the other hand, the inclination of the magnetisation, given by $I = \sin^{-1}(m_z/m)$, requires a correction for the finite range of integration.

METHOD I: FIELD EXAMPLE

The methodology outlined in the previous section has been applied to analysis of publicly available aeromagnetic data from northern NSW, over the southern part of the Thompson Fold Belt. Anomalies over inferred intrusions, corresponding to four prominent discrete equidimensional anomalies within a relatively subdued background field, have been studied in detail. Pratt et al. (2012) modelled the sources of these anomalies, which they labelled Pipes A-D, and estimated magnetisations of the causative bodies. The northern pair of pipes are clearly reversely magnetised (Figure 1), indicating that their magnetisations are dominated by reverse polarity remanence, whereas the southern pair of anomalies (Figure 2) have magnetisations of normal polarity, making the presence of remanence less obvious. However, detailed analysis of these latter anomalies shows that their magnetisations are somewhat oblique to the present field direction, showing that remanence also contributes to the total magnetisation of these bodies.

Vector and gradient tensor components were calculated from the gridded TMI data by Fourier filtering, as described by Schmidt and Clark (1998). Grids of tensor invariants were then calculated from the tensor elements. Figure 3 shows images of the invariants μ and λ_2 over the northernmost anomaly (Pipe A). The NSS is almost radially symmetric and lies within a very quiet background, implying that the source is isolated and compact, with minimal interference from neighbouring anomalies, hence it is ideal for application of Helbig-type analyses. NSS anomalies for the other pipes are qualitatively very similar. The centroid of the source is inferred to lie directly beneath the centre of the NSS anomaly. The negative sign of the λ_2 anomaly indicates that the magnetisation is reversed and its slight asymmetry suggests that the magnetisation is steep, but slightly off vertical.

Source centroid locations and magnetic moments were calculated using equations (4)-(13) for each of the four anomalies. The results were then compared with parameters obtained using several other methods:

A. conventional Helbig analysis based on integral moments of vector components,
B. Helbig-type analysis of gradient tensor elements, following Phillips et al. (2007),
C. point-by-point inversion of the anomalous vectors and tensors as described by Clark et al. (2009) and Clark (2012a,b),
D. quadratic regressions of $1/\sqrt{\mu}$ versus x and y, which from equation 2, yield estimates of x_0, y_0, h, m.
E. linear regressions of $1/\sqrt{\mu}$ versus x, y, and $\rho^2 = x^2+y^2$ which from equation 2, yield radially averaged estimates of x_0, y_0, h, m.
F. source location based on the vector gradient of the NSS (Clark, 2012b)
G. the inversion results of Pratt et al. (2012).
H. Table 1 summarises the results obtained for the four pipes using method I of the previous section.

Table 1. Inverted parameters for Pipes A-D using Method I

Parameter	PIPE A	PIPE B	PIPE C	PIPE D
x_0 (mN)	6693498	6691678	6675979	6673529
y_0 (mE)	476931	476293	504074	505905
h (m)	312	287	547	741
m (Am²)	1.09×10^8	1.06×10^8	1.34×10^8	3.88×10^8
m_x (Am²)	2.42×10^6	-2.54×10^7	2.57×10^7	1.31×10^7
m_y (Am²)	2.77×10^7	-5.39×10^6	3.38×10^6	2.55×10^7
m_z (Am²)	7.42×10^7	7.43×10^7	-9.84×10^7	-2.83×10^8
m* (Am²)	7.92×10^7	7.84×10^7	1.02×10^8	2.84×10^8
Dec (°)	85.0	192.4	7.5	62.8
Inc (°)	+69.5	+71.4	–75.2	–84.2

*magnitude of moment calculated from components of m

Table 2 compares magnetisation directions obtained using method I, methods A-C and the inversion results (G). All the other methods give quite good agreement with the directions from the inversion model, which are assumed to be accurate due to the good fits to the data and the palaeomagnetic plausibility of the results. Directions from tensor Helbig analysis (method C) are inherently insensitive to the radius of integration and agree particularly well with the inversion results, but accurate estimates of moment magnitudes depends on a substantial correction that requires accurate estimation of h using method I. Caratori Tontini and Pedersen (2008) suggested a method for estimating the centre of magnetisation from second order integral moments of vector components, but it fails to estimate depths

correctly for this data set, possibly because of the steepness of the magnetisations and the large corrections required for finite integration area because of the slow fall-off of the integrands.

All methods indicate moments of about 10^8 Am² for pipes A-C and a somewhat larger moment, ~3 $\times 10^8$ Am², for pipe D. Methods C-F, which directly estimate source location are in good agreement for both horizontal location and depth. Table 3 compares magnetic moment and depth estimates for all pipes. Note that Pratt et al. (2012) give depths to the tops of the modelled pipes, not depths to centroids. Twice the difference between the two depths may give an indication of the depth extent of the pipes.

Table 2. Directions of resultant magnetisation of northern NSW pipes obtained using different methods

Method	Direction of magnetisation: dec°, inc°; (angular difference from inversion result °)			
	PIPE A	**PIPE B**	**PIPE C**	**PIPE D**
Method I (this paper)	85.0, +69.5; (12.6)	192.4, +71.4; (11.4)	7.5, –75.2; (7.6)	62.8, –84.2; (10.8)
A (vector Helbig)	58.6, +65.0; (4.8)	219.5, +58.1; (15.4)	226.9, –83.3; (19.9)	219.5, –78.2; (15.5)
B (tensor Helbig)	60.7, +63.4; (3.0)	222.9, +64.2; (9.1)	349.2, –80.6; (7.3)	332.2, –83.6; (2.1)
C (vector-tensor invers.)	60.8, +71.6; (11)	208.6, +61.8; (13.6)	350.4, –70.9; (4.3)	344.8, –83.7; (3.3)
G (inversion model)	63.3, +60.5; (0)	229.6, +73.0; (0)	337.2, –74.1; (0)	321.5, –82.0; (0)

Table 3. Magnetic moment and depth estimates for northern NSW pipes obtained using different methods

Method	**PIPE A** ***m*** **(Am²);** ***h*** **(m)**	**PIPE B** ***m*** **(Am²);** ***h*** **(m)**	**PIPE C** ***m*** **(Am²);** ***h*** **(m)**	**PIPE D** ***m*** **(Am²);** ***h*** **(m)**
Method I (this paper)	$9.4 \pm 1.5 \times 10^7$; 312	$9.2 \pm 1.4 \times 10^7$; 287	$1.02 \pm 0.16 \times 10^8$; 547	$2.84 \pm 0.52 \times 10^8$; 741
A (vector Helbig)	9.2×10^7; -	9.2×10^7; -	1.2×10^8; -	3.2×10^8; -
B (tensor Helbig)	9.9×10^7; -	9.0×10^7; -	1.0×10^8; -	3.6×10^8; -
C (vector-tensor invers.)	8.1×10^7; 279	8.6×10^7; 313	1.4×10^8; 594	2.3×10^8; 660
D ($1/\sqrt{\mu}[x,y, x^2,y^2]$)	1.1×10^8; 276	1.4×10^8; 211	1.6×10^8; 554	2.5×10^8; 653
E ($1/\sqrt{\mu}[x,y, \rho^2]$)	8.9×10^7; 278	9.1×10^7; 257	1.2×10^8; 554	2.5×10^7; 653
G (inversion model)	-; 160*	-; 115*	-; 370*	-; 470*

*depths to top of models (not centroids)

METHOD II: USING A STATIC GRADIOMETER TO DETERMINE MAGNETISATION

The second method presented here extends the theory given by Clark et al. (1998) to exploit the sensitivity of SQUID-based magnetometers and gradiometers to detect local perturbations of anomalies associated with time-varying magnetisation induced by geomagnetic variations. Figure 4 illustrates the principle of the method. Clark et al. (1998)

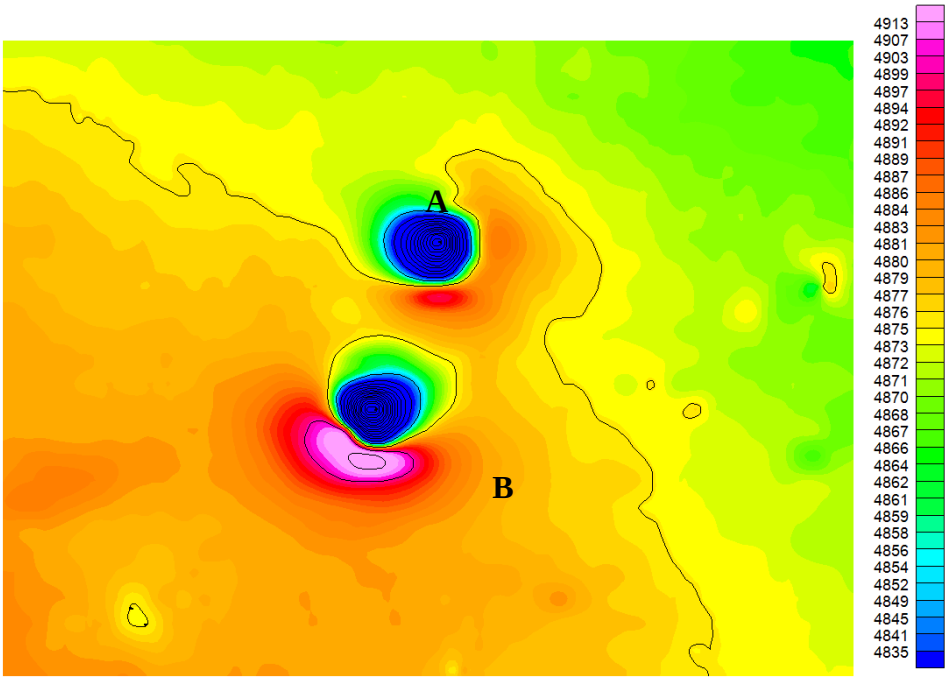

Figure 1. TMI anomalies over the northern pair of pipes (A & B of Pratt et al. (2012)), showing evident reversed polarity. Normalised colour stretch, contour interval is 25 nT.

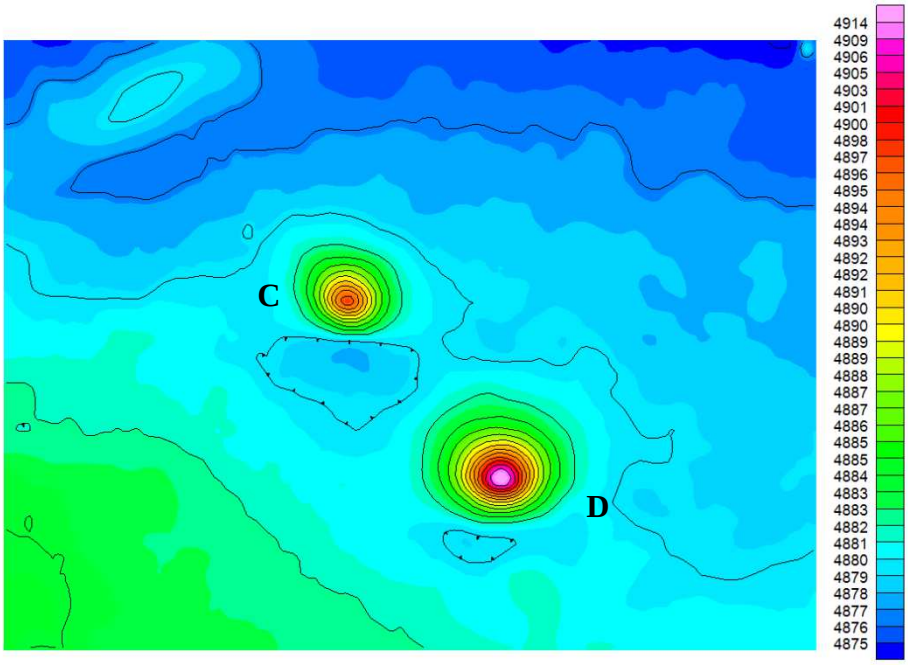

Figure 2. TMI anomalies over the southern pair of pipes (C & D of Pratt et al. (2012)), showing subtle signs of normal polarity magnetisation steeper than the present field. Linear colour stretch, contour interval is 10 nT.

showed that the anomalous field vector **b**, measured at a fixed location within the anomaly, is related to the source magnetisation vector **J** by the matrix equation

$$\mathbf{b} = \mathbf{A}\mathbf{J}, \tag{14}$$

where **A** is the second order gradient tensor of the pseudo-gravitational potential. The susceptibility is assumed to be isotropic and the magnetisation of the source is assumed to be uniform, at least in direction. **A** depends on the geometry and location of the source, but is independent of the magnetisation. A geomagnetic variation $\delta\mathbf{F}$ produces a change $\delta\mathbf{J} = k\delta\mathbf{F}$ in the induced magnetisation, which also equals the change in the resultant magnetisation $\mathbf{J}_{\text{res}}$, because the remanence is unaffected. This in turn produces a change in the anomalous field and its gradient. By continuously monitoring geomagnetic variations and gradient perturbations the contributions of induced and remanent magnetisations can be separated. Fluctuations in the vertical gradients of **b**, for example, are given by

$$\delta\left(\frac{\partial\mathbf{b}}{\partial z}\right) = \frac{\partial\mathbf{A}}{\partial z}\delta\mathbf{J} = k\frac{\partial\mathbf{A}}{\partial z}\delta\mathbf{F}. \tag{15}$$

Time series of the gradients and $\delta\mathbf{F}$ yield least squares estimates of the elements of $k\partial\mathbf{A}/\partial z$. The resultant magnetisation of the source, divided by the unknown susceptibility, can then obtained by inverting the relationship, analogous to equation (14), between the gradient anomaly and the resultant magnetisation

$$\mathbf{J}_{\text{res}}/k = \left(k\frac{\partial\mathbf{A}}{\partial z}\right)^{-1}\frac{\partial\mathbf{b}}{\partial z}. \tag{16}$$

Equation (16) determines the direction of the resultant magnetisation, which is crucial information for accurate modelling, but not its absolute magnitude. Similar analysis of the orthogonal gradients provides data redundancy, allowing consistency checks and improving error estimates. Because the direction of the induced magnetisation is known, the direction of remanence and the Koenisberger ratio Q can also be calculated, using

$$(\mathbf{J}_{\text{rem}}/k) = (\mathbf{J}_{\text{res}}/k) - \mathbf{F}, \tag{17}$$

$$Q = \left|\mathbf{J}_{\text{rem}}\right| / kF = \left|\mathbf{J}_{\text{rem}} / k\right| / F. \quad (18)$$

As noted by Clark et al. (1998) eigenvector analysis of the matrix **A** (or its derivatives) can also provide a direct indication of the direction towards the centroid of a compact source.

The original differential vector magnetometry method trialled by Clark et al. (1998) required two sensitive vector magnetometers, separated by hundreds of metres and aligned to within seconds of arc. The method proposed here requires only a single rigidly mounted package containing a vector magnetometer and gradiometer, that can be placed anywhere within the anomaly and monitored over several hours to allow sufficient geomagnetic field variation. The Superconductivity and Magnetism Group at CSIRO Materials Science and Engineering is adapting a sensitive high-temperature SQUID magnetometer and tensor gradiometer package with gradient sensitivity of about 2 pT/m, developed for underwater UXO detection (Young et al., 2010), for this purpose. Field trials using this instrument are planned for April 2013.

CONCLUSIONS

Value can be added to existing high quality TMI surveys by calculating vector and tensor components and using methods developed for analysis of these types of data, although direct measurement of the gradient tensor is optimal (Clark, 2012a,b,c). For relatively isolated anomalies, analysis of integral moments of tensor invariants, particularly the normalised source strength and the intermediate eigenvalue (method I), provides useful information on source location, direction of magnetisation and total magnetic moment, even when the numerical integrations are restricted to the main portion of the anomaly. The horizontal location of the centre of magnetisation is very robust, particularly when determined from the first integral moment of μ^2, and for compact sources the depth of the centroid can be reliably estimated when a correction for the finite radius of integration is made. The centroid depth is not only important in its own right, but is a crucial parameter for applying corrections to Helbig-type analyses of vector and tensor components, which are in principle independent of source shape (for finite sources).

Magnetic moment vectors estimated using method I and other Helbig-type analyses yield directions of the resultant magnetisation (remanent plus induced), which is crucial for

accurate modelling, and give an indication of the size of the source, when plausible magnetisation intensities are assumed.

Method I, like all Helbig-type analyses, is not applicable to sources of great depth extent relative to the resolvable width of the anomaly. Vertical pipe-like bodies, not necessarily narrow or equidimensional, can be analysed by applying these methods to vertical derivatives of the field and/or tensor components and invariants derived from them (Clark, 2012b).

Method II uses time series of vector and gradient measurements to determine the following properties w*ithout making any assumptions about source geometry or location*:

1. direction of total magnetisation (required for accurate modelling; eliminates most ambiguity),
2. direction of remanence, which provides useful geological information such as age of formation or alteration,
3. Koenigsberger ratio Q, which gives information on the magnetic mineralogy of the source,
4. total magnetic moment of a compact source, which is analogous to the total anomalous mass inferred from a gravity anomaly and can indicate probable size of the source for plausible magnetisation strengths,
5. a direct indication of direction to a compact source, which can be used to site initial drill holes,
6. depth and horizontal location of the centroid of a compact source from two stations, occupied simultaneously or consecutively.

Points 1-4 can assist prioritisation of targets prior to drilling and points 1 and 4-6 aid in drill targeting. Method II is not restricted to sources of limited depth extent, allowing it to resolve pathological cases of ambiguity associated with 2D dipping sheets and axially magnetised plunging pipes of great depth extent. However, for sources of great strike extent that are effectively 2D, only the components of magnetisation in the plane normal to strike (which are the only contributors to the observed anomaly) can be determined.

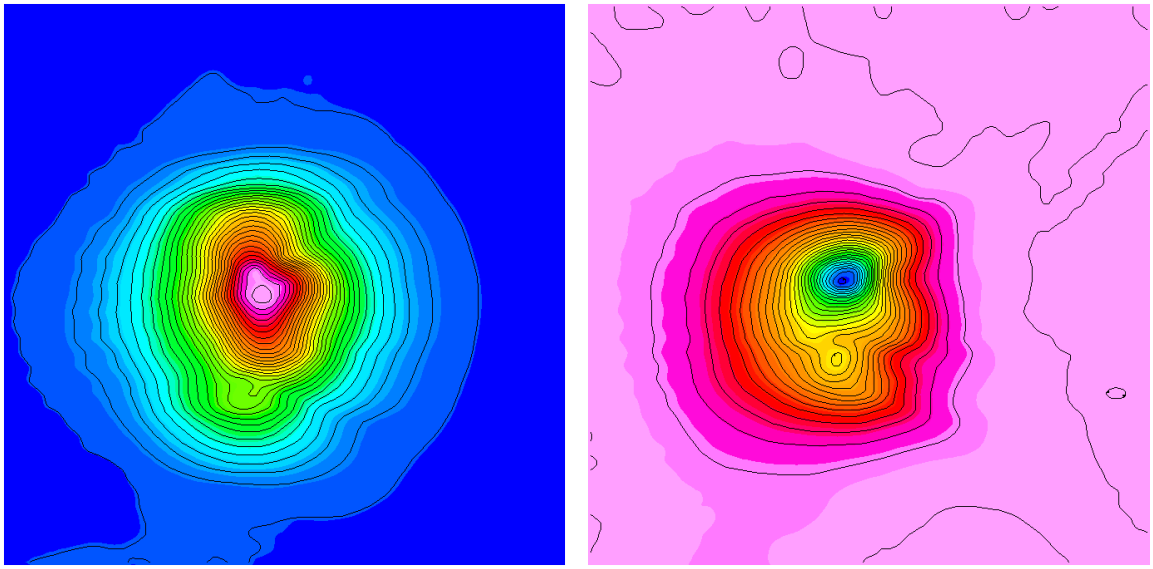

Figure 3. Tensor invariants over Pipe A. LHS is the NSS μ, RHS is the intermediate eigenvalue λ_2. Contour inteval for both is 50 pT/m.

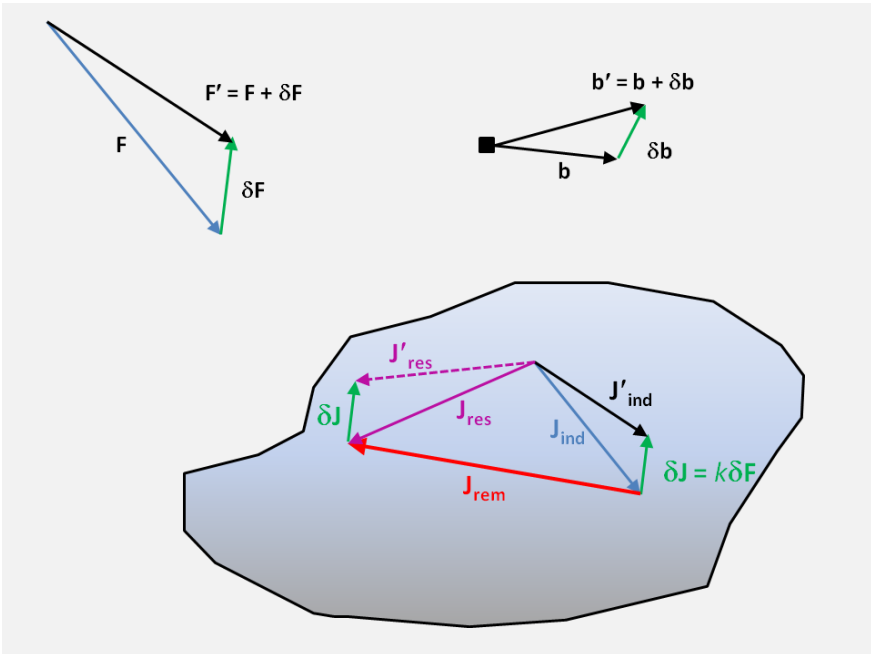

Figure 4. Principle of remote determination of *in* situ magnetic properties. The regional geomagnetic field F undergoes a fluctuation δF, which perturbs the induced magnetisation J_{ind}, but does not affect the contribution of remanence J_{rem} to the resultant magnetisation J_{res}. The change in source magnetisation produces a change in the observed field and its gradient within the anomaly.

ACKNOWLEDGMENTS

I thank Clive Foss for providing grids of vector and tensor components over the Brewarrina survey pipes. Clive Foss, Dean Hillan and Keith Leslie reviewed the manuscript. This work represents a contribution to research for a PhD at Macquarie University, under the supervision of Drs Mark Lackie and Richard Flood.

REFERENCES

Beiki, M., Clark, D.A., Austin, J.R. and Foss, C.A., 2012a, Estimating source location using normalized magnetic source strength calculated from magnetic gradient tensor data: Geophysics, **77**(6), J23-J37.

Caratori Tontini, F. and Pedersen, L.B., 2008, Interpreting magnetic data by integral moments: Geophysical Journal International, **174**, 815-824.

Clark, D.A., 2012a, New methods for interpretation of magnetic gradient tensor data: ASEG 22nd International Geophysical Conference and Exhibition, 26-29 February 2012, Brisbane, Australia, Expanded Abstracts, 11p.

Clark, D.A., 2012b, New methods for interpretation of magnetic vector and gradient tensor data I: eigenvector analysis and the normalised source strength: Exploration Geophysics, **43**, 267-282, doi:10.1071/EG12020.

Clark, D.A., 2012c, Interpretation of the magnetic gradient tensor and normalized source strength applied to the Tallawang magnetite skarn deposit, New South Wales, Australia: Society of Exploration Geophysicists Annual Meeting, Las Vegas, Expanded Abstracts, 4p.

Clark, D.A., Schmidt, P.W., Coward, D.A. and Huddleston, M.P., 1998. Remote determination of magnetic properties and improved drill targeting of magnetic anomaly sources by Differential Vector Magnetometry (DVM): Exploration Geophysics, 29, 312-319.

Clark, D.A., Young, J.A. and Schmidt, P.W., 2009, Magnetic Tensor Gradiometry in the Marine Environment: Correction of Electric And Magnetic Field And Gradient Measurements in a Conductive Medium and Improved Methods for Magnetic Target Location Using the Magnetic Gradient Tensor: MARELEC (Marine Electromagnetics) Conference, Stockholm, July, 2009, 10p.

Foss, C., 2006. Strategies to manage remanence effects in magnetic inversion. SEG Expanded Abstracts, 25, 938-942.

Helbig, K., 1963. Some integrals of magnetic anomalies and their relation to the parameters of the disturbing body: Zeitschrift für Geophysik, 29, 83-96.

Li, Y., Shearer, S., Haney, M. and Dannemiler, N., 2004. Comprehensive approaches to the inversion of magnetic data with strong remanent magnetization: SEG Expanded Abstracts, 23, 1191-1194.

Pedersen, L.B. and Rasmussen, T.M., 1990. The gradient tensor of potential field anomalies: Some implications on data collection and data processing of maps: Geophysics, 55, 1558-1566.

Phillips, J.D., 2005. Can we estimate total magnetization directions from aeromagnetic data using Helbig's integrals?: Earth Planets Space, 57, 681-689.

Phillips, J.D., Nabighian, M.N., Smith, D.V. and Li, Y., 2007. Estimating locations and total magnetization vectors of compact magnetic sources through combined Helbig and Euler analysis: SEG Expanded Abstracts, 26, 770-774.

Pilkington, M. and Beiki, M., 2012. Mitigating remanent magnetization effects in magnetic data using the normalized source strength. SEG Technical Program Expanded Abstracts 2012, 4p.

Pratt, D.A., McKenzie, K.B. and White, A.S., 2012. The remote determination of magnetic remanence. ASEG 22nd International Geophysical Conference and Exhibition, 26-29 February 2012, Brisbane, Australia, Expanded Abstracts, 5p.

Schmidt, P.W. and Clark, D.A., 1997. Directions of magnetization and vector anomalies derived from total field surveys. Preview, 70, 30-32.

Schmidt, P.W. and Clark, D.A., 1998. The calculation of magnetic components and moments from TMI: A case history from the Tuckers igneous complex, Queensland. Exploration Geophysics, 29, 609-614.

Young, J.A., S.T. Keenan, D.A. Clark, K.E. Leslie, P. Sullivan, P. Fairman, C. Williams, C.P. Foley and S.D. Billings, 2010. A Superconducting Magnetic Tensor Gradiometer for Underwater UXO Detection [Extended Abstract]: 21st International Geophysical Conference & Exhibition (ASEG-PESA 2010); Sydney, 4p.

CHAPTER 8: METHODS FOR DETERMINING REMANENT AND TOTAL MAGNETISATIONS OF MAGNETIC SOURCES - A REVIEW.

Clark, D.A., 2014. Methods for determining remanent and total magnetisations of magnetic sources - a review, accepted by *Exploration Geophysics*.

Abstract

Assuming without evidence that magnetic sources are magnetised parallel to the geomagnetic field can seriously mislead interpretation and can result in drill holes missing their targets. I review methods that are available for estimating, directly or indirectly, the natural remanent magnetisation (NRM) and total magnetisation of magnetic sources, noting the strengths and weaknesses of each approach. These methods are: (i) magnetic property measurements of samples, (ii) borehole magnetic measurements, (iii) inference of properties from petrographic/petrological information, supplemented by palaeomagnetic databases, (iv) constrained modelling/inversion of magnetic sources, (v) direct inversions of measured or calculated vector and gradient tensor data for simple sources, (vi) retrospective inference of magnetisation of a mined deposit by comparing magnetic data acquired pre- and post-mining, (vii) combined analysis of magnetic and gravity anomalies using Poisson's theorem, (viii) using a controlled magnetic source to probe the susceptibility distribution of the subsurface, (ix) Helbig-type analysis of gridded vector components, gradient tensor elements, and tensor invariants, (x) methods based on reduction to the pole and related transforms, and (xi) remote *in situ* determination of NRM direction, total magnetisation direction and Koenigsberger ratio by deploying dual vector magnetometers or a single combined gradiometer/magnetometer to monitor local perturbation of natural geomagnetic variations, operating in base station mode within a magnetic anomaly of interest.

Characterising the total and remanent magnetisations of sources is important for several reasons. Knowledge of total magnetisation is often critical for accurate determination of source geometry and position. Knowledge of magnetic properties such as magnetisation intensity and Koenigsberger ratio constrains the likely magnetic mineralogy (composition and grain size) of a source, which gives an indication of its geological nature. Determining the direction of a stable ancient remanence gives an indication of the age of magnetisation, which provides useful information about the geological history of the source and its environs.

Key words: remanence, susceptibility, magnetisation, magnetic anomalies, inversion, Koenigsberger ratio

Introduction

Magnetic anomalies are perturbations of the geomagnetic main field that are produced by magnetisation contrasts within the Earth's lithosphere. Although the distribution of magnetisation is heterogeneous over a wide range of scales, in many cases magnetic sources can be adequately represented by discrete bodies with effectively uniform magnetisation, surrounded by a uniformly magnetised medium. These sources may represent distinct rock units, ore bodies, zones of alteration (metamorphic or hydrothermal), buried ferrous objects etc., depending on the geological environment and the scale of the anomalies.

The total magnetisation **M** of a source is the vector sum of two contributions: induced magnetisation and natural remanent magnetisation (NRM):

$$\mathbf{M} = \mathbf{M}_{\mathrm{NRM}} + \mathbf{M}_{\mathrm{IND}} \qquad (1)$$

where $\mathbf{M}_{\mathrm{IND}}$ is a function of the applied field **F** and $\mathbf{M}_{\mathrm{NRM}}$ is independent of **F**. Because the geomagnetic field is relatively weak, the induced magnetisation is proportional to **F**, to a good approximation. For most geological sources the induced magnetisation vector is parallel to the inducing field, so

$$\mathbf{M}_{\mathrm{IND}} = k\mathbf{F}, \qquad (2)$$

where k is a scalar quantity, the (isotropic) magnetic susceptibility. Clark (1997) has reviewed the susceptibility and remanence properties of magnetic minerals and the rocks that contain them.

However for rocks with well-defined layers of differing magnetic mineral contents (e.g. banded iron-formations), or with preferred orientation of magnetic minerals (e.g. many metamorphic rocks and pyrrhotite-bearing ores and rocks), $\mathbf{M}_{\mathrm{IND}}$ is not always parallel to

F and the constant of proportionality between these vectors is then a second order tensor, **K**, which characterises the anisotropic susceptibility, i.e.

$$\mathbf{M}_{\mathrm{IND}} = \mathbf{KF}. \qquad (3)$$

Equation (3) is a matrix equation, where $\mathbf{M}_{\mathrm{IND}}$ and **F** are column vectors and **K** is a 3×3 symmetric matrix with the susceptibility tensor components as its elements. If the susceptibility is isotropic $\mathbf{K} = k\mathbf{I}$, where **I** is the identity matrix. Note that in SI susceptibilities are dimensionless and magnetisations are conventionally expressed in A/m, so **F** in equations (2)-(3) must also be given in A/m. For example, if the geomagnetic field is given as B = 50,000 nT, then $F = 50{,}000\times10^{-9}/(4\pi\times10^{-7}) = 39.8$ A/m.

Even if remanence is negligible and the susceptibility of the source is isotropic, the direction of the induced magnetisation may diverge significantly from that of the inducing field if the susceptibility of the source is sufficiently high. A source with strong magnetisation produces an internal field (the self-demagnetising field) that perturbs the geomagnetic field significantly. The effect is to reduce the effective inducing field and, if the source is not equidimensional, to deflect the induced magnetisation away from the inducing field direction. In this case the effective susceptibility is smaller than the intrinsic susceptibility and is anisotropic (Clark and Emerson, 1999). This macroscopic anisotropy, associated with self-demagnetisation, deflects the induced magnetisation towards the plane of a sheet-like source and towards the long axis of an elongate source. Self-demagnetisation modifies the remanent and total magnetisations analogously to an induced magnetisation (Emerson et al., 1985). As a rule of thumb, self-demagnetisation corrections are significant for susceptibilities above ~0.1 SI and are crucial for $k > 0.5$ SI.

Exact analytic corrections for self-demagnetisation are only available for ellipsoidal sources with homogeneous properties. The resultant magnetisation $\mathbf{M}'$ of an ellipsoid, in a uniform external applied field $\mathbf{F}_0$, with uniform *intrinsic* remanence $\mathbf{M}_{\mathrm{NRM}}$ and homogeneous, but anisotropic, *intrinsic* susceptibility **K**, corrected for self-demagnetisation, is given by:

$$\mathbf{M}' = (\mathbf{I} + \mathbf{KN})^{-1}(\mathbf{M}_{\mathrm{NRM}} + \mathbf{KF}_0), \qquad (4)$$

where **N** is the demagnetising tensor (Clark et al., 1986). **N** is a symmetric second order tensor, with unit trace if SI units are used. If CGS units are used the trace of **N** is 4π. Because the CGS susceptibility is a factor of 4π lower than the SI susceptibility, the product kN is the same in both systems of units. The eigenvectors $\mathbf{v}_i$ (i = 1,2,3) of the demagnetising tensor are parallel to the ellipsoid axes. The corresponding eigenvalues of **N** are the demagnetising factors N_1, N_2, N_3 along the ellipsoid axes. Clark et al. (1986) give expressions for the demagnetising factors of ellipsoids. If the susceptibility is isotropic, the magnetisation components with respect to these principal axes are:

$$M_i' = \frac{M_{NRM}^i + kF_i}{1 + kN_i}, \quad (i = 1,2,3). \tag{5}$$

Emerson et al. (1985) give formulae for the exact demagnetising factors of useful limiting cases of ellipsoids (spheres, infinite circular and elliptic cylinders, infinite sheets, prolate spheroids, and oblate spheroids), as well as approximate demagnetising factors for prisms and vertical cylinders.

The ellipsoid model has proved its worth in areas such as the Tennant Creek Field (Farrar, 1979; Clark and Tonkin, 1987; Hoschke, 1991), where discrete ironstone bodies that host Cu and Au mineralisation generally have approximately ellipsoidal shapes, and for some massive sulphide orebodies, e.g. the Elura Zn-Pb-Ag orebody (Clark and Tonkin, 1994), which occurs as two vertical pyrrhotite-rich pipes. However there are circumstances in which simple corrections for self-demagnetisation are insufficiently accurate. Hillan (2013a,b) discusses new approaches to dealing with self-demagnetisation when simple approximations break down (e.g. very magnetic sources with edges, corners, or irregular shapes that produce highly non-uniform demagnetising fields; inhomogeneous sources; or complex magnetic environments with interactions between neighbouring sources).

The computational burden of correcting calculated magnetisation distributions for self-demagnetisation and interactions can be reduced when the susceptibility is isotropic and homogeneous and the remanent magnetisation vector is uniform inside each body. The internal field within each body is given by $\mathbf{F} = \mathbf{F}_0 + \mathbf{H}_D$, where $\mathbf{H}_D = -\mathbf{N}\mathbf{M}'$ is the self-demagnetising field of the body, which is generally not uniform. The total magnetic flux

density inside the body is $\mathbf{B} = \mu_0(\mathbf{F} + \mathbf{M}')$, which obeys Maxwell's equation $\nabla.\mathbf{B} = 0$. Therefore, if the properties are homogeneous

$$\nabla.\mathbf{F} = \nabla.\mathbf{B}/\mu_0 - \nabla.\mathbf{M}' = -\nabla.\mathbf{M}' = = -\nabla.(k\mathbf{F} + \mathbf{M}_{\mathrm{NRM}}) = -k\nabla.\mathbf{F},$$

which implies that $\nabla.\mathbf{F} = 0$. It follows immediately that $\nabla.(\mathbf{F}_0 + \mathbf{H}_{\mathrm{D}}) = \nabla.\mathbf{H}_{\mathrm{D}} = 0$ and $\nabla.\mathbf{M}' = 0$.

The magnetostatic field produced by a magnetised body is attributable to (i) a volume distribution of pole density given by $-\nabla.\mathbf{M}'$, and (ii) a surface distribution of poles with density $\mathbf{M}'.\mathbf{n}$ (Blakely, 1996, p.84-85). Since the divergence of $\mathbf{M}'$ vanishes inside a body with uniform NRM and homogeneous isotropic susceptibility, as shown above, the magnetostatic field of such a body, both external and internal, arises solely from its surface and can be calculated using a surface integral. This justifies the use of surface integrals alone to calculate self-demagnetisation and interaction effects, as in the integral equation approach developed by Eskola and Tervo (1980), which was modified in order to handle thin bodies by Furness (1999, 2001).

On the other hand, the inhomogeneous demagnetising field interacts with *anisotropic* susceptibility to produce a non-vanishing divergence of the induced magnetisation. If the susceptibility is anisotropic, therefore, self-demagnetisation corrections for complex or multiple interacting bodies require a full volume integral approach. Some highly magnetic bodies, such as banded iron-formation (BIF) units, banded quartz-magnetite units and massive pyrrhotite orebodies, are highly anisotropic, so in certain environments there is a need to iteratively calculate volume integrals, using an finite volume discretisation with appropriate boundary conditions. Algorithms that can in principle incorporate anisotropic susceptibility as well as remanence into forward modelling and inversion in highly magnetic environments include those of Lelièvre and Oldenburg (2006), Hillan et al. (2013a,b), and Fullagar and Pears (2013).

Clark (2000) presented a case study where self-demagnetisation of highly magnetic sheet-like ironstone bodies significantly affects the form of the magnetic anomaly – the Osborne iron-oxide copper-gold deposit. Failure to account for self-demagnetisation in the early stages of exploration at Osborne produced an approximately 50° error in interpreted dip of

the ironstones, resulting in initial holes drilling down-dip and missing the target. Austin et al. (2014) modelled a complex, highly magnetic environment at the La Candelaria iron-oxide copper gold deposit in Chile, including self-demagnetisation and interactions between strongly magnetised bodies, which strongly distort the associated anomalies. The modelling, which used the algorithm of Hillan et al. (2013a,b) and incorporated magnetic property measurements, demonstrated that the anomalies arise predominantly from induced magnetisation, contrary to earlier suggestions that strong remanent magnetisation is required to explain the observed magnetic signatures.

The Koenigsberger ratio Q describes the relative strength of remanent and induced magnetisations, i.e.

$$Q = |\mathbf{M}_{\mathrm{NRM}}|/|\mathbf{M}_{\mathrm{IND}}|. \tag{6}$$

Q is a scalar parameter that is independent of the magnetisation direction. Other useful parameters that characterise the importance of remanence are the angular differences θ and θ_{NRM} between the inducing field and, respectively, the resultant magnetisation and the remanence, i.e.

$$\left.\begin{aligned} \theta &= \cos^{-1}(\hat{\mathbf{M}}.\hat{\mathbf{F}}) \\ \theta_{\mathrm{NRM}} &= \cos^{-1}(\hat{\mathbf{M}}_{\mathrm{NRM}}.\hat{\mathbf{F}}) \end{aligned}\right\}; \quad 0° \le \theta \le \theta_{\mathrm{NRM}} \le 180°, \tag{7}$$

where the hats indicate unit vectors.

These quantities are related by

$$\cos\theta = \frac{1 + \mathrm{Q}\cos\theta_{\mathrm{NRM}}}{\sqrt{1 + 2\mathrm{Q}\cos\theta_{\mathrm{NRM}} + Q^2}}. \tag{8}$$

Given $Q \ge 1$, θ_{NRM} is uniquely determined by θ:

$$\theta_{\mathrm{NRM}} = \cos^{-1}\left(\frac{\cos\theta\sqrt{\mathrm{Q}^2 - \sin^2\theta} - \sin^2\theta}{Q}\right), \tag{9}$$

whereas if $Q < 1$, there are two possible values of θ_{NRM}, given by

$$\theta_{\mathrm{NRM}} = \cos^{-1}\left(\frac{\pm\cos\theta\sqrt{\mathrm{Q}^2 - \sin^2\theta} - \sin^2\theta}{Q}\right). \tag{10}$$

Pratt et al. (2012) call θ the Apparent Resultant Rotation Angle (ARRA) when it is determined by inversion of a magnetic anomaly.

Cordell and Taylor (1971) noted that the minimum value of Q is constrained when the ARRA is known. In terms of our notation, their expression can be written

$$Q_{\min} = \begin{cases} \sin\theta = \sqrt{1-(\hat{\mathbf{M}}.\hat{\mathbf{F}})^2}, & (\hat{\mathbf{M}}.\hat{\mathbf{F}} \geq 0;\ 0° \leq \theta \leq 90°), \\ 1, & (\hat{\mathbf{M}}.\hat{\mathbf{F}} < 0;\ 90° \leq \theta \leq 180°), \end{cases} \tag{11}$$

which implies that the minimum NRM intensity is

$$\left(M_{NRM}\right)_{\min} = \begin{cases} M\sin\theta, & (0° \leq \theta \leq 90°), \\ M, & (90° < \theta \leq 180°). \end{cases} \tag{12}$$

Equation (11) implies that remanence is at least as important as induced magnetisation if $\theta \geq 90°$, and is at least half as intense as the induced magnetisation if θ is as small as 30°. Of course, Q can also be much larger than the values given by equation (11).

If Q is specified, the direction of remanence can be determined from the direction of total magnetisation (Cordell and Taylor, 1971). Using our notation, their expressions are equivalent to:

$$\hat{\mathbf{M}}_{\mathbf{NRM}} = \begin{cases} \frac{1}{Q}\left[\left(\cos\theta + \sqrt{Q^2 - \sin^2\theta}\right)\hat{\mathbf{M}} - \hat{\mathbf{F}}\right], & (Q \geq 1), \\ \frac{1}{Q}\left[\left(\cos\theta \pm \sqrt{Q^2 - \sin^2\theta}\right)\hat{\mathbf{M}} - \hat{\mathbf{F}}\right], & (Q < 1). \end{cases} \tag{13}$$

Note that the direction of remanence is uniquely determined by the direction of resultant magnetisation and the value of Q for $Q \geq 1$, but for $Q < 1$, there are two possible solutions. Usually Q is not known, so equation (13) gives a range of possible remanence directions, corresponding to different values of Q, within the plane containing **F** and **M**.

Conversely, if the direction of remanence is specified, from palaeomagnetic information for example, then Q can be determined if the direction of total magnetisation is known, using:

$$Q = \frac{\sin\theta}{\sin(\theta_{NRM} - \theta)}, \tag{14}$$

where θ and θ_{NRM} are given by equation (7).

Macnae (1994) suggests an alternative parameter to Q given by:

$$R = |\mathbf{M}_{\mathrm{stable}}|/|\mathbf{M}_{\mathrm{IND}} + \mathbf{M}_{\mathrm{VRM}}| = |\mathbf{M}_{\mathrm{stable}}|/|k\mathbf{F} + \mathbf{M}_{\mathrm{VRM}}| \approx |\mathbf{M}_{\mathrm{stable}}|/k_{\mathrm{eff}}F, \tag{15}$$

where $\mathbf{M}_{\mathrm{stable}}$ is the stable ancient remanence, $\mathbf{M}_{\mathrm{VRM}}$ represents the viscous remanent magnetisation (VRM) acquired in the recent geomagnetic field, and k_{eff} is an effective susceptibility that incorporates the viscous component of magnetisation. Note that the contribution of VRM to k_{eff} is not measured by susceptibility meters. R is therefore a measure of the relative importance of stable ancient remanence, which is generally oblique to the present field direction, and the effective long-term induced magnetisation that is more-or-less along the present field direction. The approximate equality on the RHS of equation (15) arises because the VRM is acquired mostly over the last 780,000 years of the Brunhes normal chron and therefore is a time-averaged vector that lies close to the present dipole field (PDF) direction as calculated from the axial geocentric dipole model, whereas the pure induced direction is parallel to the present field (PF), which reflects secular variation and may differ from the PDF by up to ~20°.

Although use of R is a reasonable suggestion, the motivation for its introduction stems from a belief that VRM is often a major contributor to the magnetisation of remanence-dominated sources (Macnae, 1994). This is almost never the case, as will be discussed

below. As described in the next section, standard palaeomagnetic techniques can resolve measured NRMs into stable and viscous components, which is useful for evaluating the contributions of each to the total remanence.

Characterising the total and remanent magnetisations of sources is important for several reasons. Knowledge of total magnetisation is often critical for accurate determination of source geometry and position. Knowledge of magnetic properties such as magnetisation intensity and Koenigsberger ratio constrains the likely magnetic mineralogy (composition and grain size) of a source, which gives an indication of its geological nature. Determining the direction of a stable ancient remanence gives an indication of the age of magnetisation, which provides useful information about the geological history of the source and its environs. Several methods exist for estimating the magnetic moment vector of a source, without any knowledge of its shape. This yields directions of the resultant magnetisation (remanent plus induced) and gives an indication of the size of the source, when plausible magnetisation intensities are assumed.

MAGNETIC PROPERTY MEASUREMENTS ON SAMPLES

Clark and Emerson (1991) describe some of the methods used to determine magnetic properties of rock and ore samples. Measurement of magnetic properties of samples taken from a magnetic source provides the most direct and, in principle, most reliable estimate of source induced, remanent and total magnetisations. In many cases samples are not available and, even if they are, there are many pitfalls and subtleties to interpretation of petrophysical measurements. Austin et al. (2013a,b) discuss some of these issues. Schmidt and Lackie (2014) presented a method for measuring remanent and induced magnetisations in the field. This method is an elaboration of a technique, originally described in 1973, that can be found in Breiner (1999). Magnetic property measurements on even a small set of samples can provide a qualitative guide to interpretation and semiquantitative constraints on modelling. However reliable quantitative estimation of magnetisation of a source (e.g. a rock unit, orebody, alteration zone, structural zone) from samples requires:

1. extensive sampling of a representative portion of the source (and its surroundings, if the environment is magnetic),
2. well-calibrated susceptibility and NRM measurements on standard samples (or with accurately determined corrections for non-standard samples),

3. correction of apparent susceptibility and remanence measurements for self-demagnetisation effects, to obtain the corresponding intrinsic properties, for sample susceptibilities greater than ~0.1 SI,
4. careful analysis of measured remanence data to determine if measured sample NRMs are contaminated by spurious components, such as drilling-induced remanence, lightning effects, or isothermal components acquired since sampling (e.g. from logging with pencil magnets), to remove these spurious components by palaeomagnetic cleaning, and to decompose complex multi-component NRM into its constituent components (each of which records a separate geological event or geomagnetic environment),
5. rigorous statistical analysis to estimate bulk mean properties, with error estimates, that recognises the vector nature of magnetisation and, if the samples are anisotropic, the tensor nature of susceptibility.

With regard to point 1 above, care should be taken to make the sample collection as representative as possible, avoiding the temptation to select the most magnetic portions, and sampling zones with obviously distinct properties (veins, shear zones etc.) in proportion to their occurrence.

Regarding point 2, laboratory susceptibility instruments are generally calibrated using known masses of chemically pure paramagnetic salts. This is very reliable for weak susceptibilities, but the accuracy of the calibration for stronger samples relies on the linearity of the instrument over many decades of susceptibility, which depends on the physical principles that underlie operation of the instrument. For example, instruments that employ air-cored coils are inherently more linear (albeit less sensitive) than those that use coils with ferromagnetic cores. It is important to have independently measured calibration specimens at the upper end of the susceptibility range for rocks.

Hand-held susceptibility meters are calibrated for measurements on flat slabs and are best suited for measurements made on smooth, flat, fresh outcrops. For the commonly used hand-held meters calibration standards in the form of blocks or cakes with diameter ≥ 30 cm and thickness ≥ 15 cm are equivalent to infinite slabs. The fall-off with distance from the surface of the sample can be determined empirically using nonmagnetic spacers and used to make approximate corrections for outcrops with pronounced rugosity or a

weathered crust. Use of these meters on drill core samples, split cores, small blocks etc. requires empirically determined correction factors that take the core diameter or block size into account (Schmidt and Lackie, 2014).

Hand-held susceptibility meter measurements made on strongly magnetic materials are affected by self-demagnetisation. The meter produces a primary field, which induces a magnetisation distribution in the sample. The meter detects the secondary field arising from this magnetisation distribution. For a homogeneous magnetic half-space of susceptibility k, the boundary conditions for **B** and **H** at the rock-air interface imply that the secondary field above the half-space is everywhere proportional to k /(1+ k /2). This result can be obtained using the method of images. Provided that the susceptibility output of the meter is proportional to this secondary field, it follows that the apparent susceptibility k' of the half-space measured by the instrument is:

$$k' = k/(1 + k/2). \qquad (16)$$

Equation (16) implies that the effective SI demagnetising factor at the interface for a homogeneous half-space is ½. The true susceptibility, found by inverting equation (9), is therefore:

$$k = k'/(1 - k'/2) \quad \text{[hand-held meter, large flat slab]}. \qquad (17)$$

For strongly magnetic rocks, equation (17) should be used to correct the apparent susceptibilities given by hand-held susceptibility meters, assuming the output of the instrument is linear in the induced secondary field. It should be checked with the manufacturer whether or not the inherent nonlinearity described by equation (16) has been incorporated into the displayed output.

Regarding point 3 above, equation (5) implies that both susceptibility and remanence measurements on strongly magnetic specimens need to be corrected for self-demagnetisation, in order to obtain the intrinsic properties of the sampled material. The effect on susceptibility is dependent on the geometry of the sample/measuring instrument system, not just the sample shape. For isotropic susceptibility and equidimensional specimens, the intrinsic susceptibility of the specimen is given by:

$$k = k'/(1 - k'N_1), \tag{18}$$

and the intrinsic remanence is given by:

$$\mathbf{M}_{\mathrm{NRM}} = (1 + kN_2)\,\mathbf{M}'_{\mathrm{NRM}}, \tag{19}$$

where k is the intrinsic susceptibility, k' is the apparent susceptibility as measured by the instrument, N_1 is the demagnetising factor for the susceptibility instrument/sample configuration, $\mathrm{M}_{\mathrm{NRM}}$ is the true remanence, $\mathrm{M}'_{\mathrm{NRM}}$ is the apparent remanence and N_2 is the isotropic demagnetising factor of the isolated specimen. In the most general case, for inequidimensional, anisotropic specimens, the generalisations of (18) and (19) that yield demagnetisation-corrected intrinsic properties are:

$$\mathbf{K} = (\mathbf{I} - \mathbf{K}'\mathbf{N})^{-1}\mathbf{K}'; \;\; \mathbf{M}_{\mathrm{NRM}} = (\mathbf{I} + \mathbf{KN})\mathbf{M}'_{\mathrm{NRM}}\,, \tag{20}$$

Analysis of the reluctance of the magnetic circuit for a ferromagnetic-cored transformer bridge shows that the SI demagnetising factor N_1 is approximately equal to the total residual gap between the specimen and the poles of the magnetic core, divided by the total gap length. Therefore, if the specimen fills the entire gap, the demagnetising factor is effectively zero (neglecting leakage flux) and if the specimen is a very thin disc the demagnetising factor approaches its maximum value of 1.

For standard palaeomagnetic specimens, which have an isotropic demagnetisation tensor, the SI demagnetising factor N_2 is 1/3, so

$$\mathbf{M}_{\mathrm{NRM}} = \mathbf{M}'_{\mathrm{NRM}}\,(1 + k/3), \tag{21}$$

where k is determined from (18).

Ideally, susceptibility instruments should operate at (i) field strengths comparable to the geomagnetic field in order to minimise nonlinearity effects, which are important for multidomain (MD) pyrrhotite grains larger than about 30 µm (Clark, 1984; Worm et al., 1993; Martín-Hernández et al., 2008), for some high-Ti titanomagnetite-bearing rocks

(Jackson et al., 1998), and for large MD hematite crystals (Guerrero-Suarez and Martín-Hernández, 2012), and (ii) at low frequencies (≤ 1 kHz) to minimise the effects of frequency dependent susceptibility and to ensure that measured susceptibility measurements are not unduly affected by high sample conductivity of, for example, massive sulphide ores (Worm et al., 1993; Yang and Emerson, 1997).

Regarding point 4 above, measured NRMs of samples are often contaminated by palaeomagnetic noise. In this context, palaeomagnetic noise refers to components that are unrepresentative of the *in situ* remanence, such as isothermal remanence (IRM) components acquired through exposure to moderate to strong magnetic fields; drilling-induced remanence acquired in the magnetic field inside the core barrel, due to stress release during coring (Audunsson and Levi, 1989; Pinto and McWilliams, 1990); chemical remanent magnetisation (CRM) components associated with alteration of magnetic minerals in surface samples by weathering; or short term viscous remanence (VRM) components acquired post-collection in weak ambient fields, either by very "soft" large MD grains or by ultrafine single domain (SD) grains around the superparamagnetic (SPM)-stable SD transition. However long term VRM acquired in the geomagnetic field since the last geomagnetic reversal is representative of the bulk *in situ* magnetisation and is not categorised here as noise, although it is an annoyance to palaeomagnetists (unless it is used for core orientation), who are mainly interested in ancient remanence components. Lightning strikes are common sources of IRM noise in outcrop and very near surface samples, particularly on hilltops and in areas with low erosion rates. Mining operations and logging with pencil magnets often contaminate measured NRMs.

The most common palaeomagnetic cleaning methods are alternating field (AF) demagnetisation, which initially removes remanence carried by grains with low coercivity then, as it proceeds, progressively higher coercivities, and thermal demagnetisation, which successively unblocks increasingly stable components of remanence (Butler, 1992; Dunlop and Özdemir, 1997). Low temperature demagnetisation, accomplished by cooling specimens in liquid nitrogen and then rewarming to room temperature in zero magnetic field, is a useful pre-treatment for removing soft palaeomagnetic noise components, such as IRMs and drilling-induced remanence, carried by MD magnetite or hematite grains, while leaving more stable remanence components relatively unaffected (Schmidt, 1993). Other less used demagnetisation methods include chemical demagnetisation (Dunlop and

Özdemir, 1997, p.457-458) which can potentially preferentially remove weathering associated CRM and can resolve CRM overprints from primary detrital remanent magnetisation (DRM) in sedimentary rocks, and microwave demagnetisation (Walton et al., 1992; Suttie et al., 2010), which can simulate thermal demagnetisation of the magnetic grains with negligible heating of the matrix, thereby avoiding potential production of new magnetic minerals in the samples during demagnetisation.

Figure 1 illustrates the principle of palaeomagnetic cleaning of measured NRMs that are unrepresentative of the bulk *in situ* remanence, in order to estimate the true contribution of remanence to the magnetisation of the sampled source. The measured NRM of the sample comprises three components: a stable ancient TRM, a VRM overprint acquired over the Brunhes chron, and an IRM noise component. If the stability spectra of three components do not overlap, appropriate stepwise demagnetisation of the NRM allows the components to be separated cleanly. In that case, successive remanence vector end-points define three linear segments; the initial segment corresponds to the IRM, the intermediate segment represents the VRM, and the final segment, which heads directly towards the origin, corresponds to the TRM. Decomposition of the NRM vector into its three constituent components is then straightforward.

As can be seen in Figure 1, if the stability spectra of the different components overlap, the demagnetisation paths are curved through the transition between linear segments, where two or more components are being demagnetised simultaneously. If overlap of stability spectra is not complete, the directions of the remanence components can be determined by fitting least-squares best-fit lines to the linear segments from individual specimens (Kirschvink, 1980; Kent et al., 1983) or groups of specimens (Schmidt, 1982). If overlap of spectra precludes well-defined linear segments, other analysis methods such as Hoffman-Day plots (Hoffman and Day, 1978; Halls, 1979) or remagnetisation circles (Halls, 1976; McFadden and McElhinny, 1988), with the caveats discussed by Schmidt (1985), can be used to extract the component directions. Once the directions associated with each component are determined, the contribution of each component to the measured NRM can

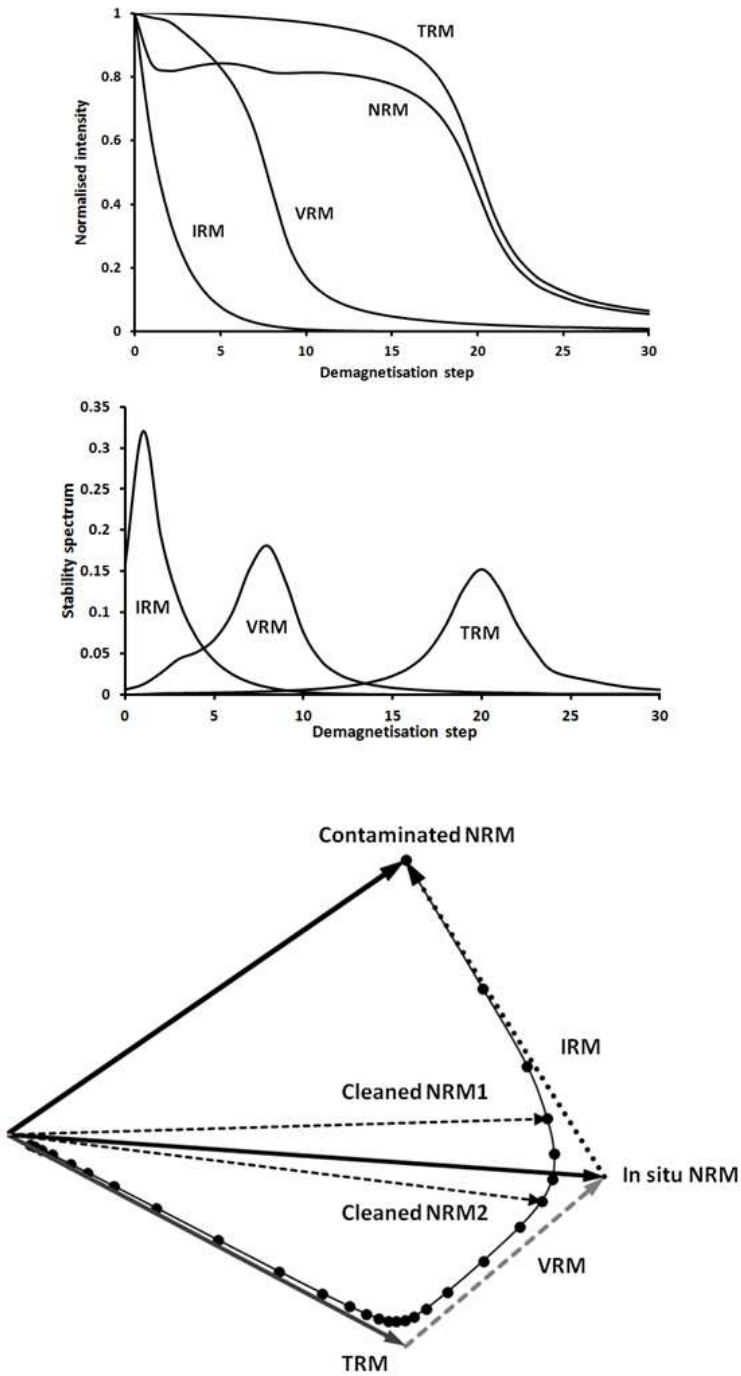

Figure 1. Palaeomagnetic cleaning of contaminated NRM to remove unrepresentative IRM noise and to estimate representative *in situ* remanence, which comprises a stable ancient TRM component and VRM acquired in the recent geomagnetic field. The dots represent successive remanence vector end-points during stepwise demagnetisation. For simplicity of presentation the three components are assumed to be coplanar. Cleaned NRM1 has not completely removed the IRM contamination, whereas cleaned NRM2 has essentially removed all the IRM, but has also removed some of the original VRM. The demagnetisation curves (top) and corresponding stability spectra (middle) of the three remanence components are also shown.

be estimated, from which the "cleaned NRM" that represents the uncontaminated *in situ* remanence of the sample can be calculated.

For the scenario shown in Figure 1, the cleaned NRM directions of multiple samples will be distributed along a great circle path between the stable TRM and the recent field direction. The uncleaned measured NRMs of a sample collection are scattered away from this trend due to the IRM contamination. Note that the vectors denoted "cleaned NRM1" and "cleaned NRM2" in Figure 1 serve as approximate estimates of the uncontaminated *in situ* NRM. The former is somewhat "undercleaned", the latter slightly "overcleaned". The uncertainty in identifying the cleaned NRM direction simply by inspection, without using the quantitative analyses of multicomponent remanence mentioned above, arises because of overlapped stability spectra for the IRM and the other components. This overlap also means that a portion of the *in situ* VRM has been demagnetised by the time the IRM has been eliminated. However, the original intensity of the VRM can be approximately estimated by extrapolation back to "zero demagnetisation" of the demagnetisation curve (intensity of vector differences versus demagnetisation step) from the corresponding linear portion of the vector demagnetisation diagram. A similar procedure can be applied to estimate the original uncleaned TRM intensity.

It is clear from the discussion above that determination of representative bulk *in situ* remanence of a source from measurements on samples can be a non-trivial task, and that careful palaeomagnetic cleaning and analysis of demagnetisation trends is essential if the NRM is multicomponent, or if significant contamination of measured NRMs occurs. Clark and Tonkin (1994) present an example of a magnetic anomaly associated with strong , relatively complex, multicomponent remanent magnetisation carried by pyrrhotitic metasediments in the Cobar area of New South Wales. Careful analysis of detailed AF and thermal demagnetisation data on oriented drillhole samples enabled resolution of sample magnetisations into a normal component of moderate stability, overprinting a more stable component that could be of either polarity. Evaluating the average contributions of each component to the bulk magnetisation of the unit, and incorporation of drilling data that defined the geometry of the magnetic zone, enabled excellent quantitative agreement between the predicted and observed anomalies, confirming that the source had been intersected and the anomaly was predominantly associated with remanence. In simple cases, where measured NRMs have well-grouped directions that are clearly ancient and

intensities are fairly consistent, analysis of NRM measurements is straightforward and very useful for constraining magnetic modelling.

Regarding point 5 above, it should be noted that magnetic properties of samples from a given unit often vary over a wide range and may exhibit strongly skewed unimodal or even multimodal distributions. Naïve application of standard statistical analyses can lead to serious errors in estimating appropriate averages. The aim of the statistical analysis should be to calculate the population mean susceptibility and the population mean remanence vector from a representative sample collection (as shown in Figure 2), because each approximately homogeneous small portion of a heterogeneous source contributes to the total magnetic moment in proportion to its magnetisation times its volume. This means that, at distances that are large compared to the scale of heterogeneity, the magnetic anomaly is proportional to the arithmetic mean magnetisation vector. In some petrophysical studies other measures of central tendency are used (e.g. median, mode, geometric mean) on the grounds that they may better represent a "typical" value of susceptibility when the probability distribution is highly skewed. However, as argued above, these measures are not the most appropriate for estimating susceptibility for modelling purposes.

Whatever the susceptibility distribution, the arithmetic mean of the sample susceptibilities is an unbiased estimator of the population mean, but it may not be the best estimator if the distribution is non-Gaussian. The arithmetic mean is not robust for strongly skewed or multimodal distributions, as it can be strongly influenced by a few outliers. In many cases the susceptibility distribution is unimodal, but is strongly skewed, so it is not well represented by a Gaussian curve. In most such cases, however, the distribution is approximately lognormal. If so, appropriate parametric statistical tools exist for estimation of the population mean from the minimum variance unbiased estimator and for calculating its confidence limits (Aitchison and Brown, 1957).

For multimodal distributions, one possible approach is to analyse each mode separately and combine the results afterwards. Nonparametric statistical methods, such bootstrapping, can be applied to data with complicated distributions. Bootstrap methods have been developed for susceptibility anisotropy data (Constable and Tauxe, 1990) and palaeomagnetic data (Tauxe et al., 1991), but as yet no published studies of nonparametric

methods applied to analysis of full vector data, with a range of intensities and variable directions, have appeared.

Although more rigorous methods for analysis of magnetisation vectors require development, there is no excuse for some abuses of data that are occasionally perpetrated. Remanent intensities should *not* be averaged without regard for the corresponding directions. As an example, the contribution of scattered magnetisations to the bulk magnetisation of a source is obviously much less than that of well-grouped vectors with similar magnitudes. Similarly, Koenigsberger ratios should not be averaged. The representative value of Q should be calculated from the best estimates of the mean remanence vector and the mean susceptibility.

BOREHOLE MEASUREMENTS

The susceptibility of a source can be measured *in situ* by a borehole logging tool, or on samples extracted from the hole. If the hole intersects the source, a triaxial vector magnetometer with its orientation monitored continuously can measure the anomalous magnetic field within the source. Levanto (1963) and Bosum et al. (1988) describe orientation methods, presentation of data, and data analysis for borehole vector field measurements. For a uniformly magnetised source the anomalous internal **H** field of the source is

$$\Delta\mathbf{H} = -\mathbf{N}\mathbf{M}, \qquad (22)$$

where **N** is the demagnetising tensor determined by the shape of the source. For ellipsoidal bodies, including limiting cases such as spheres, infinite circular and elliptic cylinders, and infinite sheets, **N** is uniform throughout the body (Clark et al., 1986). In the interior of uniformly magnetised non-ellipsoidal bodies, **N** is a slowly varying function of position within the body.

As shown in Figure 3, a magnetometer in a borehole does not measure the field $\Delta\mathbf{B} = \mu_0\Delta\mathbf{H}$ that is given by equation (22). Instead it measures the field within the cylindrical borehole cavity, $\Delta\mathbf{B}' = \mu_0\Delta\mathbf{H}'$, which has components parallel to (||) and perpendicular to (⊥) the borehole that are given by

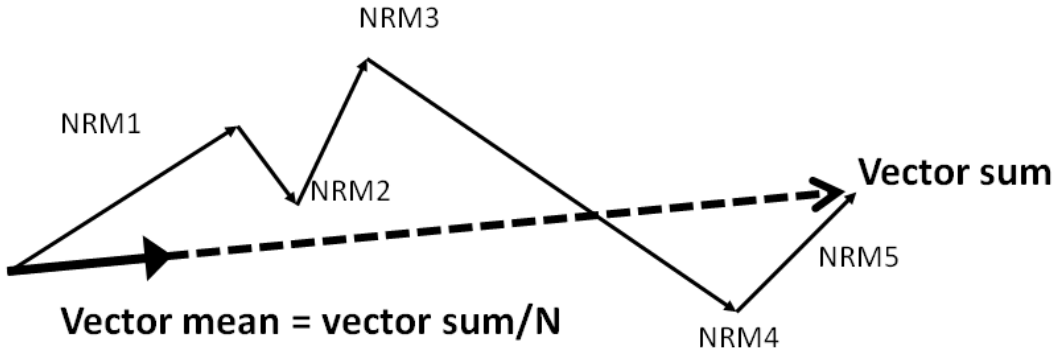

Figure 2. Calculation of vector mean NRM from measurements on five samples. The dashed line indicates the vector sum; the thick solid arrow represents the vector mean, calculated as the vector sum divided by the number of samples.

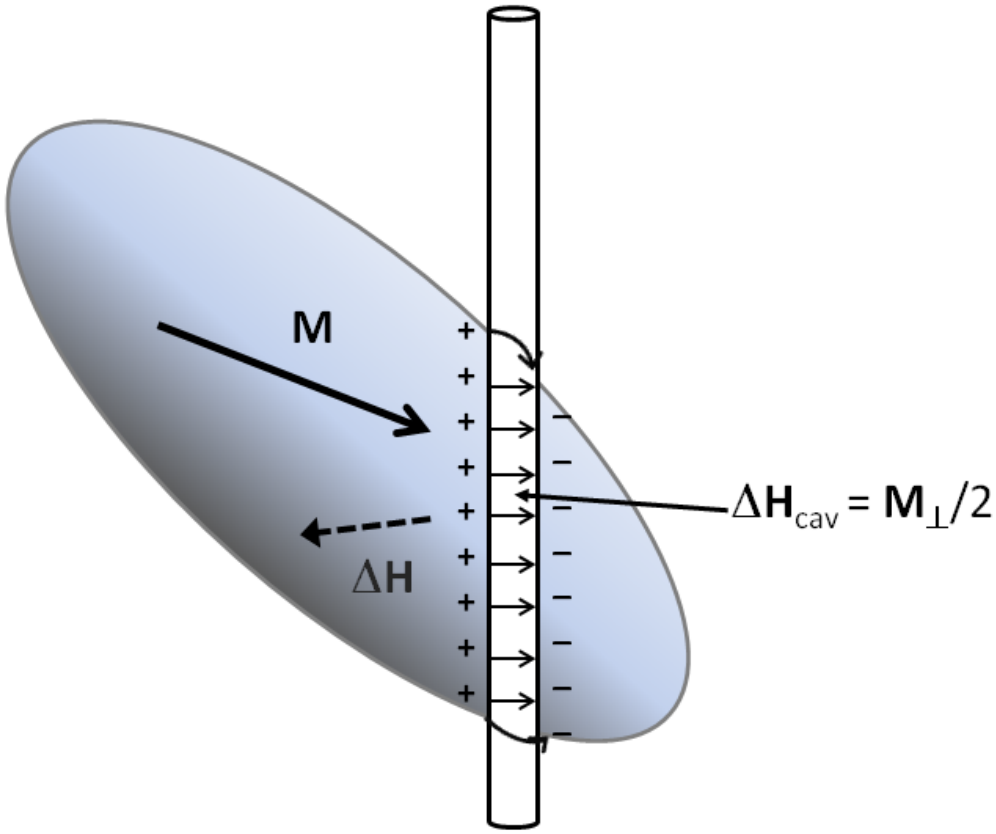

Figure 3. Relationship between internal anomalous field within a magnetised body, given by equation (22), and the field within the borehole. The magnetisation component of the body perpendicular to the hole produces poles on the flanks of the borehole. These poles give rise to a cavity field $\Delta\mathbf{H}_{cav}$, directed parallel to the magnetisation component that is perpendicular to the borehole. $\Delta\mathbf{H}_{cav}$ perturbs the anomalous internal field of the body $\Delta\mathbf{H} = -\mathbf{NM}$. The magnetisation component that is parallel to the borehole produces negligible cavity field, except near the boundary of the magnetic source.

$$\Delta B_{\|}' = \mu_0 \Delta H_{\|}, \quad \Delta \mathbf{B}_{\perp}' = \mu_0(\Delta \mathbf{H}_{\perp} + \mathbf{M}_{\perp}/2). \tag{23}$$

Hoschke (1991) presented examples of anomalous vector components within drillholes that penetrate highly magnetic ironstones. The field components are reasonably consistent within the source and show clearly the self-demagnetising field, as modified by the cavity. Other downhole vector magnetometer survey datasets have been published that clearly show abrupt changes in anomalous field direction as the sensor passes into a magnetic body, with the internal field broadly reversed with respect to the nearby external field. Internal field directions frequently have superimposed high frequency noise but, if smoothed, exhibit relatively consistent, slowly varying directions inside the source. Examples can be found in Levanto (1963), Hattula (1986), Bosum et al. (1988), Smith and Hall (1995), Mueller et al. (1997) and Liu et al. (2013). Pariso and Johnson (1993) have shown that magnetisation determined from borehole measurements through moderately magnetic gabbros (layer 3 of oceanic crust) is consistent with, but smoother and less variable than, magnetisation determined from palaeomagnetically cleaned small core samples, and is much more representative of bulk magnetisation than measurements on uncleaned samples, which are affected by drilling-induced remanence.

Equation (23) is valid for a smooth-walled borehole within the body, when measurements are taken at least several borehole diameters beneath its upper boundary, or above its lower boundary, provided the magnetisation is uniform over several borehole diameters around the measurement point. Close to the boundary more complicated equations given by Pozzi et al. (1988) or Gallet and Courtillot (1989) can be used. If the geometry of the source is known or assumed, **N** is specified and the magnetisation can then be deduced from equations (22) and (23).

In practice small scale heterogeneity adjacent to the borehole and rugosity of its wall often make vector measurements inside a strongly magnetic source quite noisy. However these local perturbations average to zero over larger distances, so the bulk magnetisation of the source can be estimated reasonably accurately by averaging measured vectors throughout the borehole intersection. The major source of noise in downhole vector measurements is misorientation of the magnetometer. Orientation errors of ~0.1° produce errors of several tens of nT in vector components, which translate to errors in estimated magnetisation components of ~10-100 mA/m.

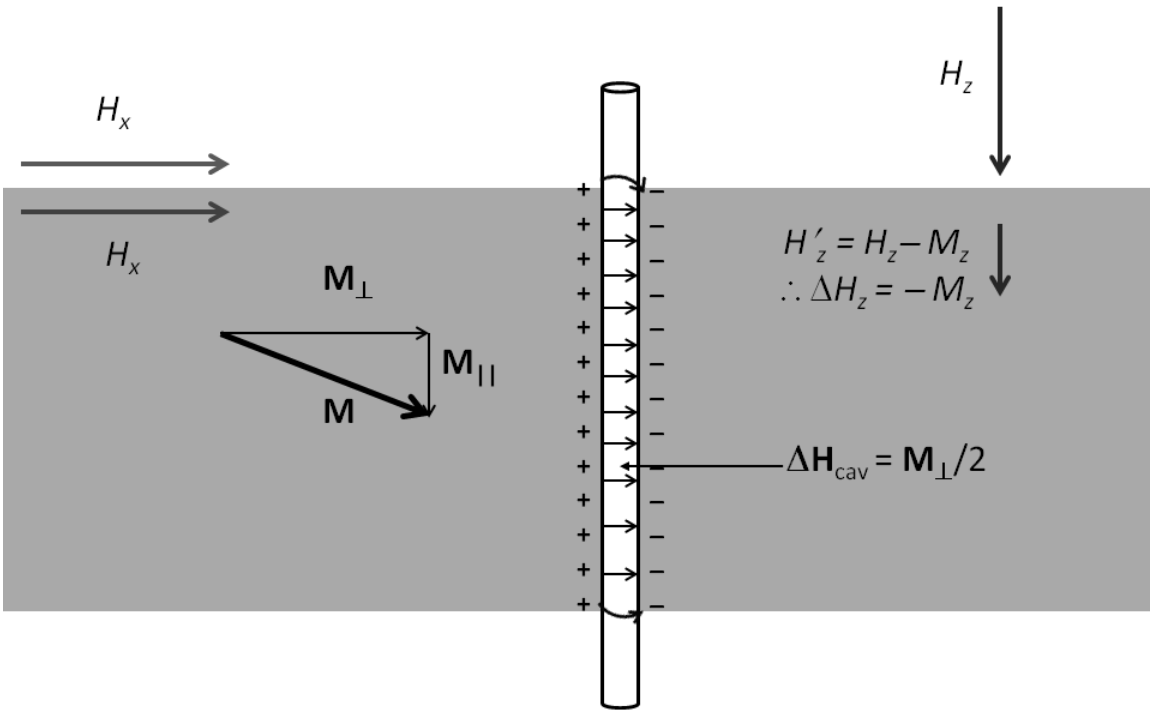

Figure 4. Determination of magnetisation vector for a thick homogeneously magnetised layer, using borehole vector magnetometry. The external anomalous field is zero. Within the layer the internal anomalous field is uniform and is antiparallel to the magnetisation component that is perpendicular to the plane of the magnetised sheet. For a horizontal sheet, as shown, the anomalous internal field is vertical: $\Delta\mathbf{B} = \mu_0\Delta\mathbf{H} = -\mu_0 M_z\hat{\mathbf{z}}$. Within a vertical borehole the anomalous horizontal components of the field are $\Delta B_x = \mu_0 M_x/2$, $\Delta B_y = \mu_0 M_y/2$, $\Delta B_z = -\mu_0 M_z$, so $\mathbf{M} = (1/\mu_0)\,(2\Delta B_x, 2\Delta B_y, -\Delta B_z)$. If the susceptibility is also measured, $\mathbf{M}_{\mathrm{NRM}}$ can be obtained from $\mathbf{M}$ by subtraction: $\mathbf{M}_{\mathrm{NRM}} = \mathbf{M} - k\mathbf{H}'$, where $\mathbf{H}' = (H_x, H_y, H_z - M_z)$.

One simple case where the magnetisation of the rock units intersected by a borehole can be determined unambiguously is that of a layered earth, with horizontal or dipping layers (Pozzi et al. 1988; Gallet and Courtillot, 1989). If the susceptibility of the layers is also measured, the remanent magnetisation can be calculated using equations (1) and (2). A particularly simple case occurs when the borehole intersects a single sheet-like source in a nonmagnetic background. For this case the demagnetising factor in the plane of the sheet is zero and the SI demagnetising factor normal to the sheet is 1. If the sheet is thick compared to the hole diameter and the hole is perpendicular to the sheet, then the field components well inside the sheet are $\Delta B_{\parallel} = -\mu_0 M_{\parallel}$ parallel to the hole and $\Delta \mathbf{B}_{\perp}' = \mu_0 \mathbf{M}_{\perp}/2$ perpendicular to the hole, i.e. in the plane of the sheet (see Figure 4). This method actually determines the magnetisation contrast across each interface. However, by keeping track of successive magnetisation contrasts from the surface, the absolute magnetisations in each layer can be determined.

INFERENCE FROM PETROLOGIC AND PALAEOMAGNETIC INFORMATION

Detailed petrographic descriptions of samples, including estimates of magnetic mineral grain size ranges, compositions and modal percentages can be used to infer their magnetic properties, particularly susceptibility. If the rock unit has a known simple geological history, palaeomagnetic data can also be used to infer probable remanence directions. Clark (1997) plotted ranges of susceptibility, remanence intensity and Koenigsberger ratio for various magnetic mineral compositions, domain states and type of NRM. With the exception of CRM carried by MD hematite (see below), subsequent studies do not require revision of these ranges.

Clark et al. (2004) presented a petrophysical model for the magnetic properties and densities of iron oxide-rich ores and alteration zones in iron oxide copper-gold (IOCG) systems, which contain hydrothermal magnetite and hematite with end-member compositions. This model can be applied more generally to the magnetic properties of rocks and ores that contain relatively pure, well crystallised magnetite ± hematite. Both minerals are assumed to be in their respective true multidomain size ranges (> 20 µm for magnetite; > 100 µm for hematite). As elaborated by Clark (2014), if the volume fractions of magnetite and hematite in the rock or ore are f_{mt} and f_{hm} respectively then the estimated SI susceptibility k is given by

$$k = 20f_{mt} /[1 + 4.8(1- f_{mt})] + 0.04f_{hm} . \quad (24)$$

The contribution of magnetite in equation (24) is based on a theoretical relationship that incorporates self-demagnetisation of magnetite grains, modified by a Lorentz field contribution to account for grain interactions (Clark, 1997). The formula assumes an intrinsic susceptibility of 20 SI for the magnetite grains, in accord with Stacey and Banerjee's (1974) estimates of intrinsic susceptibility of large MD magnetite grains, and an estimated average effective SI demagnetising factor of $N = 0.24$ for MD magnetite grains (Parry, 1980). For dilute dispersions of magnetite ($f_{mt} < 0.1$), equation (20) reduces to

$$k \approx 3.45\, f_{mt} + 0.04f_{hm} . \quad (25)$$

The magnetite contribution in equation (21) agrees well with the empirical relationship between susceptibility and magnetite content of rocks found by Puranen (1989). The contribution of hematite in equations (24) and (25) is approximate (susceptibilities of pure end-member MD hematite typically range from ~0.01 SI to ~0.1 SI, depending on crystallinity, stress, stoichiometry etc.), but the hematite contribution to the susceptibility of rocks and ores, even massive iron oxide, is subordinate to that of magnetite if more than ~1-2% magnetite is present.

Monoclinic pyrrhotite, with composition ~Fe_7S_8 and 4C superstructure (hereafter simply called pyrrhotite), is an important contributor to magnetic anomalies in many areas. The susceptibility of pyrrhotite is substantially less than that of magnetite, but much greater than that of hematite, and is strongly grain size dependent (Clark, 1984; Worm et al., 1993). Figure 5 shows the dependence of susceptibility on magnetic mineral content and microstructure for MD magnetite, hematite and pyrrhotite.

Unlike TRM of MD hematite, which has been extensively studied, CRM carried by MD hematite is not well understood. Clark (2014) has reviewed the scanty evidence regarding CRM of MD hematite and concluded that the maximum CRM intensity acquired in a typical geomagnetic field of 50,000 nT is ~ 5 A/m. This is lower than the range Clark (1997) gave for CRM carried by MD hematite, which was calculated using theory developed for MD magnetite by Stacey and Banerjee (1974). However, their theory

assumes that the coercivity of the MD grains is less than their self-demagnetising fields, which does not apply to hematite.

Taking this new predicted upper limit for hematite into account, the intensity of grain-growth CRM acquired by hydrothermal iron oxides well below the Curie temperatures (580°C for magnetite; 680°C for hematite) is predicted to be:

$$\text{CRM (A/m)} \approx 18 f_{\text{mt}} + M_{\text{CRM}}(\text{hm})\, f_{\text{hm}}, \qquad (26)$$

where $M_{\text{CRM}}(\text{hm}) \leq 5$ A/m.

While CRM carried by MD hematite has only moderate intensity, MD hematite does acquire intense TRM if cooled in the Earth's field from above its Curie temperature of 680°C (Kletetschka et al., 2000; Dunlop and Kletetschka, 2001). TRM intensity acquired on cooling of magnetite and/or hematite-bearing rocks and ores in a field of 50,000 nT is predicted to be

$$\text{TRM (A/m)} \approx 80 f_{\text{mt}} + 1000 f_{\text{hm}}\,. \qquad (27)$$

The corresponding Koenigsberger ratios Q are given by: Q_{CRM} (magnetite) ≈ 0.13; Q_{CRM} (hematite) ≤ 3; Q_{TRM} (magnetite) ≈ 0.6 (Dunlop and Özdemir, 1997, p.239); Q_{TRM} (hematite) ≈ 600. As an example of the efficiency of TRM acquisition by MD hematite, extremely high Koenigsberger ratios have been reported for NRMs of a contact metamorphosed coarse-grained massive hematite deposit, which gives rise to a remanence-dominated magnetic anomaly of more than 30,000 nT, by Schmidt et al. (2007).

The *in situ* induced magnetisation of MD magnetite-bearing rocks is augmented by viscous remanent magnetisation (VRM), subparallel to the induced magnetisation, acquired predominantly over the duration of the Brunhes chron. The contribution of this VRM can be significant for detailed modelling of anomalies. An upper limit for VRM carried by MD magnetite can be obtained by noting that the magnetisation of an isolated magnetite grain, subject to self-demagnetisation, that has fully equilibrated with the ambient field H attains a maximum intensity of $H/N \approx 40/0.24 = 166$ A/m (Shive, 1989). This is about 20% higher than the induced magnetisation of the grain, calculated using equation (18), suggesting an

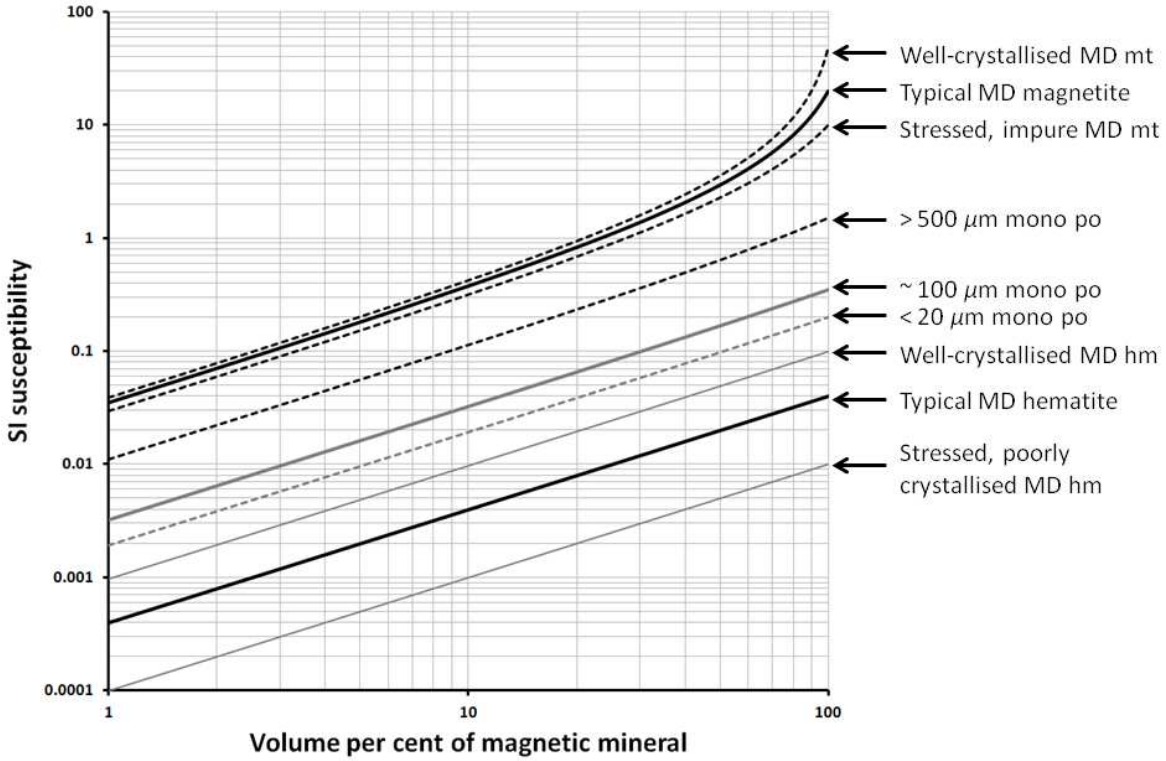

Figure 5. Susceptibility versus volume percent for true multidomain magnetite (> 20 μm), monoclinic pyrrhotite (> 10 μm) and hematite (> 100 μm), for varying degrees of crystallinity and residual stresses in grains.

upper limit of ~0.2 for Q_{VRM} of MD magnetite. Shive (1989) obtains $Q_{VRM} \leq 0.25$, using slightly different assumptions. For high concentrations of magnetite, the constraint imposed by self-demagnetisation is somewhat relaxed, due to grain interactions, but values of Q_{VRM} greater than unity would require very high contents (≥ 90%) of very low coercivity magnetite. Based on palaeomagnetic cleaning studies, Clark and Tonkin (1987) and Clark (1988a, 1994) have found Q_{VRM} typically falls in the range 0.1 – 0.3 for semi-massive and massive magnetite ores of hydrothermal origin, so $Q_{VRM} \approx 0.2$ is a reasonable assumption for modelling MD magnetite-bearing rocks and magnetite-rich orebodies if remanence measurements are unavailable.

Ultrafine magnetic mineral grains can also exhibit substantial magnetic viscosity. Viscous SPM particles fall into a very narrow size range around the SPM-stable SD threshold, which is ~0.03 μm for magnetite and ~0.08 μm for titanomagnetite with $x \approx 0.6$ (Dunlop and Özdemir, 1997, p.131). Slightly larger grains have relaxation times of billions of years and can carry stable, relatively intense remanence with high Q. Slightly smaller grains have relaxation times << 1 s and contribute to the induced magnetisation only, with negligible viscous remanence. SPM magnetite grains slightly smaller than the threshold size have susceptibilities that are one to two orders of magnitude higher than typical SD or MD magnetite susceptibilities and, if present, tend to reduce the Koenigsberger ratio by boosting the induced magnetisation.

The presence of significant quantities of viscous SPM grains in a sample can be ascertained quite definitively in several ways: (i) relatively large frequency dependence of susceptibility; (ii) a substantial phase lag response to a weak alternating field, manifested as quadrature susceptibility; (iii) substantial acquisition of VRM in the laboratory (and viscous decay in zero field); (iv) anomalously slow, superexponential decay of dB/dt, showing an approximate $1/t$ dependence, in a transient electromagnetic type measurement; (v) a distinct positive slope around room temperature of a low field thermomagnetic (k-T) curve, indicating unblocking of fine magnetic particles with successively larger volumes with increasing temperature. In point (ii) above, quadrature susceptibility is also referred to as the imaginary component of the complex susceptibility, which corresponds to the component of the total susceptibility that lags an applied sinusoidal field by 90°. These seemingly quite different tests are in fact closely related, via the connection between relaxation times, temperature, and grain volumes and coercivities (Shcherbakov and

Fabian, 2005; Egli, 2009). Wasp-waisted strong field hysteresis loops also suggest the presence of a significant quantity of SPM grains, together with high coercivity stable SD magnetic grains, but is not a definitive indicator of a grain size distribution that straddles the SPM- stable SD threshold as wasp-waisted loops can also result from mixtures of high and low coercivity populations, associated with a strongly bimodal grain size distribution or produced by a mixture of different magnetic minerals (Dunlop and Özdemir, 1997, p.323-324).

Given the factors discussed above, VRM acquired by viscous SPM grains is normally only a small fraction of NRM carried by fine magnetic particles (Dunlop and Özdemir, 1997, p.275) and, like VRM carried by MD grains, cannot be the predominant contributor to high Q values found in many rocks. This conclusion contradicts the speculations of Macnae (1994) that VRM may dominate many strong measured NRMs and account for their corresponding high Koenigsberger ratios. In practice long term VRM, when present, is easily recognisable by its direction and its soft character, in particular its ready removal by mild heating. Dunlop and Özdemir (1997, p.274-275) show that thermal demagnetisation to 200°C is sufficient to erase VRM acquired by fine magnetite grains over 1 Ma.

Determination of palaeomagnetic poles uses the axial geocentric dipole model to calculate palaeopole positions from palaeofield directions that have been defined by palaeomagnetic cleaning of sample NRMs. Once palaeopole positions for various ages are established for a given terrane, this process can be inverted to predict the palaeofield direction for a specific locality from the corresponding palaeopole position (Clark, 1983). If the palaeopoles for the terrane of interest are not known directly, they can be determined using its reconstruction to another terrane for which the palaeopoles are known. Butler (1992, p.233-234) gives expressions for the expected palaeofield direction, and its oval of confidence, at a specified site, given a palaeopole position and its estimated error. If the latitude and longitude of the site and the palaeopole are, respectively, (λ_s,ϕ_s) and (λ_p,ϕ_p), then the declination D and inclination I of the palaeofield are given by:

$$\cos D = (\sin\lambda_p - \sin\lambda_s \cos p)/(\cos\lambda_s \sin p); \quad I = \tan^{-1}(2\cot p), \qquad (28)$$

where the colatitude p of the palaeopole is found from:

$$\cos p = \sin\lambda_p \sin\lambda_s + \cos\lambda_p \cos\lambda_s \cos(\phi_p - \phi_s). \quad (29)$$

The corresponding errors in D and I are:

$$\Delta D = \sin^{-1}(\sin A_{95} / \sin p); \quad \Delta I = \frac{2A_{95}}{1+3\cos^2 p}, \quad (30)$$

where A_{95} is the radius of the 95% confidence circle around the palaeopole.

If a remanently magnetised rock unit has experienced tectonic rotation since acquisition of the remanence, this needs to taken into account in order to predict the *in situ* remanence direction. Clark (1983) gave expressions for calculating the effects on remanence directions of folding about horizontal or plunging axes. Clark and Schmidt (1994) noted that remanence carried by BIFs in the Hamersley Basin is pre-folding in areas with low metamorphic grade and post-folding in areas with higher metamorphic grade. This produces substantially different magnetic anomaly patterns.

Figure 6 shows an apparent polar wander path (APWP) for Australia, from the Early Devonian to the present, and corresponding palaeofield directions for a site in central Queensland. The sense of the palaeofield direction (normal or reversed) can be determined, with varying degrees of certainty, from the geomagnetic polarity time scale (see Butler, 1992, Chapter 9). Remanence acquired during the Cretaceous normal-polarity superchron (~118-83 Ma) is expected to have normal polarity, with almost 100% probability, whereas remanence acquired in the interval ~312-262 Ma (the Permo-Carboniferous reversed-polarity superchron) is almost certainly reversed. For other time intervals, reversals were frequent and prediction of likely polarity requires precise ages (e.g. better than 0.5 Ma for the Cenozoic). In most cases, however, the polarity of a remanence-dominated magnetic source is obvious from the form of the anomaly.

For a given assemblage of magnetic mineral grains, the intensity of stable remanence depends on the palaeofield intensity. With the exception of TRM carried by MD hematite, which almost saturates in fields of the order of the geomagnetic field (Dunlop and Kletetschka, 2001), the intensity of weak-field TRM and CRM is proportional to the

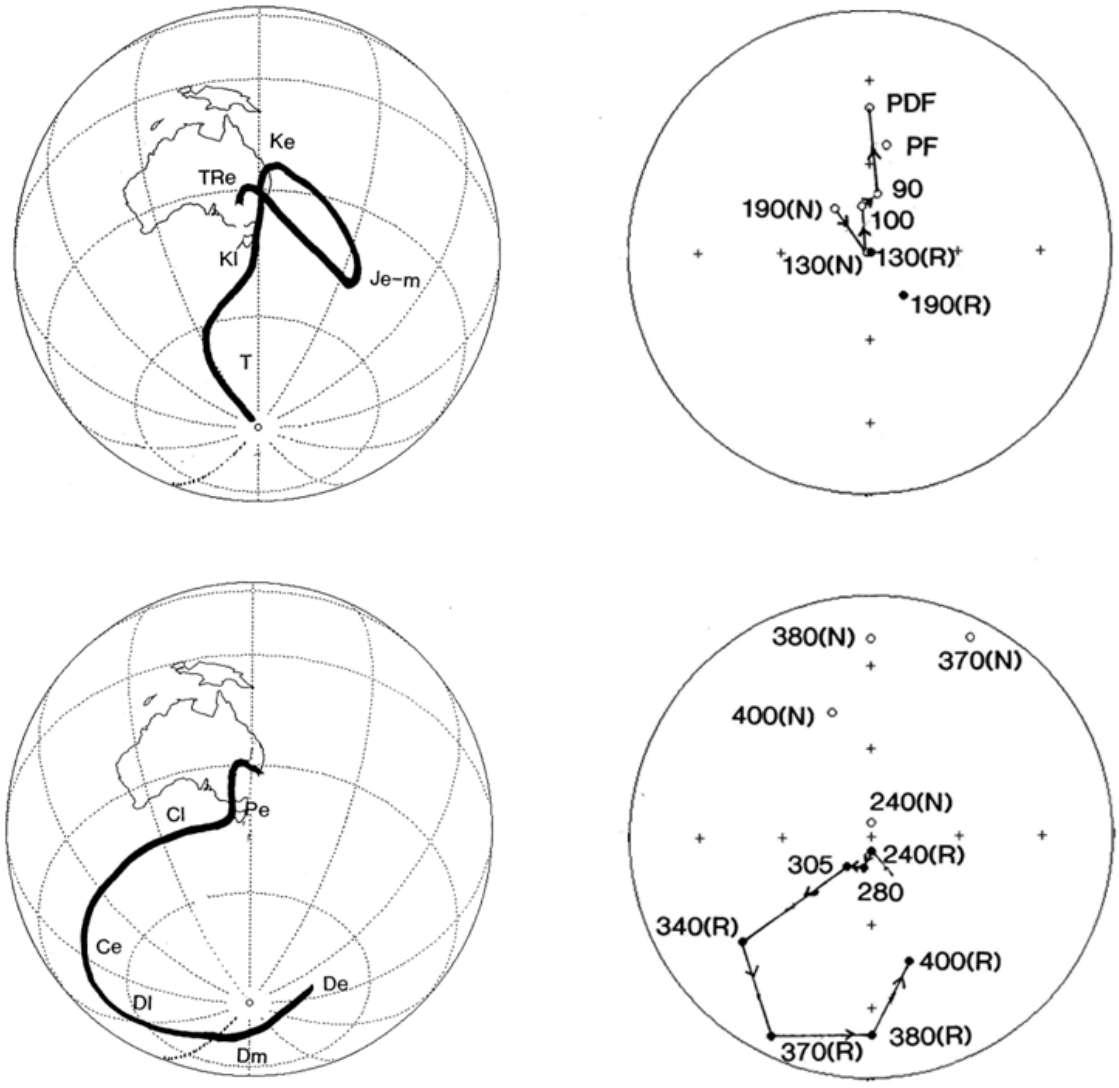

Figure 6. Devonian-present APWP for Australia, based on Schmidt and Clark (2000), (LHS) with corresponding predicted palaeofield directions (RHS) for a site in central Queensland (23°S, 150°E). T = Tertiary (< 65 Ma), Kl = Late Cretaceous (90 & 100 Ma), Ke = Early Cretaceous (130 Ma), Je-m = Early-Middle Jurassic (190 Ma), TRe = Early Triassic (240 Ma), Pe = Early Permian (280 Ma) , Cl = Late Carboniferous (305 Ma), Ce = Early Carboniferous (340 Ma), Dl = Late Devonian (370 Ma), Dm = Middle Devonian (380 Ma), De = Early Devonian (400 Ma); N = normal polarity; R = reversed polarity; PF = present field direction; PDF = present dipole direction, approximating the field direction averaged over the Brunhes chron.

applied field during acquisition. As discussed by Clark et al. (1992), The palaeofield intensity depends principally on two factors: the palaeolatitude, which can be determined from the APWP, and the magnitude of the ancient dipole moment, which is known to have varied through geological time and for which rough estimates are available (McElhinny and McFadden, 2000, p.26).

Koenisberger ratio Q reflects composition and microstructure of magnetic carriers. High Q and strong specific NRM intensity is associated with:

- Ultrafine (< 10 µm) (titano)magnetite and deuterically oxidised titanomagnetite with ilmenite lamellae,
- Monoclinic pyrrhotite of all grain sizes (but *Q* is particularly high for fine grains),
- PSD-MD (> 15 µm) hematite *carrying thermoremanence*, particularly martite with relict magnetite and/or maghemite. Maximum TRM intensity is acquired by hematite grains that are 100 µm in size, or larger. Note that the remanence intensity – size relationship is opposite for magnetite and hematite,
- Hemo-ilmenite (ferrian ilmenite with fine exsolution lamellae of titanohematite) and ilmeno-hematite (titanohematite with ilmenite exsolution).

Ferromagnetic intermediate to felsic granitoid rocks contain multidomain magnetite, which is associated with Koenigsberger ratios less than unity (usually Q < 0.5, typically Q ~ 0.2). Furthermore, the remanence carried by such grains is generally unstable and is dominated by viscous remanence acquired in the recent field. However some, but not all, gabbros, norites and mafic diorites contain ultrafine pseudosingle domain to single domain magnetite hosted within silicate minerals, such as pyroxenes, olivine or plagioclase, as well as discrete multidomain grains. The ultrafine (<10 µm) grains are capable of carrying intense remanence and these rocks may accordingly exhibit Q values substantially greater than unity. Thus magnetisation by induction can be assumed as a first approximation for the more felsic granitoids, whereas remanent magnetisation, possibly oblique to the present field, may be significant for mafic plutonic rocks.

High Koenigsberger ratios are typical for fresh volcanic rocks that contain primary (titano)magnetite. This includes nearly all basalts and andesites, as well as felsic volcanics that belong to relatively oxidised magmatic suites. In the oceanic crust, the mid-ocean ridge basalts, sheeted dykes, and underlying gabbros all carry significant stable remanence,

typically dominating the induced magnetisation (Pariso and Johnson, 1993). All three layers contribute to the ridge-parallel magnetic stripes – the anomalies, approximately symmetric about the ridge, that reflect geomagnetic reversals as newly formed oceanic crust migrates away from the mid-ocean ridge.

BIF is another important rock type for which remanence makes an important contribution to anomalies. The remanence often lies close to the bedding plane. BIFs are highly anisotropic, with the susceptibility parallel to bedding typically 2-4 times larger than that normal to bedding, and often have Koenigsberger ratios in the range 1-2 (Clark and Schmidt, 1994).

Clark (1983), Thompson et al. (1991), Clark and Tonkin (1994), Pucher (1994), Airo and Louskola-Ruskeeniemi (2004), and Direen et al. (2008) have presented case studies of remanence-dominated anomalies due to pyrrhotite. Such anomalies are often associated with metasediments derived from reduced protoliths, such as carbonaceous shales and siltstones; within contact metamorphosed pyritic sediments around large intrusions; in reduced skarn deposits (e.g. Sn- and Sn-W skarns; Au-bearing distal skarns associated with reduced intrusions); in some volcanogenic massive sulphide deposits; in nickel sulphide orebodies; and in some relatively reduced IOCG deposits that have a magnetite + pyrrhotite assemblage, rather than magnetite + hematite.

Intense remanence carried by finely exsolved hemo-ilmenite and ilmeno-hematite is attributed to the recently recognised mechanism of lamellar magnetism (Robinson et al., 2004). Remanence-dominated anomalies due to these mineral phases are associated with (i) high metamorphic grade rocks derived from highly oxidised protoliths, (ii) anorthosites, (iii) certain layered mafic intrusions, and (iv) ilmenite ores occurring as cumulates within mafic layered intrusions (Brown and McEnroe, 2008; McEnroe et al., 2009a,b).

Most unmetamorphosed volcanic rocks and many unmetamorphosed mafic/intermediate intrusive rocks are likely to carry a TRM dating from the time of formation. High grade metamorphic rocks may carry thermo- or thermochemical remanence acquired during post-metamorphic cooling. Pyrrhotite bearing rocks are expected to carry remanence dating from the time of cooling after the last thermal event of ≥ 300°C they have experienced.

Some general points about estimating magnetic properties from petrographic data and information about geological history include:

1. Except where ultrafine magnetic grains are abundant, good petrographic information on magnetic mineral composition, modal abundance and grain size range allows reasonably reliable estimation of susceptibility.
2. It is very useful to supplement reflected light petrography with microprobe analyses, and particularly with rock magnetic characterisation of compositions and domain states of magnetic minerals, which can provide definitive information on relative contributions of different phases and/or grain size populations and detect particles that are too small to identify petrographically.
3. Estimation of remanence intensities from petrographic information and geological history is more complex, and subject to much greater uncertainties, than estimation of susceptibilities.
4. However, in principle the remanence intensity for a simple NRM (e.g. a thermoremanence of an igneous intrusion unaffected by subsequent metamorphism or metasomatism) can be estimated by multiplying the specific remanence intensities for each of the magnetic minerals in the rock by their volume proportions, normalising for the palaeofield intensity (if known). Specific remanence intensities for the most common magnetic minerals are discussed above; a more comprehensive compilation can be found in Clark (1997). The palaeofield intensity reflects the palaeolatitude of the site, which can be estimated from palaeomagnetic data and the geomagnetic dipole moment at the time of remanence acquisition.
5. Remanence is particularly strong when acquired at high latitudes at a time of high geomagnetic dipole moment. The inclination dependence of the time-averaged field accounts for a factor of two between the poles and the equator. Thus the Koenigsberger ratio corresponding to a particular mineral and type of stable remanence can vary by a factor of up to four, if the terrane has moved far with respect to the pole since acquisition (Q is doubled for movement from the pole to the equator and halved for the opposite migration).
6. For a given remanence intensity, the Koenigsberger ratio depends on the present field intensity, as well as the susceptibility. To first order the present field intensity reflects latitude. Large areas of interest to explorers for mineral deposits such as

porphyry, epithermal and IOCG deposits are in low latitudes with correspondingly low geomagnetic inclinations that present problems for magnetic interpretation.

7. Furthermore some substantial areas in South America and southern Africa have anomalously low field intensities, which tends to increase the relative importance of remanence acquired when the local field was stronger (either acquired in higher latitudes or when the dipole moment was stronger). This effect may explain the substantially higher *Q* values for southern African kimberlites compared to Siberian kimberlites (Clark et al., 1992). Mesozoic kimberlites in Africa acquired remanence in relatively high latitudes, but now sit in an anomalously low field, whereas Devonian kimberlites in Siberia acquired remanence in low latitudes at a time of relatively low dipole moment, but now sit in high latitudes with a particularly strong field.

CONSTRAINED MODELLING OF MAGNETIC SOURCES

Determination of magnetisation direction from analysis of magnetic anomalies has a long history, dating back at least to Hall (1959). Modelling of magnetic anomalies without independent geological information can be ambiguous. For example, the magnetisation direction of a semi-infinite dipping sheet cannot be uniquely determined from its anomaly, unless the dip is known (see Figure 7). If the sheet also produces a well-defined gravity anomaly, however, the dip is constrained and the ambiguity is resolved. In this case the magnetisation direction within the plane normal to strike can be determined by applying Poisson's theorem (see below). Of course, any other method that determines the dip, such as drill hole intersections or seismic data, also suffices to determine the effective magnetisation in the plane perpendicular to strike, $\mathbf{M}_{\perp}$.

In the following a "compact source" is a magnetised body that can be totally enclosed by a sphere (or a circle in the 2D case) for which the closest point of approach of the magnetic sensor to its surface is several times the sphere radius. For isolated compact sources, the magnetic moment and direction of magnetisation (3D case), or the magnetic moment per unit length and magnetisation direction projected onto the plane normal to strike (2D case), can be modelled accurately without any knowledge of the size and shape of the source. On the other hand, if the geometry of an arbitrary homogeneous source is known (e.g. defined by drilling or other geophysical methods) determination of the magnetisation of the source

from the observed anomaly is a straightforward linear inversion problem (Bott, 1973; Blakely, 1996, p.225-228).

Inversion of potential field data, including magnetic, is fundamentally non-unique. Perhaps the most basic form of non-uniqueness results from the fact that magnetic anomalies arise from lateral magnetisation contrasts, rather than absolute magnetisations. Although this should always borne in mind, in many cases the magnetisation of host rocks surrounding a magnetic source can be safely assumed to be negligible (e.g. if the host rocks are known to be weakly magnetic sediments), or is known from sampling. If a discrete magnetic anomaly occurs within a featureless magnetic background, the background magnetisation is almost certainly small, because naturally occurring heterogeneity of magnetic rocks always gives rise to some measurable magnetic variations.

The existence of magnetic annihilators, i.e. idealised magnetisation distributions that produce no external anomaly, precludes determination of the complete magnetisation distribution in all circumstances. If in addition to a magnetic source that produces an anomaly there is, for example, a uniformly magnetised horizontal layer of uniform thickness, the magnetisation of that layer contributes nothing to the observed field and cannot be deduced from it. There are many circumstances, however, in which the inherent non-uniqueness of magnetic inversion is not as serious a problem as is commonly suggested, as some important information can be extracted without any *a priori* information and even minimal additional information can greatly constrain acceptable models (Saltus and Blakely, 2011).

Anomalies that clearly arise from topographic features provide especially simple analyses, because the surrounding medium (air on land, seawater in the case of seamounts) has zero magnetisation and the shape of the source, or at least its upper surface, is clearly defined. In an early study of this type, Richards et al. (1967) derived average magnetisations for 21 seamounts, a laccolith and two volcanoes, assuming uniform magnetisation, and obtained results that could be sensibly interpreted in terms of petrophysical and palaeomagnetic information. Emilia and Massey (1974) modified this approach by relaxing the requirement for uniform magnetisation, inverting instead for the distribution of magnetisation intensity and for the direction of magnetisation, assuming that this is uniform. Parker et al. (1987) presented a method that inverts for the non-uniform

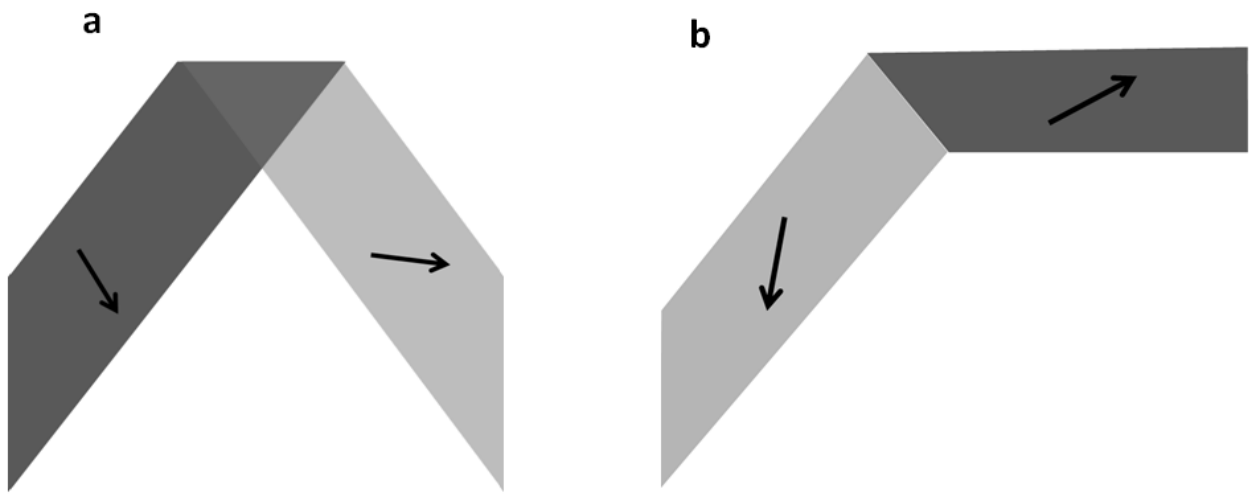

Fig.7 Strictly equivalent 2D sources: (a) equivalent dipping sheets, (b) equivalent sloping step and dipping sheet. The dipping sheets have infinite depth extent, the sloping step extends to infinity towards the RHS. Radhakrishna Murthy (1985) showed that any two dipping sheets, with differing magnetisations, that form an anticline are equivalent to a step whose sloping face coincides with the axial plane of the anticline.

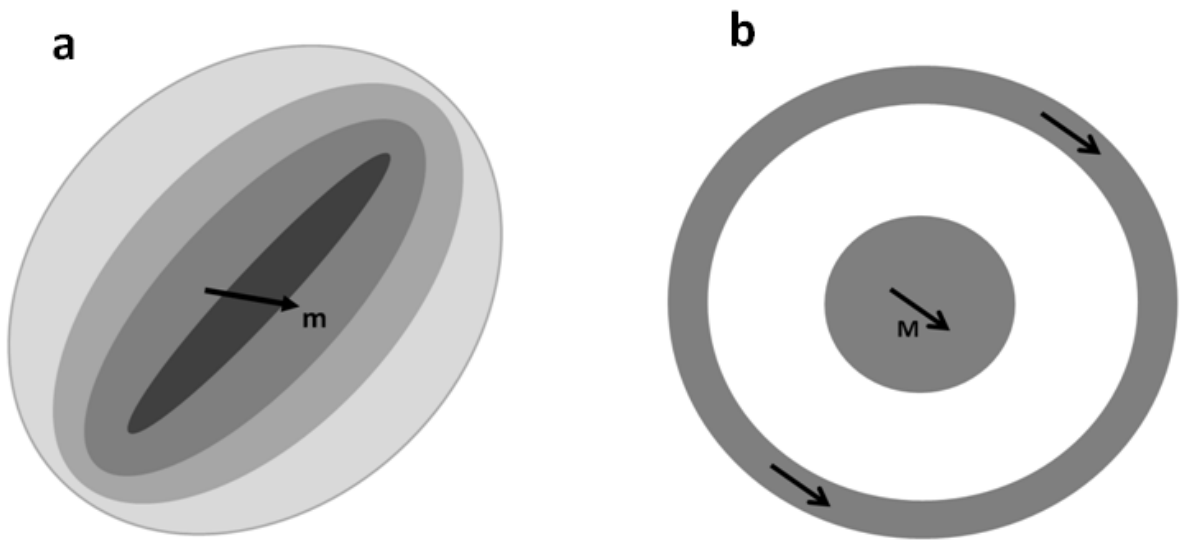

Figure 8. (a) Equivalent 3D confocal ellipsoids with the same moment **m** = **M*V***, which produce identical anomalies at every external point, (b) spherical shell, equivalent to concentric sphere or spherical shell of different radius or thickness, but same total moment. The equivalence of confocal ellipsoids follows from the expressions of Clark et al. (1986).

magnetisation *vector* distribution that (i) best fits the data, and (ii) is closest to a uniform distribution. This method produced an estimate of the mean magnetisation vector of a seamount that was much closer to that expected from palaeomagnetic data than an estimate obtained assuming uniform magnetisation.

Woodward (1993) described a method that infers variations in near-surface apparent magnetisation, using digital terrain models, assigned lithologies based on geological information, and magnetic survey data. Like all such methods, the reliability of the results depends on how closely the subsurface conforms to the assumptions of the method, particularly the assumption that the observed anomalies are due to the magnetised topography. The upper surface of the magnetic layer is defined by the topography, the lower surface is either a flat layer or parallel to the upper surface, and the magnetisation is allowed to vary laterally but is assumed constant with depth within this layer. The apparent magnetisations are sensitive to the thickness of the assumed magnetic layer, the form of the lower layer, and reflect long wavelength variations due to deeper sources, so the results can only be regarded as semiquantitative.

The method of Silva and Hohmann (1984) makes a number of simplifying assumptions to produce a map of apparent susceptibility, k_{app}, which approximates true susceptibility in favourable circumstances. The magnetisation is assumed to be induced only, which allows accurate reduction to the pole (RTP), provided the geomagnetic inclination is not too low. The RTP grid is continued downward to the ground surface (or to the top of magnetic basement, if there is nonmagnetic overburden), where it can be interpreted as arising from an assemblage of narrow vertical prisms with vertical magnetisation. This is equivalent to a distribution of magnetic poles on the upper surface, with surface density $\sigma = M_z = k_{\mathrm{app}}F$. In practice the pole distribution can be calculated in the wavenumber domain or by spatial domain convolution filters. The estimated apparent susceptibility approximates the actual susceptibility if remanence is negligible and the magnetic sources have flat tops at a constant level, have vertical sides, and are homogeneous to great depths.

Apparent susceptibility mapping can produce useful pseudo-geological maps from complex magnetic maps, with reasonable inferred susceptibilities. Apart from the obvious problems caused by departures from the underlying assumptions about source geometry, the transformation is inherently unstable, due to noise amplification by the downward

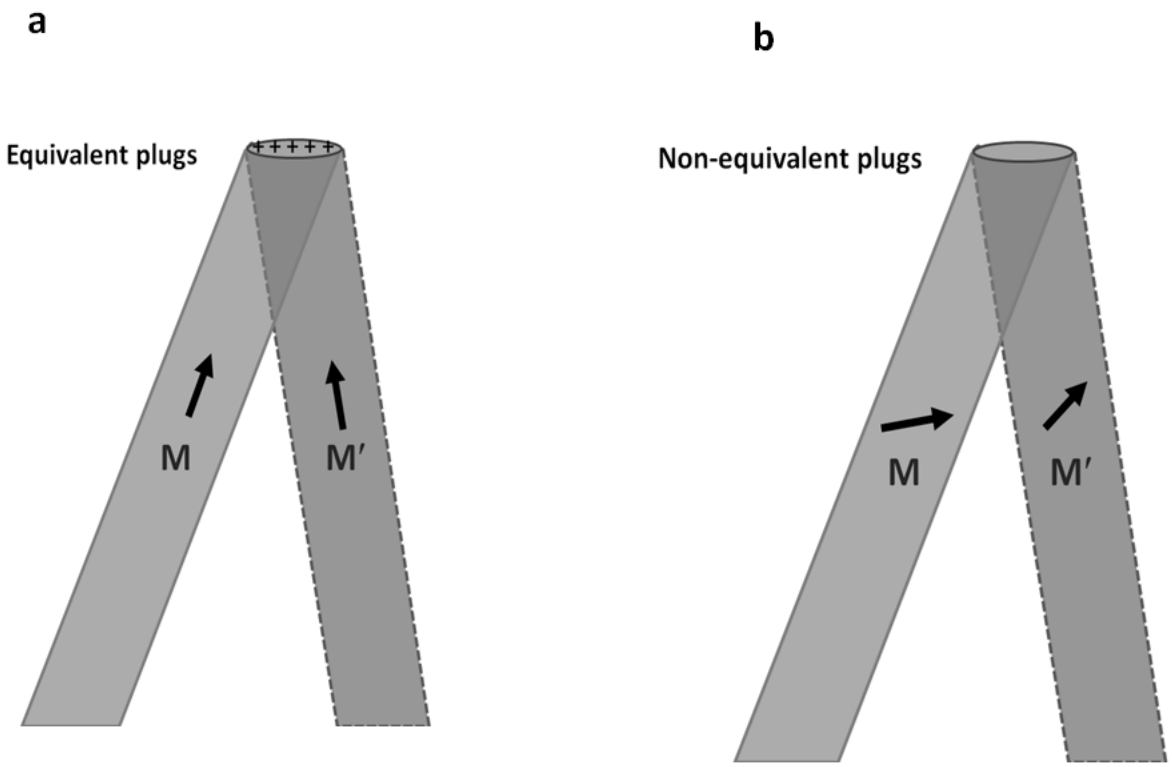

Figure 9. (a) Equivalent plunging pipes of infinite depth extent with axial magnetisation, (b) non-equivalent pipes with non-axial magnetisations. For case (a) the anomaly arises purely from the poles induced on the top surface of the pipes. Since both pipes produce an identical pole distribution, their anomalies are identical. When there is a non-axial component of magnetisation, as shown in (b), the poles induced on the flanks of the pipes ensure that pipes with different plunges produce different anomaly patterns over the measurement plane.

continuation, and must be carefully regularised. Apparent susceptibility values are subject to an offset if the correct base level is not subtracted from the magnetic field. The correct base level should correspond to zero susceptibility wherever the magnetic field is essentially featureless. Provided the correct zero susceptibility areas are identified, other features that exhibit negative apparent susceptibilities represent sources with dominant remanence of overall reverse polarity.

Silva et al. (2010) have further developed the apparent susceptibility mapping method by employing entropic regularisation to produce solutions characterised by regions with almost constant magnetisations, separated by sharp discontinuities. As for other apparent magnetisation mapping methods the interpretation model is a grid of flat-topped vertical, juxtaposed prisms in both horizontal directions, but Silva et al. (2010) assume known constant depth to the bottoms of the prisms, as well as to the tops, rather than assuming bottomless prisms.

The apparent susceptibility mapping method can be extended to the case of variable depth to magnetic basement (Pilkington, 1989). This introduces an extra degree of freedom to the solution, because to each solution an arbitrary amount of magnetic annihilator, appropriate to the basement topography, can be added without affecting the measured field. The annihilator is determined by inverting the magnetisation distribution for the topography, using a starting model of uniform nonzero magnetisation, assuming zero field over the area. For his study area, Pilkington (1989) estimated the amount of annihilator to be added to the inversion solution by modelling several discrete anomalies to estimate absolute magnetisations at selected points.

There is vast literature on inversion of magnetic survey data (see e.g. Li (2012) and references therein), most of which concentrates on solving for source location and geometry and is therefore beyond the scope of this review, which is concerned with determination of source magnetisation. A number of points can be made about estimation of magnetisation by unconstrained inversion of magnetic anomaly data.

1. In general non-uniqueness is much more serious for inversion of source geometry than for determination of magnetisation. Magnetisation direction is often uniquely determined, even though magnetisation intensity may not be.

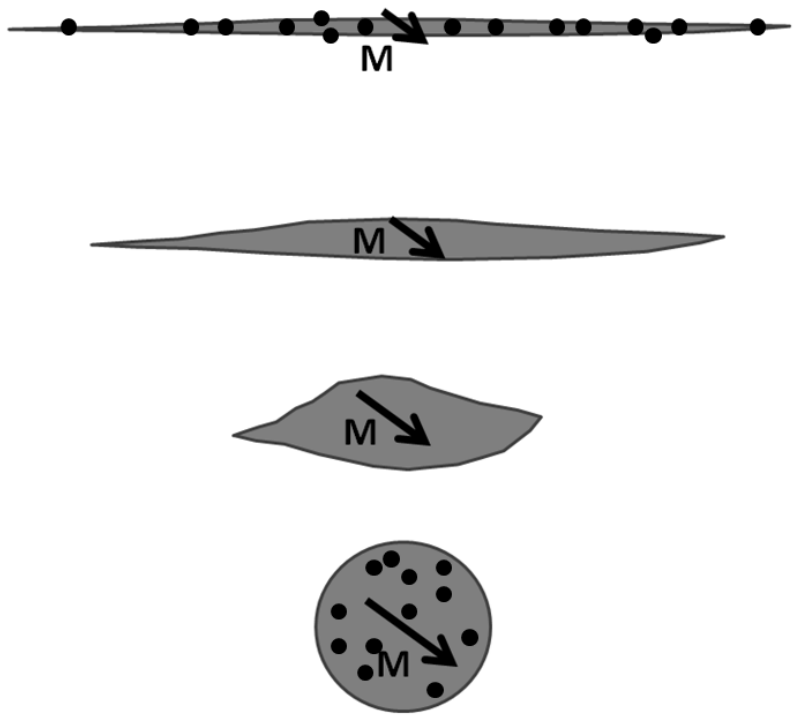

Figure 10. Equivalent lenses at different depths. If the sources are homogeneous with smooth boundaries, the shallower, broader sources mimic deeper, more compact sources with higher magnetisation intensity, but identical moment. Given typical naturally occurring heterogeneity (indicated by dots that represent strongly magnetised portions of the sources) and irregularity of boundaries for real sources, however, the anomalies of the shallowest sources exhibit short wavelength “geological noise”, superimposed on the smooth long wavelength anomaly, that is absent from anomalies due to deep sources.

2. For 2D sources, the along-strike component of magnetisation does not contribute to the observed anomaly, so this component is indeterminate. For approximately 2D sources that have segments with differing strikes, this indeterminacy can be overcome in principle, provided the source has a consistent magnetisation direction throughout. For example, Tucker (1972) deduced the magnetisation of a magnetic metasedimentary unit that had magnetisation dominated by pre-folding remanence, by modelling magnetic profiles over portions of anticlinal structures with differing strikes. Clark and Schmidt (1994) presented examples of 2D modelling of profiles across folded BIF units of known geometry that enables discrimination between pre- and post-folding remanence and inference of magnetic properties.
3. For 2D sources with compact cross-section, the direction, but not the intensity, of $\mathbf{M}_\perp$ is uniquely determined, as is the product $|\boldsymbol{M}_\perp|A$, where A is the cross-section area of the source.
4. For a non-compact, but depth-limited, homogeneous 2D source with planar boundaries and no cavities or re-entrant flanks, such that it can be represented by a polygonal cross-section with a few sides, the geometry is in principle uniquely determinable from a long noise-free profile (Al-Chalabi, 1971). Therefore the effective magnetisation vector $\mathbf{M}_\perp$ is also determinable by linear inversion.
5. Canonical examples of strictly equivalent laterally bounded and depth-limited sources, such as 2D concentric cylinders and confocal elliptical cylinders, and 3D concentric spheres and confocal ellipsoids, as shown in Figure 8, have smooth curved surfaces. Thus they can be regarded as having an infinite number of sides, which makes unique inversion of the geometry impossible. However the effective magnetic moment per unit strike length $|\mathbf{M}_\perp|A$ (in the 2D case) and the magnetic moment $\mathbf{m} = \mathbf{M}V$ (in the 3D case, where V is the volume) are uniquely determined by the magnetic anomaly.
6. For 2D sources of infinite extent perpendicular to strike, such as dipping sheets of infinite depth extent or sloping steps of semi-infinite horizontal extent, the direction of magnetisation is indeterminate unless the dip of the sheet or of the sloping face of the step are known independently (Figure 7), as shown by Radhakrishna Murthy (1985). However the magnetisation-thickness product is uniquely determined. This parameter can be resolved into magnetisation intensity and thickness if the body is not too thin (i.e. if thickness > depth).

7. For 3D compact sources of arbitrary shape the magnetic moment **m** = **M***V* is uniquely determined, but cannot be resolved into magnetisation intensity and volume unless independent information about body dimensions is available.
8. For non-compact depth-limited 3D sources without cavities, re-entrant flanks or pathological shapes (such that all vertical lines pass through at most a single line segment of the body) *with specified density*, the geometry can in principle be uniquely determined from its gravity anomaly (Silva et al., 2002). Poisson's theorem, which is given in the next section, implies a similar conclusion for the magnetic field produced by a similar source *with specified magnetisation intensity*. For example, the ambiguity between the equivalent confocal ellipsoids shown in Figure 8(a) is resolved if the magnetisation intensity is specified. Figure 8(b) demonstrates the necessity for the source to have no cavities, as a hollow sphere can produce the same anomaly as a smaller concentric solid sphere that has identical magnetisation intensity, as well as direction.
9. For non-compact depth-limited 3D sources that can be represented by a homogeneous polyhedron (i.e. its boundaries are essentially planar with straight edges), without cavities, re-entrant *flanks or pathological* shapes, the geometry and density contrast can in principle be uniquely determined from its gravity anomaly (Silva et al., 2002). Applying Poisson's theorem to this result implies that, given some reasonable restrictions on allowable shap*es, the geometry and magnetisation con*trast of a homogeneous polyhedral source can in principle be uniquely determined from its magnetic anomaly. Because many sources are fault-bounded, intruded along planes of weakness, or otherwise controlled by more-or-less planar structures, these restrictions are not as artificial as they might seem.
10. The theoretical uniqueness of inversion for 3D polyhedral bodies partially breaks down for bodies of infinite depth extent, but is not as serious as in the 2D case. For example bottomless pipe-like bodies with different plunges, but identical upper faces, are indistinguishable if they happen to be axially magnetised (i.e. the magnetisation is up- or down-plunge), as shown in Figure 9(a). However the plunge and magnetisation can be resolved independently, provided there is a significant magnetisation component perpendicular to the plunge (Figure 9(b)). Well-defined gravity anomalies can distinguish otherwise equivalent axially magnetised pipes, provided they have sufficient density contrast.

11. Medeiros and Silva (1995) show that the magnetic moment, magnetisation direction, centroid location, and orientation of symmetry axes for an important class of 3D sources can be determined from a magnetic survey over a plane above a discrete source. The method assumes (i) the magnetisation is uniform in direction, but not necessarily in intensity, (ii) the source is finite, (iii) the source is sufficiently distant from the measurement plane that octupole and higher order multipole moments can be neglected, (iv) the source has orthorhombic or higher symmetry (e.g. homogeneous or symmetrically zoned ellipsoids, finite prisms, finite elliptic cylinders). The source can also be disjoint. For example two equidimensional pods, close to one another, satisfy (iv). In practice requirement (iii) is not very stringent – the method is accurate if the depth to the centre of magnetisation is greater than the radius of the smallest sphere that can enclose the source. If original observation plane does not comply with this criterion, requirement (iii) can be satisfied after upward continuation. Subject to requirement (iv), the method is independent of the shape of the source. For deep, compact, or equidimensional sources the orientation estimates are imprecise, but the magnetic moment vector is robust. Medeiros and Silva (1995) report that accurate and robust estimates of the magnetisation direction and of the horizontal location of the centre of dipole moment on the observation plane are still possible when the source is too shallow and the assumption of symmetry is no longer true, or when the direction of magnetisation is not constant. In the case of variable magnetisation direction, good and stable estimates are obtained for the mean magnetisation direction.
12. The theoretical equivalence of deep compact sources and shallower broader sources, as depicted in Figure 10, assumes homogeneity and shapes that are contrived to produce identical anomalies. The magnetic moment is defined by the anomaly, but sources at different depths have different volumes. This implies that the magnetisation direction, but not the intensity, is uniquely determined from the anomaly, unless the depth to the top of the source is constrained. Saltus and Blakely (2011) demonstrate that slight departures from the idealised shape for the relatively shallow “equivalent” bodies produce short wavelength anomalies superimposed on the deep body signature, enabling shallow sources to be distinguished from deep ones. Similarly, the natural heterogeneity of real sources, shown schematically in Figure 10, allows discrimination of ostensibly equivalent shallow sources from deep sources, which helps to constrain the intensity of magnetisation.

In practice, estimation of magnetisation by inversion of magnetic anomalies requires that the assumptions made in the analysis, as discussed above, are at least approximately satisfied, the data coverage and quality are adequate, and the inversion algorithm is numerically stable. Even when inverted source geometry is subject to large uncertainties, inverted magnetisation directions are relatively robust. Many forward modelling and inversion studies on synthetic and field data (e.g. Foss, 2006; Li et al., 2010; Foss and McKenzie, 2011; Foss et al., 2012; Pratt et al., 2012) have confirmed the reliability of inversion of discrete magnetic anomalies for magnetisation when, as commonly occurs, the criteria discussed above are fulfilled. As an example, Pratt et al. (2012) used inverted source magnetisations, the known induced magnetisation direction, and palaeofield directions for a range of ages, to infer plausible ages and magnetic properties for some igneous plugs.

When remanence or self-demagnetisation effects are important, inversions that assume magnetisation parallel to the geomagnetic field, and seek to determine a susceptibility distribution from the magnetic survey data, are likely to seriously mislead interpretation. Clearly, it is better to seek the subsurface distribution of the magnetisation vector, if possible. Recent studies have demonstrated the utility and robustness, if suitably constrained, of inversion of magnetic survey data over substantial areas for the subsurface distribution of magnetisation vectors (Ellis et al., 2012; Liu et al., 2013; MacLeod and Ellis, 2013). An alternative to inverting directly for a subsurface distribution of magnetisation vectors is a two stage process that first inverts a transformed parameter that is weakly dependent on magnetisation direction to define source geometry, then uses this geometry to invert the original data for the magnetisation. Li et al. (2010) recommend the magnitude of the magnetic anomaly vector, $|\mathbf{b}|$, as a suitable parameter for inversion of source geometry. Liu et al. (2013) inverted $|\mathbf{b}|$ measured downhole to invert for a 2D distribution of effective magnetisation vector.

It should be noted , however, that total *in situ* magnetisation is not an intrinsic rock property, and magnetisation inversions are therefore less closely related to geology than a susceptibility model. In a highly magnetic environment, where non-uniform magnetisation reflects inhomogeneous self-demagnetising and interaction fields but for which remanence can be neglected, it is therefore desirable to invert for a susceptibility distribution that

explains the overall variations in magnetisation direction and intensity, rather than attempting to interpret the inverted magnetisation distribution (Fullagar and Pears, 2013). For example, a deposit of semi-massive to massive coarse-grained hydrothermal magnetite is best interpreted in terms of a susceptibility distribution, which can then be related directly to magnetite content.

Rather than attempt to invert for the subsurface magnetisation distribution, an alternative approach to analysing anomalies due to isolated sources is to determine the magnetisation distribution of a layer of equivalent sources, without any *a priori* information about the source, under the assumption of a constant direction of magnetisation. Although this equivalent source distribution bears no resemblance to the actual source geometry, the magnetisation direction (provided it is uniform throughout the source) is accurately estimated. Nicolosi et al. (2006) presented an equivalent source method that is suitable for the interpretation of isolated magnetic sources for which magnetisation is expected to be uniform in direction, but not necessarily in intensity. Once the magnetisation direction that best fits the measured data is determined, this information can be used to constrain forward modelling or inversion for the source geometry.

DIRECT INVERSIONS FOR SIMPLE SOURCES

The point dipole model, which has a multitude of applications, is applicable to any sufficiently compact magnetised body. Outside a spherical surface that completely encloses an arbitrary magnetised body, the field can be expressed as a sum of multipole contributions, with a $1/r^3$ fall-off for the dipole term, $1/r^4$ fall-off for the quadrupole, $1/r^5$ fall-off for the octupole term, and so on. The quadrupole term is equivalent to the effect of adjacent, oppositely directed, dipoles; the octupole term is equivalent to the effect of adjacent, oppositely directed, quadrupoles. As an example consider a compact source that has a consistent magnetisation direction throughout, but comprises a subvolume with relatively weak magnetisation, with the rest of the body having a stronger magnetisation. To first order, the near-field of this source is a dipole field, with dipole moment parallel to the magnetisation and located at the centre of the body, but a better representation of the near-field, corresponding to second order terms in the multipole expansion, would be a dipole source supplemented by a quadrupole contribution.

However, for any compact body with a non-zero dipole moment the far field is always dominated by the dipole term. More specifically, the external fields and gradients due to a uniformly magnetised sphere are identical to that of a point dipole, because the quadrupole and all higher multipole moments vanish identically. Expressions for the magnetic field component anomalies due to a point dipole with arbitrary orientation of the magnetic moment were derived in a geophysical context by Hall (1959). Wynn (1999) gives a detailed account of methods for determining the location and magnetic moment of dipole sources from magnetic measurements. Clark (2010) developed a novel method for locating a dipole source and estimating its moment vector, in the presence of background interference, from a single profile of gradient tensor measurements.

There are many methods for determining the location of a dipole source and other simple sources such as narrow vertical pipes, 2D thin sheets, 2D contacts, and 2D horizontal cylinders from magnetic data. Examples of commonly used methods include Euler deconvolution and Werner deconvolution (Blakely, 1996, p.242-250). Clark (2012a,b; 2013a) presented some new methods for determining source location from vector or gradient tensor data. Once the location of a dipole is known, its magnetic moment can be calculated simply from the anomalous field vector or its gradient *at any point*. In terms of the field vector **b** and displacement vector **r** from the dipole source to the sensor, the moment **m** is given by:

$$\mathbf{m} = \mathbf{M}V = \frac{r^3}{C}\left[\frac{3\mathbf{b}.\mathbf{r}}{2r^2}\mathbf{r} - \mathbf{b}\right], \tag{31}$$

where V is the volume of the source with average magnetisation **M** and C has the numerical value of 100 if the field is in nT, r is in metres and the moment is in Am². Similarly the moment can be determined from the magnetic gradient tensor $\mathbf{B} = \nabla\mathbf{b} = [B_{ij}]$ ($i,j = x,y,z$) measured at a single point **r**:

$$\mathbf{m} = \frac{r^4}{3C}\left[\mathbf{B}\hat{\mathbf{r}} - \frac{3}{2}(\hat{\mathbf{r}}^T\mathbf{B}\hat{\mathbf{r}})\hat{\mathbf{r}}\right]. \tag{32}$$

In many cases measurements of the anomalous field vector or gradient tensor are not available. However these quantities can be calculated from a sufficiently dense grid of total magnetic intensity (TMI) data as described by Clark (2013a). Equation (31) or (32)

can be applied to multiple observation points within an anomaly and the results averaged to estimate the mean magnetic moment vector.

Clark (2012) noted that the direction of magnetisation of a narrow vertical pipe can be analysed by calculating vertical derivatives of the field or gradient tensor components measured over the pipe. Applying equation (31) with $\partial\mathbf{b}/\partial z$ replacing **b,** or equation (32) to $\partial\mathbf{B}/\partial z$ replacing **B**, yields $\mathbf{m}_L = \mathbf{M}A$, where A is the cross-section area of the pipe.

Clark (2012a) also gave expressions for anomalous vector and tensor components produced by 2D thin sheets, 2D contacts, and 2D horizontal cylinders. Given the locations of the sources, these expressions can be inverted to calculate source strength vectors that are proportional to the magnetisation. The location of the top of a semi-infinite 2D thin sheet can be readily determined from a magnetic profile, independent of the magnetisation direction. Because of the dip/magnetisation direction ambiguity illustrated in Figure 7(a), the magnetisation direction can only be determined if the dip is specified. The magnetic field components measured at point x along the profile can be used to define the magnetisation-thickness product $\mathbf{M}'t$ of a vertical sheet, located at $x = x_0$, $z = -h$, that is equivalent to the actual dipping sheet:

$$\begin{bmatrix} M'_x t \\ M'_z t \end{bmatrix} = -\frac{1}{2C}\begin{bmatrix} h & x - x_0 \\ x - x_0 & -h \end{bmatrix}\begin{bmatrix} b_x \\ b_z \end{bmatrix}. \tag{33}$$

Similarly, the components of $\mathbf{M}'t$ for the equivalent vertical sheet can be calculated from the two independent gradient tensor components:

$$\begin{bmatrix} M'_x t \\ M'_z t \end{bmatrix} = \frac{1}{2C}\begin{bmatrix} 2(x - x_0)h & (x - x_0)^2 - h^2 \\ (x - x_0)^2 - h & -2(x - x_0)h \end{bmatrix}\begin{bmatrix} B_{xx} \\ B_{xz} \end{bmatrix}. \tag{34}$$

If the actual dip of the sheet is known independently, or specified *a priori*, the true magnetisation direction can be obtained from the direction of $\mathbf{M}'$ by rigid rotation about the strike direction until the vertical sheet aligns with the actual sheet.

The same type of analysis can be applied to a thick dipping sheet. Provided the thickness $2b$ is greater than the depth h, the centre of the top of the sheet, the depth and the half-

width b can be readily determined from the magnetic profile. If the origin of the x profile is placed above the centre of the sheet, the magnetisation components obtained from the field components at any point (x, 0) along the profile are:

$$\begin{bmatrix} M'_x \\ M'_z \end{bmatrix} = \frac{1}{2C[(\varphi_2-\varphi_1)^2+\ln^2(r_2/r_1)]}\begin{bmatrix} \varphi_2-\varphi_1 & \ln(r_2/r_1) \\ -\ln(r_2/r_1) & \varphi_2-\varphi_1 \end{bmatrix}\begin{bmatrix} b_x \\ b_z \end{bmatrix}, \tag{35}$$

where $\varphi_{1,2} = \tan^{-1}[(x\pm b)/h]$; $r_{1,2} = \sqrt{[(x\pm b)^2 + h^2]}$.

Similarly the magnetisation components can be calculated from the tensor components at (x, 0):

$$\begin{bmatrix} M'_x \\ M'_z \end{bmatrix} = \frac{1}{4Cb}\begin{bmatrix} 2xh & (x^2-b^2-h^2) \\ (x^2-b^2-h^2) & -2xh \end{bmatrix}\begin{bmatrix} B_{xx} \\ B_{xz} \end{bmatrix}. \tag{36}$$

For a 2D vertical contact of infinite depth extent, with the top corner at $x = x_0$, $z = -h$:

$$\begin{bmatrix} M'_x \\ M'_z \end{bmatrix} = \frac{1}{2C}\begin{bmatrix} -h & x-x_0 \\ x-x_0 & h \end{bmatrix}\begin{bmatrix} B_{xx} \\ B_{xz} \end{bmatrix}. \tag{37}$$

For a 2D horizontal cylinder (equivalent to an infinite line of dipoles) of cross-section area A, with centre at $x = x_0$, $z = -h$, the effective magnetisation direction normal to strike and the effective dipole moment per unit strike length, $\mathbf{M}_\perp A$, can be determined uniquely from the field vector or the gradient tensor:

$$\begin{bmatrix} M_xA \\ M_zA \end{bmatrix} = -\frac{1}{2C}\begin{bmatrix} (x-x_0)^2-h^2 & -2(x-x_0)h \\ -2(x-x_0)h & h^2-(x-x_0)^2 \end{bmatrix}\begin{bmatrix} b_x \\ b_z \end{bmatrix}, \tag{38}$$

$$\begin{bmatrix} M_xA \\ M_zA \end{bmatrix} = \frac{1}{4C}\begin{bmatrix} (x-x_0)[3h^2-(x-x_0)^2] & h[h^2-3(x-x_0)^2] \\ h[h^2-3(x-x_0)^2] & (x-x_0)[(x-x_0)^2-3h^2] \end{bmatrix}\begin{bmatrix} B_{xx} \\ B_{xz} \end{bmatrix}. \tag{39}$$

COMPARING MAGNETIC DATA ACQUIRED PRE- AND POST-MINING

Occasionally good quality magnetic survey data are available before and after removal of a magnetic source. This allows the magnetic signature of the source, clearly separated from background magnetisation, regional gradients and interfering anomalies, to be determined by subtraction. This scenario is more commonly applicable to near-surface geophysical applications where, for example, some unexploded ordnance or a buried steel drum has been excavated after having been located using magnetics.

A particularly interesting scenario involves orebodies that have been extracted since the advent of high resolution magnetic surveys in the 1980s. Comparison of post-extraction survey data with that acquired before mining can define the signature of the missing material. Given the knowledge, acquired during deposit delineation and mining, of the orebody geometry, the bulk *in situ* magnetisation of the orebody can be inferred retrospectively. A detailed model of the magnetisation distribution can be developed using this constraint, supplemented by information on the distribution of magnetic minerals throughout the deposit and on magnetic properties of ore and country rocks, which is often acquired throughout the history of the mine. Hoschke (2013) presented a case history where the bulk magnetisation of the source of a remanence-dominated anomaly, the Red Dome gold skarn deposit in Queensland (Collins, 1987), could be inferred from pre- and post-mining magnetic surveys.

Hashimoto et al. (2011) presented an example of the opposite process, where changes over ten years in the magnetic field recorded over an active volcano record the acquisition of thermoremanence during cooling of newly emplaced near-surface magmatic intrusions.

COMBINED ANALYSIS OF MAGNETIC AND GRAVITY ANOMALIES

When gravity and magnetic anomalies are produced by the same source, with magnetisation contrast $\Delta\mathbf{M}$ and density contrast $\Delta\rho$, information on the magnetisation direction can be obtained by exploiting Poisson's relation between the gravitational potential U and the magnetic scalar potential V (Blakely, 1996, p.91-93):

$$V = -\frac{C\Delta\mathbf{M}.\nabla U}{G\Delta\rho} = -\frac{C\Delta\mathbf{M}.\mathbf{g}}{G\Delta\rho}, \qquad (40)$$

where G is the universal gravitational constant and $\mathbf{g}$ is the anomalous gravitational field vector. Equation (40) states that, at any observation point outside the source, the magnetic scalar potential is proportional to the anomalous gravitational component in the direction of magnetisation. It is valid independent of the form and position of the source, provided the magnetisation and density contrasts are uniform within the volume of the source. In fact this restriction can be relaxed somewhat, as the magnetisation intensity may vary, provided the direction of magnetisation is uniform and $\Delta\mathbf{M}/\Delta\rho$ is constant throughout.

Differentiating equation (40) yields:

$$\mathbf{b} = -\nabla V = \frac{C\Delta\mathbf{M}.\nabla\mathbf{g}}{G\Delta\rho} = \frac{C\Delta\mathbf{M}.\boldsymbol{\Gamma}}{G\Delta\rho}, \tag{41}$$

where $\boldsymbol{\Gamma} = \nabla\mathbf{g}$ is the gravity gradient tensor. In terms of the vertical component of gravity, g_z, which is the quantity measured in conventional gravity surveys:

$$b_z = \frac{C}{G\rho}(M_x\Gamma_{xz} + M_y\Gamma_{yz} + M_z\Gamma_{zz}) = \frac{C}{G\rho}(M_x\frac{\partial g_z}{\partial x} + M_y\frac{\partial g_z}{\partial y} + M_z\frac{\partial g_z}{\partial z}). \tag{42}$$

The RHS of equation (42) can be regarded as the vertical pseudomagnetic anomaly calculated from the observed gravity (Blakely, 1996, p.347). If a linear regression of b_z versus the derivatives of g_z yields a good fit within a coincident magnetic and gravity anomaly, then the assumption of a common source for the anomalies is probably correct. Garland (1951) applied an equivalent relation to equation (42) to measured vertical magnetic field and gravity data, in order to identify likely common gravity and magnetic sources, to test whether the magnetisation direction is close to the geomagnetic field, and to estimate k/ρ when the assumption of induced magnetisation only appears to be justified. This parameter was then used to discriminate between sources of different lithology and identify possible source types. Wilson (1970) showed that equation (42) can be used to separate anomalies due to neighbouring sources with differing magnetisation directions and/or values of $|\Delta\mathbf{M}|/\Delta\rho$, provided the property contrasts are known, and can be used to detect pre-folding remanence that has been rotated into different orientations within a deformed rock unit.

The vertical derivative of the gravity anomaly can be calculated from a grid of g_z by convolution filters or Fourier domain processing or may be directly measured by modern gravity gradiometer surveys; the horizontal derivatives can be obtained by filtering or by numerical differentiation of the g_z grid, or by direct measurement. Application of equation (42) and following equations derived from it require that the magnetic and gravity components are either measured on the same observation surface, or have been analytically continued to the same plane. Blakely (1996, Chapter 12) gives the necessary theory for upward/downward continuation and derivative calculation. The vertical magnetic field component can be derived from a TMI grid by Fourier domain processing, as described by Blakely (1996, pp. 328-329, 342-343), provided the geomagnetic inclination is not too low. Clark (2013a) gives an algorithm for calculating components of **b** from gridded TMI data, including an iterative correction for perturbation of the regional geomagnetic field direction by intense local anomalies.

The relationship between the measured TMI anomaly T, corrected to a true potential field if necessary, and the associated gravity anomaly can be obtained from equation (41):

$$T = \mathbf{b}.\hat{\mathbf{F}} = \frac{C\Delta\mathbf{M}.\nabla\mathbf{g}.\hat{\mathbf{F}}}{G\Delta\rho} = \frac{C\Delta\mathbf{M}.\mathbf{\Gamma}.\hat{\mathbf{F}}}{G\Delta\rho}. \tag{43}$$

From equation (42), the reduced to the pole (RTP) anomaly b_z' is directly proportional to the vertical gradient of the gravity anomaly:

$$b_z' = \frac{C\Delta M_z}{G\Delta\rho}\frac{\partial g_z}{\partial z}. \tag{44}$$

Within a discrete magnetic and gravity anomaly, equation (40) implies that there is a linear relationship between the calculated RTP anomaly and the vertical derivative of gravity, provided (i) the same source gives rise to the magnetic and gravity anomalies, (ii) the magnetisation and density of the source are uniform or, slightly less stringently, the magnetisation direction is uniform and the ratio $|\mathbf{M}|/\rho$ is constant throughout the source, and (iii) the correct direction of magnetisation has been used to calculate the RTP anomaly. Kanasewich and Agarwal (1970) applied the frequency domain equivalent of equation (44), comparing RTP TMI data with pseudomagnetic data calculated from the observed gravity, and obtained a reasonable range of $|\Delta\mathbf{M}|/\Delta\rho$ values for mafic intrusive rocks that

produced the majority of anomalies in an area of northern Saskatchewan. Chandler et al. (1981) applied equation (44) within a moving window, with a constant term added to represent background shifts due to neighbouring or deeper sources, to identify common gravity and magnetic sources and to estimate $|\mathbf{M}|/\rho$ variations over extensive areas.

Muniruzzaman and Banks (1989) compared the pseudomagnetic field (calculated from the gravity field assuming vertical magnetisation) and the RTP magnetic field, in the frequency domain. This method searches for the magnetisation direction that, when used for calculating the RTP anomaly, maximises its correlation with the pseudomagnetic field. Ates and Kearey (1995) and Bilim and Ates (2004) used an alternative approach that cross-correlates the observed gravity and the pseudogravity, calculated from the measured magnetic anomaly using a range of assumed magnetisation directions. Which approach is to be preferred depends on the noise characteristics of the data. The pseudomagnetic transform amplifies short wavelength noise in the gravity data, whereas the pseudogravity transform amplifies long wavelength contamination of the magnetic field.

Trialling different directions of magnetisation, until the best fit to equation (44) is obtained, affords a way of estimating the direction of magnetisation of the source, as well as the value of $|\Delta\mathbf{M}|/\Delta\rho$. However in favourable circumstances b_z can be calculated independently of any assumptions about magnetisation direction, so equation (38) can be applied to suitably processed magnetic and gravity grids to obtain least-squares best-fit estimates of $\Delta M_i/\Delta\rho$ ($i = x, y, z$) from which the direction of magnetisation and $|\Delta\mathbf{M}|/\Delta\rho$ can be determined. Lundbak (1956) applied this method to deduce the resultant magnetisation directions and anomalous magnetisation/density ratios of deeply buried basement sources in Denmark and northern Holland and to infer possible remanence directions of the sources. Application of equation (43) to TMI data is slightly more complicated, because all elements of the gravity gradient tensor, either measured or calculated, are required to solve for the components of $\Delta\mathbf{M}/\Delta\rho$.

Mendonça (2004) developed a method for determination of the magnetisation-density ratio and the inclination of the effective magnetisation for 2D sources. The magnetisation-density ratio can be determined independently of the actual magnetisation direction, since the magnitude of the anomalous magnetic field vector $|\mathbf{b}|$ is independent of $\hat{\mathbf{M}}$ for 2D sources, and is given by:

$$\frac{\Delta M}{\Delta\rho} = \frac{G\,|\,\mathbf{b}\,|}{C\,|\,\nabla g_z\,|} = \frac{G\,|\sqrt{b_x^2 + b_z^2}}{C\,|\sqrt{\Gamma_{xz}^2 + \Gamma_{zz}^2}}. \tag{45}$$

From equation (42), if the magnetisation is vertical, the anomalous magnetic vector $\mathbf{b}'$ is related to the gravity anomaly by:

$$\mathbf{b}' = \frac{C\Delta M_z}{G\Delta\rho}\nabla g_z. \tag{46}$$

At any point outside a 2D source, the angle between the anomalous magnetic field vectors $\mathbf{b}$ and $\mathbf{b}'$ that obtain for the actual magnetisation direction, and for vertical magnetisation, is everywhere equal to the angle between the actual magnetisation and the vertical down direction. Mendonça (2004) uses this fact and an equivalent to equation (42) to show that the apparent inclination of the effective magnetisation $\mathbf{M}_\perp$ is given by:

$$I'_M = 90° - \cos^{-1}\frac{\mathbf{b}.\mathbf{b}'}{|\,\mathbf{b}\,||\,\mathbf{b}'\,|} = 90° - \cos^{-1}\left(\frac{\mathbf{b}.\nabla\mathbf{g}_z}{|\,\mathbf{b}\,||\,\nabla\mathbf{g}_z\,|}\right) = \sin^{-1}\left(\frac{b_x\Gamma_{xz} + b_z\Gamma_{zz}}{\sqrt{(b_x^2 + b_z^2)(\Gamma_{xz}^2 + \Gamma_{zz}^2)}}\right). \tag{47}$$

Mendonça and Meguid (2008) extended this approach to 3D and provided computer programs to calculate $\Delta M/\Delta\rho$ and the inclination of magnetisation from the 3D generalisations of equations (46)-(47).

Using frequency domain expressions for derivatives (Blakely, 1996, p.324-326) and taking the Fourier transform of equation (42), gives:

$$\tilde{b}_z(k_x, k_y) = \frac{C}{G\rho}(iM_x k_x + iM_y k_y + M_z\,|\,\mathbf{k}\,|)\tilde{g}_z(k_x, k_y), \tag{48}$$

where k_x, k_y are the wavenumbers along the x and y directions, $|\mathbf{k}| = \sqrt{(k_x^2 + k_y^2)}$, and Fourier transforms are indicated by tildes. Rearranging equation (48) yields a frequency domain expression that can be solved in a least squares sense for the components of $\mathbf{M}/\rho$:

$$i(M_x/\rho)k_x + i(M_y/\rho)k_y + (M_z/\rho)|\mathbf{k}|) = \frac{G}{C}\frac{\tilde{b}_z(k_x,k_y)}{\tilde{g}_z(k_x,k_y)}. \tag{49}$$

A good linear correlation between the Fourier coefficients of b_z and those of the derivatives of g_z over a broad range of wavenumbers validates the assumption of a common source. Kanasewich and Agarwal (1970) assess the validity of the assumptions of the Poisson analysis, using a coherence function given by:

$$Coh^2_{b,g}(k_x,k_x) = \frac{|P_{b,g}(k_x,k_x)|^2}{P_b(k_x,k_x)P_g(k_x,k_x)}, \tag{50}$$

where $P_{b,g}$, P_b, P_g are the cross-power spectrum for b_z and g_z, the auto-power spectrum for b_z, and the auto-power spectrum for g_z respectively.

A smooth systematic change in regression coefficients from small to large wavenumbers can in principle give information about variations of $\mathbf{M}/\rho$ with decreasing depth. Cordell and Taylor (1971) developed Fourier domain relationships between measured TMI (rather than b_z) and gravity anomalies that were similar to, but somewhat more complicated than, equations (44)-(45). They applied these relationships to surveys over seamounts to derive (i) the ratio $|\Delta\mathbf{M}|/\Delta\rho$ (ii) the total magnetisation direction $\Delta\mathbf{M}/|\Delta\mathbf{M}|$, and (iii) the minimum possible value of the Koenigsberger ratio, using equation (11), without any knowledge of the source shape. These authors also pointed out that the direction of remanent magnetisation can be determined using an assigned value or suite of values of Q, using equation (12), and were able to derive plausible palaeomagnetic poles from the seamount data.

The theory behind using Poisson's relation to determine the magnetisation direction of a common gravity and magnetic source implies that, if coincident gravity and magnetic anomalies can be successfully modelled with a geologically plausible common source, then the modelled magnetisation is probably accurate. Schmidt et al. (2007) give an example of a strongly remanently magnetised and dense massive iron oxide deposit for which the magnetic model, constrained by drill intersections, also explained the gravity anomaly using measured ore and host rock densities. The magnetisation required by the model

agreed well with measurements on samples, as expected from the concordance of the magnetic and gravity models.

USING A CONTROLLED MAGNETIC SOURCE

Active source magnetics is a technique that can potentially be applied to mapping subsurface magnetisation distributions using the inhomogeneous time-varying primary field of a loop or dipole source (e.g. a superconducting magnet) and a roving receiver (Schmidt and Clark, 1997; Clark and Schmidt, 1999). Figure 11 illustrates the principle of the method and highlights the differences with other methods. In conventional magnetic surveys, the inducing field is essentially static and uniform, whereas for differential vector magnetometry (DVM) in base station mode (discussed in a later section) the inducing field is uniform but time-varying. In active source magnetics the inhomogeneity of the primary field provides a spatial resolution that overcomes much of the non-uniqueness of interpreted sources in conventional surveys and the time-varying field discriminates between induced and remanent contributions to the anomaly field.

For a compact active source and a compact target, the combination of $1/r^3$ fall-offs from the active source to the target and from the target back to sensor produces an overall $1/r^6$ dependence of the signal. Given this rapid fall-off, this technique is only practicable for fairly shallow sources. The depth of investigation can be increased by using a large loop source, as in a ground transient electromagnetic (TEM) survey, but there is a corresponding loss in spatial resolution of subsurface magnetisation distribution as the applied field is more uniform.

For a 2D geological structure a long current-carrying cable parallel to strike can be used as the exciting source. The fall-off with height above a compact 2D structure is $1/r^4$. Tsirul'skiy (1972) demonstrates the theoretical uniqueness of the magnetic scalar potential (and hence of any field component) along a profile over a homogeneous 2D body with a star domain cross-section. The restriction on the shape of the domain is not too stringent - it requires that there is a point within the cross-section from which a line drawn to any other point in the shape lies totally within the domain. This does not require a polygonal cross-section; it includes all convex homogeneous shapes, for example, as well as non-pathological concave shapes; but excludes hollow shapes. Inversion of controlled source

data over such a structure can define both the shape and the susceptibility. Similar results apply to the 3D case.

Frequency domain EM systems operating at relatively low frequencies can be regarded as giant moving susceptibility meters. Over a homogeneous half-space the low frequency in-phase secondary field, due to magnetisation induced by the primary field, is negative, almost frequency independent, and provides a measure of magnetic susceptibility (Fraser, 1981). Provided the frequency is sufficiently low that the conductivity signal is negligible, the in-phase signal is proportional to k' given by equation (16). The true susceptibility, corrected for self-demagnetisation, is then given by equation (17). Note that the method yields an apparent susceptibility, analogous to apparent resistivity, that will differ from the true susceptibility when the subsurface is inhomogeneous at the scale sampled by the primary field. The approach using half-space models can be extended to simultaneous mapping of susceptibility, resistivity and permittivity using in-phase and quadrature responses from sufficiently broadband multifrequency EM systems (Huang and Fraser, 2000; 2001).

Because lower frequencies penetrate to greater depths than higher frequencies, multifrequency EM data inherently contain information on the depth distribution of susceptibility (Zhang and Oldenburg, 1997; 1999). Those authors developed a method to invert frequency domain EM data from a horizontal co-planar system to yield a 1D distribution of susceptibility, using specified conductivities of the layers. In most circumstances the conductivities must be obtained by other means, such as inversion of resistivity surveys or of broadband EM data. Zhang and Oldenburg (1999) demonstrate the potential for simultaneously extracting information from an EM data set on susceptibility and conductivity structure of a layered earth down to ~150-200 m. Tschirhart et al. (2013) have shown that forward modelling of the magnetic field produced by the shallow susceptibility distribution obtained from inversion of a helicopter-borne frequency domain EM survey provided an estimate of the contribution of shallow sources to the observed TMI data. This method of regional/residual separation can also identify areas where remanence effects are important.

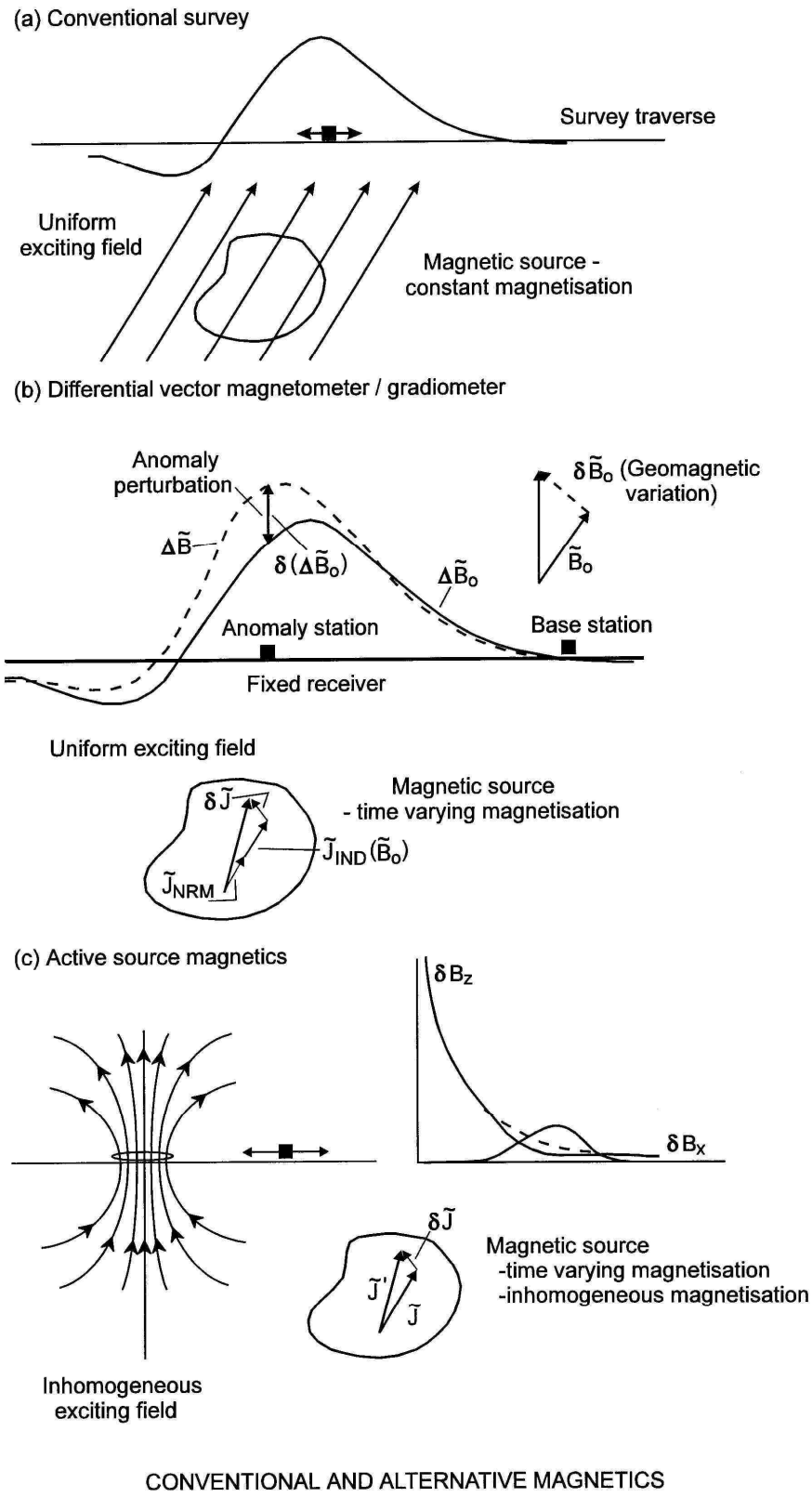

Figure 11. Comparison of (a) conventional magnetic surveys, (b) differential vector magnetometry in base station mode, (c) active source for magnetic tomography.

Pavlov and Zhdanov (2001) showed that the susceptibility of highly magnetic bodies significantly affects time domain EM (TDEM) responses, particularly at late times. The effect is most important for bodies that are both conductive and magnetic. The implication is that TDEM surveys can provide useful information about the subsurface susceptibility distribution and susceptibility should be included in the inversion of TDEM data, as well as conductivity. Zhdanov and Pavlov (2001) developed a method for simultaneously estimating the conductance and susceptibility-thickness product for a conductive and magnetic horizontal thin sheet, using time domain EM data. This method could be a useful complement to a conventional magnetic survey, for which a uniformly magnetised horizontal sheet is undetectable.

The subaudio magnetic (SAM) method of Cattach et al. (1994) could also possibly be adapted to give information about the shallow subsurface susceptibility distribution, using magnetic field measurements made when the positive and negative primary field is on, provided the data are corrected for eddy current and IP effects that are extracted from the data, or wait times are sufficient to allow these EM effects to decay to negligible levels.

The permeability contrast (hence the susceptibility contrast) of a magnetic, conductive buried sphere can, in principle, be determined uniquely from sufficiently broadband EM measurements, without any knowledge of the true location, size or conductivity of the sphere. If the active source applies an effectively uniform alternating primary field at angular frequency ω across the buried sphere, and the horizontal component of the secondary field $H(\omega)$ is measured at any nearby point over a wide range of frequencies, then Ward (1959) showed that:

$$R_H = \frac{H(\omega = 0)}{H(\omega = \infty)} = \frac{-2(\mu_1/\mu_2 - 1)}{\mu_1/\mu_2 + 2}, \qquad (51)$$

where $H(\omega = 0)$ is the horizontal field component extrapolated to zero frequency, $H(\omega = \infty)$ is the horizontal field component extrapolated to infinite frequency, $\mu_1 = \mu_0(1+ k_1)$ is the permeability of the sphere, and $\mu_2 = \mu_0(1+ k_2)$ is the permeability of the host. Validity of

the method requires that displacement currents are negligible (i.e. $\varepsilon_1\omega << \sigma_1$) and that the wavelength in the host medium be much greater than the sphere radius R (i.e. $|(i\sigma_2\mu_2\omega - \varepsilon_2\mu_2\omega^2)^{1/2} R| << 1$). The alternating field can be regarded as quasi-DC if $[\sigma_1\mu_1\omega R^2]^{1/2} < 0.5$ and can be regarded as effectively infinite if $[\sigma_1\mu_1\omega R^2]^{1/2} > 1000$. Thus a frequency range of over six decades would be required to implement Ward's method in its original form. A more sophisticated analysis of measurements made over a smaller frequency range, spanning the transition from a regime where eddy current effects are minor to a regime where eddy currents are significant, could in principle extract the permeability ratio. The analysis can also be applied to a sufficiently strong dipole source of primary field, provided the source is sufficiently distant from the boundary of the sphere. Inverting equation (51) gives:

$$\mu_1 / \mu_2 = \frac{1+k_1}{1+k_2} = \frac{2(1-R_H)}{R_H+2}, \tag{52}$$

which determines the susceptibility of the sphere if the susceptibility of the host rock is known. If the host rock is nonmagnetic, equation (52) reduces to:

$$k_1 = \frac{-3R_H}{R_H+2}. \tag{53}$$

Important features of controlled source methods include:

1. These methods map susceptibility distribution only and are unaffected by remanence. In terrains where magnetite is the most common magnetic mineral, the inverted susceptibility map can be converted to a magnetite concentration map using relations like equation (24).
2. Combining controlled source methods and conventional magnetic surveys can allow separation of induced and remanent contributions to total magnetisation and provide information on the shallow subsurface distribution of remanence magnitude and direction.
3. Controlled source methods are independent of the geomagnetic field direction, unlike conventional magnetics.
4. Controlled source methods sample only the relatively shallow subsurface, whereas conventional magnetic surveys reflect deep as well as shallow sources. The skin

depth $\delta = \sqrt{(2/\sigma_2\mu_2\omega)}$ gives an indication of the depth of penetration of the method. Some resolution of source depth is in principle obtainable within the depth range sampled by the applied field.

5. Controlled source methods generally provide higher spatial resolution than conventional magnetics, because of the localised nature of the exciting field.
6. Controlled source methods are very sensitive to sensor height above the top of the magnetic layer. For closely coupled transmitting and receiving coils with separation s at a height h above a half-space, the secondary field response is proportional to $(s/h)^3$ provided $s << h$ (Huang and Fraser, 2000). In-phase and quadrature responses must be corrected for height variations, although ratios of these components, or of single components at different frequencies, are independent of height.
7. At high frequencies susceptibility mapping using frequency domain EM is affected by subsurface conductivity. An upper limit to the desirable measurement frequency f can be obtained using the dimensionless induction number $\alpha = [2\pi f\sigma\mu h^2]^{½}$, where σ is the subsurface conductivity and $\mu = \mu_0(1+k)$ is the magnetic permeability. The apparent susceptibility is independent of frequency and can be determined uniquely from the in-phase response provided $\alpha < 0.1$. Determination of k is possible provided $\alpha < 4$, which is attainable by normal airborne surveys, even for very conductive terrains, provided $f \leq 900$ Hz (Huang and Fraser, 2000).
8. The reliability of the susceptibilities mapped by controlled source methods is contingent on the validity of the assumptions about homogeneity. For methods based on the half-space model, inverted susceptibilities are only accurate if the subsurface is reasonably homogeneous over the effective lateral extent of the applied field, down to the effective depth of penetration. Similarly, 1D models require lateral homogeneity and, additionally, vertical homogeneity of layers over their resolvable depth extents.

HELBIG-TYPE ANALYSIS OF VECTOR, TENSOR AND TENSOR INVARIANT DATA

In a landmark paper Helbig (1963) investigated the information about a compact magnetised source that could be extracted from integrals of anomalous quantities over a horizontal plane and showed that it was possible in principle to determine the magnetic

moment vector of an arbitrary finite source by calculating various integral moments of magnetic vector components over an entire horizontal plane above the source. It was shown that the mean values over a horizontal plane of anomalous field components due to an arbitrary compact source vanish, which in principle allows the base level for these components to be determined. Furthermore the total dipole moment of the source can be estimated from first order integral moments of measured field components and some information about the "centre of magnetisation" (analogous to a centre of mass for the gravitational case) can be determined from second order integral moments. Andersen and Pedersen (1979) gave a corresponding treatment for 2D sources, incorporating an important correction for finite range of integration.

Helbig (1963) showed that the integrals over the horizontal plane of the anomalous magnetic field components due to a finite source are zero and that some first integral moments of the components are related to the components of the total magnetic moment of the source:

$$\begin{aligned} &\int_{-\infty}^{+\infty}\int_{-\infty}^{+\infty} xb_z\,dxdy = -2\pi Cm_x;\ \int_{-\infty}^{+\infty}\int_{-\infty}^{+\infty} yb_z\,dxdy = -2\pi Cm_y; \\ &\int_{-\infty}^{+\infty}\int_{-\infty}^{+\infty} xb_x\,dxdy = \int_{-\infty}^{+\infty}\int_{-\infty}^{+\infty} yb_y\,dxdy = -2\pi Cm_z. \end{aligned} \tag{54}$$

The other first integral moments of magnetic components are zero.

In its original form, Helbig analysis requires gridded values of all three anomalous magnetic components. The method was largely neglected over subsequent decades, probably because vector data were rarely available. Because measurements of the magnetic field vector are very sensitive to orientation errors, vector magnetic surveys tend to be noisy. It is generally preferable to calculate anomalous magnetic components from high quality TMI data, except near the magnetic equator where the process becomes unstable. This is most easily accomplished using Fourier domain filtering (Lourenço and Morrison, 1973; Blakeley, 1995, p.342-343). Purucker (1990) described and evaluated the strengths and weaknesses of the available methods (Fourier filtering, convolution filtering, and equivalent source techniques) for calculating vector components from TMI. Schmidt and Clark (1998) revived the Helbig method, with some modifications, by applying it to vector

components calculated by Fourier processing of a conventional TMI survey over a strongly remanently magnetised contact aureole and comparing the results with palaeomagnetic measurements. Li et al. (2004) used the Helbig method to estimate magnetisation directions, which were then used to constrain inversion of source geometry. Phillips (2005) developed an algorithm for estimating resultant magnetisation directions from windowed vector magnetic data and demonstrated its applicability to determining magnetization directions for isolated compact sources or for scanning gridded data sets for sources with a specified magnetisation direction. Phillips' (2005) moving window approach can efficiently process datasets over large areas, at the expense of necessarily underestimating magnetic moments due to the limited area of integration, but generally produces robust inverted magnetisation directions. Foss (2006) demonstrated the necessity for good separation of the residual anomaly from the regional trends or interfering anomalies to achieve accurate results from Helbig analysis. Caratori Tontini and Pedersen (2008) gave a method for correcting conventional Helbig analysis of vector components for finite integration area, to give an improved estimate of the total dipole moment and for defining the horizontal and vertical centres of magnetisation of a 3D source. Phillips et al. (2007) extended the Helbig method to calculation of magnetic moments from gridded elements of the magnetic gradient tensor, using the following relations:

$$\begin{aligned}
&\int_{-\infty}^{+\infty}\int_{-\infty}^{+\infty} x^2 B_{xz}\,dxdy = 2\int_{-\infty}^{+\infty}\int_{-\infty}^{+\infty} xyB_{yz}\,dxdy = 4\pi Cm_x,\\
&\int_{-\infty}^{+\infty}\int_{-\infty}^{+\infty} y^2 B_{yz}\,dxdy = 2\int_{-\infty}^{+\infty}\int_{-\infty}^{+\infty} xyB_{xz}\,dxdy = 4\pi Cm_y,\\
&\int_{-\infty}^{+\infty}\int_{-\infty}^{+\infty} x^2 B_{xx}\,dxdy = \int_{-\infty}^{+\infty}\int_{-\infty}^{+\infty} y^2 B_{yy}\,dxdy = 2\int_{-\infty}^{+\infty}\int_{-\infty}^{+\infty} xyB_{xy}\,dxdy,\\
&= -\int_{-\infty}^{+\infty}\int_{-\infty}^{+\infty} x^2 B_{zz}\,dxdy = -\int_{-\infty}^{+\infty}\int_{-\infty}^{+\infty} y^2 B_{zz}\,dxdy = 4\pi Cm_z.
\end{aligned} \tag{55}$$

The integrals of equation (55) converge more slowly than those of equation (54), in spite of the greater compactness of gradient anomalies about the source, due to the higher power of horizontal coordinates in the integrands. If regional gradients have been correctly removed, the other second order integral moments of the tensor elements, as well as all first order moments, are zero. Provided the area of integration is well centred around the source and extends well beyond the horizontal dimensions of the source, and the source can be assumed to be depth limited, with bottom depth comparable to the radius of

integration or smaller, integral moment methods are in principle independent of source geometry. With the above caveats, estimated parameters are quite robust and do not depend on assumptions about source shape and size. The method is sensitive, however, to erroneous base levels in the vector and tensor components, to integration areas that are offset with respect to the source centroid, and to regional trends, which must be removed before applying the method.

Clark (2013b) applied Helbig-type analysis to rotational invariants of the gradient tensor [see Chapter 7]. Integral moments of tensor invariants locate the horizontal and vertical centres of magnetisation and estimate the magnetisation direction. Consider an isolated source with magnetisation **M**, which produces an anomalous field vector **b** and a corresponding anomalous gradient tensor $\mathbf{B} = \nabla\mathbf{b}$. **B** is a symmetric traceless second order tensor, which after diagonalisation can be characterised by its eigenvalues and eigenvectors. Rotational invariants of the tensor, such as the canonical invariants I_1, I_2 of Pedersen and Rasmussen (1990), can always be expressed in terms of the eigenvalues of the tensor. The normalised source strength (NSS) μ is a particularly useful invariant, because it is completely independent of magnetisation direction for a number of simple, but useful source types: spheres, compact sources that can be represented by a dipole, axially magnetised thin pipes, and 2D sources of arbitrary shape (Beiki et al. 2012; Clark, 2012a,b; 2013a,b), and is only weakly dependent on magnetisation direction for 3D sources in general (Pilkington and Beiki, 2012). The NSS is defined by

$$\mu = \sqrt{-\lambda_2^2 - \lambda_1\lambda_3}, \tag{56}$$

where $\lambda_1 \geq \lambda_2 \geq \lambda_3$ are the eigenvalues of the tensor in nonincreasing order, which sum to zero due to the tracelessness of the tensor. For a dipole source at (x_0, y_0, h) the NSS takes the simple form

$$\mu = \frac{3C\,|\mathbf{m}|}{r^4} = \frac{3Cm}{[(x-x_0)^2 + (y-y_0)^2 + h^2]^2}, \tag{57}$$

where r is the distance from the dipole to the measurement point (x,y,0). Clearly from equation (57), the NSS measured over a plane peaks directly over a dipole source (where r is a minimum) and is independent of orientation of **m**. The depth of the dipole is simply

related to the halfwidth of the NSS anomaly. This suggests that measurements of μ over a plane can provide robust estimates of dipole location, unaffected by magnetisation direction.

The intermediate eigenvalue λ_2 for a dipole source is given by Clark (2012a) as

$$\lambda_2 = \mu \cos\phi = \frac{3C\mathbf{m}.\hat{\mathbf{r}}}{r^4}, \tag{58}$$

where ϕ is the angle between the magnetic moment vector and the displacement vector **r** from the dipole to the observation point. Equation 58 shows that λ_2 depends on the orientation of the moment, and therefore can provide information about the magnetisation direction.

The horizontal location (x_0, y_0) of the centre of magnetisation of a laterally finite source can be estimated from first integral moments of μ or μ^2:

$$x_0 = \frac{\int_{-\infty}^{+\infty}\int_{-\infty}^{+\infty} x\mu dxdy}{\int_{-\infty}^{+\infty}\int_{-\infty}^{+\infty} \mu dxdy} = \frac{\int_{-\infty}^{+\infty}\int_{-\infty}^{+\infty} x\mu^2 dxdy}{\int_{-\infty}^{+\infty}\int_{-\infty}^{+\infty} \mu^2 dxdy}, y_0 = \frac{\int_{-\infty}^{+\infty}\int_{-\infty}^{+\infty} y\mu dxdy}{\int_{-\infty}^{+\infty}\int_{-\infty}^{+\infty} \mu dxdy} = \frac{\int_{-\infty}^{+\infty}\int_{-\infty}^{+\infty} y\mu^2 dxdy}{\int_{-\infty}^{+\infty}\int_{-\infty}^{+\infty} \mu^2 dxdy}. \tag{59}$$

In practice the numerical integration is carried out over a finite area to obtain initial estimates of (x_0, y_0). The area of integration is then centred on this point and the integrals recalculated to make any necessary small corrections to the location, which is subsequently used as the origin of coordinates for calculation of all other integral moments. The depth of the centre of magnetisation, h, of a compact source, or an equidimensional source that can be adequately represented by a dipole, can be found from

$$h = \frac{\int_{-\infty}^{+\infty}\int_{-\infty}^{+\infty} \mu dxdy}{\left[3\pi \int_{-\infty}^{+\infty}\int_{-\infty}^{+\infty} \mu^2 dxdy\right]^{1/2}}. \tag{60}$$

The magnitude of the magnetic moment, m, is given by

$$m = \frac{\left[\int_{-\infty}^{+\infty}\int_{-\infty}^{+\infty} \mu dxdy\right]^3}{9\pi^2 C \int_{-\infty}^{+\infty}\int_{-\infty}^{+\infty} \mu^2 dxdy}. \tag{61}$$

Equations (59)-(61) are exact for a point dipole source, which is equivalent to a uniformly magnetised sphere, and is also very accurate for compact sources of arbitrary shape and for fairly equidimensional sources buried at moderate depths, for which the dipole contribution dominates the anomaly. The horizontal location of the centre of magnetisation is also well estimated, even for sources of complex geometry, due to the high centricity of the NSS over arbitrary 3D sources (Pilkington and Beiki, 2012). The depth of the centre of magnetisation can be expected to be reasonably accurate, provided the depth extent of the source is smaller than the radius of integration.

Assuming a source that can be reasonably represented by a dipole the centroid depth estimate itself can be corrected for the finite radius of integration. Such sources range from very compact bodies, even if irregular in shape or non-equidimensional or inhomogeneously magnetised, to large equidimensional, sufficiently uniformly magnetised bodies that can be reasonably represented by a sphere model. This revised depth estimate allows more accurate correction of the integral moments of vector and tensor components, as used in Helbig (1963) analysis and its offshoots, which can also be accurately corrected for the finite radius of integration, allowing numerical integrations to be confined to the main part of the anomaly. This reduces contamination of the integral moments by neighbouring sources and greatly improves parameter estimation.

The first step is to correct the initial estimated depth of the centroid, h', obtained from equation (60) when the integration is performed over a disc of radius R:

$$h' = \frac{\iint_{\rho<R} \mu\rho d\rho d\vartheta}{\left[3\pi \iint_{\rho<R} \mu^2 \rho d\rho d\vartheta\right]^{1/2}} = R\sqrt{\frac{1+(R/h)^2}{3+3(R/h)^2+(R/h)^4}}. \tag{62}$$

In equation (62) ρ and ϑ are polar coordinates centred on (x_0, y_0). Solving equation (62) for the true depth h in terms of the known quantities R and h' gives

$$h = h' \sqrt{\frac{2}{1 - 3(h'/R)^2 + \sqrt{1 - 2(h'/R)^2 - 3(h'/R)^4}}} \tag{63}$$

Once the true depth of the centroid has been estimated, all other integral moments used in the subsequent analysis can be corrected for the finite area of integration using analytic integrals based on the theoretical fall-off rate of a point dipole anomaly, as done for conventional Helbig analysis by Schmidt and Clark (1998) and Caratori Tontini and Pedersen (2008).

While it is often more convenient to carry out 2D integrations over square or rectangular areas, rather than discs, it turns out that the corrections for finite discs and for squares of equivalent area (with side $X = R\sqrt{\pi}$) are almost identical for the integral moments of interest, differing by at most ~1% over a wide range of R/h. Therefore the corrections based on discs of integration, which are much easier to calculate, can be used, even though the numerical integrations are performed using square windows.

The corrected magnitude of the magnetic moment, based on the initial estimate m' from equation (61) is:

$$m = m'[1 + 3(h/R)^2 + 3(h/R)^4]. \tag{64}$$

The corrected components of the magnetic moment $\mathbf{m} = (m_x, m_y, m_z)$ are given by

$$m_x = \frac{h}{2\pi C} \int_{-\infty}^{+\infty} \int_{-\infty}^{+\infty} (x - x_0)\lambda_2 dxdy = \frac{h}{2\pi C} \frac{\int_0^{2\pi} \int_0^{R} (x - x_0)\lambda_2 \rho d\rho d\theta}{1 - \frac{1 + 3R^2/2h^2}{\left(1 + R^2/h^2\right)^{3/2}}}, \tag{65}$$

$$m_y = \frac{h}{2\pi C}\int_{-\infty}^{+\infty}\int_{-\infty}^{+\infty}(y-y_0)\lambda_2 dxdy = \frac{h}{2\pi C}\frac{\int_0^{2\pi}\int_0^{R}(y-y_0)\lambda_2\rho d\rho d\theta}{1-\frac{1+3R^2/2h^2}{\left(1+R^2/h^2\right)^{3/2}}}, \tag{66}$$

$$m_z = -\frac{h^2}{2\pi C}\int_{-\infty}^{+\infty}\int_{-\infty}^{+\infty}\lambda_2 dxdy = -\frac{h^2}{2\pi C}\frac{\int_0^{2\pi}\int_0^{R}\lambda_2\rho d\rho d\theta}{\left[1-\frac{1}{\left(1+R^2/h^2\right)^{3/2}}\right]}. \tag{67}$$

Note that the declination of the magnetisation, (which is given by dec = $\tan^{-1}(m_y/m_x)$ if $m_x > 0$, or dec = $\tan^{-1}(m_y/m_x)+180°$ if $m_x < 0$), is independent of the radius of integration (provided the integral is centred correctly above the source). On the other hand, the inclination of the magnetisation, given by $I = \sin^{-1}(m_z/m)$, requires a correction for the finite range of integration.

Provided the radius of integration is large enough to ensure that beyond this radius the source is well represented by a dipole, the integrals in equation (54), calculated over the whole horizontal plane, can be inferred from integrals calculated over a finite disc centred on the source. For example:

$$\int_0^{2\pi}\int_0^{R}(x-x_0)b_x\rho d\rho d\vartheta = \int_0^{2\pi}\int_0^{\infty}(x-x_0)b_x\rho d\rho d\vartheta\left[1-\frac{1+3R^2/2h^2}{(1+R^2/h^2)^{3/2}}\right]. \tag{68}$$

The correction factors for the other integrals in equation (54) are identical. Since the magnitudes of all components of the magnetic moment, calculated using the original Helbig method, are reduced by the same factor due to a finite range of integration, the ratios of these components are independent of the radius of integration. Thus the correction to the total magnetic moment that is required to account for the finite range of integration is independent of the magnetisation direction, as noted by Schmidt and Clark (1998). Furthermore, calculation of magnetisation *directions* from well-centred finite integral moments of magnetic components is robust, even when the integration range is quite small, as demonstrated empirically by Phillips (2005).

Given an estimated depth of the centre of magnetisation, the corrected estimate of the true moment **m** is related to the initial estimate **m′**, obtained from finite integrals, centred on the source, of the integrands in equation (54), by:

$$\mathbf{m} = \mathbf{m}'\left[1 - \frac{1 + 3R^2/2h^2}{(1 + R^2/h^2)^{3/2}}\right]^{-1}. \tag{69}$$

Equation (69) pertains to the original Helbig method, which uses first integral moments of field components. A similar analysis of the integrals of equation (55) yields the following expression for the corrected moment, based on second integral moments of gradient tensor components:

$$\mathbf{m} = \mathbf{m}''\left[1 - \frac{1 + (5/2)(R^2/h^2) + (33/16)(R^4/h^4)}{(1 + R^2/h^2)^{5/2}}\right]^{-1}, \tag{70}$$

where the components of $\mathbf{m}''$ are calculated from finite integrals, centred on the source, of the integrands that take the form x^2B_{ij} or y^2B_{ij} in equation (55). For integrands of the form xyB_{ij}, the correction factor is slightly different:

$$\mathbf{m} = \mathbf{m}''\left[1 - \frac{1 + (5/2)(R^2/h^2) + (15/8)(R^4/h^4)}{(1 + R^2/h^2)^{5/2}}\right]^{-1}. \tag{71}$$

Caratori Tontini and Pedersen (2008) showed that the horizontal and vertical centres of magnetisation of an arbitrary finite source, not just a compact one, can be determined in principle from specific second order integral moments of field components. The relationships needed are:

$$\begin{gathered}\int_{-\infty}^{+\infty}\int_{-\infty}^{+\infty} xyb_z\,dxdy = -2\pi C(m_x y_0 + m_y x_0); \quad \int_{-\infty}^{+\infty}\int_{-\infty}^{+\infty}\left(x^2 - y^2\right)b_z\,dxdy = 4\pi C(m_y y_0 - m_x x_0); \\ \int_{-\infty}^{+\infty}\int_{-\infty}^{+\infty}\left[3(y^2 b_x - x^2 b_y) - (b_x - b_y)xy\right]dxdy = 2\pi C(m_y - m_x)h + 2\pi C m_z(y_0 - x_0),\end{gathered} \tag{72}$$

which can be simply solved for (x_0, y_0, h) given (m_x,m_y, m_z) from equation (54), (55) or (65)-(67), provided the magnetisation is not vertical. This approach can be extended to third order integral moments of the gradient tensor. The corresponding relationships to equation (72) are:

$$\int_{-\infty}^{+\infty}\int_{-\infty}^{+\infty}(xy^2B_{xz}-x^2yB_{yz})dxdy=\frac{1}{3}\int_{-\infty}^{+\infty}\int_{-\infty}^{+\infty}(y^3B_{yz}-x^3B_{xz})dxdy=4\pi C\left(m_y y_0-m_x x_0\right) \tag{73}$$

$$\int_{-\infty}^{+\infty}\int_{-\infty}^{+\infty}x^2yB_{xz}dxdy=\int_{-\infty}^{+\infty}\int_{-\infty}^{+\infty}xy^2B_{yz}dxdy=4\pi C\left(m_x y_0+m_y x_0\right), \tag{74}$$

$$\int_{-\infty}^{+\infty}\int_{-\infty}^{+\infty}\left[3\left(xy^2B_{xx}-x^2yB_{yy}\right)+\left(x^2y-xy^2\right)B_{xy}\right]dxdy=4\pi C\left(m_x-m_y\right)h+4\pi Cm_z\left(x_0-y_0\right). \tag{75}$$

Equations (73)-(74) are new. Although equations (72) or (73)-(74) are in principle applicable to general finite sources, rather than just compact sources, they require accurate removal of base levels and gradients. Determination of h requires that $m_x \neq m_y$, but this singular case can always be avoided by reorienting the grid. Large areas of integration are required, because the integrals in these equations converge slowly. An iterative scheme, whereby finite integrals are re-centred on updated estimates of (x_0, y_0) and corrected for finite radius of integration, using updated estimates of h, gives better results. McKenzie et al. (2012a) found that the horizontal location of a compact source could be found to within 5% of its depth for R/h = 2, with a corresponding error in magnetisation direction of ~5°.

Significant aspects of the Helbig method and its offshoots include:

1. For relatively isolated anomalies, analysis of integral moments of tensor invariants, particularly the normalised source strength and the intermediate eigenvalue, provides useful information on source location, direction of magnetisation and total magnetic moment, even when the numerical integrations are restricted to the main portion of the anomaly.
2. The horizontal location of the centre of magnetisation is very robust, particularly when determined from the first integral moment of μ^2, and for compact sources the depth of the centroid can be reliably estimated when a correction for the finite radius of integration is made. Note that the integral moments, originally proposed

by Helbig (1963) for centroid location, do not converge. Table 1 summarises the ratios of finite to infinite extent integrals that can be used in Helbig analysis. The integral moments in equations (72)-(75) converge, albeit slowly, wherease those in equations (59)-(60) converge relatively rapidly.

3. The centroid depth is not only important in its own right, but is a crucial parameter for applying corrections to Helbig-type analyses of vector and tensor components, which are in principle independent of source shape (for finite sources).
4. Corrections of the calculated integrals for the finite ranges of x and y are necessary to account for the tails of the anomaly, which are buried in noise, obscured by interfering anomalies, or may lie outside the survey area.
5. Equation (69) implies that the direction of magnetisation can be derived accurately from well-centred integral moments of vector components (the original Helbig method), even for relatively small areas of integration. However the magnitude of the magnetic moment can be substantially underestimated unless the corrections for finite integration radius are applied. For example, for $R = 2h$ the finite integrals of $(x-x_0)B_i$ are only 37% of the infinite integrals, whereas the corresponding ratios are 80%, 99% and 91% for μ, μ^2 and λ_3 respectively. Even for $R = 10h$ the finite integrals of $(x-x_0)b_i$ are only 85% of the corresponding integrals over the entire horizontal plane.
6. Equations (70) and (71) imply that the direction of magnetisation can be derived accurately from well-centred integral moments of tensor elements, following the method of Phillips et al. (2007), even for relatively small areas of integration. However the magnitude of the magnetic moment can be grossly underestimated unless the corrections for finite integration radius are applied. For example, for $R = 2h$ the finite integrals of $(x-x_0)^2B_{ij}$ and $(x-x_0)\ (y-y_0)B_{xy}$ are only 21% and 27% respectively of the infinite integrals. Even for $R = 10h$ the finite integrals of $(x-x_0)^2B_{ij}$ and $(x-x_0)\ (y-y_0)B_{xy}$ are only 80% and 81% of the corresponding integrals over the entire horizontal plane.
7. Helbig-type analyses are not applicable to sources of great depth extent relative to the resolvable width of the anomaly. Vertical pipe-like bodies and vertical prisms, not necessarily narrow or equidimensional, can be analysed, however, by applying these methods to vertical derivatives of the field and/or tensor components and invariants derived from those derivatives (Clark, 2012a).

8. In favourable circumstances Helbig-type methods can yield good estimates of source magnetic moment vectors for finite sources, independent of the source shape and size. This requires correct determination of base levels of components and removal of regional trends. Offsets in components can be estimated by analysis of zero order integral moments of field components. In principle, removal of the average values of the components over a large area, extending well beyond the anomaly of interest, yields the correct base levels. In practice, averages of field components over a limited area are biased by omission of the slowly decaying flanks of the anomaly. More accurate results can be obtained by (i) implementing a correction, dependent on the estimated magnetisation direction and R/h, of the estimated base level, or (ii) analysing the gradient tensor and its invariants, which suppresses effects of base level offsets in field components. Because gradient anomalies are more focussed around the source, they are less contaminated by neighbouring sources. Furthermore, regional gradients can be readily recognised and removed from gradient tensor data over the relatively isolated sources that are the target of Helbig-type methods.

METHODS BASED ON REDUCTION TO THE POLE AND RELATED TRANSFORMS

The RTP transformation assumes a direction of magnetisation and calculates the vertical field anomaly (equivalent for weak fields to the TMI anomaly at the magnetic pole) that would be produced by the same sources if they were vertically magnetised (Blakely, 1996, p.330-335). Provided the correct magnetisation direction is used, this process produces predominantly positive anomalies, which are more symmetric than TMI anomalies that reflect the inclined geomagnetic field, and moves the anomalies more directly over the sources. For compact sources, correctly calculated RTP anomalies lie directly above the sources, whereas for broad sources with steeply dipping contacts the RTP anomalies overlie the source boundaries. For extended sources with shallow dipping contacts, however, the symmetry of the RTP anomalies is imperfect and the anomalies are somewhat displaced from the contacts. The magnetisation direction/dip ambiguity illustrated in Figure 7 shows that any method based purely on the magnetic anomaly, including RTP-based methods, will struggle to determine the magnetisation direction for tabular shallow

dipping bodies of considerable strike extent. The RTP transformation is unstable when the geomagnetic inclination is too low, so its use is problematic in low latitudes.

Attempts to estimate direction of magnetisation of isolated sources from analysis of the symmetry of their anomalies have a long history. For example Schnetzler and Taylor (1984) used the position and relative magnitudes of the TMI maximum and minimum to infer the declination and inclination of the source magnetisation. However this and similar methods are relatively ineffective near the equator and are very sensitive to errors in anomaly base level, regional gradients and interfering anomalies.

Bott et al. (1966) calculated the pseudogravity transformation from the magnetic anomaly for many possible directions of the magnetisation and searched for directions that gave purely positive anomalies. The pseudogravity transformation has a phase spectrum identical to that of the RTP transformation and an amplitude spectrum weighted by $1/|k|$ with respect to RTP (Blakely, 1996, p.343-346), so it suffers from similar distortion due to shallow dips and, as it amplifies long-wavelength noise, requires good separation of the residual anomaly from the regional background.

Fedi et al. (1994) developed a method of distortion analysis of RTP anomalies that has come to be known as the Maxi-Min method. This method is based on the observation that induced anomalies at the pole are predominantly positive and relatively symmetric, flanked by a relatively inconspicuous magnetic low. By trialling different magnetisation directions, the direction that produces the smallest negative RTP anomaly around the source gives the best estimate of the true magnetisation direction. This method is unaffected by base level errors, but like alternative methods is compromised by interfering anomalies and background gradients.

Stavrev and Gerovska (2000) proposed transforming gridded TMI data to obtain parameters that are relatively insensitive to magnetisation direction, in contrast to RTP anomalies, and are well centred over sources, irrespective of magnetisation direction. Their favoured parameters $T_a = |\mathbf{b}|$, $|\nabla T_a|$, $\nabla^2 T_a$, $(T_a \nabla^2 T_a)^{1/2}$, and $(\nabla^2 T_a^2)^{1/2}$ are functions of anomalous vector components, which may be directly measured or calculated from TMI data. Calculation of these magnitude transforms is unstable at very low (< 5°) geomagnetic inclinations, but the instability is less severe than for the RTP transform. For

2D sources the independence of magnetisation direction is exact for these quantities, but is only approximate for 3D sources. The parameters of Stavrev and Gerovska (2000) are less sensitive to magnetisation direction of 3D sources than the formerly popular analytic signal amplitude (ASA), otherwise known as the total gradient of TMI. Clark (2012a, 2013b) and Pilkington and Beiki (2013) suggest the NSS, given by equation (56), as an alternative high centricity parameter, as it is completely independent of magnetisation direction for the important cases of dipolar sources and axially magnetised narrow pipes, as well as all 2D sources.

The high centricity parameters discussed above are useful for defining horizontal locations of source centroids and/or boundaries, but provide little or no information about magnetisation direction, whereas RTP maps are highly sensitive to orientation of the assumed magnetisation. Comparison of a map of a high centricity parameter over an isolated source with the corresponding RTP anomaly therefore provides a test of whether the correct magnetisation direction has been used for calculation of the RTP. If RTP anomalies have been calculated with the correct direction of magnetisation, they should closely coincide in location with corresponding high centricity parameters such as $|\mathbf{b}|$ or the NSS and exhibit similar symmetry. Provided the two transforms that are used in the cross-correlation have the same fall-off rate with height, asymmetry of the anomalies that arises from shallow dips should be similar for the two transformed datasets, so distortion produced by shallow dips is much less problematic.

Roest and Pilkington (1993) compared the total gradient of the RTP TMI with the horizontal gradient of the pseudogravity anomaly, calculated for a variety of magnetisation directions. When the correct direction of magnetisation is chosen, the positions of the maxima of the two functions coincide and the correlation between them is maximised. The correlated quantities match best for broad sources with small vertical thickness, and the method is affected by thickness of the sources. Dannemiller and Li (2006) pointed out that the different fall-off rates with height for the quantities used by Roest and Pilkington (1993) result in sensitivity to source geometry, particularly dip.

Dannemiller and Li (2006) used the correlation between the vertical gradient and the total gradient of RTP, calculated for a wide range of assumed magnetisation directions. These quantities have the same fall-off rate with distance to source and empirically have the

highest correlation when the correct magnetisation direction is used to calculate the RTP anomaly over a source. This method is more suited to 3D anomalies, in particular, than the method of Roest and Pilkington (1993). Because the asymmetry produced by dipping contacts is similar for both calculated quantities when the assumed magnetisation direction corresponds to that of the actual magnetisation, this method is not adversely affected by shallow dipping source boundaries. The method assumes that sources included within the analysis window have the same magnetisation direction and the method breaks down if this assumption is violated.

Gerovska et al. (2009) calculated a total magnetic amplitude (T_a = |**b**|) map to aid identification and isolation of anomalies due to distinct sources, then compared T_a with the RTP map, calculated with many different assumed magnetisation directions, to ascertain the direction for which the correlation is maximised over the anomalies of interest. Some errors occur for compact sources, because of the slight dependence of T_a on magnetisation direction. Employing the NSS instead of T_a would eliminate this error.

McKenzie et al. (2012b) evaluated several alternative transforms for determining magnetisation direction of isolated sources, including a symmetry analysis of reduced-to-the-equator (RTE) anomalies designed for when the geomagnetic inclination is low. The RTP maxi-min method of Fedi et al. (1994) works well for moderate to high geomagnetic inclinations and compact anomalies. For elongate anomalies correlation methods between RTP and other high-centricity transforms work better than the maxi-min method. Estimation of magnetisation direction from RTE symmetry can be more accurate than the maxi-min or correlation methods for elongate anomalies with moderate to low inclination geomagnetic fields.

Overall RTP-based methods work well on discrete anomalies when sources are simple and dips/plunges are steep. Reasonable results can be obtained when contacts are shallow, if the true RTP anomaly (calculated with the correct assumed magnetisation) and transformed data with which it is compared have similar asymmetry. This requires that the two quantities have the same fall-off rate, e.g. the transforms used by Dannemiller and Li (2006), otherwise relative responses to shallow and deeper portions of a dipping contact will differ. For 2.5D bodies of considerable strike extent the accuracy of the results suffers due to the dip-magnetisation ambiguity. Methods based on RTP and similar transforms are

particularly suited to scanning large areas to detect features with anomalous magnetisation direction, which can then be analysed in more detail using other methods described in this review.

BASE STATION VECTOR AND GRADIENT MEASUREMENTS

The very slowly varying main geomagnetic field produced by the Earth's core is perturbed by rapidly time-varying electric currents flowing in the ionosphere and magnetosphere. Because the induced magnetisation responds to the resultant applied field, including geomagnetic fluctuations such as pulsations, magnetic storms and diurnal variations, whereas remanent magnetisation is unaffected by these small fluctuations, the core-crust-magnetosphere system can be regarded as a giant laboratory that can, in principle, be used to separate effects due to induced and remanent magnetisations. Figure 12 illustrates the principle of the method.

Goldstein and Ward (1966) used sensitive Rb-vapour magnetometers to detect perturbation of total field fluctuations in the vicinity of some sources that produce prominent magnetic anomalies. By making some simplifying assumptions about the polarisation of the time-varying magnetic fields, those authors were able to distinguish predominantly induced from predominantly remanent sources. For predominantly induced sources, semiquantitative estimates of source susceptibility could be derived by incorporating geological information about source geometry. In general, however, TMI measurements do not provide sufficient information to uniquely separate induced and remanent contributions, or to derive detailed information on magnetic properties.

Parkinson and Barnes (1985) detected the local amplification of geomagnetic variations over the Savage River, Tasmania, magnetite deposit, using two separated fluxgate magnetometers. By assuming that the remanence was parallel to the induced magnetisation, Parkinson and Barnes derived an estimate of $Q \approx 0.4$, which is reasonable for a massive magnetite deposit. Lesur and Gubbins (2000) developed a method for analysing long term geomagnetic secular variation, recorded by geomagnetic observatories, to separate induced from remanent contributions to regional magnetic anomalies.

Clark et al. (1998) showed that the anomalous field vector **b**, measured at a fixed location within an anomaly, is related to the source magnetisation vector **M** by the matrix equation

$$\mathbf{b} = \mathbf{AM}, \tag{76}$$

where $\mathbf{A} = \nabla\nabla U'$ is a symmetric and traceless matrix representing the second order gradient tensor of the pseudogravitational potential U'. The magnetisation of the source is assumed to be uniform, at least in direction. **A** depends on the geometry and location of the source, but is independent of the magnetisation intensity, direction or origin. For example, Clark et al. (1998) showed that for a spherical source of volume V, at an observation point $\mathbf{r} = (x_1, x_2, x_3)$, $\mathbf{A} = [a_{ij}]$ is given by:

$$a_{ij}(\mathbf{r}) = V\frac{3x_i x_j - r^2\delta_{ij}}{r^5}, \tag{77}$$

where δ_{ij} is the Kronecker delta, with elements equal to one when $i = j$, and zero otherwise. The eigenvalues of **A** in equation (77) are $2V/r^3$, $-V/r^3$, $-V/r^3$. The eigenvector corresponding to the positive, and largest, eigenvalue is directed towards (or directly away from) the centre of the sphere and measurements at two or more locations therefore suffice to estimate the centre location by triangulation.

A geomagnetic variation $\delta\mathbf{F}$ produces a change $\delta\mathbf{M} = k\delta\mathbf{F}$ in the induced magnetisation, which also equals the change in the resultant magnetisation **M**, because the remanence is unaffected. This in turn produces a change in the anomalous field and its gradient. By continuously monitoring geomagnetic variations and gradient perturbations the contributions of induced and remanent magnetisations can be separated. Unique separation of these contributions by measurements at a single point within the anomaly requires a further assumption that the induced magnetisation is parallel to the inducing field, i.e. that anisotropy and self-demagnetisation effects are negligible. In that case, fluctuations in the anomalous field vector are given by:

$$\delta\mathbf{b} = \mathbf{A}\delta\mathbf{M} = k\mathbf{A}\delta\mathbf{F}. \tag{78}$$

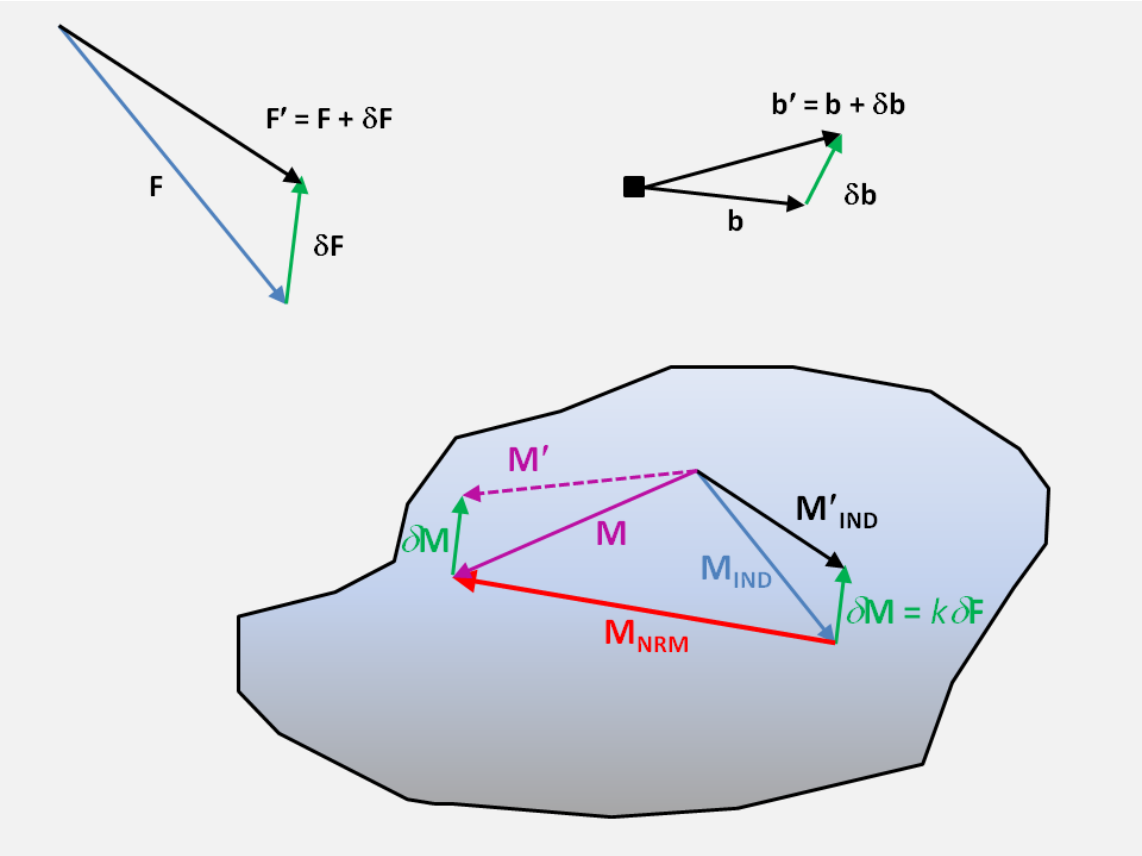

Figure 12. Principle of remote determination of *in* situ magnetic properties. The regional geomagnetic field **F** undergoes a fluctuation δ**F**, which perturbs the induced magnetisation $\mathbf{M}_{IND}$, but does not affect the contribution of remanence $\mathbf{M}_{NRM}$ to the resultant magnetisation **M**. The change in source magnetisation from **M** to **M′** produces a change in the observed field and its gradient within the anomaly.

Figure 11(b) illustrates the Differential Vector Magnetometry (DVM) method developed by Clark et al. (1998). Three component natural geomagnetic fluctuations $\delta\mathbf{F}$ are recorded by a vector magnetometer at a base station that lies outside the anomaly of interest and by another vector magnetometer within the anomaly. The differences between the respective components represent the components of $\delta\mathbf{b}$. From equation (78), time series of the components of $\delta\mathbf{b}$ and $\delta\mathbf{F}$ yield least squares estimates of the elements of $k\mathbf{A}$ at the within-anomaly station. Given $k\mathbf{A}$ and the known vector anomaly at the observation point, the resultant magnetisation of the source, divided by the unknown susceptibility, can then be derived from equation (76):

$$\mathbf{M}/k = (k\mathbf{A})^{-1}\mathbf{b}. \tag{79}$$

Equation (79) determines the direction of the resultant magnetisation, which is crucial information for accurate modelling, but not its absolute magnitude. Because the direction of the induced magnetisation is known, the magnitude of $\mathbf{M}_{\mathrm{NRM}}/k$, the direction of remanence, and the Koenisberger ratio Q can also be calculated. From equations (1)-(2), (6) and (79):

$$(\mathbf{M}_{\mathrm{NRM}}/k) = (\mathbf{M}/k) - \mathbf{F} = (k\mathbf{A})^{-1}\mathbf{b} - \mathbf{F}, \tag{80}$$

$$|\mathbf{M}_{\mathrm{NRM}}/k| = |(\mathbf{M}/k) - \mathbf{F}|, \tag{81}$$

$$\hat{\mathbf{M}}_{\mathrm{NRM}} = (\mathbf{M}_{\mathrm{NRM}}/k)/|\mathbf{M}_{\mathrm{NRM}}/k|, \tag{82}$$

$$Q = |\mathbf{M}|/kF = |\mathbf{M}/k|/F = |(k\mathbf{A})^{-1}\mathbf{b}|/F. \tag{83}$$

Similarly, fluctuations in the vertical gradients of $\mathbf{b}$, for example, are given by

$$\delta\left(\frac{\partial\mathbf{b}}{\partial z}\right) = \delta\begin{bmatrix} B_{xz} \\ B_{yz} \\ B_{zz} \end{bmatrix} = \frac{\partial\mathbf{A}}{\partial z}\delta\mathbf{M} = k\frac{\partial\mathbf{A}}{\partial z}\delta\mathbf{F}. \tag{84}$$

Time series of the gradients and $\delta\mathbf{F}$ yield least squares estimates of the elements of $k\partial\mathbf{A}/\partial z$. $\mathbf{M}/k$ can then obtained by inverting the relationship, analogous to equation (76), between the gradient anomaly and the resultant magnetisation:

$$\mathbf{M}/k = \left(k\frac{\partial \mathbf{A}}{\partial z} \right)^{-1} \frac{\partial \mathbf{b}}{\partial z}. \tag{85}$$

If the complete gradient tensor is measured within the anomaly, along with the vector field, similar analysis of the orthogonal gradients provides data redundancy, allowing consistency checks and improving error estimates.

The original DVM method trialled by Clark et al. (1998) required two sensitive vector magnetometers, separated by as much as several hundred metres, aligned to within seconds of arc, which is a very demanding requirement. An alternative method requires only a single package containing a rigidly mounted vector magnetometer and gradiometer, plus sensitive tiltmeters, which can be placed anywhere within the anomaly and monitored over several hours to allow sufficient geomagnetic field variation. The Superconductivity and Magnetism Group at CSIRO Materials Science and Engineering is adapting a sensitive high-temperature SQUID magnetometer and tensor gradiometer package with gradient sensitivity of about 2 pT/m, developed for underwater UXO detection (Young et al., 2010), for this purpose.

The overall signal-to-noise ratio for DVM depends on the magnitude of the anomaly, the amplitude of the geomagnetic fluctuation, and the Koenigsberger ratio of the source. The method is best suited to strong anomalies and sources with moderate Q. In the limit of very high Q, the induced magnetisation has little effect, making it difficult to solve for the parameters that are given by equations (80)-(83). In that case the method simply establishes a lower limit for Q. This is useful information in itself, because it limits the possible source types and also because the remanence direction is constrained to be close to the total magnetisation direction when $Q >> 1$. Thus, if the direction of resultant magnetisation is determined by one of the other methods discussed in this paper, this also represents the approximate remanence direction.

For more common situations, Q ~1, the typical diurnal variation of about 0.1% in **F** gives perturbations in the anomalous components of ~0.05%, so a static anomaly of 10,000 (1000) nT gives a signal of about 5 (0.5) nT. If the centroid of a compact source is at 100 m depth, the gradient signal is about 0.15 nT/m (15 pT/m), and if the depth is 200 m these signals are 75 pT/m and 7.5 pT/m respectively. Table 2 summarises the signal strengths expected for a range of geomagnetic variations, anomaly magnitudes, Q values, and source depths. Note that geomagnetic storms, albeit rare, are especially favourable for the method, as they produce fluctuations of several hundred, and occasionally several thousand, nT. Diurnal variation can generally be relied on to produce substantial changes of tens of nT in all three components over several hours. Geomagnetic pulsations with periods 1-100 s produce smaller fluctuations, ~1-10 nT, but allow considerable signal stacking.

In summary, DVM, or its single station magnetometer/gradiometer variant, uses time series of vector and gradient measurements to determine (i) the direction of time-averaged total magnetisation, (ii) the direction of remanence, and (iii) the Koenigsberger ratio Q, *without making any assumptions about source geometry or location*. In addition, for a compact source this method yields the total magnetic moment of the source and provides a direct indication of direction to its centroid (which can be used to site initial drill holes). The depth and horizontal location of the centroid of a compact source can be obtained from measurements at two or more stations, occupied simultaneously or consecutively. The method is not restricted to sources of limited depth extent, allowing it to resolve pathological cases of ambiguity associated with 2D dipping sheets and axially magnetised plunging pipes of great depth extent. However, for sources of great strike extent that are effectively 2D, only the components of magnetisation in the plane normal to strike (which are the only contributors to the observed anomaly) can be determined.

CONCLUSIONS

Many methods are available to tackle the problem of estimating remanent and total magnetisations of magnetic sources, most of which provide only partial information. Because these methods each have strengths and weaknesses, they are complementary. It is desirable, therefore, to use more than one method to improve confidence in estimated magnetisations. Foss and McKenzie (2009, 2011), for example, presented examples of improved results, validated by comparison with palaeomagnetic studies, obtained by using

Helbig methods to provide initial estimates of magnetisation direction, which are then used to constrain staged 3D inversions. Table 3 summarises the range of applicability of the methods described in this paper and the information that can be provided by each.

Estimation of the total magnetisation direction is invaluable for constraining modelling of source geometry and position. Magnetisation intensity and Koenigsberger ratio constrains the magnetic mineralogy and geological nature of a source. Determining the direction of a stable ancient remanence gives an indication of the age of magnetisation, which provides useful information about the geological history of the source and its environs. Estimation of the magnetic moment vector of a source yields the total magnetisation direction and can give an indication of the size of the source, when plausible magnetisation intensities are assumed.

ACKNOWLEDGEMENTS

This paper represents a contribution towards a Ph.D. in the Department of Earth and Planetary Sciences at Macquarie University, under the supervision of Drs Mark Lackie and Richard Flood. I thank Phil Schmidt and Dave Pratt for helpful comments that improved the manuscript.

REFERENCES

Airo, M. L., & Loukola-Ruskeeniemi, K. (2004). Characterization of sulfide deposits by airborne magnetic and gamma-ray responses in eastern Finland. Ore Geology Reviews, 24(1), 67-84.

Aitchison, J., and Brown, J. A. C, 1957, The lognormal distribution: Cambridge University Press.

Al-Chalabi, M., 1971, Some studies relating to nonuniqueness in gravity and magnetic inverse problems: Geophysics, 36, 835-855.

Andersen, F.H. and Pedersen, L.B., 1979. Some relations between potential fields and the strength and center of their sources. Geophysical Prospecting, 27, 205-221.

Ates, A. and Kearey, P., 1995. A new method for determining magnetization direction from gravity and magnetic anomalies: application to the deep structure of Worcester graben. Journal of the Geological Society, London, 152, 561–566.

Audunsson H. and Levi S., 1989. Drilling-induced remanent magnetization in basalt drill cores, Geophysical Journal International, 98, 613–622.

Austin, J., Geuna, S., Hillan, D., Clark, D., 2012. Magnetic modelling of the Candelaria IOCG deposit, Chile: The Influence of Remanent Magnetism and Self-demagnetisation (Poster). Society of Economic Geologists Conference, Lima. (http://www.academia.edu/download/29334276/Magnetic_Modelling_of_the_Candelaria_IOCG_12102012.pdf)

Austin, J. R., Schmidt, P. W., Foss, C. A., 2013a. Magnetic modeling of iron oxide copper-gold mineralization constrained by 3D multiscale integration of petrophysical and geochemical data: Cloncurry District, Australia: Interpretation, 1(1), T63-T84.

Austin, J., Clark, D., Schmidt, P., Hillan, D. and Foss, C., 2013b, Magnetic anomalies to mines: Practical insights into the myths, methods and mysteries in relating mineralisation and magnetisation: A Forum on the Application of Remanent Magnetisation and Self-

Demagnetisation Estimation to Mineral Exploration. 23rd ASEG Conference and Exhibition, Melbourne.

Beiki, M., Clark, D.A., Austin, J.R. and Foss, C.A., 2012a, Estimating source location using normalized magnetic source strength calculated from magnetic gradient tensor data: Geophysics, **77**(6), J23-J37.

Bilim, F. and Ates, A., 2004. An enhanced method for estimation of body magnetization direction from pseudogravity and gravity data. Computers and Geosciences, 30(2), 161-171.

Blakely, R.J., 1996, Potential Theory in Gravity and Magnetic Applications, Cambridge University Press.

Bosum, W., Eberle, D., and Rehli, H. J., 1988. A gyro-oriented 3-component borehole magnetometer for mineral prospecting, with examples of its application: Geophysical Prospecting, 36(8), 933-961.

Bott, M.H.P., 1973. Inverse methods in the interpretation of magnetic and gravity anomalies, In: Bruce A. Bolt, Editor, Methods in Computational Physics: Advances in Research and Applications, 13, 133-162, Elsevier. http://dx.doi.org/10.1016/B978-0-12-460813-9.50010-2.

Bott, M. H. P., Smith, R. A. and Stacey, R. A., 1966. Estimation of the direction of magnetization of a body causing a magnetic anomaly using a pseudo-gravity transformation. Geophysics, 31(4), 803-811.

Breiner, S., 1999. Applications manual for portable magnetometers. Geometrics, available from: ftp://geom.geometrics.com/pub/mag/Literature/AMPM-OPT.PDF

Brown, L. L., & McEnroe, S. A. (2008). Magnetic properties of anorthosites: A forgotten source for planetary magnetic anomalies?. Geophysical Research Letters, 35(2), L02305. doi:10.1029/2007GL032522

Butler, R.F., 1992. Paleomagnetism: Magnetic Domains to Geologic Terranes. Blackwell Scientific Publications. (Electronic edition available from http://www.pmc.ucsc.edu/~njarboe/pmagresource/ButlerPaleomagnetismBook.pdf)

Caratori Tontini, F. and Pedersen, L.B., 2008. Interpreting magnetic data by integral moments: Geophysical Journal International, 174, 815-824.

Cattach, M. K., Stanley, J. M., Lee, S. J., and Boyd, G. W., 1994. Sub-Audio Magnetics (SAM): a high resolution technique for simultaneously mapping electrical and magnetic properties. Exploration Geophysics, 24(4), 387-400.

Chandler, V., Koski, J., Hinze, W. and Braile, L., 1981. Analysis of multisource gravity and magnetic anomaly data sets by moving-window application of Poisson's theorem. Geophysics, 46, 30–39. doi: 10.1190/1.1441136

Clark, D.A., 1983. Comments on Magnetic Petrophysics. Bulletin of the Australian Society of Exploration Geophysicists, 14, 49-62.

Clark, D.A.,1984. Hysteresis properties of sized dispersed monoclinic pyrrhotite grains. Geophysical Research Letters, 11, 173-176.

Clark, D.A., 1988. Magnetic properties and magnetic signatures of the Trough Tank and Starra copper-gold deposits, Eastern Mt Isa Block. RIR 1745R, 50p. https://wiki.csiro.au/confluence/download/attachments/457769088/Clark+1988+CSIRO+1745R.pdf

Clark. D.A., 1994. Magnetic properties and magnetite contents of ores from the Ernest Henry deposit, eastern Mount Isa Inlier. CSIRO Division of Exploration and Mining Report 23C, 79p.

Clark, D.A., 1997, Magnetic petrophysics and magnetic petrology: aids to geological interpretation of magnetic surveys: AGSO Journal of Australian Geology and Geophysics, 17, 83-103.

Clark, D.A., 2000. Self-demagnetisation in practice: the Osborne Cu-Au deposit. Preview, 85, 31-36.

Clark, D.A., 2010, Method and apparatus for detection using magnetic gradient tensor. U.S. Patent Application Pub. No.: US 2010/0211337 Al, Pub. Date: Aug. 19, 2010 (US patent 8,229,688 B2 granted July 24, 2012).

Clark, D.A., 2012a, New methods for interpretation of magnetic vector and gradient tensor data I: eigenvector analysis and the normalised source strength: Exploration Geophysics, 43, 267–282, http://dx.doi.org/10.1071/EG12020.

Clark, D.A., 2012b, Interpretation of the magnetic gradient tensor and normalized source strength applied to the Tallawang magnetite skarn deposit, New South Wales, Australia: SEG Technical Program Expanded Abstracts 2012, pp.1-5, 2012: pp. 1-5.
doi: 10.1190/segam2012-0700.1.

Clark, D.A., 2013a, New methods for interpretation of magnetic vector and gradient tensor data II: Application to the Mount Leyshon Anomaly, Queensland: Exploration Geophysics, 44, 114–127, http://dx.doi.org/10.1071/EG12066.

Clark, D.A., 2013b, New approaches to dealing with remanence: magnetic moment analysis using tensor invariants and remote determination of *in situ* magnetisation using a static tensor gradiometer (Extended Abstract): ASEG-PESA 23rd International Geophysical Conference and Exhibition, Melbourne, pp.1-7. http://dx.doi.org/10.1071/ASEG2013ab049

Clark, D.A.,2014. Magnetic effects of hydrothermal alteration in porphyry copper and iron-oxide copper–gold systems: A review, Tectonophysics (published online December 11, 2013), http://dx.doi.org/10.1016/j.tecto.2013.12.011

Clark, D.A., Geuna, S.E., Schmidt, P.W., 2004. Predictive magnetic exploration models for porphyry, epithermal and iron oxide Cu-Au deposits: P700 Final Report, 398 p. + CD Atlas of Geophysical Signatures + Relational Database of Porphyry, Epithermal and Iron Oxide Cu-Au Deposits, AMIRA International.

Clark, D.A. and Emerson, D.W., 1991. Notes on rock magnetization characteristics in applied geophysical studies. Exploration Geophysics, 22, 547-555.

Clark, D.A. and Emerson, D.W., 1999. Self-demagnetisation. Preview, 79, 22-25.

Clark, D.A., Saul, S.J. and Emerson, D.W., 1986. Magnetic and gravity anomalies of a triaxial ellipsoid: Exploration Geophysics, 17, 189-200.

Clark, D. A. and Schmidt, P. W., 1994. Magnetic properties and magnetic signatures of BIFs of the Hamersley Basin and Yilgarn Block, Western Australia. In: M.C. Dentith, K.F. Frankombe, S.E. Ho, J.M. Shepherd, D.I. Groves and A. Trench (Eds), Geophysical Signatures of Western Australian Mineral Deposits.: (Geology and Geophysics Department (Key Centre) and UWA Extension, The University of Western Australia); 1994: 343-354.

Clark, D.A., Schmidt, P.W. and French, D.H., 1992. Magnetic Petrology of kimberlites. Part I: basic magnetic properties, magnetic modelling and palaeomagnetism. CSIRO Division of Exploration Geoscience Restricted Report 276R, 237p.

Clark, D. A., Schmidt, P. W., Coward, D. A. and Huddleston, M. P., 1998, Remote determination of magnetic properties and improved drill targeting of magnetic anomaly sources by Differential Vector Magnetometry (DVM): Exploration Geophysics, 29, 312-319.

Clark, D. A. and Schmidt, P. W., 1999. Magnetic tomography. CSIRO Exploration and Mining Research Review: CSIRO Division of Exploration and Mining, p.84-87.

Clark, D.A. and Tonkin, C., 1987. Magnetic properties of ironstones and host rocks from the Tennant Creek area. CSIRO Division of Mineral Physics and Mineralogy Restricted Investigation Report 1691R, 124pp.
https://wiki.csiro.au/confluence/download/attachments/457769088/Clark%26Tonkin+1987+CSIRO+1691R.pdf

Clark, D. A. and Tonkin, C., 1994. Magnetic anomalies due to pyrrhotite: examples from the Cobar area, N.S.W., Australia. Journal of Applied Geophysics, 32, 11-32.

Collins, S., 1987. The geophysics of the Red Dome gold mine and surrounding areas. 5th ASEG Conference, Extended Abstracts, 19-20.

Constable, C. and Tauxe, L., 1990, The bootstrap for magnetic susceptibility tensors: Journal of Geophysical Research, 95(B6), 8383–8395, doi:10.1029/JB095iB06p08383.

Cordell, L. and Taylor, P., 1971, Investigation of magnetization and density of a North Atlantic seamount using Poisson's theorem: Geophysics, 36(5), 919–937, doi: 10.1190/1.1440224.

Dannemiller, N. and Li, Y., 2006. A new method for determination of magnetization direction. Geophysics, 71(6), L69–L73. doi: 10.1190/1.2356116

Direen, N. G., Pfeiffer, K. M. and Schmidt, P. W., 2008. Strong remanent magnetization in pyrrhotite: A structurally controlled example from the Paleoproterozoic Tanami orogenic gold province, northern Australia. Precambrian Research, 165(1), 96-106.

Dunlop, D.J. and Kletetschka, G., 2001. Multidomain hematite: a source of planetary magnetic anomalies? Geophysical Research Letters, 28 (17), 3345-3348.

Dunlop, D. J. and Özdemir, Ö., 1997. Rock magnetism: fundamentals and frontiers: Cambridge University Press.

Egli, R., 2009. Magnetic susceptibility measurements as a function of temperature and frequency I: inversion theory. Geophysical Journal International, 177, 395-420.

Ellis R.G., de Wet, B., Macleod I.N., 2012. Inversion of magnetic data for remanent and induced sources. *ASEG Extended Abstracts*. http://dx.doi.org/10.1071/ASEG2012ab117.

Emerson, D.W., Clark, D.A. and Saul, S.J., 1985, Magnetic exploration models incorporating remanence, demagnetisation and anisotropy: HP 41C handheld computer algorithms: Exploration Geophysics, 16, 1-122.

Emilia, D. and Massey, R., 1974. Magnetization estimation for nonuniformly magnetized seamounts. Geophysics, 39(2), 223–231. doi: 10.1190/1.1440423

Eskola, L. and Tervo, T., 1980. Solving the magnetostatic field problem (a case of high susceptibility) by means of the method of subsections, Geoexploration, 18, 79-95 http://dx.doi.org/10.1016/0016-7142(80)90022-8.

Farrar, L.J.D., 1979. Some comments on detailed magnetic investigations of ellipsoidal bodies at Tennant Creek. Bulletin of the Australian Society of Exploration Geophysicists, 10, 26-33.

Fedi, M., Florio, G., and Rapolla, A., 1994. A method to estimate the total magnetization direction from a distortion analysis of magnetic anomalies. Geophysical Prospecting, 42, 261–274.

Foss, C., 2006, Evaluation of strategies to manage remanent magnetization effects in magnetic field inversion: 76th Annual International Meeting Expanded Abstracts, Society of Exploration Geophysics, 938-942.

Foss, C. and McKenzie, K. B., 2009. Strategies to invert a suite of magnetic field anomalies due to remanent magnetization: an example from the Georgetown area of Queensland. ASEG Extended Abstracts, 2009, 1-18.

Foss, C. and McKenzie, B., 2011. Inversion of anomalies due to remanent magnetisation: an example from the Black Hill Norite of South Australia: Australian Journal of Earth Sciences, 58(4), 391-405.

Foss, C., McKenzie, K. and Hillan, D., 2012. A robust approach to estimation of magnetization direction from interpretation of magnetic field data. SEG Technical Program Expanded Abstracts 2012: pp. 1-5. doi: 10.1190/segam2012-1550.1

Fraser, D. C., 1981. Magnetite mapping with a multicoil airborne electromagnetic system. Geophysics, 46(11), 1579-1593.

Fullagar, P.K. and Pears, G.A., 2013. 3D magnetic modelling and inversion incorporating self-demagnetisation and interactions. Extended Abstract, 23rd ASEG Conference and Exhibition, Melbourne, pp.1-4. http://dx.doi.org/10.1071/ASEG2013ab089

Furness, P., 1999. A versatile integral equation technique for magnetic modelling. Journal of Applied Geophysics, 41(4), 345-357.

Furness, P., 2001. A note on magnetic modelling with remanence. Journal of Applied Geophysics, 48(4), 257-261.

Gallet, Y. and Courtillot, V., 1989. Modeling magnetostratigraphy in a borehole. Geophysics, 54(8), 973-983.

Garland, G. D., 1951. Combined analysis of gravity and magnetic anomalies. Geophysics, 16(1), 51-62.

Gerovska, D., Araúzo-Bravo, M.J. and Stavrev, P., 2009. Estimating the magnetization direction of
sources from southeast Bulgaria through correlation between reduced-to-the- pole and total magnitude anomalies. Geophysical Prospecting, 57, 491–505.

Goldstein, N. and Ward, S., 1966. The separation of remanent from induced magnetism in situ. Geophysics, 31(4), 779–796. doi: 10.1190/1.1439810

Guerrero-Suarez, S. and Martín-Hernández, F., 2012. Magnetic anisotropy of hematite natural crystals: increasing low-field strength experiments. International Journal of Earth Sciences, 101, 625-636, doi:10.1007/s00531-011-0666-y

Hall, D.H., 1959, Direction of polarization determined from magnetic anomalies: Journal of Geophysical Research, 64, 1945-1959.

Halls, H. C., 1976. A least-squares method to find a remanence direction from converging remagnetization circles. Geophysical Journal of the Royal Astronomical Society, 45: 297–304. doi: 10.1111/j.1365-246X.1976.tb00327.x

Halls, H.C., 1979. Separation of multicomponent NRM: combined use of difference and resultant magnetization vectors, Earth and Planetary Science Letters, Volume 43, 303-308, http://dx.doi.org/10.1016/0012-821X(79)90215-2

Hashimoto, T., Utsugi, M., Nakatsuka, T., Okuma, S., Koyama, T. and Kanda, W., 2011. Temporal magnetic changes possibly due to cooling magmas as revealed by repeat helicopter-borne surveys over an active volcano. Proceedings of the 10th SEGJ International Symposium, Kyoto, 276-279.

Hattula, A., 1986. Magnetic 3-component borehole measurements in Finland, In Killeen, P., (ed.), Borehole geophysics for mining and geotechnical applications, Geological Survey of Canada Paper 85-27, 237-250.

Helbig, K., 1963, Some integrals of magnetic anomalies and their relation to the parameters of the disturbing body: Zeitschrift für Geophysik, 29, 83-96.

Hillan, D., 2013a, Modelling Self-Demagnetisation and Body-Body Interactions in the Fourier Domain: EAGE 2013 Extended Abstract, 1-4.

Hillan, D., 2013b, Self-demagnetisation: implications and corrections in magnetic modelling: A Forum on the Application of Remanent Magnetisation and Self-Demagnetisation Estimation to Mineral Exploration. 23rd ASEG Conference and Exhibition, Melbourne.

Hoffman, K. A. and Day, R., 1978. Separation of multicomponent NRM: A general method. Earth and Planetary Science Letters, 40, 433–438.

Hoschke, T., 1991. Geophysical discovery and evaluation of the West Peko copper-gold deposit, Tennant Creek. Exploration Geophysics, 22, 485-495.

Hoschke, T., 2013. Determining and accounting for magnetic remanence in mineral exploration. A Forum on the Application of Remanent Magnetisation and Self-Demagnetisation Estimation to Mineral Exploration. 23rd ASEG Conference and Exhibition, Melbourne.

Huang, H. and Fraser, D. C., 2000. Airborne resistivity and susceptibility mapping in magnetically polarizable areas. Geophysics, 65(2), 502-511.

Huang, H. and Fraser, D. C., 2001. Mapping of the resistivity, susceptibility, and permittivity of the earth using a helicopter-borne electromagnetic system. Geophysics, 66(1), 148-157.

Jackson, M., Moskowitz, B., Rosenbaum, J. and Kissel, C., 1998. Field-dependence of AC susceptibility in titanomagnetites: Earth and Planetary Science Letters, 157, 129-139.

Kanasewich, E. R. and Agarwal, R. G., 1970. Analysis of combined gravity and magnetic fields in wave number domain. Journal of Geophysical Research, 75(29), 5702-5712.

Kent, J. T., Briden, J. C. and Mardia, K. V., 1983. Linear and planar structure in ordered multivariate data as applied to progressive demagnetization of palaeomagnetic remanence. Geophysical Journal of the Royal Astronomical Society, 75(3), 593-621.
doi: 10.1111/j.1365- 246X.1983.tb05001.x

Kirschvink, J. L., 1980. The least-squares line and plane and the analysis of palaeomagnetic data, Geophysical Journal of the Royal Astronomical Society, 62, 699–718.

Kletetschka, G., Wasilewski, P.J. and Taylor, P.T., 2000. Unique thermoremanent magnetization of multidomain sized hematite: implications for magnetic anomalies. Earth and Planeter. Sci. Lett., 176, 469-479.

Lelièvre, P.G. and Oldenburg, D.W., 2006. Magnetic forward modelling and inversion for high susceptibility. Geophysical Journal International, 166(1), 76-90.

Lesur, V. and Gubbins, D., 2000. Using geomagnetic secular variation to separate remanent and induced sources of the crustal magnetic field. Geophysical Journal International, 142(3), 889-897, doi: 10.1046/j.1365-246x.2000.00190.x

Levanto, A.E., 1963. On magnetic measurements in drill holes: Geoexploration, 1(2), 8-20.

Li, Y., 2012. Recent advances in 3D generalized inversion of potential-field data. SEG Technical Program Expanded Abstracts 2012: pp. 1-7. doi: 10.1190/segam2012-0535.1

Li, Y., Shearer, S., Haney, M. and Dannemiller, N., 2004. Comprehensive approaches to the inversion of magnetic data affected by remanent magnetization. SEG Technical Program Expanded Abstracts, 1191-1194. doi: 10.1190/1.1851092

Li, Y., Shearer, S., Haney, M. and Dannemiller, N., 2010. Comprehensive approaches to the inversion of magnetic data affected by remanent magnetization. Geophysics, 75(1), L1-L11, doi: 10.1190/1.3294766.

Liu, S., Hu, X., Liu, T., Feng, J., Gao, W. and Qiu, L., 2013. Magnetization vector imaging for borehole magnetic data based on magnitude magnetic anomaly. Geophysics, 78(6), D429-D444. doi:10.11190/GEO2012-0454.1.

Lourenço, J.S. and Morrison, H.F., 1973. Vector magnetic anomalies derived from measurements of a single component of the field. Geophysics, 38, 359-368.

Lundbak, A., 1956. Combined analysis of gravimetric and magnetic anomalies and some palaeomagnetic results. Geophysical Prospecting, 4, 226-235.

MacLeod, I.N. and Ellis, R.G., 2013. Magnetic Vector Inversion, a simple approach to the challenge of varying direction of rock magnetization. A Forum on the Application of Remanent Magnetisation and Self-Demagnetisation Estimation to Mineral Exploration. 23rd ASEG Conference and Exhibition, Melbourne.
http://www.geosoft.com/media/uploads/resources/technical-papers/aseg_2013_mvi_simple_approach_challenge_varying_direction_rock_magnetization.pdf

Macnae, J., 1994. Viscous magnetization: Misleading Koeningsberger's Q: SEG Technical Program Expanded Abstracts, 456-458. doi: 10.1190/1.1932125

Martín-Hernández, F., Dekkers, M.J., Bominaar-Silkens, I. M. A., and Maan, J.C., 2008. Magnetic anisotropy behaviour of pyrrhotite as determined by low- and high-field experiments. Geophysical Journal International, 174(1): 42-54.

McEnroe, S.A., Fabian, K., Robinson, P., Gaina, C. and Brown, L.L., 2009a. Crustal magnetism, lamellar magnetism and rocks that remember. Elements, 5, 241-246.

McEnroe, S.A., Brown, L.L. and Robinson, P., 2009b. Remanent and induced magnetic anomalies over a layered intrusion: Effects from crystal fractionation and magma recharge. Tectonophysics, 478, 119-134, http://dx.doi.org/10.1016/j.tecto.2008.11.021.

McElhinny, M. W., & McFadden, P. L., 2000. Paleomagnetism: continents and oceans, Academic Press.

McKenzie, B., Foss, C. and Hillan, D., 2012a. Issues related to determination of the horizontal centre of magnetization. ASEG Extended Abstracts, 2012, 1-4.

McKenzie, B., Foss, C. and Hillan, D., 2012b. An improved search for magnetization direction. ASEG Extended Abstracts 2012: 22nd Geophysical Conference: pp. 1-4.

McFadden, P.L. and McElhinny, M.W., 1988. The combined analysis of remagnetization circles and direct observations in palaeomagnetism. Earth and Planetary Science Letters, 87, 161-172. http://dx.doi.org/10.1016/0012-821X(88)90072-6

Medeiros, W. E. and Silva, J. B., 1995. Simultaneous estimation of total magnetization direction and 3-D spatial orientation. Geophysics, 60(5), 1365-1377.

Mendonça, C.A., 2004. Automatic determination of the magnetization-density ratio and magnetization inclination from the joint interpretation of 2D gravity and magnetic anomalies. Geophysics, 69(4), 938-948.

Mendonça, C. A. and Meguid, A., 2008. Programs to compute magnetization to density ratio and the magnetization inclination from 3-D gravity and magnetic anomalies. Computers & Geosciences, 34(6), 603-610.

Mueller, E.L., Morris, W.A., Killeen, P.G. and Balch, S., 1997. Combined 3-D interpretation of airborne, surface, and borehole vector magnetic at the McConnell nickel deposit: In: A.G. Gubins (Ed.), Proceedings of Exploration 97: Fourth Decennial International Conference on Mineral Exploration, 657-666.

Muniruzzaman, M. and Banks, R.J., 1989. Basement magnetization estimates by wavenumber domain analysis of magnetic and gravity maps. Geophysical Journal International, 97(1), 103-117.

Nicolosi, I., Blanco-Montenegro, I., Pignatelli, A. and Chiappini, M., 2006. Estimating the magnetization direction of crustal structures by means of an equivalent source algorithm. Physics of the Earth and Planetary Interiors, 155(1), 163-169.

Pariso, J. E. and Johnson, H. P., 1993. Do layer 3 rocks make a significant contribution to marine magnetic anomalies? In situ magnetization of gabbros at Ocean Drilling Program Hole 735B. Journal of Geophysical Research: Solid Earth, 98(B9), 16033-16052.

Parker, R. L., Shure, L. and Hildebrand, J. A., 1987. The application of inverse theory to seamount magnetism. Reviews of Geophysics, 25(1), 17-40.

Parkinson, W. D. and Barnes, C. D., 1985. In situ determination of Koenigsberger ratio. Australian Journal of Earth Sciences, 32(1), 1-5.

Parry, L.G., 1980. Shape related factors in the magnetization of immobilised magnetite particles. Phys. Earth Planet. Inter., 22, 144-154.

Pavlov, D. A. and Zhdanov, M. S., 2001. Analysis and interpretation of anomalous conductivity and magnetic permeability effects in time domain electromagnetic data: Part I: Numerical modeling. Journal of Applied Geophysics, 46(4), 217-233.

Pedersen L. B. and Rasmussen T. M. 1990. The gradient tensor of potential anomalies: Some implications on data collection and data processing of maps. Geophysics, 55, 1558-1566.

Phillips, J.D., 2005, Can we estimate total magnetization directions from aeromagnetic data using Helbig's integrals?: Earth Planets Space, 57, 681-689.

Phillips, J.D., Nabighian, M.N., Smith, D.V. and Li, Y., 2007, Estimating locations and total magnetization vectors of compact magnetic sources through combined Helbig and Euler analysis: SEG Expanded Abstracts, 26, 770-774.

Pilkington, M., 1989. Variable-depth magnetization mapping: Application to the Athabasca basin, northern Alberta and Saskatchewan, Canada. Geophysics, 54(9), 1164-1173.

Pilkington, M. and Beiki, M., 2013. Mitigating remanent magnetization effects in magnetic data using the normalized source strength. Geophysics, 78(3), J25–J32. doi: 10.1190/geo2012-0225.1

Pinto, M.J. and McWilliams, M., 1990. Drilling-induced isothermal remanent magnetization. Geophysics, 55, 111-115.

Pozzi, J. P., Martin, J. P., Pocachard, J., Feinberg, H., and Galdeano, A., 1988, In-situ magnetostratigraphy: interpretation of magnetic logging in sediments: Earth and Planetary Science Letters, 88, 357-373.

Pratt, D.A., McKenzie, K.B. and White, A.S., 2012, The remote determination of magnetic remanence: *ASEG Extended Abstracts*, 1–5, http://dx.doi.org/10.1071/ASEG2012ab337.

Pucher, R., 1994. Pyrrhotite-induced aeromagnetic anomalies in western Germany. Journal of Applied Geophysics, 32(1), 33-42.

Puranen, R., 1989. Susceptibilities, iron and magnetite content of Precambrian rocks from Finland. Geological Survey of Finland Report of Investigations, 90, 45 pp.

Purucker, M. E., 1990. The computation of vector magnetic anomalies: A comparison of techniques and errors. Physics of the Earth and Planetary Interiors, 62(3), 231-245.

Radhakrishna Murthy, I.V., 1985. Magnetic equivalence of dipping beds, faults and anticlines. Pure and Applied Geophysics, 123, 893-901.

Richards, M. L., Vacquier, V. and Van Voorhis, G. D., 1967. Calculation of the magnetization of uplifts from combining topographic and magnetic surveys. Geophysics, 32(4), 678-707.

Robinson, P., Harrison, R. J., McEnroe, S. A., and Hargraves, R. B., 2004. Nature and origin of lamellar magnetism in the hematite-ilmenite series. American Mineralogist, 89(5-6), 725-747.

Roest W. and Pilkington M., 1993. Identifying remanent magnetization effects in magnetic data. Geophysics, 58, 653–659.

Saltus, R.W. and Blakely, R.J., 2011, Unique geologic insights from “non-unique” gravity and magnetic interpretation: GSA Today, 21(12), 4-11, doi: 10.1130/G136A.1.

Schmidt, P. W., 1982. Linearity spectrum analysis of multi-component magnetizations and its application to some igneous rocks from south-eastern Australia. Geophysical Journal of the Royal Astronomical Society, 70: 647–665. doi: 10.1111/j.1365-246X.1982.tb05978.x

Schmidt, P.W., 1985. Bias in converging great circle methods, Earth and Planetary Science Letters, 72, 427-432.

Schmidt, P.W., 1993. Palaeomagnetic cleaning strategies. Physics of the Earth and Planetary Interiors, 76, 169-178.

Schmidt, P.W. and Clark. D.A., 1997, Field trialling next generation magnetics: Exploration and Mining Report 391R, 64p.

Schmidt, P. W. and Clark, D.A., 1998, The calculation of magnetic components and moments from TMI: a case study from the Tuckers igneous complex, Queensland: Exploration Geophysics, 29, 609-614.

Schmidt, P.W. and Clark, D.A., 2000, Paleomagnetism, apparent polar wander path and paleolatitude, *in* Veevers, J.J., ed., Billion-year Earth History of Australia and Neighbours in Gondwanaland. Gemoc Press, p. 12-17.

Schmidt, P.W., McEnroe, S.E., Clark, D.A., Robinson, P., 2007. Magnetic properties and potential field modeling of the Peculiar Knob metamorphosed iron formation, South Australia: An analog for the source of the intense Martian magnetic anomalies? Journal of Geophysical Research, 112, B03102, doi:10.1029/2006JB004495.

Schmidt, P.W. and Lackie, M.A., 2014, Practical considerations: making measurements of susceptibility, remanence and Q in the field. A Forum on the Application of Remanent Magnetisation and Self-Demagnetisation Estimation to Mineral Exploration. Exploration Geophysics (in press).

Schnetzler. C.C. and Taylor, P.T., 1984. Evaluation of an observational method for estimation of remanent magnetization. Geophysics, 49(3), 282-290.

Shcherbakov, V.P. and Fabian, K., 2005. On the determination of magnetic grain-size distributions of superparamagnetic particle ensembles using the frequency dependence of susceptibility at different temperatures. Geophysical Journal International, 162, 736-746.

Shive, P.N., 1989. Can remanent magnetization in the deep crust contribute to long wavelength magnetic anomalies? Geophysical Research Letters, 16, 89-92.

Silva, J. B. and Hohmann, G. W., 1984. Airborne magnetic susceptibility mapping. Exploration Geophysics, 15(1), 1-13.

Silva, J., Medeiros, W., and Barbosa, V., 2002, Practical applications of uniqueness theorems in gravimetry: Part I- Constructing sound interpretation methods: Geophysics, 67(3), 788–794. doi: 10.1190/1.1484522.

Silva, J. B., Vasconcelos, S. S. and Barbosa, V. C., 2010. Apparent-magnetization mapping using entropic regularization. Geophysics, 75(2), L39-L50.

Smith, P. and Hall, D., 1995. Application of geophysics to the White Devil Gold Deposit, NT. Exploration Geophysics, 26(3), 116-123.

Stacey, F.D., Banejee, S.K., 1974. The Physical Principles of Rock Magnetism. Elsevier, Amsterdam.

Stavrev, P. and Gerovska, D., 2000. Magnetic field transforms with low sensitivity to the direction of source magnetization and high centricity. Geophysical Prospecting, 48(2), 317-340.

Suttie, N., Shaw, J., and Hill, M. J., 2010. Direct demonstration of microwave demagnetization of a whole rock sample with minimal heating. Earth and Planetary Science Letters, 292(3), 357-362. http://dx.doi.org/10.1016/j.epsl.2010.02.002

Tauxe, L., Kylstra, N. *and* Constable, C., 1991, Bootstrap statistics for paleomagnetic data, Journal of Geophysical Research, *96(*B7*)*, 11723–11740, *doi:10.1029/91JB00572.*

Thomson, G.F., Cornwell, J.D. and Collinson, D.W., 1991. Magnetic characteristics of some pyrrhotite-bearing rocks in the United Kingdom. Geoexploration, 28(1), 23-41.

Tsirul'skiy, A.V., 1972. Uniqueness of the solution of the inverse problem of potential theory in the artificial magnetization method. Izvestiya, Earth Physics, 9, 64-67.

Tschirhart, P., Morris, B. And Hodges, G., 2013. A new regional/residual separation for magnetic data sets using susceptibility from frequency-domain electromagnetic data. Geophysics, 78, B351-B359, doi:10.1190/GEO2012-0506.1.

Tucker, D.H., 1972. Magnetic and gravity interpretation of an area of Precambian sediments in Australia. Ph.D. thesis, University of Adelaide.

Walton, D., Shaw, J., Share, J. and Hakes, J., 1992. Microwave demagnetization: Journal of Applied Physics 71, 1549; http://dx.doi.org/10.1063/1.351230

Ward, S.H., 1959. Unique determination of conductivity, susceptibility, size, and depth in multifrequency electromagnetic exploration. Geophysics, 24(3), 531–546. doi: 10.1190/1.1438623

Wilson, G.D.V., 1970. The use of the Poisson relationship for separating the anomalies due to neighboring bodies, and for recongnizing inhomogeneities and structural deformation. Bolletino di Geofisica Teorica ed Applicata, 12, 158-182.

Woodward, D. J., 1993. Inversion of aeromagnetic data using digital terrain models. Geophysics, 58(5), 645-652.

Worm, H. U., Clark, D. and Dekkers, M. J., 1993, Magnetic susceptibility of pyrrhotite: grain size, field and frequency dependence: Geophysical Journal International, 114, 127-137.

Wynn, W.M., 1999, Detection, localization, and characterization of static magnetic-dipole sources, *In* C.E. Baum (Ed.), Detection and Identification of Visually Obscured Targets, Taylor & Francis, Philadelphia, pp. 337-374.

Yang, Y. P. and Emerson, D. W., 1997, Electromagnetic conductivities of rock cores: theory and analog results: Geophysics, 62(6), 1779-1793.

Young, J.A., Keenan, S.T., Clark, D.A., Leslie, K.E., Sullivan, P., Fairman, P., Williams, C., Foley, C.P. and Billings, S.D. 2010. A Superconducting Magnetic Tensor Gradiometer for Underwater UXO Detection. ASEG Extended Abstracts 2010: 21st Geophysical Conference: pp. 1-4.

Zhang, Z. and Oldenburg, D. W., 1997. Recovering magnetic susceptibility from electromagnetic data over a one-dimensional earth. Geophysical Journal International, 130(2), 422-434.

Zhang, Z. and Oldenburg, D. W., 1999. Simultaneous reconstruction of 1-D susceptibility and conductivity from electromagnetic data. Geophysics, 64(1), 33-47.

Zhdanov, M. S. And Pavlov, D. A., 2001. Analysis and interpretation of anomalous conductivity and magnetic permeability effects in time domain electromagnetic data: Part II: Sμ-inversion. Journal of Applied Geophysics, 46(4), 217-233.

Table 1. Ratios of finite range to infinite range integral moments for Helbig analysis (point dipole model)

	Finite integral/infinite integral (%)												
R/h	$(x-x_0)b_i$, $(y-y_0)b_i$	$(x-x_0)^2B_{xj}$	$(x-x_0)\ (y-y_0)B_{xy}$	λ_3	μ	μ^2	h'	m'	$x\mu$	$(x-x_0)\lambda_2$	$x\mu^2$	$(x-x_0)\lambda_2^2$	$(x-x_0)^2\mu^2$
0.5	1.6	–0.4	0.3	28	20	49	29	1.6	20	1.6	49	18	10
1	12	0.2	5	65	50	88	53	14	50	12	88	69	50
2	37	21	27	91	80	99	80	52	80	37	99	97	90
3	54	40	45	97	90	100	90	73	90	54	100	100	97
4	66	52	56	99	94	100	94	83	94	64	100	100	99
5	71	61	64	99	96	100	96	89	96	71	100	100	100
6	76	67	70	100	97	100	97	92	97	76	100	100	100
8	81	75	77	100	98	100	98	95	98	81	100	100	100
10	85	80	81	100	99	100	99	97	99	85	100	100	100
15	90	86	88	100	100	100	100	99	100	90	100	100	100
20	93	90	91	100	100	100	100	99	100	93	100	100	100

h' and m' correspond to the quantities in equations (62) and (64) respectively

Table 2. Signal strength for DVM and combined magnetometry/gradiometry methods

Anomaly magnitude (nT)	Geomagnetic variation (nT)	Local field perturbation (nT)			Local gradient perturbation* (pT/m) Centroid depth 100 m			Local gradient perturbation* (pT/m) Centroid depth 200 m		
		***Q* = 0**	***Q* = 1**	***Q* = 9**	***Q* = 0**	***Q* = 1**	***Q* = 9**	***Q* = 0**	***Q* = 1**	***Q* = 9**
10,000	100	20	10	1	600	300	30	300	150	15
10,000	10	2	1	0.1	60	30	3	30	15	1.5
10,000	1	0.2	0.1	0.01	6	3	0.3	3	1.5	0.15
1000	100	2	1	0.1	60	30	3	30	15	1.5
1000	10	0.2	0.1	0.01	6	3	0.3	3	1.5	0.15
100	100	0.2	0.1	0.01	6	3	0.3	3	1.5	0.15
100	10	0.02	0.01	0.001	0.6	0.3	0.03	0.3	0.15	0.015

* Gradient signals refer to compact sources at the given depths. For a pipe-like source with top at the given depths, the corresponding gradient signals, are reduced by about one third. The same decrease applies to a source of compact cross-section, with considerable strike length, at the given depths. For a thin sheet source with top at the given depths, the corresponding gradient signals, are reduced by about two thirds.

Table 3. Comparison of different methods for determination of source magnetisation

METHOD	ASSUMPTIONS/RESTRICTIONS/ REQUIREMENTS	PARAMETERS ESTIMATED	LIMITATIONS
Sample measurements	• Representative sampling • Sufficient sampling • NRM uncontaminated or cleanable • Adequate statistical analysis and appropriate treatment of vectors	k or $\mathbf{K}$, $\mathbf{M}_{\mathrm{IND}}$, $\mathbf{M}_{\mathrm{NRM}}$, $\mathbf{M}$, Q	• Unavailability of samples • Available samples unrepresentative • Remanence contaminated • Weathering • Heterogeneity, nugget effect • Requires sophisticated equipment for complex NRM
Borehole measurements (vector magnetometer + susceptibility logging)	• Uniform properties within intersected source • Layered earth with known dips, or known shape of intersected source • Hole intersects source(s)	k , $\mathbf{M}_{\mathrm{IND}}$, $\mathbf{M}_{\mathrm{NRM}}$, $\mathbf{M}$, Q	• Source geometry may be unknown (possibly can be modelled by external measurements) • Orientation noise on vector measurements • Noisy vectors due to heterogeneity and rugosity
Petrology + palaeopole database	• Good petrographic descriptions • Known geological history • Events with well-defined ages or plausible age range	k , $\mathbf{M}_{\mathrm{IND}}$, $\sim\lvert\mathbf{M}_{\mathrm{NRM}}\rvert$, $\sim\mathbf{M}$, $\sim Q$	• Petrological information may be insufficient • Complex history • Age uncertainty • APWP poorly known • Unknown local tectonic rotations
Constrained modelling/inversion	• Source assumed to be non-pathological • Magnetic data only: unique inversion of geometry requires assuming homogeneity, planar faces, single intersection with every vertical line through body, noise-free data • Magnetics + geometry from other methods: requires assuming homogeneity	*Compact 2D source*: $\mathbf{M}_{\perp}A$, $\mathbf{M}_{\perp}/\lvert\mathbf{M}_{\perp}\rvert$ *Compact 3D source*: $\mathbf{m} = \mathbf{M}V$, $\mathbf{M}/\lvert\mathbf{M}\rvert$ *2D finite equivalent sources*: $\mathbf{M}_{\perp}A$, $\mathbf{M}_{\perp}/\lvert\mathbf{M}_{\perp}\rvert$ *3D finite equivalent sources*: $\mathbf{m} = \mathbf{M}V$, $\mathbf{M}/\lvert\mathbf{M}\rvert$ *Unique 2D polygon*: $\mathbf{M}_{\perp}$ *Unique 3D polyhedron*: $\mathbf{M}$ *Defined 2D geometry*: $\mathbf{M}_{\perp}$ *Defined 3D geometry*: $\mathbf{M}$	• Geometry can be non-unique if unconstrained, implying magnetisation intensity is indeterminate and direction may be inaccurate • Uniqueness requires special assumptions or extra information • Sensitive to noise, unremoved regional trends, undersampling etc.

Table 3 (continued). Comparison of different methods for determination of source magnetisation

Simple direct inversions for simple sources	• Source type must be assumed or constrained, e.g. dipole model: compact 3D source/homogeneous sphere/equidimensional source not too close to sensor • Source location must be inverted first	$\mathbf{m} = \mathbf{M}V$, $\mathbf{M}/\lvert\mathbf{M}\rvert$ (dipole) $\mathbf{M}A$, $\mathbf{M}/\lvert\mathbf{M}\rvert$ (narrow vertical pipe) $\mathbf{M}_\perp A$, $\mathbf{M}_\perp/\lvert\mathbf{M}_\perp\rvert$ (2D horizontal cylinder) $\mathbf{M}_\perp t$, $\mathbf{M}_\perp/\lvert\mathbf{M}_\perp\rvert$ (2D thin sheet) $\mathbf{M}_\perp$, $\mathbf{M}_\perp/\lvert\mathbf{M}_\perp\rvert$ (2D thick sheet/contact)	• Source may not conform to assumed form • Requires vector or gradient tensor data to be measured or to be accurately calculable from sufficiently high quality TMI data
Comparison of magnetic surveys before and after removal of source	• Known geometry of removed material (to determine $\overline{\mathbf{M}}$) • Homogeneous magnetisation (to determine $\mathbf{M}$)	$\mathbf{m} = \mathbf{M}V$; $\overline{\mathbf{M}}$, $\mathbf{M}$, $\mathbf{M}_{\mathrm{IND}}$, $\mathbf{M}_{\mathrm{NRM}}$, $\mathbf{M}$, Q (if k of removed material has been measured	• Requires high quality magnetic surveys both before and after removal of source • Requires 3D delineation of source
Combined magnetics and gravity (based on Poisson's relation)	• Assumes common source for magnetic and gravity anomalies (shape does not need to be known) • Assumes homogeneous density and magnetisation, or at least constant $\lvert\mathbf{M}\rvert/\rho$ and constant direction of $\mathbf{M}$	$\lvert\mathbf{M}\rvert/\rho$, $\mathbf{M}/\lvert\mathbf{M}\rvert$,	• Sources of gravity and magnetic anomalies are often not identical • Density or magnetisation contrast may be insufficient to generate anomaly that can be accurately separated from background trends and noise
Active source magnetics	• Roving primary source field is accurately known across survey area • Measurements are made sufficiently long after switching primary field that eddy currents in subsurface have decayed • For frequency domain methods: f is low enough to provide required penetration depth; subsurface is (i) homogeneous half-space, or (ii) 1D, over footprint of system	k , $\mathbf{M}_{\mathrm{IND}}$	• Rapid fall-off restricts method to shallow sources, with tradeoff between depth of penetration and spatial resolution of subsurface magnetisation distribution • Complex geology/dipping interfaces/high conductivities can make apparent susceptibilities inaccurate • Does not detect remanence

Table 3 (continued). Comparison of different methods for determination of source magnetisation

Helbig-type analysis	• Source has limited lateral and depth extents (geometry otherwise arbitrary) and is well separated from neighbouring sources • Magnetic data are sufficiently high quality to define vector and/or tensor components accurately over extensive area	$\mathbf{m} = \mathbf{M}V$, $\mathbf{M}/\lvert\mathbf{M}\rvert$	• Source may extend beyond survey area, or have large depth extent • Interference from neighbouring anomalies • Unremoved regional trends • Requires depth of centroid estimate for accurate calculation of moment magnitude, corrected for finite range of integration
Methods based on RTP and other transforms	• Stable algorithm for RTP and other transforms, such as pseudogravity • Assumes constant direction of magnetisation throughout source • Works best for compact sources, steeply dipping tabular bodies, steeply plunging pipes and steep contacts	$\mathbf{M}/\lvert\mathbf{M}\rvert$	• Instability of RTP at low latitudes • Sources may have shallow dipping sides • Interference from neighbouring anomalies with different directions of **M**
Base station DVM/magnetometry-gradiometry	• Assumes homogeneous source • Assumes induced magnetisation is parallel to inducing field (deflection due anisotropy or self-demagnetisation requires multiple stations)	*Compact 2D source*: $\mathbf{M}_\perp A$, $\mathbf{M}_\perp/\lvert\mathbf{M}_\perp\rvert$, $\mathbf{M}_\perp/k$, $(\mathbf{M}_\perp)_{NRM}/k$, $(\mathbf{M}_\perp)_{NRM}/\lvert(\mathbf{M}_\perp)_{NRM}\rvert$, Q, centroid *Compact 3D source*: $\mathbf{m} = \mathbf{M}V$, $\mathbf{M}/\lvert\mathbf{M}\rvert$, $\mathbf{M}/k$, $\mathbf{M}_{NRM}/k$, $\mathbf{M}_{NRM}/\lvert\mathbf{M}_{NRM}\rvert$, Q, centroid *Arbitrary 2D source*: $\mathbf{M}_\perp/k$, $\mathbf{M}_\perp/\lvert\mathbf{M}_\perp\rvert$, $(\mathbf{M}_\perp)_{NRM}/k$, $(\mathbf{M}_\perp)_{NRM}/\lvert(\mathbf{M}_\perp)_{NRM}\rvert$, Q, centroid *Arbitrary 3D source*: $\mathbf{M}/k$, $\mathbf{M}/\lvert\mathbf{M}\rvert$, $\mathbf{M}_{NRM}/k$, $\mathbf{M}_{NRM}/\lvert\mathbf{M}_{NRM}\rvert$, Q, centroid	• Non-compact source may be inhomogeneous • Induced magnetisation may be deflected by strong anisotropy or self-demagnetisation • Very high Q may make induced signal indeterminate and solution unobtainable • Requires very sensitive gradiometers, or very accurately aligned vector magnetometers

CHAPTER 9 . MAGNETIC EFFECTS OF HYDROTHERMAL ALTERATION IN PORPHYRY COPPER AND IRON-OXIDE COPPER-GOLD SYSTEMS: A REVIEW

Clark, D.A.,2014. Magnetic effects of hydrothermal alteration in porphyry copper and iron-oxide copper–gold systems: A review, Tectonophysics (2014), http://dx.doi.org/10.1016/j.tecto.2013.12.011

Abstract

Magnetic anomaly patterns can be used as a tool for mapping lithology, metamorphic zones and hydrothermal alteration systems, as well as identifying structures that may control passage of magmas or hydrothermal fluids associated with mineralisation. Reliable geological interpretation of mineralised systems requires an understanding of the magmatic, metamorphic and hydrothermal processes that create, alter and destroy magnetic minerals in rocks. Predictive magnetic exploration models for porphyry copper and iron oxide copper-gold (IOCG) deposits can be derived from standard geological models by integrating magnetic petrological principles with petrophysical data, deposit descriptions, and modelling of observed magnetic signatures of these deposits. Even within a particular geological province, the magnetic signatures of similar deposits may differ substantially, due to differences in the local geological setting. Searching for "look-alike" signatures of a known deposit is likely to be unrewarding unless pertinent geological factors are taken into account. These factors include the tectonic setting and magma type, composition and disposition of host rocks, depth of emplacement and post-emplacement erosion level, depth of burial beneath younger cover, post-emplacement faulting and tilting, remanence effects contingent on ages of intrusion and alteration, and metamorphism. Because the effects of these factors on magnetic signatures are reasonably well understood, theoretical magnetic signatures appropriate for the local geological environment can qualitatively guide exploration and make semiquantitative predictions of anomaly amplitudes and patterns. The predictive models also allow detectability of deposit signatures to be assessed, for example when deposits are buried beneath a considerable thickness of nonmagnetic overburden, are covered by highly magnetic heterogeneous volcanic rocks, or there is a strong regional magnetic gradient. This paper reviews the effects of hydrothermal alteration on magnetic properties and magnetic signatures of porphyry copper and iron oxide copper-gold systems and presents examples of predictive magnetic exploration models, and their predicted signatures, in various geological circumstances.

Keywords: hydrothermal alteration, magnetic anomalies, magnetic petrology, porphyry copper, iron oxide copper-gold deposits, predictive magnetic exploration models

Introduction

Magnetic surveys rapidly provide cost-effective information on the magnetisation distribution of the Earth's crust, at all scales from local to global. In particular, aeromagnetics is the most widely used geophysical method in hard rock mineral exploration from prospect to province scales. The anomaly patterns revealed by such surveys can be used as a tool for mapping lithology, metamorphic zonation and hydrothermal alteration assemblages, as well as identifying structures that may control passage of magmas or hydrothermal fluids associated with mineralisation. Magnetic anomalies can also provide a direct indication of certain types of ore deposit or mineralised system. A non-exhaustive list includes Kiruna-type magnetite-apatite deposits, iron oxide copper-gold (IOCG) deposits, gold-rich porphyry copper deposits, magnetite and/or pyrrhotite-bearing volcanogenic massive sulfide deposits, pyrrhotite-rich massive nickel sulfide deposits, and diamondiferous kimberlite pipes. Magnetic signatures of mineralisation are not always associated with strongly magnetic sources, but can be indicated by zones of anomalously weak magnetisation. For example, epithermal precious metal deposits hosted by mafic or intermediate volcanic rocks are often associated with smooth magnetic lows, produced by magnetite-destructive alteration, surrounded by the characteristic short wavelength, large amplitude magnetic anomaly patterns of the heterogeneously magnetised unaltered volcanics.

Interpretation of magnetic survey data is inherently ambiguous unless constrained by other geological, petrophysical or geophysical information. Reliable geological interpretation requires an understanding of magnetic petrology. Magnetic petrology is a multidisciplinary field that combines rock magnetism and conventional petrology in order to define the processes that create, alter and destroy magnetic minerals in rocks. Improved geological interpretation results from relating observed magnetic anomalies to magnetic mineralogy, bulk magnetic properties and petrology.

There is as yet no textbook on magnetic petrology, although many specific studies have been published. McIntyre (1980), Grant (1985a,b), and Frost (1991a,b) have given useful summaries of magnetic petrological principles. Puranen (1989) and Henkel (1991, 1994)

have analysed large petrophysical databases from Scandinavia and related magnetic mineralogy and magnetic properties to geological factors. Clark et al. (1992) presented several magnetic petrological case studies, Clark (1997) tabulated magnetic properties of rock-forming minerals and reviewed general aspects of magnetic petrophysics and magnetic petrology, and Clark (1999) reviewed the magnetic petrology of intrusive igneous rocks and discussed exploration implications for intrusion-related mineral deposits.

Useful general references on hydrothermal alteration include Meyer and Hemley (1967), Rose and Burt (1979), Guilbert and Park (1986), Lentz (1994), Reed (1997) and Burnham (1997). Hydrothermal alteration exerts a major influence on magnetic properties of rocks and on associated magnetic anomaly patterns. Magnetic surveys can therefore be very useful for mapping mineralised systems and, in some cases, for defining ore deposits within those systems. The magnetic effects depend not only on the physical state (temperature, pressure etc.) and chemical composition of the fluids, but also on the fluid/rock ratio and on the hydraulic permeability and composition of the protolith.

Studemeister (1983) points out that the redox state of iron in rocks is a useful indicator of hydrothermal alteration. Large volumes of fluid or high concentrations of exotic reactants, such as hydrogen or oxygen, are required to shift Fe^{3+}/Fe^{2+}. When reactions associated with large water/rock ratios occur, the change in redox state of the rocks produces large changes in magnetic properties due to creation, destruction, or modification (changes of composition or microstructure) of ferromagnetic minerals. Processes other than redox reactions can also affect magnetic properties. For example acid-base reactions and Fe metasomatism influence iron speciation, hence magnetic mineralogy. For example the reaction

$$Fe_2O_3 + H_2O + Fe^{2+} \leftrightarrow Fe_3O_4 + 2H^+, \qquad (1)$$

represents transformation of hematite to magnetite by reaction with Fe^{2+}-bearing hydrothermal fluid, generating acidity in the process, or the reverse transformation of magnetite by acidic solutions to hematite, with excess ferrous iron passing into solution (Ohmoto, 2003). This is an acid-base reaction, *not* a redox reaction, because the ferric and

ferrous ion contents are unchanged. The forward reaction represents Fe-metasomatism, whereas the reverse reaction describes leaching of ferrous iron from the rock.

Useful case histories of magnetic signatures of hydrothermal alteration effects include Criss and Champion (1984), Criss et al. (1985), Lapointe et al. (1985), Allis (1990), Irvine and Smith (1990), Finn (2001, 2002, 2007) and Airo (2002).

Predictive magnetic exploration models

Clark et al. (2004) developed the concept of predictive magnetic exploration models for porphyry copper, volcanic-hosted epithermal and IOCG deposits. Purucker and Clark (2011) presented some examples of these models. The predictive models are based on magnetic petrological principles, standard geological models, deposit descriptions, magnetic petrophysical data from deposits and observed magnetic signatures. They are designed to predict what the magnetic signatures of these deposits should look like in a variety of different geological settings, by taking into account the geological factors that control the magnetic signatures. These factors include the tectonic setting and magma type, composition and disposition of host rocks, depth of emplacement and post-emplacement erosion level, depth of burial beneath younger cover, post-emplacement faulting and tilting, remanence effects contingent on ages of intrusion and alteration, and metamorphism. Even within a particular geological province, these factors may vary greatly and the magnetic signatures of similar deposits may therefore differ substantially. Searching for “look-alike” signatures of a known deposit is likely to be unrewarding unless the local geological setting is taken into account.

Igneous rocks associated with mineralised systems can be classified into four groups on the basis of the oxidation state: strongly reduced, reduced, oxidised, or strongly oxidised (Champion and Heinemann, 1994). These categories can be determined on the basis of chemistry, if ferrous and ferric iron contents are known, as shown in Figure 1, or mineralogy (see Table 1). Significant differences in magnetic susceptibility, at equivalent degrees of differentiation, are found for mantle-derived (M-type) intrusions, found typically in island arcs, and I-type granitoids in continental arcs. Intrusions associated with gold-rich porphyry copper deposits are more oxidised than those associated with gold-poor porphyry copper deposits, and accordingly contain more abundant igneous

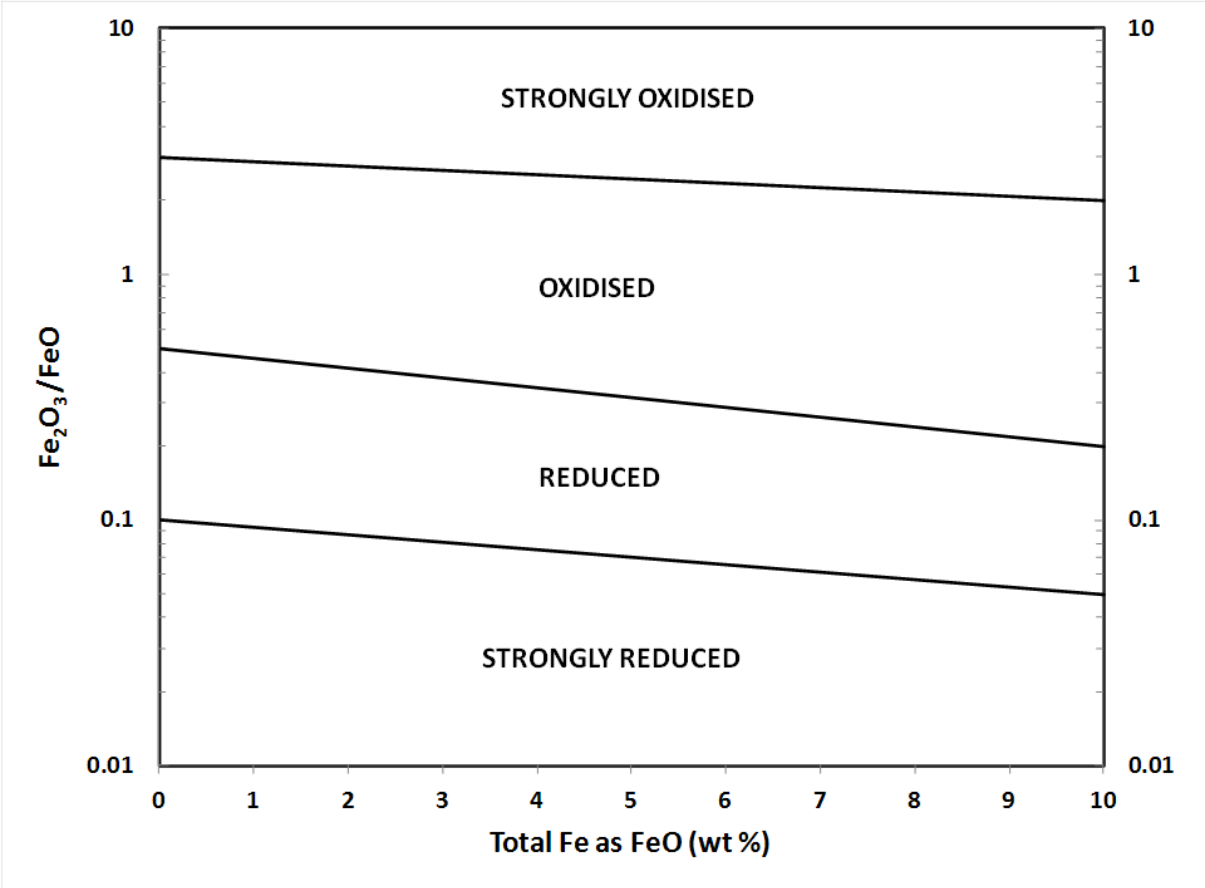

Figure 1. Classification of oxidation state of igneous rocks on the basis of Fe_2O_3/FeO (both expressed as weight per cent). Fields for strongly oxidised, oxidised, reduced and strongly reduced rocks are taken from Champion and Heinemann (1994), following Ishihara et al. (1979) and Blevin and Chappell (1992). Note that total Fe as FeO is calculated from weight percentages of ferric and ferrous oxide as $FeO^T = 0.9\ Fe_2O_3 + FeO$, and the ferric/ferrous iron ratio can be simply calculated from the weight percentages of the oxides using the relation: $Fe^{3+}/Fe^{2+} = 0.9[Fe_2O_3\ (wt\ \%)/FeO\ (wt\ \%)]$.

Table 1. Characteristic mineralogy for oxidation classes of igneous rocks (Champion and Heinemann, 1994)

Oxidation state category	**Mineralogy**
Strongly oxidised	magnetite + primary sphene ± hematite
Oxidised	magnetite ± ilmenite (high Fe^{3+} or Mn)
Reduced	ilmenite without magnetite
Strongly reduced	ilmenite (low Fe^{3+} and Mn) + pyrrhotite; magnetite absent

(titano)magnetite and produce greater quantities of hydrothermal magnetite during early potassic alteration. Although primary magmatic hematite can also occur in association with magnetite, magmas that are sufficiently oxidised to precipitate abundant hematite, with little or no magnetite, are unusual (Table 1). An empirical association between Au-rich (> 0.4 g/t) porphyry copper deposits and abundant magnetite in the potassic core has been documented by Sillitoe (1979, 1990, 1996) and confirmed by many other workers.

The corresponding magnetic signatures also differ profoundly, with more prominent anomalies associated with gold-rich porphyry copper deposits than with gold-poor deposits. For development of a magmatic Cu-Au deposit, the magma must remain sulfur undersaturated throughout most or all of its evolution (Wyborn and Sun, 1994). Sulfur saturation of the magma is strongly affected by oxidation state, as well as by sulfur content. At high oxygen fugacities, sulfur becomes more soluble in the magma, dissolving as an anhydrite component. Early precipitation of sulfides is suppressed and ore metals are retained in the melt and concentrated during fractional crystallisation, greatly enhancing the chances of producing economic mineralisation from late stage, evolved fluids. The magnetite content of the unaltered intrusive rocks, and the generation of early hydrothermal magnetite, are both boosted by high oxygen fugacity in the magma, particularly for relatively K-rich magmas.

Host rock compositions control magnetic signatures of mineralised systems in two important ways:

1. Magnetic anomalies arise from magnetisation *contrasts* – thus the magnetic properties of the unaltered country rocks inherently influence the magnetic signature of the mineralised system. For example, a moderately magnetic intrusion emplaced into weakly magnetic, unreactive country rocks, such as quartzites or silicic volcanics, will have an associated reduced-to-the-pole (RTP) magnetic high. On the other hand, a similar intrusion emplaced into strongly magnetic rocks, e.g. normally magnetised fresh basalts, will have a RTP magnetic low.
2. Alteration assemblages, including magnetic minerals, that are associated with a particular alteration phase around a mineralising system are strongly controlled by the protolith composition, as well as the chemical and physical state of the hydrothermal fluid. Protolith rheology also influences the distribution of alteration assemblages. For example, quartzite host rocks are more likely to fracture to

produce veins and breccias, whereas mica- and clay-rich lithologies develop more pervasive alteration.

It is obvious that exhumation of a buried mineralised system by erosion can dramatically change its magnetic signature. Burial of the system under younger cover can compromise its detectability. A thick sequence of nonmagnetic sediments broadens anomalies, reduces their amplitudes, and blurs zonation patterns, simply because the magnetic sources are deeper. Burial under magnetic volcanics with typical strong, short wavelength anomalies obscures the signature of an underlying deposit and may render it undetectable. Examples of the dependence of signatures on erosion level, post-emplacement tilting and faulting are given in following sections.

Hydrothermal magnetite in porphyry systems is generally well-crystallised, of nearly pure end-member composition, with grain sizes in the true multidomain range (i.e. > 20 µm). Thermoremanent magnetisation (TRM) or chemical remanent magnetisation (CRM) carried by such grains is magnetically soft and subordinate to induced magnetisation, with Koenigsberger ratio $Q < 1$ (Clark, 1997). This is also the case for CRM carried by hydrothermal magnetite and hematite in IOCG systems, although multidomain hematite, i.e. larger than 100 µm, could acquire in principle an intense TRM during cooling from above its Curie temperature (680°C), following high grade metamorphism of an IOCG deposit.

The magmatic-hydrothermal evolution of mineralised porphyry systems typically spans more than a million years, during which one or more geomagnetic reversals may occur. Therefore any stable remanence carried by intrusive rocks and altered host rocks in a mineralised porphyry system is likely to be multicomponent, reflecting partial overprinting of normal components by reversed components and vice versa, unless the system develops within a geomagnetic superchron. These opposing components produce partial or complete cancellation of the bulk remanence of large volumes of rock, and remanence effects on magnetic anomalies are therefore generally small.

Dual polarity remanence carried by a subordinate population of magnetically stable carriers is frequently found in mineralised porphyry systems, e.g. Porgera, Papua New Guinea (Schmidt et al., 1997). Hoschke (2010, 2011) reports dual polarity remanence in

the Batu Hijau (Indonesia), Grasberg (Indonesia) and Bajo de la Alumbrera (Argentina) Cu-Au porphyries, and Astudillo et al. (2010) found normal and reversed polarity remanence in distinct zones within the El Teniente Cu-Mo porphyry system in Chile. These porphyry systems are all of Tertiary age. Similarly, both normal and reverse polarities are found in the Cretaceous La Candelaria (Chile) IOCG deposit, implying partial overprinting of the remanence acquired during hydrothermal alteration by a considerably younger thermal or chemical event (Austin et al., 2012). On the other hand the stable remanence of the Early Permian breccia-hosted, porphyry-related Au system at Mount Leyshon (Australia) is consistently reversed, because the magmatic-hydrothermal evolution of this system occurred wholly within the Permo-Carboniferous Reverse Superchron (Clark and Lackie, 2001).

Because observed magnetic signatures of any given model depend on the local geomagnetic inclination, it is necessary to convert the predicted signatures into a standard form that is independent of the field inclination and can easily be compared with suitably processed observations. Signatures are predicted for vertical field inclination so that they can be directly compared to RTP observed data, which can be calculated by standard techniques (Blakely, 1996). In areas of very low geomagnetic inclination, RTP processing is unstable. For those areas signatures can be calculated for zero inclination (reduced to the equator) to allow comparison with measured total magnetic intensity anomalies.

1. General Features of Porphyry Copper Deposits

Porphyry deposits are intrusion-related, large tonnage, low grade mineral deposits with metal assemblages that may include all or some of copper, molybdenum, gold and silver. Their genesis is related to the emplacement of intermediate to felsic subvolcanic porphyritic intrusions that are commonly generated above subduction zones. Hunt (1991) summarises the critical phases in the generation of porphyry copper deposits.

McMillan and Panteleyev (1995) discuss general aspects of the classification of porphyry copper deposits of the Canadian Cordillera, including morphological/depth-zoning models and a chemical classification based on alkalinity. Corbett and Leach (1998) have comprehensively reviewed porphyry and related deposits in the southwest Pacific. The U.S. Geological Survey has recently published a comprehensive review of all aspects of

porphyry copper systems (John et al., 2010), with detailed discussions of genetic models, alteration assemblages and zonation patterns, descriptive geological models, tectonic settings, and geophysical and geochemical exploration exploration methods.

The types of hydrothermal alteration that are important in porphyry copper systems and their magnetic effects are summarised in Table 2. Alteration zoning patterns within carbonate wall rocks, which are highly reactive and acid-neutralising, differ profoundly from those in silicate wall rocks. Porphyry systems emplaced into carbonate host rocks develop mineralogically and magnetically zoned skarns. Einaudi (1982) describes the general zonation of calcic skarns developed within limestone around oxidised porphyry copper intrusions. The overall magnetite content of these calcic skarns ranges from trace amounts to 10% by volume, accompanied by 2-15% sulfides. A proximal garnet zone with pyrite > chalcopyrite passes outwards into a garnet-pyroxene zone with pyrite ≈ chalcopyrite, thence into garnet-wollastonite with bornite and chalcopyrite (±sphalerite), and finally into marble with sphalerite, chalcopyrite and minor pyrite. Magnetite ± hematite is concentrated near the intrusive contact, in the garnet-rich zone, and also near the marble contact. It is scarce within the wollastonite zone. Pyrrhotite may occur in the distal zones. Magnesian (forsterite-talc-serpentine) skarns developed within dolomitic rocks, on the other hand, have lower sulfide contents (< 6%) and more abundant magnetite (20-35%), which is distributed throughout the zone of skarn alteration.

Oxygen fugacity exerts a strong influence on assemblages developed during skarn formation (Kwak, 1994). In calcic (low F and B) ore skarns, early prograde assemblages contain andraditic garnet and/or magnetite-bearing skarns with Mg-rich pyroxene in oxidised environments, whereas hedenbergitic pyroxene + grossularitic garnet occurs in reduced skarns. Pyrrhotite is common, sometimes abundant, in reduced skarns. Oxidised skarns, produced by magmatic fluids derived from oxidised intrusions (± oxidised meteoric fluids), or by reaction with relatively oxidised host rock sequences (e.g. packages containing redbeds or oxidised volcanics) often contain hematite as well as magnetite. Reduced skarns, associated with reduced ilmenite-series intrusions or with reduced host rock sequences (e.g. containing carbonaceous shales) often contain pyrrhotite.

Einaudi et al. (1981), Einaudi (1982) and Meinert (1992, 1993, 1995) have provided detailed discussions of skarn zonation patterns that can be used in predictive magnetic

models of porphyry copper systems emplaced into carbonate rocks. Table 3 lists magnetic properties of skarns inferred from these descriptions and Table 4 gives estimated zonation of magnetic susceptibility inferred from reported modal mineralogy for a typical copper skarn.

Supergene alteration has profound effects on the economics of many intrusive-related ore deposits, particularly by supergene enrichment of grades and modification of metallurgical characteristics. Primary mineralogy, gangue minerals and ore assemblages are all affected. Iron oxides, oxyhydroxides and sulfates derive from decomposition of Fe-bearing sulfides. Acid derived from oxidation of pyrite reacts with K-silicate minerals to produce jarosite at low pH, whereas hematite and goethite are produced at higher pH. Acid attack on K-silicate minerals produces an assemblage that mimics advanced argillic alteration. Weathering of rocks with more than ~5% sulfide generally produces an assemblage with alunite, allophane and jarosite. Magnetite and pyrrhotite are never preserved in intensely weathered zones of intrusive-related systems, although magnetite is relatively resistant to moderate weathering of otherwise unaltered intrusive rocks.

The magnetic mineralogy of the altered rock depends on the abundance and composition of primary magnetic minerals, their stability under the prevailing hydrothermal conditions, and on the ability of the protolith to create secondary magnetic minerals during reaction of the hydrothermal fluid with the pre-existing mineralogy. For example, mafic wall rocks have greater capacity to form secondary magnetite during potassic alteration than do relatively iron-poor felsic rocks. Arkosic sedimentary rocks develop potassic, phyllic and propylitic alteration assemblages that resemble those developed in granitic wall rocks, although they may less perfectly developed, possibly due to the planar fabric (Lowell, 1974). On the other hand, quartzites are relatively poor indicators of alteration zoning, because quartz is essentially non-reactive. Mafic and intermediate igneous rocks contain high Mg, Fe and moderate calcium. Where these are the dominant wall rocks, wide zones of propylitic alteration are favoured, potassic alteration is dominated by biotite, and biotite and chlorite tend to proxy for sericite in intervening zones, reducing or eliminating the phyllic zone. Table 5 summarises the differences between alteration assemblages developed around porphyry copper deposits in mafic, felsic and carbonate host rocks.

Table 5. Porphyry copper deposits: equivalent alteration stages/differing host rocks (Beane, 1994)

Stage	Quartz Monzonite	Diorite	Limestone
Early	K-feldspar + biotite + pyrite + magnetite or hematite	Biotite + KF + albite + epidote + magnetite	Garnet + pyroxene
Copper mineralisation	KF + chlorite + sericite + pyrite ± hematite	Chlorite + epidote + pyrite + magnetite	Actinolite + epidote + pyrite + magnetite
Late	Sericite + pyrite	Chlorite + anhydrite + pyrite + hematite + ?zeolite	Quartz + pyrite

Iron oxide copper gold deposits

Since the discovery of a hitherto unrecognised style of mineralisation at the giant Olympic Dam Cu-U-Au-Ag-REE deposit in South Australia, much has been written on genesis of Olympic Dam-type deposits and on relationships to a wide variety of other Fe oxide hydrothermal deposit types. A comprehensive set of reviews and deposit descriptions has been compiled by Porter (2002). These deposits are characterised by:

- an abundance of hydrothermal magnetite and/or hematite, with relatively low iron sulfide contents
- a chemically distinctive suite of elements (REE-Cu-Co-Au-Ag-U), often with elevated Ba, P, F
- a mineralogical assemblage of iron oxides with one or more copper sulfides and pyrite, with associated K feldspar or sericite or albite or biotite and chlorite within the host rocks. Carbonate is also common.

However IOCG deposits occur in a wide variety of geological settings, have very variable distributions and volumes of associated alteration and are associated, directly or indirectly, with a wide range of magmas. Deposits that have been assigned to this category range in age from Archaean to Tertiary. A range of tectonic settings, including orogenic basin collapse, anorogenic continental rifting, and extensional environments within a subduction-

related continental margin has been inferred for these deposits (Hitzman, 2000). Magmatism related to mantle underplating, high heat flow, and relatively oxidised source rocks (subaerial basalts, oxidised sediments and/or oxidised igneous rocks) are features common to these tectonic settings. Hitzman (2000) argues that IOCG deposits generally do not appear to have a direct spatial relationship with specific intrusions, but are localised along high- to low-angle faults that are usually splays off major, crustal-scale faults. Because IOCG deposits are so diverse and their genesis is as yet poorly understood, their classification is currently based on descriptive models and is somewhat controversial. Recent discussions of classification into subtypes include Corriveau (2007) and Groves et al. (2010).

The origins of the ore-forming fluids are still debated. Barton and Johnson (2000) suggest that two end members occur. The first type, which has relatively high-temperature mineralisation and high K/Na and Si/Fe, is related to magmatic fluids. This type overlaps with porphyry Cu-Au and related deposits. The second end-member corresponds to more oxide-rich, sulfide-poor mineralisation, low Si/Fe ratios and voluminous alkali-rich metasomatism, generally with sodic dominating over potassic alteration. This latter type is related to non-magmatic fluids, such as basinal brines. Some IOCGs represent hybrids between the two end-members.

An association between sedimentary sequences with evaporitic rocks and the occurrence of IOCG deposits has been suggested, but Pollard (2006) points out that many host rock sequences lack evaporites and suggests that the coexisting hypersaline and CO_2-rich fluid inclusions that are typical of these deposits may have resulted from unmixing of an original H_2O-CO_2-salts fluid of magmatic origin. Syn- to post-mineralisation Na-Ca-rich fluids that are present in many deposits may represent meteoric and/or connate fluids that mixed with hypersaline magmatic fluids. Pollard (2006) also points out a general association with magnetite-series, high-K, mildy alkaline intrusive rocks, ranging from diorite to granite in composition. These types of intrusives resemble those associated with porphyry Cu-Au mineralisation.

Haynes (2000) states that IOCG deposits universally occur within host successions that have little or no elemental carbon, reduced carbon compounds, or reduced sulfur minerals, i.e. the successions are relatively oxidised. Within such successions, magnetite is

invariably present and variably abundant, producing a magnetically active environment. On the other hand, Haynes (2000) recognises an iron sulfide copper-(gold) (ISCG) class of deposit that typically occurs near the boundaries between discrete reduced and oxidised domains. The Mount Isa Inlier, Australia, is an example of an area that hosts both types of deposit. The reduced domains have an abundance of carbonaceous rocks or reduced carbon minerals and have relatively subdued magnetic patterns.

Extensive sodic and/or sodic-calcic alteration, often of regional extent, is associated with all IOCG deposits and most ISCG deposits (Haynes, 2000). This alteration produces an albite-magnetite-chlorite or actinolite assemblage, usually with scapolite, hematite, epidote, calcite and sphene. Alteration zones are typically tens to hundreds of km^2 in area. These types of alteration have a different character to sodic and sodic-calcic alteration developed around deep levels of some porphyry systems, which are produced by convecting meteoric or connate waters and are magnetite-destructive. The sodic and sodic-calcic alteration types associated with IOCGs involve substantial iron metasomatism, i.e. the fluids are Na-Ca-Fe rich. Another fundamental difference in the alteration fluids of IOCG and porphyry systems appears to be that IOCG-related fluids are rich in CO_2, whereas porphyry-related fluids are usually very low in CO_2.

The main types of alteration recognised in IOCG systems are listed in Table 6. The sericite-hematite type of alteration has also been termed “argillic” or “hydrolytic”. The acronym HSCC (hematite-sericite-chlorite-carbonate) is also used for this alteration type. Sodic and sodic-calcic alteration styles tend to be early (pre-mineralisation) and particularly extensive. Potassic alteration is more restricted in area, more closely associated with mineralisation, and occurs at higher levels in the system. Sericite-hematite alteration is magnetite-destructive and occurs at upper levels of the system. Sodic-potassic, potassic, potassic-calcic or sericite-hematite alteration may all be associated with mineralisation, depending on the degree of interaction with meteoric or connate fluids (Hitzman, 2000).

Haynes (2000) suggests that, in general, copper precipitation in IOCG deposits results from reduction of oxidised, copper and sulfate-bearing fluids, precipitating copper sulfides, ferric iron-bearing minerals and producing acid. The reducing agent is ferrous iron, either

in solution (in the case of mixing of the metal-bearing fluid with a reduced fluid), or in iron-rich rocks. A generalised reaction is:

$$2Cu^{+} + SO_4^{2-} + 8\ H_2O + 8Fe^{2+} \rightarrow\ 4Fe_2O_3 + 16\ H^{+} + Cu_2S. \qquad (2)$$

The hydrogen ions produce a strongly acidic fluid, which is neutralised by hydrolysis of feldspars. In the case of fluid mixing or reaction with rocks rich in ferrous iron-bearing silicates, this process produces magnetite and/or hematite. Reaction of the oxidised fluid with magnetite-rich rocks precipitates copper sulfides by coupling reduction of the sulfate with oxidation of magnetite to hematite. Thus magnetite-rich rocks represent favourable sites for precipitation of copper sulfides, with some or all of the magnetite being converted to hematite during the mineralising process.

Smith (2002) has reviewed geophysical signatures of IOCG deposits, emphasising the role of magnetic and gravity surveys. Austin and Foss (2012) recently presented modelling studies of a number of Australian IOCGs and reviewed magnetic and gravity characteristics of these deposits. Hayward et al. (2013) have demonstrated the potential for identification of probable IOCG systems within a prospective province through integrated processing and interpretation of magnetic and gravity surveys, informed by physical property measurements. Esdale et al. (2003) provide a detailed geophysical case history of the Olympic Dam deposit. The Olympic Dam deposit is inferred to have formed at very shallow depths and is dominated by sericite-hematite ± quartz ± chlorite ± siderite ± fluorite ± barite alteration. Magnetite has been totally replaced by hematite in the central and upper portions of the deposit, but is present in deeper and peripheral zones. The regional tectonic setting of the Olympic Dam deposit is still enigmatic. Recent attempts to characterise the deep crustal structures and crustal composition beneath and around the Olympic dam province using geophysics include Heinson et al. (2006), Drummond et al. (2006) and Direen and Lyons (2007).

As found at Olympic Dam, IOCG systems tend to be zoned vertically from magnetite-dominant at depth to hematite-dominant at upper levels. Magnetite is also abundant peripheral to the ore zones. This pattern may be altered by tectonic tilting of the system or by faulting. Therefore the magnetic and gravity signatures of IOCG deposits should generally reflect *superposed* or *juxtaposed* gravity and magnetic anomalies. Positive

gravity anomalies arise from both magnetite-rich and hematite-rich zones, whereas the deeper, peripheral, or adjacent magnetic sources correspond to the magnetite-rich zones.
The simplistic notion of *coincident* magnetic and gravity anomalies is misleading, as the sources of the anomalies are spatially separated. I therefore prefer the term *superposed* magnetic and gravity anomalies. Detailed modelling of the gravity and magnetic sources should usually resolve vertical zonation of iron oxides by inferring a deeper source for the magnetic anomaly than for the gravity source. An exception to this expectation could occur when hematite-rich bodies have been heated above 680°C by contact or regional metamorphosism and have thereby acquired sufficient remanence to produce substantial magnetic anomalies.

The total mass of iron oxide minerals within typical IOCG systems is very large, which raises questions about sources of Fe, transportation of Fe in solution and deposition mechanisms of the iron oxides. Iron may be derived from magma or leaching of iron-bearing rocks by metamorphic fluids or basinal brines. Ferrous iron is much more soluble than ferric iron, so it is transported as Fe^{2+}. IOCG deposits and their alteration envelopes often exhibit evidence of replacement of magnetite by hematite (martitisation), or vice versa, forming mushketovite. Similar replacements of one iron oxide by another are also common in skarns. These transformations are often assumed to be redox reactions (i.e. oxidation of magnetite to hematite or reduction of hematite to magnetite), although as Ohmoto (2003) points out, the acid-base reaction given by equation (1) can also explain transformations between magnetite and hematite.

Hanneson (2003) devised a method, based on susceptibility and density trends, for discriminating between magnetic and gravity signatures of barren magnetite-bearing mafic rocks, such as gabbros, and potentially mineralised magnetite-rich and hematite or sulfide-rich hydrothermal deposits. Clark et al. (2004) developed a petrophysical model for the magnetic properties and densities of iron oxide-rich ores and alteration zones in IOCG systems. Both minerals are assumed to be in their respective true multidomain size ranges (> 20 µm for magnetite; > 100 µm for hematite). If the volume fractions of magnetite and hematite in the rock or ore are f_{mt} and f_{hm} respectively then the estimated SI susceptibility k is given by

$$k = 20f_{mt} /[1 + 4.8(1- f_{mt})] + 0.04f_{hm} . \qquad (3)$$

The contribution of magnetite in equation (3) is based on a theoretical relationship that incorporates self-demagnetisation of magnetite grains, modified by a Lorentz field contribution to account for grain interactions (Clark, 1997). The formula assumes an intrinsic susceptibility of 20 SI for the magnetite grains, in accord with Stacey and Banejee's (1974) estimates of intrinsic susceptibility of large MD magnetite grains, and an estimated average effective SI demagnetising factor of $N = 0.24$ for MD magnetite grains (Parry, 1980). For dilute dispersions of magnetite ($f_{mt} < 0.1$), equation (3) reduces to

$$k \approx 3.45\, f_{mt} + 0.04 f_{hm}\,. \qquad (4)$$

The magnetite contribution in equation (4) agrees well with the empirical relationship between susceptibility and magnetite content of rocks found by Puranen (1989). The contribution of hematite in equations (3) and (4) is approximate approximate (susceptibilities of pure end-member MD hematite typically range from ~0.01 SI to ~0.1 SI, depending on crystallinity, stress, and stoichiometry), but the hematite contribution to the susceptibility of massive iron oxide is subordinate to that of magnetite if more than ~1-2% magnetite is present.

Unlike TRM of MD hematite, which has been extensively studied (e.g. Kletetschka et al., 2000; Dunlop and Kletetschka, 2001), CRM carried by MD hematite is not well understood. Theory developed for CRM of MD magnetite (Stacey and Banerjee, 1974) cannot be applied to CRM of MD hematite, because this theory makes the assumption that the coercive force of the grains is smaller than their self-demagnetising fields; a condition that is not satisfied for hematite. No experimental data have ever been published on the acquisition of chemical remanence by hydrothermally grown MD hematite. The most relevant data set is that of Stokking and Tauxe (1990), who found that grain-growth CRM acquired by an assemblage of 0.1-10 µm SD hematite grains in 50 µT had quite low intensity (~0.02 A/m), possibly reflecting poor crystallinity. The CRM intensity was about 0.15 times that of the TRM acquired in the same field (~0.13 A/m), in reasonable agreement with SD theory. TRM intensities of other SD (0.12-2 µm) hematite samples, acquired in 50 µT, range from ~6.5 A/m to ~30 A/m (Özdemir and Dunlop, 2002; 2005).

The theory of grain-growth CRM acquisition in SD grains (Dunlop and Özdemir, 1997, p.367-373) and Stokking and Tauxe’s TRM versus CRM data suggest that CRM intensities

for well-crystallised hydrothermal large SD hematite grains should typically fall in the range ~1-5 A/m. Continued grain growth to true MD size can only reduce this intensity, as domain walls nucleate to generate oppositely magnetised domains within the crystals. Reduction of CRM intensity due to grain growth of cobalt particles from SD to MD size clearly illustrates this phenomenon (Dunlop and Özdemir, 1997, p.369-371).

Taking these considerations into account, grain-growth CRM acquired well below the Curie temperatures of the iron oxides (580°C for magnetite; 680°C for hematite) within undisrupted rocks or acquired post-brecciation within iron oxide-rich breccias is predicted to have intensity

$$\text{CRM (A/m)} \approx 18 f_{\text{mt}} + J_{\text{CRM}}(\text{hm})\, f_{\text{hm}}, \qquad (5)$$

where $J_{\text{CRM}}(\text{hm}) \leq 5$ A/m.

Brecciation of previously acquired remanence randomises the remanence directions, so in most cases breccia zones within IOCG deposits are expected to have negligible CRM, when averaged over substantial volumes of rock.

While CRM carried by MD hematite has only moderate intensity, MD hematite does acquire intense TRM if cooled in the Earth's field from above its Curie temperature (Kletetschka et al., 2000; Dunlop and Kletetschka, 2001). If an IOCG system undergoes high grade contact or regional metamorphism, attaining maximum temperatures above the Curie points of the magnetic minerals (i.e. $T_{\text{max}} >$ 580°C for magnetite; $T_{\text{max}} >$ 680°C for hematite) the TRM intensity acquired on cooling is predicted to be

$$\text{TRM (A/m)} \approx 80 f_{\text{mt}} + 1000 f_{\text{hm}}\,. \qquad (6)$$

The corresponding Koenigsberger ratios Q are given by: Q_{CRM} (magnetite) ≈ 0.13; Q_{CRM} (hematite) ≤ 3; Q_{TRM} (magnetite) ≈ 0.6 (Dunlop and Özdemir, 1997, p.239); Q_{TRM} (hematite) ≈ 600. Extremely high Koenigsberger ratios have been reported for NRMs of contact metamorphosed coarse-grained massive hematite deposits by Schmidt et al. (2007).

The *in situ* induced magnetisation of MD magnetite-bearing rocks is augmented by viscous remanent magnetisation (VRM), subparallel to the induced magnetisation, acquired predominantly over the duration of the Brunhes chron. The contribution of this VRM can be significant for detailed modelling of anomalies. An upper limit for VRM carried by MD magnetite can be obtained by noting that the magnetisation of an isolated magnetite grain, subject to self-demagnetisation, that has fully equilibrated with the ambient field H attains a maximum intensity of $H/N \approx 40/0.24 = 166$ A/m (Shive, 1989). This is about 20% higher than the induced magnetisation of the grain, suggesting an upper limit of ~0.2 for Q_{VRM} of MD magnetite. For high concentrations of magnetite, the constraint imposed by self-demagnetisation is somewhat relaxed, due to grain interactions, but values of Q_{VRM} greater than unity would require very high contents (≥ 90%) of very low coercivity magnetite with exceptionally high intrinsic susceptibility. Based on palaeomagnetic cleaning studies, Clark and Tonkin (1987) and Clark (1988a, 1994) have found Q_{VRM} typically falls in the range 0.1 – 0.3 for semi-massive and massive magnetite ores in several IOCG systems, so $Q_{VRM} \approx 0.2$ is a reasonable assumption for modelling massive magnetite bodies if remanence measurements are unavailable.

Because the susceptibilities of magnetite-rich zones in IOCG systems are so high, accurate modelling requires macroscopic self-demagnetisation of the magnetic bodies, and in some cases interactions between them, to be taken into account. Examples of IOCG deposits for which modelling has incorporated these effects include several Tennant Creek ironstone bodies (Clark and Tonkin, 1987; Hoschke, 1991), Osborne (Clark, 1988a, 2000) and La Candelaria (Austin et al., 2012).

Oxidised gold-rich porphyry copper models

Sillitoe (1979, 1990, 1996) noted that Au-rich (> 0.4 g/t) porphyry copper systems are usually associated with oxidised, magnetic felsic intrusions and have magnetite-rich ± hematite potassic zones. The gold-rich porphyry copper models developed by Clark et al. (2004) conform to general geological models of this type of deposit (e.g. Sillitoe 1979, 1993), but are closely based on deposits that may be regarded as archetypes for particular settings. In particular, the model adopted for mafic-intermediate host rocks is based upon the Bajo de la Alumbrera deposit in Argentina (Guilbert, 1995; Proffett, 2003), and the model for carbonate host rocks is based upon the Grasberg/Ertsberg Cu-Au deposits, Papua

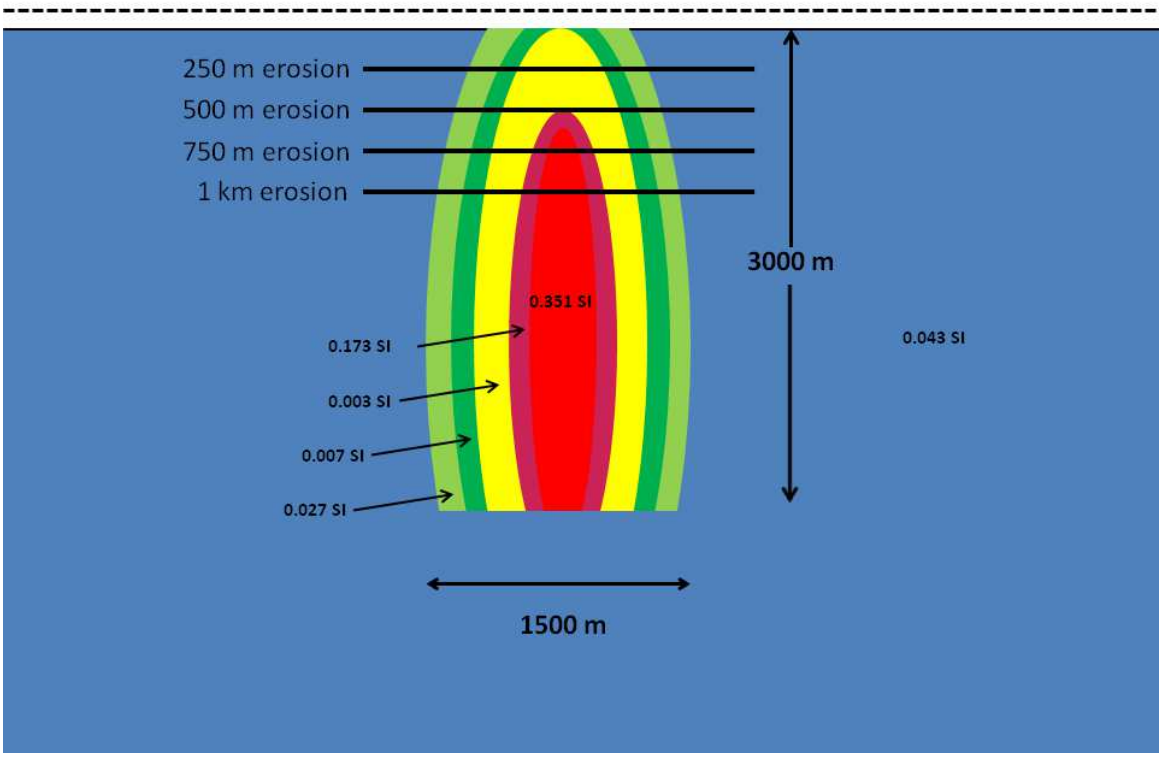

Figure 2. Alteration zonation model of a gold-rich porphyry copper system with maximal development of a biotite-magnetite assemblage in the potassic zone. There is no vertical exaggeration. Intense potassic alteration in the core of the deposit is shown in bright red, the surrounding shells of less intense potassic, phyllic, intense propylitic and moderate propylitic alteration are shown in purple, yellow, dark green and light green respectively. The host rock shown in blue represents magnetic mafic-intermediate rocks (nominally andesite) belonging to an oxidised magmatic suite. The location of the calculated magnetic profile over the uneroded deposit is indicated by the dashed black line. The black horizontal lines indicate exposure level of the system after removal of 250, 500, 750 and 1000 m by erosion.

New Guinea (MacDonald and Arnold, 1994; Potter, 1996). The assumed zoning is concentric and conforms to the quartz-monzonite model, i.e. a magnetite-rich potassic core surrounded by a shell of phyllic alteration passing outwards into propylitic alteration (in silicate host rocks) or zoned skarn alteration (in a carbonate host).

Figure 2 shows the geometry of an end-member gold-rich porphyry copper model, with maximal development of magnetite in the potassic zone, hosted by intermediate-mafic oxidised igneous rocks (nominally "andesite"). In this case there has been insufficient erosion to expose the deposit. The top of the mineralisation lies 500 m below the surface and the only sign of the mineralised system at the surface is a patch of propylitic alteration that could easily be overlooked or, if observed, assumed to be of little significance. The susceptibilities and dimensions of the zones are listed in Table 7.

The inner potassic zone is strongly mineralised and magnetite-rich. It is surrounded by an outer potassic zone that contains less abundant, but still significant, magnetite. The inner potassic zone represents relatively intense development of quartz-magnetite-K feldspar veins, whereas the outer potassic zone corresponds to biotite-K feldspar-quartz-magnetite alteration. A shell of magnetite-destructive phyllic alteration with very low susceptibility envelops the potassic zones. At upper levels this alteration may grade into intermediate argillic and shallow advanced argillic alteration, but the magnetic properties are equivalent for these alteration types and a single shell is sufficient to model the effects. The phyllic zone is surrounded by a zone of intense propylitic alteration, which is partially magnetite-destructive, which passes out into weak propylitic alteration and then into unaltered andesite.

Figure 3 shows theoretical RTP magnetic profiles over the gold-rich porphyry copper model of Figure 2. The magnetic signature is very sensitive to the current level of exposure. For the uneroded deposit the signature is a magnetic low, reflecting demagnetisation of the host rocks throughout the large volume of magnetite-destructive alteration surrounding and above the magnetic core. As deeper levels of the system are exposed by erosion, a central magnetic high overlying the potassic core becomes increasingly prominent.

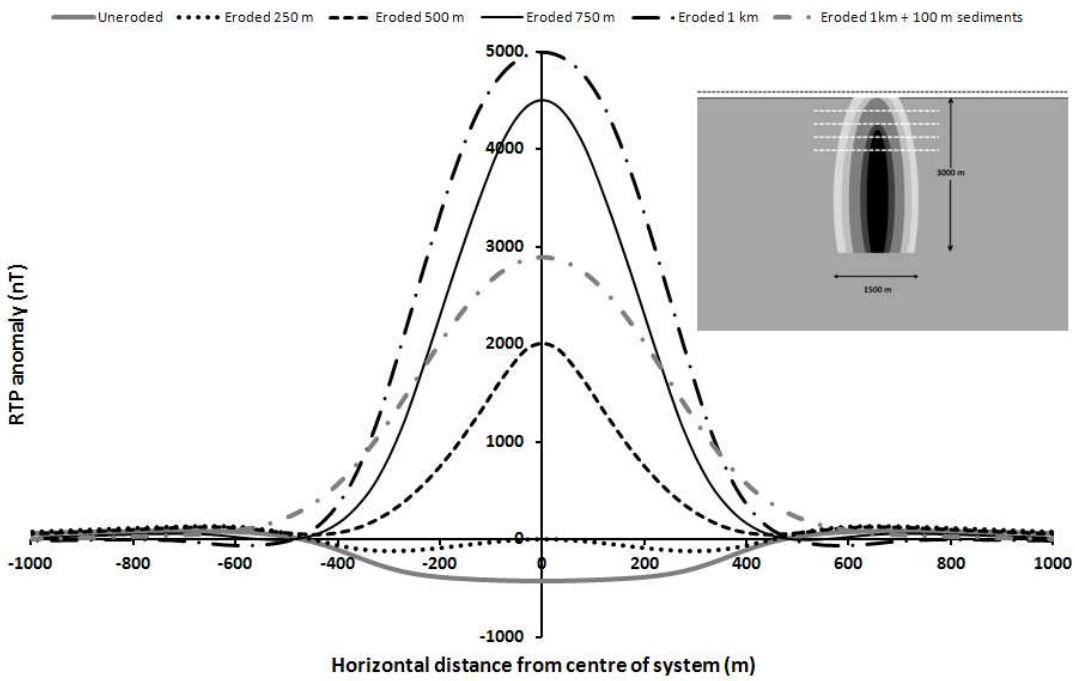

Figure 3. Theoretical RTP magnetic profiles over a gold-rich porphyry copper model with a maximum development of a biotite-magnetite assemblage in the potassic alteration zone. Such deposits tend to be either relatively mafic systems in island arc environments or are associated with alkaline (e.g. high-K calc-alkaline to shoshonitic) magmatism in continental settings. Profiles are shown for an uneroded deposit and after removal of 250 m, 500 m, 750 m, and 1000 m by erosion, as shown in Figure 2 and in the inset. The dimensions and susceptibilities of the alteration zones and host rock are given in Table 7. The effect of burying the 1 km eroded deposit beneath 100 m of younger nonmagnetic overburden is shown by the grey dash-dot profile. Profiles were calculated assuming a geomagnetic field intensity of 50,000 nT and a sensor height of 100 m above the terrain. Geological models and magnetic signatures for this and subsequent Figures were calculated using the Noddy structural history-based modelling software (Jessel and Valenta, 1996).

Alternative models include deposits hosted by different country rocks, including unreactive sedimentary rocks (e.g. quartzites), and carbonates. Quartzites (unaltered and within the propylitic and phyllic zones) and unaltered carbonates have zero susceptibility. Magnetite-skarn, developed distally within a carbonate host, near the marble contact 700 m from the intrusion, is 100 m wide and has k = 0.2 SI. Inner and outer potassic zones are assigned SI susceptibilities of 0.18 and 0.08, respectively, corresponding to ~5 vol% (8.5 wt %) and 2.2 vol % (4 wt %) magnetite, which are typical values for the inner and outer potassic zones at Grasberg.

Table 7. Dimensions and susceptibilities of zones comprising the gold-rich porphyry copper model with maximal development of a magnetite-rich potassic core

Zone	**Diameter* (m)**	**Width* (m)**	**Depth extent (m)**	**Susceptibility (SI)**
Inner potassic	360	360	2400	0.351
Outer potassic	600	120	2500	0.173
Phyllic	1000	200	3000	0.003
Strong propylitic	1200	100	3000	0.007
Weak propylitic	1500	150	3000	0.027
Andesite/Basalt/ Diorite/Gabbro	Very large	Very large	3000	0.043

* Diameters and widths of zones are maxima (at a depth 2000 m below the top of the phyllic zone for the propylitic and phyllic zones, and 1000 m below the top of the phyllic zone for the potassic zones).

Figure 4 shows the effect of differing host rocks on predicted magnetic profiles, for an uneroded gold-rich porphyry copper model with a maximum development of a biotite-magnetite assemblage in the potassic alteration zone. For magnetic mafic-intermediate igneous host rocks the signature is a magnetic low, as in Figure 3. For weakly magnetic felsic host rocks the effects of magnetite-destructive alteration are less important and the signature is a broad high, reflecting the deeply buried magnetic potassic core of the system. For a carbonate host the magnetic high is broadened by the contribution of magnetite-bearing distal skarn alteration. For unreactive host rocks such as quartzites, the magnetic high represents the contribution of the central magnetic intrusion, with overprinting

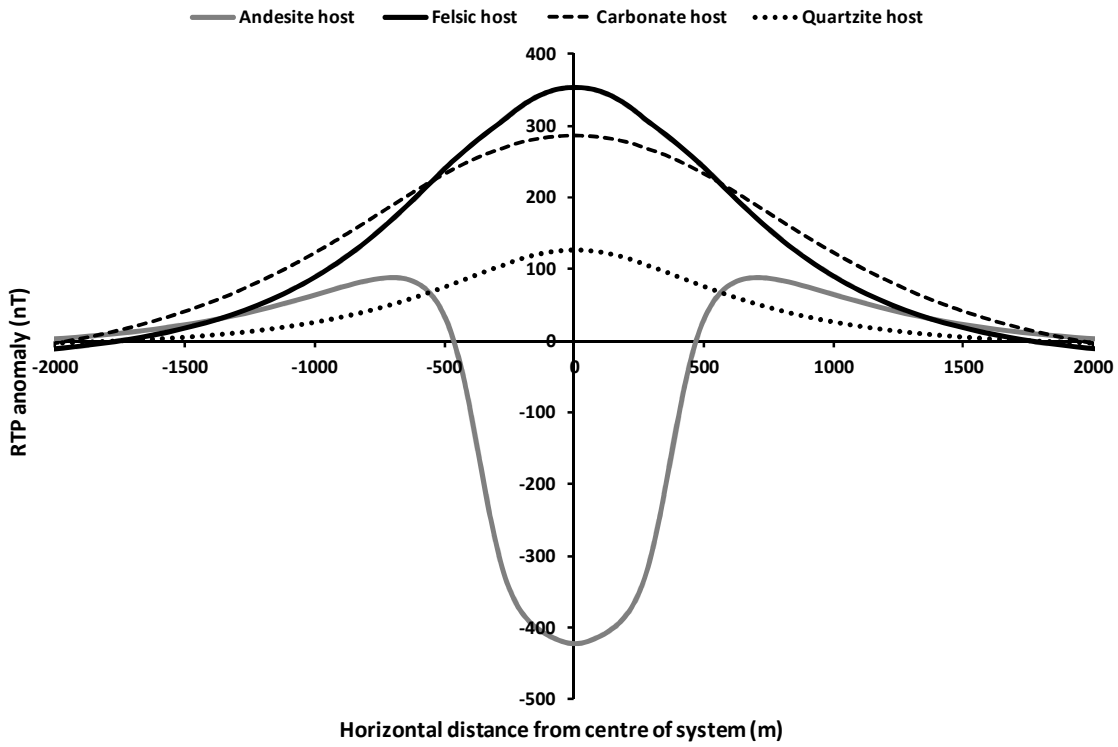

Figure 4. Theoretical RTP magnetic profiles, for differing host rocks, over an uneroded gold-rich porphyry copper model with a maximum development of a biotite-magnetite assemblage in the potassic alteration zone. Profiles were calculated as described in Figure 3. Figure 2 and Table 7 give SI susceptibilities for the unaltered andesite host and weak propylitic, strong propylitic and phyllic zones within it, concentrically zoned around a potassically altered intrusion with SI susceptibilities of 0.173 and 0.351 in its outer and inner zones, respectively. The unaltered felsic host has a susceptibility of 0.004 SI, decreasing to 0.003, 0.002 and 0.001 in the weak propylitic, strong propylitic and phyllic zones respectively, developed around an intrusion with the same properties as for the andesite host. Quartzites (unaltered, and within the propylitic and phyllic zones) and unaltered carbonates have zero susceptibility. For these sedimentary hosts, the potassically altered intrusion has susceptibility 0.18 SI, surrounded by phyllically altered intrusive with zero susceptibility. Magnetite-skarn, developed distally within a carbonate host, near the marble contact 700 m from the intrusion, is 100 m wide and has k = 0.2 SI.

potassic alteration, alone. The magnetisation of the quartzite host rocks is unaffected by alteration and remains essentially zero.

The model described above corresponds to Au-rich porphyry Cu deposits with particularly well developed magnetite-rich potassic zones. Such deposits tend to be either relatively mafic, strongly oxidised systems in island arc environments or associated with alkaline (e.g. high-K calc-alkaline to shoshonitic) magmatism in continental settings. An alternative suite of models with lesser secondary magnetite was also produced. The latter models are applicable to less strongly oxidised or relatively felsic systems, or low-medium K calc-alkaline associations, typically in areas with thick continental crust.

Figure 5 compares theoretical RTP magnetic profiles over gold-rich porphyry copper models, emplaced into magnetic mafic-intermediate rocks, with either maximum development, or a more typical development, of a biotite-magnetite assemblage in the potassic alteration zone. As erosion exposes deeper levels of the system, the model with lesser development of the potassic zone exhibits an “archery target” signature with a central high surrounded by an annular alteration low. The signature resembles that of the Bajo de la Alumbrera (Catamarca Province, Argentina) porphyry copper-gold deposit, described by Guilbert (1995) and displayed and discussed by Hoschke (2008, 2010, 2011).

Table 8 summarises measured magnetic properties from the Bajo de la Alumbrera mineralised system and its host rocks, which clearly document the zoning of magnetisation that gives rise to this classic magnetic anomaly pattern. The measurements, combined with those from other similar systems, provide an empirical basis for the generic properties listed in Table 7. Note that remanence polarities are mixed within and around Bajo de la Alumbrera and substantial cancellation of remanent contributions, averaged over substantial volumes, reduces the contribution of remanence to the magnetic signature. Normal and reversed polarities can be found at different locations within the same rock unit or alteration zone and are also often present within individual specimens as a remanence component of one polarity overprinting a more stable component of the opposite polarity. Of the well-defined “cleaned” remanence directions obtained from individual rock and ore specimens, 39 had normal polarity and 23 were reversed. As mentioned above, this behaviour is quite common in porphyry systems emplaced during

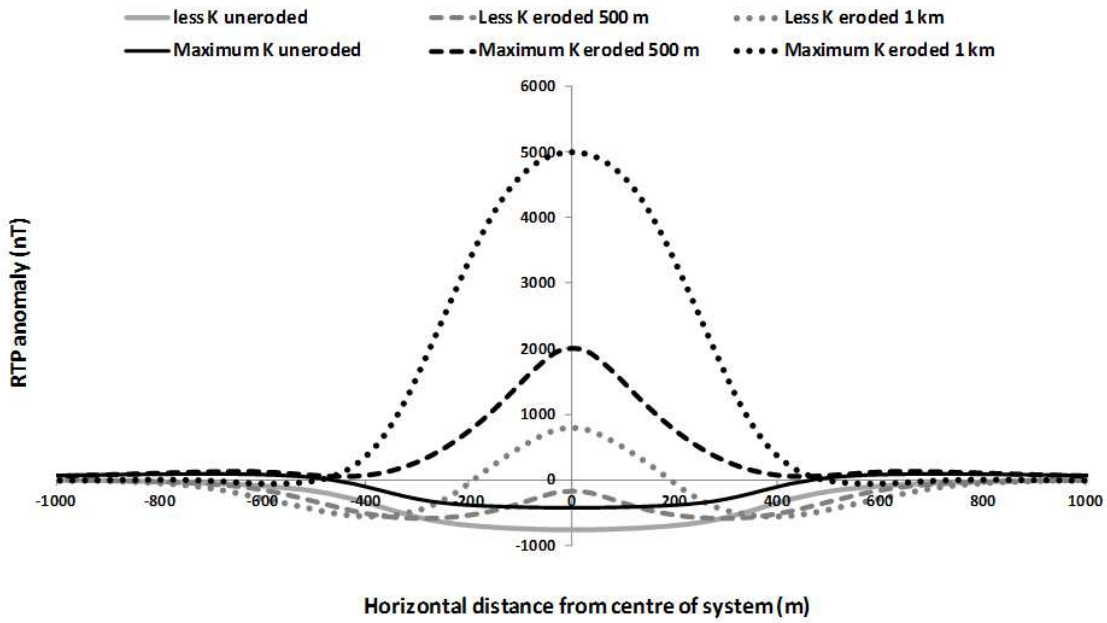

Figure 5. Theoretical RTP magnetic profiles over gold-rich porphyry copper models, emplaced into magnetic mafic-intermediate rocks, with either maximum development ("maximum K" in the legend), or a more typical development ("less K"), of a biotite-magnetite assemblage in the potassic alteration zone. "Maximum K" represents relatively mafic systems in island arc environments or systems associated with alkaline (e.g. high-K calc-alkaline to shoshonitic) magmatism in continental settings. "Less K" represents less strongly oxidised or relatively felsic systems, or low-medium K calc-alkaline associations, typically in areas with thick continental crust. Profiles were calculated as described in Figure 3 and are shown for uneroded deposits and after removal of 500 m and 1000 m by erosion.

periods when geomagnetic reversal were frequent, as their magmatic-hydrothermal evolution can record one or more reversal.

Figure 6 shows the RTP anomaly pattern developed over the Bajo de la Alumbrera Cu-Au system. This “type” magnetic signature occurs because the mineralising intrusion was emplaced into relatively homogeneous host rocks and the deposit has not been subsequently tilted or disrupted by faulting, but the system has been exposed by uplift and erosion. Similar signatures are seen at the Batu Hijau porphyry Cu-Au deposit (Ferneyhough and Qarana, 1996; Hoschke, 2008, 2010, 2011) and the Elang porphyry Cu-Au deposits (Hoschke, 2008, 2010, 2011, 2012) in Indonesia. The predictive model based on the Alumbrera deposit has been incorporated into an automated grid analysis tool that has been successfully applied to identification of porphyry systems in Pakistan, Indonesia and Papua New Guinea (Holden et al., 2010, 2011; Hope et al., 2010).

Figure 7 shows magnetic profiles over an uneroded gold-rich porphyry copper model with a typical development of a biotite-magnetite assemblage in the potassic alteration zone, for differing host rocks and erosion levels. For magnetic mafic-intermediate igneous host rocks (represented by andesite in Figure 7) the signature of the uneroded deposit is a magnetic low, reflecting the negative magnetisation contrast between the large volume of the magnetite-destructive phyllic and propylitic zones and the surrounding magnetic unaltered rocks. As deeper levels of the system are exposed the signature gains a central high within an annular low. For weakly magnetic felsic host rocks the effects of magnetite-destructive alteration are less important and the signature for an eroded system is a broad high, reflecting the deeply buried magnetic potassic core of the system. For an uneroded system hosted by felsic rocks the signature is very weak (amplitude 31 nT), as the most significant magnetisation contrast corresponds to the deeply buried potassic core, which has lower magnetisation than the corresponding zone in Figure 4.

Figure 8 illustrates the dramatic effect post-emplacement tilting can have on magnetic signatures. A deep uneroded Cu-Au porphyry system emplaced into magnetic mafic host rocks exhibits a symmetric magnetic low, but after tilting has an asymmetric signature with a magnetic high appearing adjacent to the alteration low, above the potassic core which has been laterally displaced and brought to shallower levels by the tectonic rotation and accompanying removal of overburden by erosion.

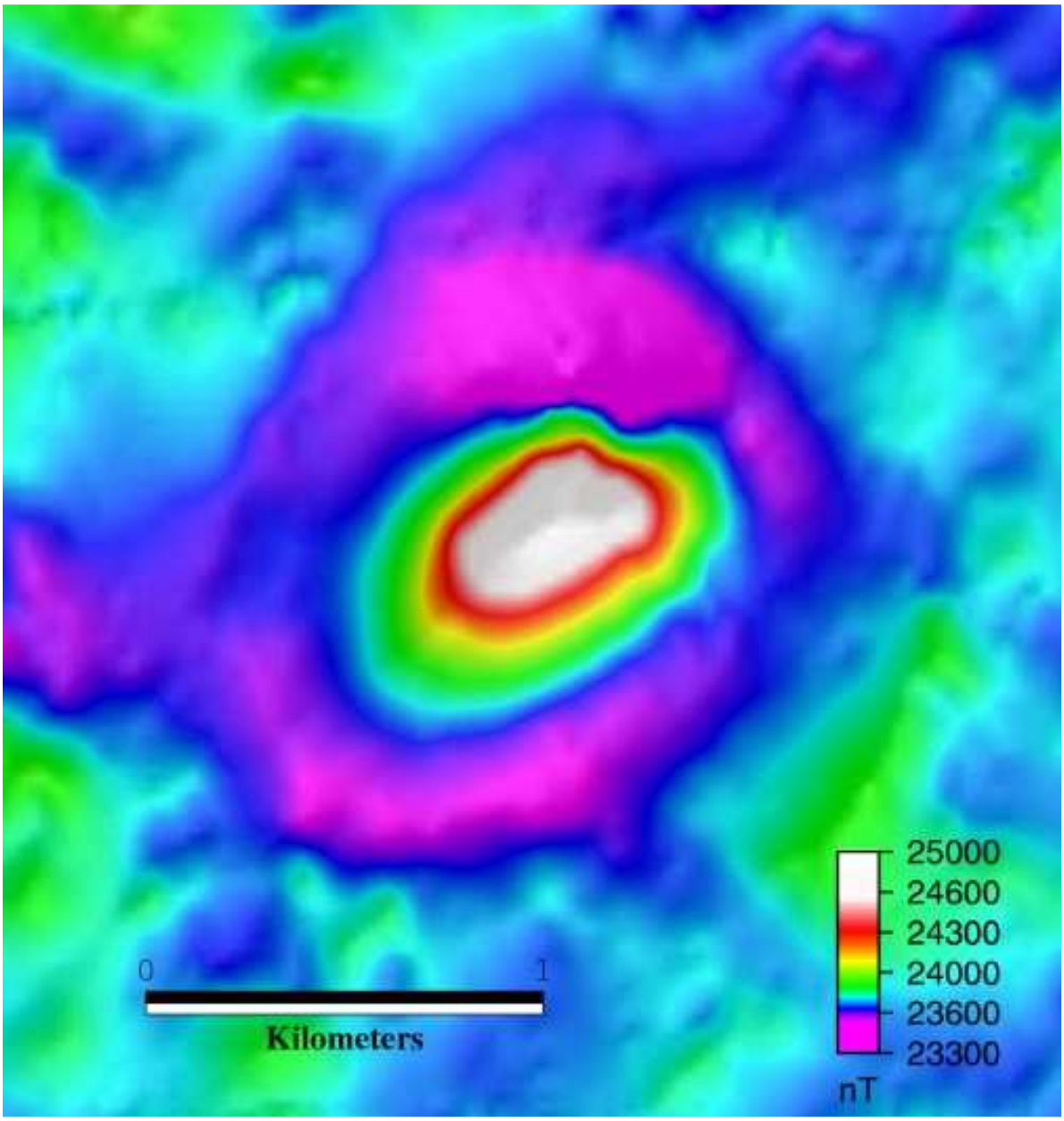

Figure 6. RTP magnetic anomaly pattern over the Bajo de la Alumbrera Cu-Au porphyry deposit, Catamarca Province, Argentina, hosted by magnetic andesitic volcanics of the Farallon Negro Formation. The central magnetic high is due to the potassic (biotite-magnetite) core zone and the annular magnetic low is due to magnetite destruction within the surrounding phyllic zone. In the outer propylitic zone the magnetic response gradually returns to the background level and to the busy texture associated with the andesitic host rocks.

Table 8. Magnetic properties of rocks and ores from the ~7 Ma Bajo de la Alumbrera Cu-Au deposit, Catamarca Province, Argentina (605 Mt at 0.54% Cu, 0.64 g/tonne Au)

Protolith	**Alteration**	**N**	**k (10^{-3} SI)**	**J (mA/m)**	**Q**
Dacitic porphyry stocks & dykes	POT+min	8	680 (3-3185)	690 (40-5260)	0.17 (0.02-0.95)
Dacitic porphyry stocks & dykes	(PHY)/POT+min	3	12 (4-26)	58 (19-106)	0.46 (0.1-1.2)
Dacitic porphyry stocks & dykes	PHY/POT+min	3	2.2 (0.09-6.0)	54 (3-204)	0.93 (0.07-1.8)
P2 Monzonite Porphyry	POT+min	2	460 ± 210	10,080 (2680-17600)	0.86 (0.61-1.5)
P2 Monzonite Porphyry	(PHY)/POT+min	2	126±29	870 (575-1560)	0.40 (0.34-0.57)
P3 Monzonite Porphyry	POT+min	2	135±43	960 (310-1850)	0.40 (0.19-0.59)
High grade mineralisation	POT+min	3	350±120	3570 (1430-7080)	0.58 (0.47-0.69)
Combined potassic core, no phyllic overprint	POT+min	4	410±110	4250 (870-1080)	0.60 (0.17-0.86)
Combined potassic core, ± phyllic overprint	POT+min; (PHY)/POT+min; PHY/POT+min	7	250±100	3330 (50-1080)	0.75 (0.17-0.93)
El Durazno feldspar porphyry*	Unaltered	2	44±4	220 (220-373)	0.29 (0.21-0.44)
Farallon Negro Andesite (host)	POT	5	31±8	200 (120-930)	0.43 (0.76-1.3)
Farallon Negro Andesite (host)	PHY	3	0.016±0.002	1.8 (0.9-3.3)	6.5 (2.7-13.5)
Farallon Negro Andesite (host)	PROP	3	7.0±1.8	67 (40-168)	0.54 (0.26-1.1)
Farallon Negro Andesite (host)	(PROP)	3	27±2	190 (150-270)	0.39 (0.29-0.67)
Farallon Negro Andesite (host)	Unaltered (fresh hornblende)	2	43±9	580 (560-680)	0.77 (0.62-1.1)

*Analogue of unaltered nearby Alumbrera porphyries. POT = potassic (Kfsp-bio-qtz-mt); POT+min = potassic alteration + mineralisation; (PHY)/POT = partial phyllic overprinting of potassic alteration; PHY/POT = strong phyllic overprinting of potassic alteration; PROP = strong propylitic alteration; (PROP) = weak propylitic alteration. k given as mean ± 1 SE. J = NRM intensity, calculated as vector mean using only oriented samples; Koenigsberger ratio Q = J/kH, where H = 17.5 A/m (F = 22 µT). Data from Clark et al. (2004) and Hoschke (2011).

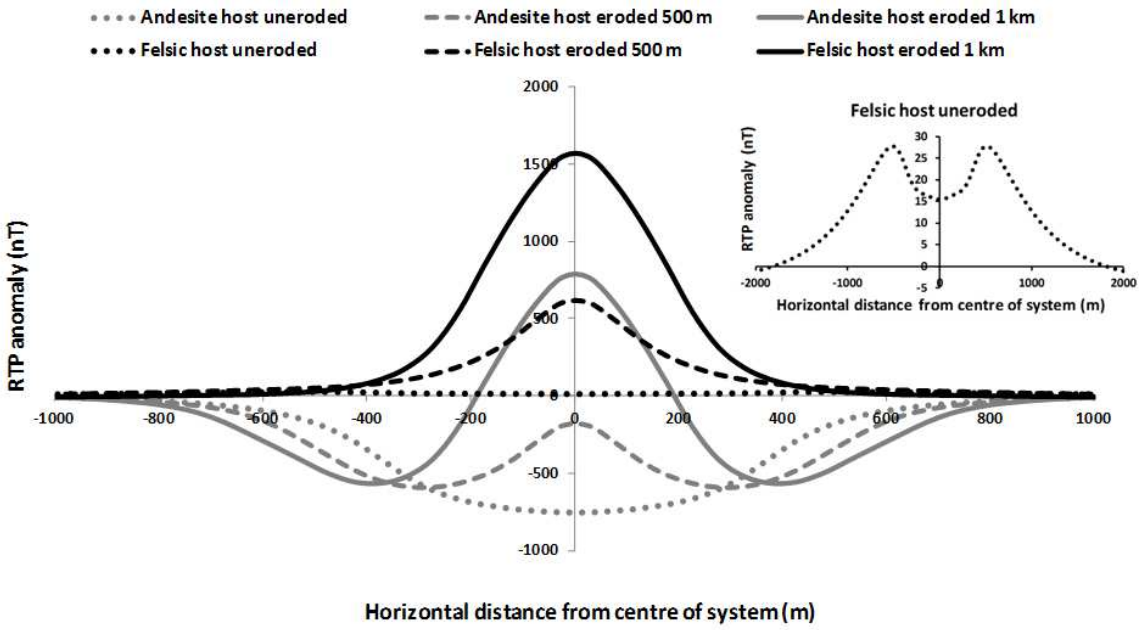

Figure 7. Theoretical RTP magnetic profiles over a gold-rich porphyry copper model with a typical development of a biotite-magnetite assemblage in the potassic alteration zone, for differing host rocks and erosion levels. Profiles were calculated as described in Figure 3. The inset shows the low amplitude (30 nT) signature of the uneroded system in felsic host rocks, which is not clearly visible at the scale of the main plot.

Such post-emplacement disruption of porphyry systems is common. Wilkins and Heidrick (1995) report that ~45% of the deposits of the southwestern North American porphyry copper province of Laramide age have been significantly faulted, extended and rotated during Oligocene and Miocene time. Tilting through more than 50° is common. Geissman et al. (1982) have quantified rotations in the Yerington district using palaeomagnetism. A palaeomagnetic study of the Porgera Intrusive Complex by Schmidt et al. (1997) showed that the upper levels of this complex have been disrupted by thin-skinned tectonics. The exposed intrusions have undergone substantial, but varying, degrees of tilting and rotation about vertical axes. Lum et al. (1991) point out the prevalence of local block rotations that distort outcrop patterns of high level intrusions and porphyry and epithermal alteration systems in the tectonically very active southwest Pacific. Rotation rates of 20°-30° in 100,000 years are unexceptional.

High sulfur quartz monzonite models

The classic porphyry copper model of Lowell and Guilbert (1970), based predominantly on Laramide porphyry deposits of southwest North America, neatly summarised the characteristics of an important class of porphyry copper deposits. In these systems the mineralising porphyry intrusions typically were quartz monzonites. Quartz-monzonite type porphyry copper deposits that have substantial magnetite within their potassic zones are similar to the gold-rich porphyry copper models discussed above. These deposits tend to associated with intrusions that have lower sulfur contents than quartz monzonite deposits that are characterised by extensive magnetite-destructive alteration, as noted by Williams and Forrester (1995) who pointed out that alteration patterns around porphyry intrusions differ greatly between high-S and low-S porphyries. Sulfur contents of porphyry copper intrusions range up to 8 wt%. High sulfur content encourages development of broad magnetite-destructive alteration envelopes. Sulfur contents in the range 7-8 wt% produce very large quartz-sericite aureoles, with extensive retrograde alteration relative to the size of the intrusion. Substantially lower sulfur contents result in the inner potassic and outer propylitic zones adjoining, with minimal development of intervening sericitic or argillic zones.

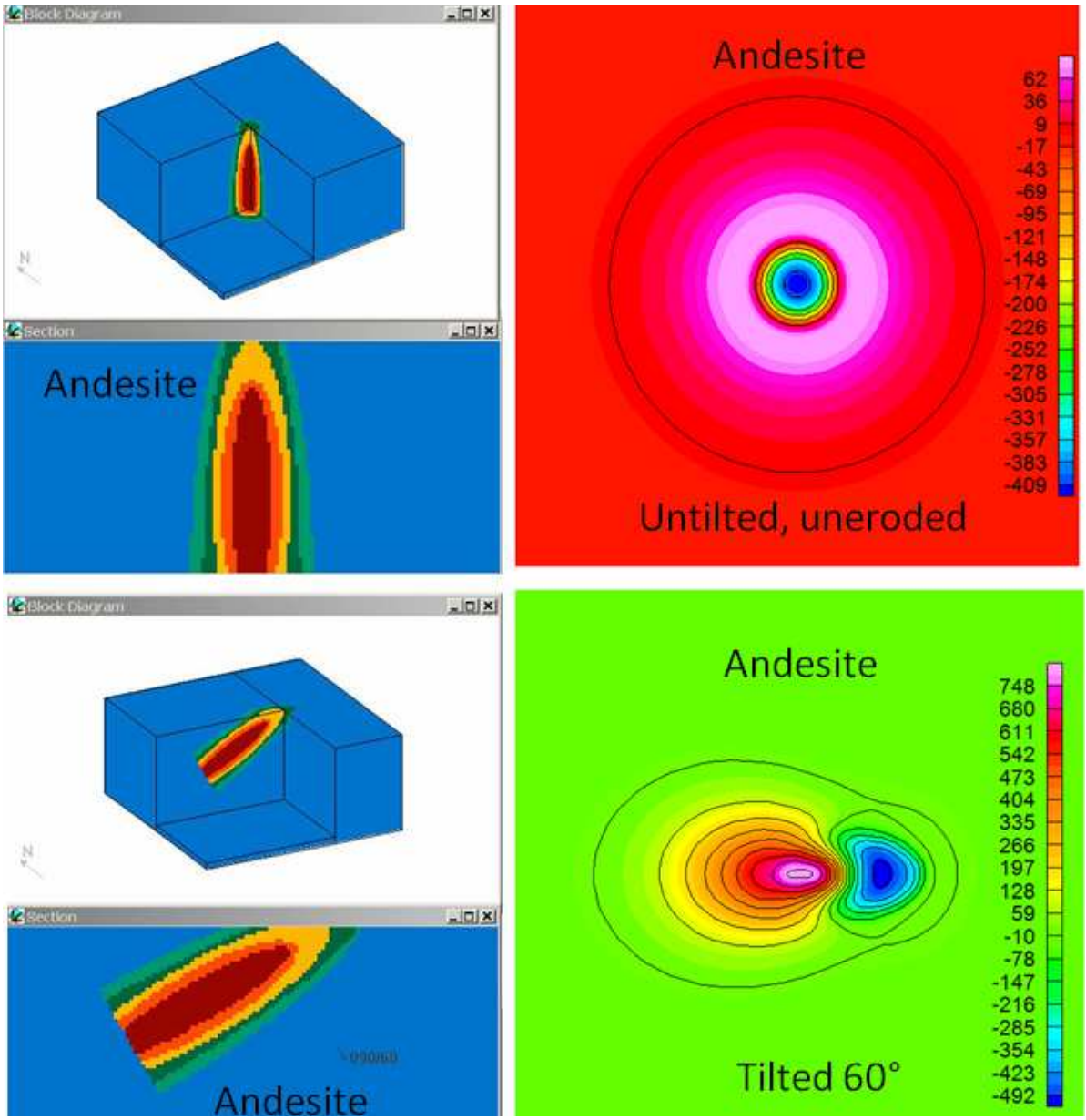

Figure 8. Models and theoretical RTP magnetic signatures of a gold-rich porphyry copper model, with maximum development of a biotite-magnetite assemblage in the potassic alteration zone. Top: uneroded deposit hosted by magnetic mafic rocks, with geometry and susceptibilities given in Figure 2; Bottom: same deposit after tilting through 60° so that originally vertical porphyry stock now plunges 30° to left of figure. Colour bar indicates RTP anomaly in nT. Contour interval for both RTP images is 100 nT. Dimensions of the block model are 6.4 km × 6.4 km × 3 km and the images are 6.4 km × 6.4 km.

Areas that have thick continental crust that was underlain by a shallow subduction zone (e.g. the Laramide porphyry province of SW North America) tend to produce magmas with substantial crustal contamination, including high sulfur magmas. Magnetite is relatively scarce in the potassic zones of such deposits, as it is mostly replaced by pyrite. For example, the Bingham Canyon porphyry Cu-Au-Mo deposit is notable among gold-rich porphyry coppers for having little magnetite within its potassic zone, which contains instead abundant pyrite. For this type of deposit, the phyllic zones are well-developed in the intrusion and within suitable host rocks, and are surrounded by broad propylitic zones with extensive pyritisation of magnetite in country rocks. Thus the general signature of such deposits, if they are hosted by moderately or strongly magnetic rocks, is an alteration low. The situation is different if the intrusion is hosted by carbonate rocks. In this case extensive skarn formation occurs, often with associated zoned mineralisation, as seen close to Bingham Canyon at Carr Fork, Utah (see Table 4). Some zones within the skarns tend to be strongly magnetic, producing a pronounced magnetisation contrast with both the weakly magnetic altered intrusion and unaltered sedimentary rocks.

Table 9 lists the dimensions and susceptibilities for a model of a porphyry copper system associated with a high sulfur magma, based on the quartz monzonite model of Lowell and Guilbert (1970). Figure 9 shows theoretical RTP magnetic profiles over this model, which has a potassic core that contains pyrite at the expense of magnetite, surrounded by magnetite-destructive phyllic and propylitic zones. Magnetic anomaly amplitudes are substantially smaller than for typical gold-rich porphyry copper models. The magnetic signature is very sensitive to the current level of exposure. Profiles are shown for an uneroded deposit and after removal of 1 km and 2 km by erosion. For the uneroded deposit the signature is a magnetic low, reflecting decrease in susceptibility of the host rocks throughout the large volume of magnetite-destructive alteration surrounding and above the magnetic core. As deeper levels of the system are exposed by erosion, a weak central magnetic high overlying the weakly altered lower levels of the moderately magnetic central intrusion develops. After removal of 2 km of overburden the central magnetic high becomes prominent.

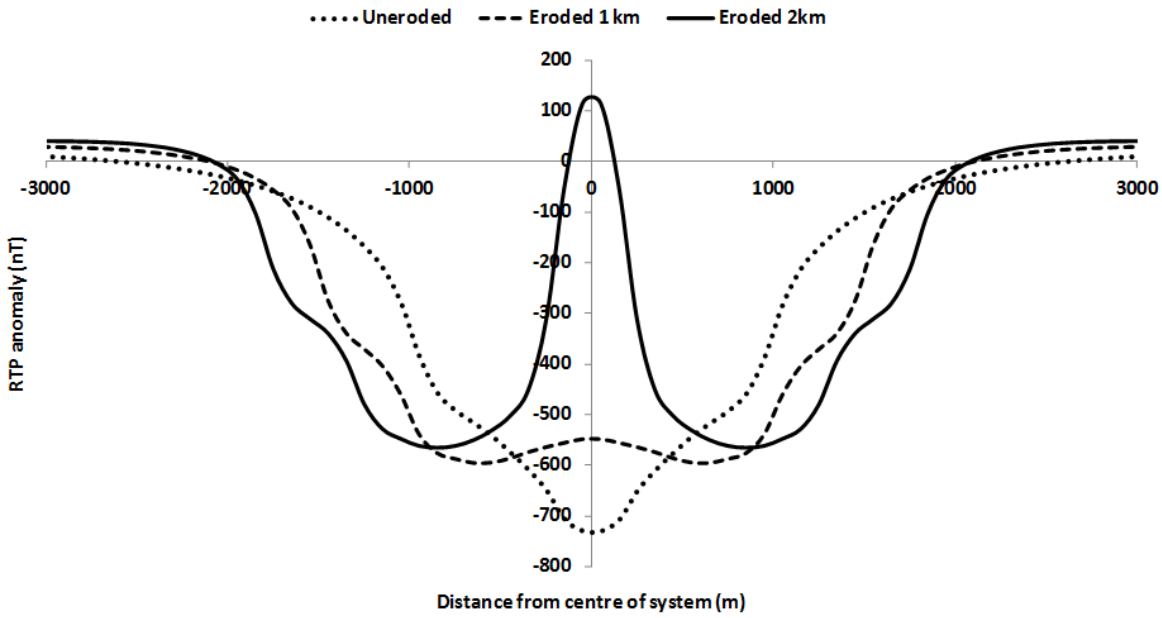

Figure 9. Theoretical RTP magnetic profiles over a Laramide-type high sulfur quartz-monzonite porphyry copper model, with a potassic core that contains pyrite at the expense of magnetite, surrounded by magnetite-destructive phyllic and propylitic zones. Profiles are shown for an uneroded deposit and after removal of 1 km and 2 km by erosion.

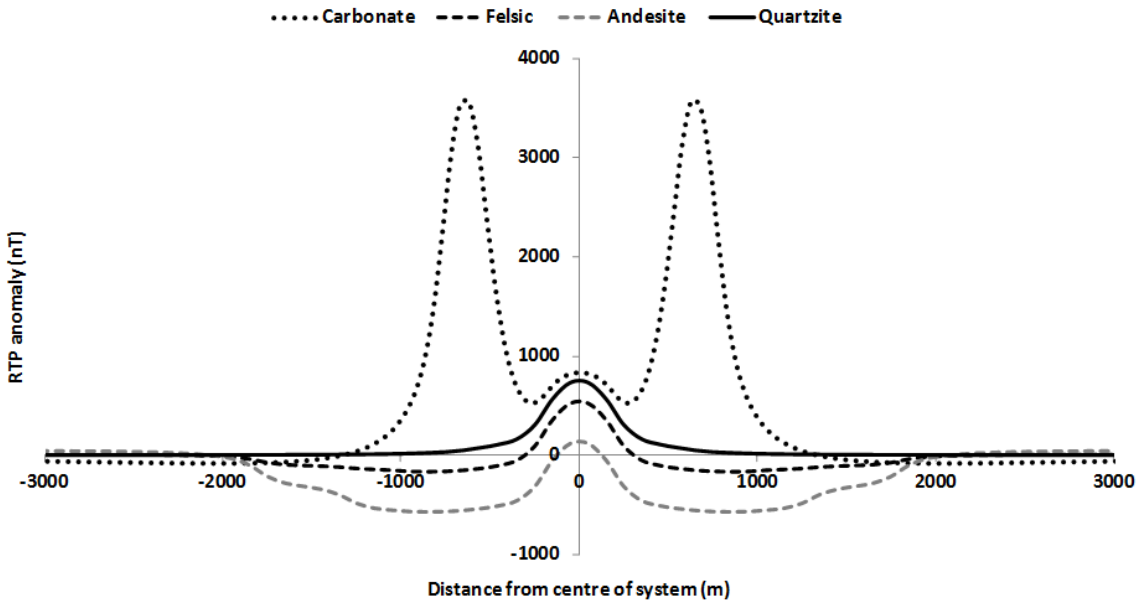

Figure 10. Theoretical RTP magnetic profiles over a Laramide-type high sulfur quartz-monzonite porphyry copper model with a potassic core that contains pyrite at the expense of magnetite, surrounded by magnetite-destructive phyllic and propylitic zones. Profiles are shown for the deposit emplaced into different host rocks, after removal of 2 km by erosion.

Table 9. Dimensions and susceptibilities of zones comprising the quartz monzonite model associated with a high sulfur magma intruded into mafic host rock

Zone	**Diameter* (m)**	**Width* (m)**	**Depth extent (m)**	**Susceptibility (SI)**
Inner/deep potassic	600	600	2600	0.05
Outer/upper potassic	900	150	3100	0.0035
Ore shell	1500	300	3600	0.0025
Phyllic	2200	350	3600	0.003
Strong propylitic	3000	400	4000	0.003
Weak propylitic	4000	500	4000	0.015
Andesite	Very large	Very large	4000	0.03

* Diameters and widths of zones are maxima (at a depth 4000 m below the surface). The tops of the phyllic zone and ore shell are 400 m below the surface, the top of the outer/upper potassic zone is at 900m depth and the inner/deep potassic zone is buried 2400 m.

Table 10. Dimensions and susceptibilities of zones in the Chilean giant porphyry copper model with mafic host rock

Zone	**Diameter (m)**	**Width (m)**	**Depth extent (m)**	**Susceptibility (SI)**
Mt-destructive Zone (phyllic, AA, ser-chl)	2600	2600	3500*	0.0001
Potassic		600×2000	3500*	0.018
Propylitic	6600	2000	4000	0.003
Supergene blanket	6000	6000	500*	0.0001
Andesite	Very large	Very large	4000	0.0055

* at thickest part of blanket

Figure 10 shows theoretical RTP magnetic profiles over a Laramide-type high sulfur quartz-monzonite porphyry copper model with a potassic core that contains pyrite at the expense of magnetite, surrounded by magnetite-destructive phyllic and propylitic zones. Profiles are shown for the deposit hosted by different lithologies, after removal of 2 km by erosion. In all cases a central high is associated with the weakly altered deeper levels of the central intrusion. For unreactive quartzite host rocks, this is the only signature. For andesitic or similar host rocks this high is surrounded by an annular alteration low. For less magnetic felsic host rocks this low is less prominent. For carbonate host rocks prominent magnetic highs occur over distal skarns and flank the subordinate central high.

The expected signatures of these systems are greatly modified by post-emplacement tectonic movements, analogous to the scenario shown in Figure 8. Laramide porphyry systems have often been disrupted by faulting and tectonic rotations. In fact, the Lowell and Guilbert (1970) porphyry copper model is largely based on a reconstruction of the San Manuel and Kalamazoo porphyry deposits in Arizona, which originally formed a single intrusion-centred ore body with concentric zoning, before being tilted and disrupted by faulting (Lowell, 1968; Force et al., 1995; Guilbert and Lowell, 1995). The present disposition of intrusive rocks and alteration zones in and around these ore bodies differs greatly from the idealised model, but when the displacement along the San Manuel fault is removed and the intact porphyry system restored to the vertical, it is apparent that the original system conforms closely to the model.

Chilean giant porphyry copper models with supergene blankets

Giant porphyry copper deposits of the Chilean Andes are characterised by extensive magnetite-destructive alteration within their mineralised zones, which are surrounded by broad pyrite-rich propylitic halos. As a consequence of Late Tertiary-Recent physiography and climatic conditions of the Atacama desert they are generally overlain by thick supergene blankets that contribute much of their economic value. Supergene blankets are most developed over deposits that have abundant hypogene pyrite, which are also those that have the highest intensity and extent of magnetite-destructive alteration, such as phyllic, advanced argillic and sericite-chlorite alteration. Secondary magnetite is locally associated with early potassic alteration of relatively mafic rocks, but is much less

developed than in gold-rich porphyry copper systems. The magnetic signatures are much weaker than those of gold-rich porphyry copper deposits and are distinctly different in character. The geometry of the basic Chilean porphyry copper model for an andesitic host is shown in Figure 11. The Escondida deposit (Padilla Garza et al., 2001) was used as a basis for this model. Chilean-type porphyry copper models can also be used to represent large, high sulfur quartz monzonite type deposits that have developed thick supergene blankets.

The calc-alkaline andesitic rocks of this region generally have lower susceptibility than the high-K calc-alkaline to shoshonitic andesites of the Farallon Negro Volcanics that host the Alumbrera deposit, reducing the magnetisation contrast between the unaltered country rocks and the predominantly magnetite-destructive alteration within the deposit. The dimensions and susceptibilities of the zones are given in Table 10.

Alternative models include deposits hosted by different country rocks. Felsic country rocks are assigned SI susceptibilities of 0.004 SI (unaltered), 0.002 (propylitic zone), 0.006 (potassic zone). Susceptibilities within the magnetite-destructive core and supergene blanket are as above (0.0001). Carbonate host rocks and marble are assumed to have zero susceptibility. A 200 m wide skarn zone is assigned a susceptibility of 0.022. The 2600 m diameter magnetite-destructive zone has k = 0.0005. The supergene zone is more restricted in area, occurring only over mineralised igneous rocks rather than mineralised carbonates. Quartzite host rocks have zero susceptibility, including within the weakly developed propylitic zone. The local potassic zone is assigned a susceptibility of 0.001 and the magnetite-destructive core has k = 0.0005.

Figure 12 shows predicted RTP profiles over Chilean porphyry copper models for different host rock lithologies. For moderately magnetic igneous host rocks the signature is a broad alteration low, within which local magnetic highs may occur over relict potassic alteration zones that have not been strongly overprinted by magnetite-destructive alteration. The amplitudes of the broad lows and local highs are somewhat stronger for more mafic host rocks. For quartzite or other unreactive host rocks the signature is a weak magnetic high associated with less altered, deeper portions of the porphyry intrusion. Relatively prominent magnetic highs are developed over magnetite-bearing skarns developed within carbonate wall rocks.

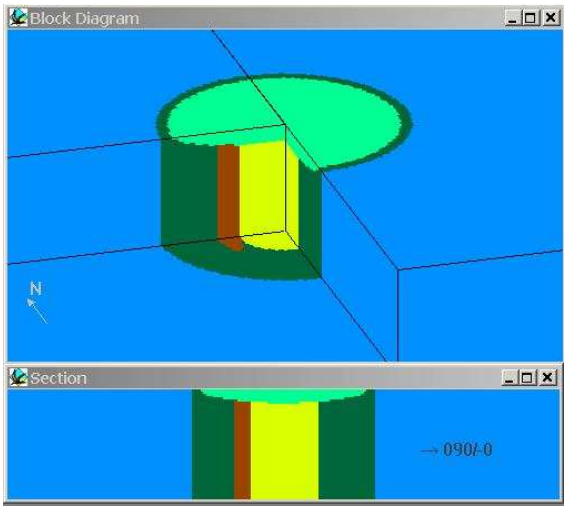

Figure 11. Model for a Chilean type (Atacama Desert) giant porphyry copper deposit with a well developed supergene enrichment blanket (pale green) overlying a broad core of magnetite-destructive phyllic, advanced argillic and sericite-chlorite alteration (yellow), and a relict body of early biotite-magnetite alteration that has escaped strong phyllic overprinting (brown). The propylitic zone is shown in olive green and mafic moderately oxidised host rock in blue. The depth extent of the model is 4000 m and there is no vertical exaggeration.

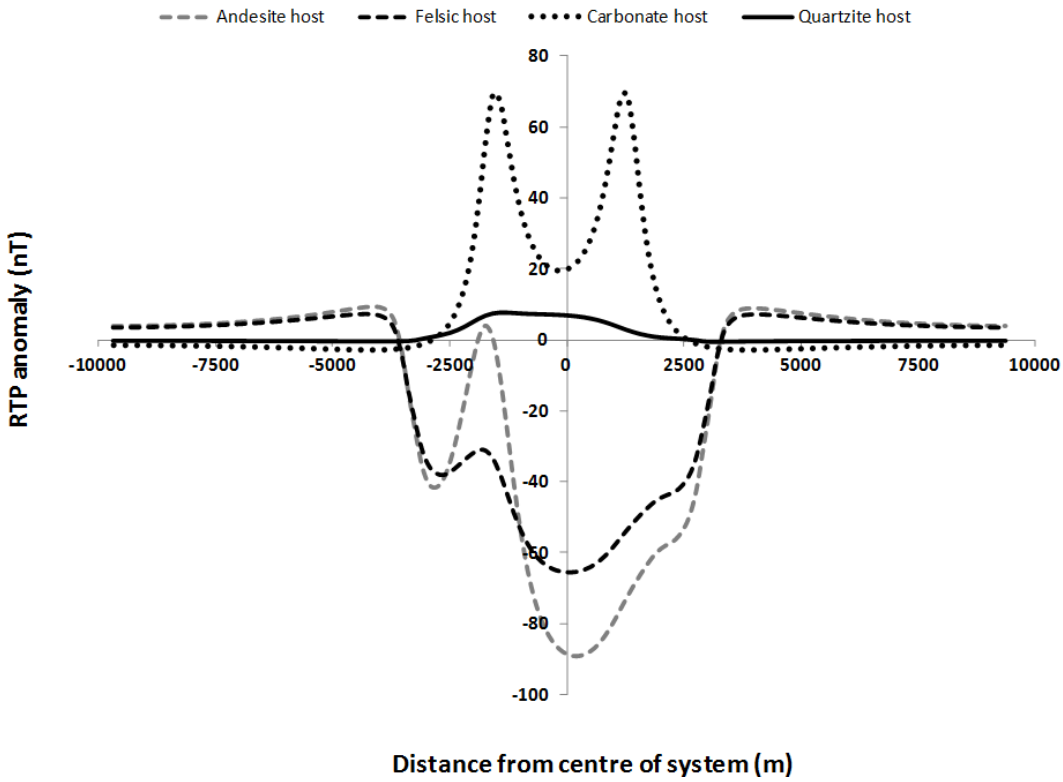

Figure 12. Theoretical RTP magnetic profiles over a Chilean type (Atacama Desert) giant porphyry copper deposit with a well developed supergene enrichment blanket, as shown in Figure 10, for different host rock types.

Figure 13 shows images and contour maps of predicted RTP signatures for deposits hosted by moderately magnetic mafic rocks, somewhat less magnetic felsic rocks, and for systems emplaced along a contact between mafic and felsic rocks or mafic rocks and carbonates. Mineralising porphyry intrusions often exploit pre-existing zones of weakness such as faulted contacts, so it is quite common for deposits to be found along contacts between contrasting lithologies. This produces asymmetric zoning patterns, with consequent modification of predicted magnetic signatures.

1. IOCG models

In a typical vertically zoned IOCG system, magnetite-destructive, hematite-rich HSCC alteration dominates upper levels, whereas magnetite-rich alteration dominates at depth. Thus the current erosion level determines whether the exposed or near-surface portions of the system are hematite-rich or magnetite-rich. Magnetite is also abundant peripheral to the upper hematite-rich zones.

The general zoning pattern inferred for IOCG deposits is shown in Figure 14 and the magnetic properties of the zones are listed in Table 11. This pattern may be altered by tectonic tilting of the system or by faulting. Therefore the magnetic and gravity signatures of IOCG deposits should generally reflect *superposed* or *juxtaposed* gravity and magnetic anomalies. Positive gravity anomalies arise from both magnetite-rich and hematite-rich zones, whereas the deeper, peripheral, or adjacent magnetic sources correspond to the magnetite-rich zones.

Figure 15 shows images and contour maps of predicted RTP signatures of IOCG systems. Uneroded systems produce substantial magnetic anomalies whether developed within mafic or felsic host rocks, due to high concentrations of iron oxides, associated with strong Fe metasomatism, over large volumes. Magnetic signatures are predicted to be stronger for more mafic systems and amplitudes also increase substantially if deeper levels of the system are exposed by erosion. Up faulting of the magnetite-rich deeper portion of the system (Figure 14, bottom left) results in strong signatures over this segment of the system, juxtaposed with more subdued anomalies over the hematite-rich segment. This scenario is analogous to the Prominent Hill, South Australia IOCG deposit, where the Cu-Au mineralisation occurs within a weakly magnetic massive hematite zone that is outlined by a gravity high, separated by a fault from the strongly magnetic and dense magnetite-rich

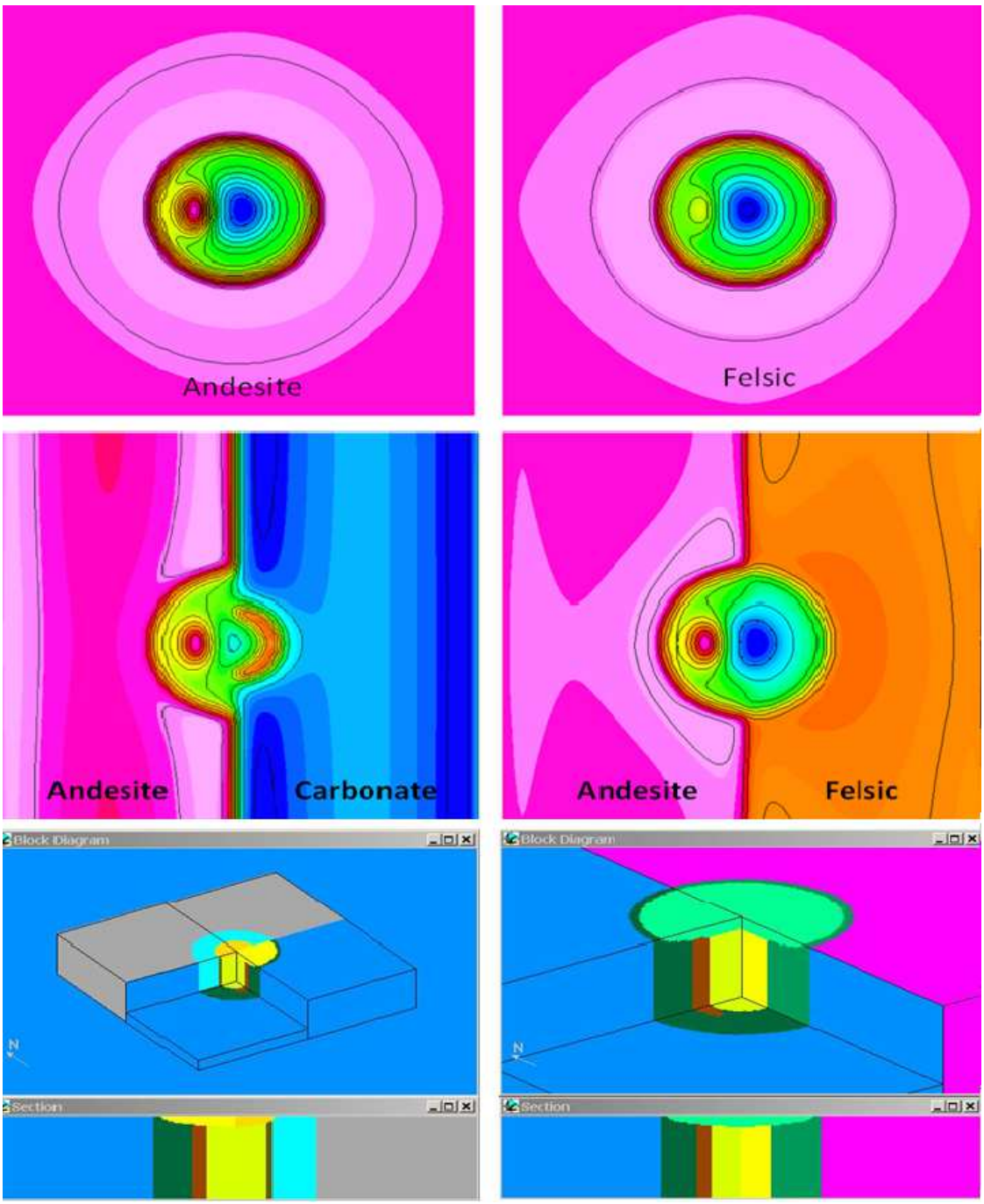

Figure 13. Theoretical RTP signatures of a Chilean type (Atacama Desert) giant porphyry copper deposit with a well developed supergene enrichment blanket. Top left: mafic host rocks (contour interval 5 nT); top right: felsic host rocks (contour interval 5 nT). The model geometry for these two cases is given in Figure 11. Centre left: emplaced at a contact between mafic and carbonate rocks (contour interval 10 nT); bottom left: corresponding model geometry, with andesite in blue,carbonate in grey; centre right: emplaced at a contact between mafic and felsic rocks (contour interval 10 nT); bottom right: corresponding model geometry, with andesite in blue, felsic host in pink. Colours of alteration zones are as in Figure 11. Dimensions of the block models are 19.2 km $\times$ 19.2 km $\times$ 4 km and the magnetic images are 19.2 km $\times$ 19.2 km.

zone that represents an originally deeper portion of the system, prior to faulting (Belperio et al., 2007). Juxtaposed hematite-rich and magnetite-rich segments of an IOCG system can also result from tectonic tilting (figure 14, bottom right) with a predicted signature shown in Figure 15 (bottom right).

Discussion and conclusions

The predictive models developed for the AMIRA P700 Atlas of Geophysical Signatures (Clark et al., 2004) were designed to bridge the gap between purely geological models (both idealised models and detailed deposit descriptions) and empirical magnetic signatures. This process has suggested the following conclusions for deposits that have not been significantly modified by post-emplacement tectonism or metamorphism:

1. The majority of gold-rich porphyry copper deposits (classic morphology, quartz-monzonite zoning) hosted by magnetic mafic-intermediate volcanics are predicted to have large (> 1000 nT) positive bullseye RTP anomalies over the potassic core, with incipient to prominent development of the archery target signature, depending on the extent of the phyllic zone, *providing erosion has exposed or nearly exposed the potassic zone*. This signature should be easily detectable beneath 100 m of sedimentary cover, and even beneath a similar thickness of magnetic volcanics.
2. For a completely buried, uneroded or slightly eroded, gold-rich porphyry copper system hosted by mafic rocks the signature is basically an alteration low due to the large volume of magnetite-destructive alteration surrounding the deeply buried magnetic core. At intermediate levels of exposure a more complex pattern of a central high surrounded by an alteration low occurs, with the relative amplitude of the high and low dependent on the erosion level.
3. Similar deposits emplaced into weakly magnetic felsic rocks or unreactive rocks, such as quartzites or shales, are characterised by a strong bullseye high, without a surrounding low. If emplaced into limestone the bullseye high associated with the potassically altered intrusion is likely to be supplemented by skarn anomalies (possibly remanently magnetised) associated with proximal magnetite-garnet skarn in favourable horizons, with discrete anomalies associated with distal skarn bodies, developed near the marble interface in structurally controlled zones. The skarn signature should be more strongly developed if the host rocks are dolomitic.

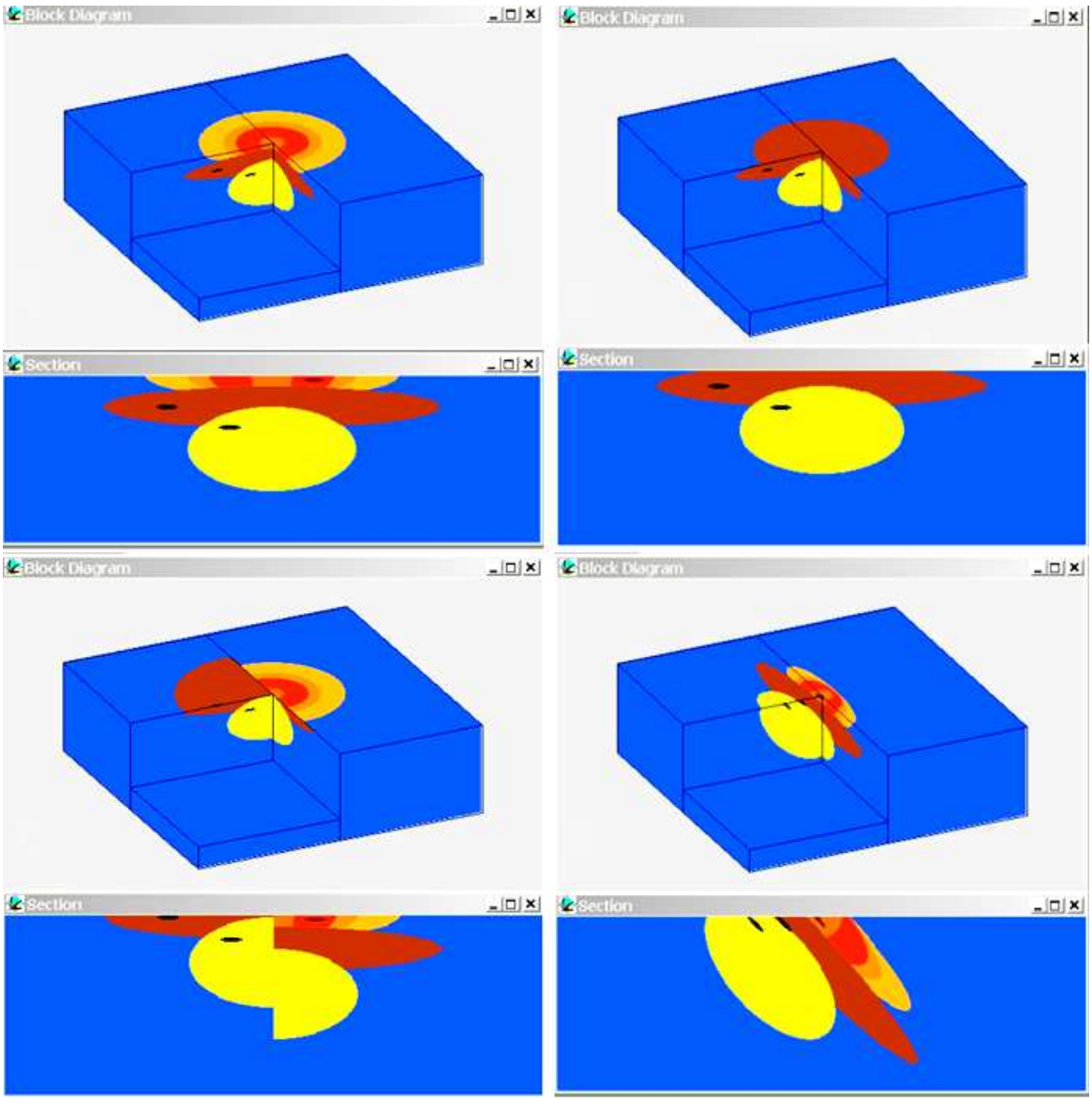

Figure 14. IOCG models hosted by an oxidised mafic lithology (blue). Dimensions of the block models are 12.8 km × 12.8 km × 4 km. The other zones are: outer hematite halo (yellow), inner hematite halo (orange), hematite breccia (red), quartz-hematite core (light brown), potassic alteration (mid brown), massive hematite (dark brown), deep sodic alteration (lemon yellow), discrete massive magnetite bodies (black). Top left: uneroded system; top right:after 400 m removed by erosion; bottom left: after vertical dip-slip fault has juxtaposed magnetite- and hematite-rich portions of system; bottom right: after tilting of system through 45°.

4. Alkalic porphyry Cu-Au deposits typically exhibit diorite model zonation, with poorly developed phyllic zones, and produce strong bullseye highs over the potassic core.
5. In areas of greater crustal influence on magmas (e.g. the Laramide province), magmas with relatively high sulfur content generate large volumes of magnetite-destructive alteration. Porphyry Cu and Cu-Au deposits of this type are associated with alteration lows, if emplaced into magnetic host rocks, or very weak signatures if emplaced into non-magnetic host rocks.
6. Giant porphyry copper deposits of the Atacama desert are characterised by large volumes of magnetite-destructive alteration, with locally developed magnetite-bearing potassic alteration, and thick overlying supergene blankets. The signature of such deposits, when hosted by moderately magnetic rocks, is an areally extensive alteration low, with a typical amplitude of –100 nT. Such deposits will be visible to magnetics if they are covered by non-magnetic overburden, but cover by magnetic volcanics renders them difficult to see. When hosted by non-magnetic rocks the magnetic signature is inconspicuous, apart from local highs associated with remnant zones of potassic alteration within the broad zones of phyllic overprinting. These deposits are ringed by chargeable zones due to pyrite-bearing propylitic halos.
7. Phyllic alteration produced by magmatic, rather than meteoric, fluids tends to be "inside-out" with respect to the potassic zone, producing a doughnut magnetic signature (central magnetic alteration lows flanked by annular highs). Another source of this reverse zoning pattern may be structurally controlled access of meteoric fluids to deeper portions of a deposit. This type of signature is to be expected in two main settings: Volcanic morphological models, with small intrusive spines within comagmatic volcanics, tapped off a large mother magma chamber, and plutonic/batholithic porphyry deposits. Examples of the latter type include the cluster of Cu-Au porphyry deposits within the Goonumbla Volcanic Complex, central New South Wales, which exhibit subtle doughnut signatures. This inside-out zoning reflects phyllic overprinting by late magmatic-derived fluids, centred on narrow intrusive spines, tapped off an underlying magma chamber, which locally overprints a halo of early biotite-magnetite alteration developed around the intrusions (Clark and Schmidt, 2001).

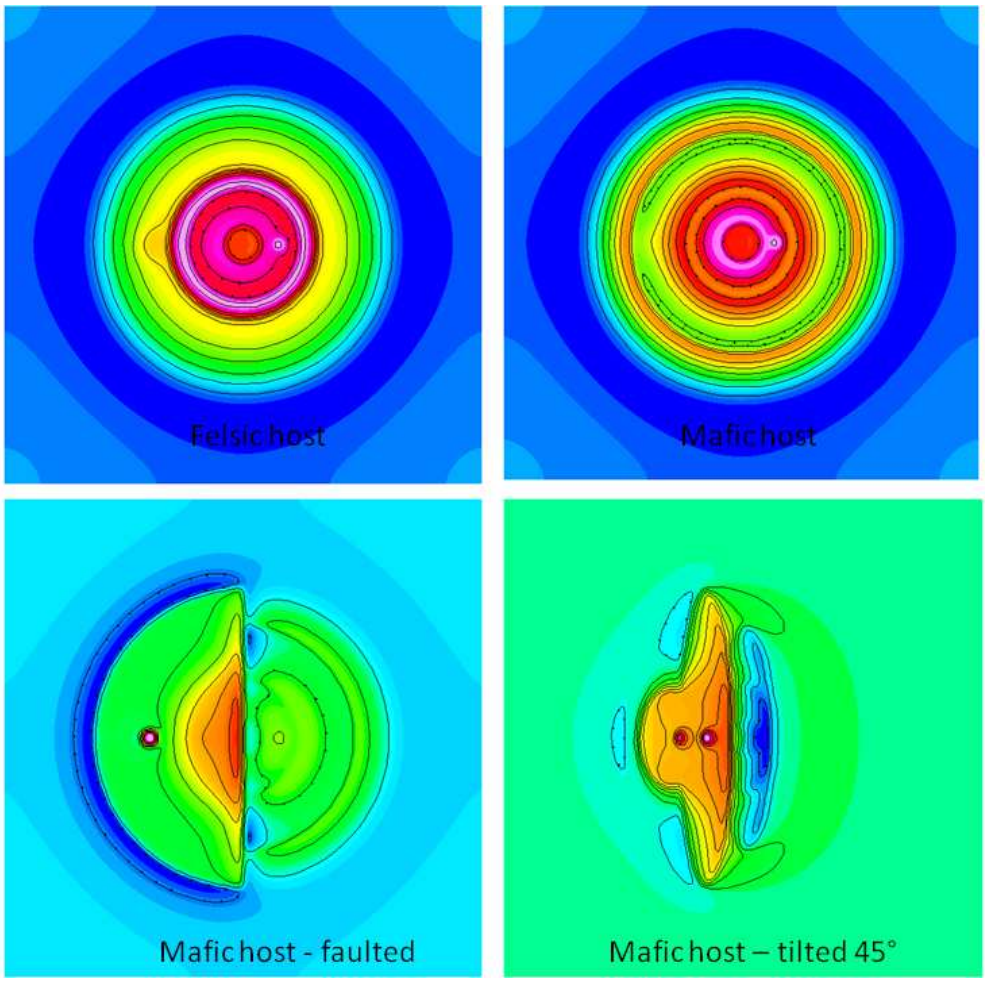

Figure 15. Predicted magnetic signatures of IOCG systems depicted in Figure 14. Top left: uneroded system hosted by moderately magnetic oxidised felsic rocks (contour interval 200 nT); top right: uneroded system hosted by oxidised magnetic mafic rocks (contour interval 200 nT); bottom left: faulted system hosted within mafic rocks (contour interval 600 nT); system hosted by mafic rocks, tilted 45° (contour interval 500 nT). Dimensions of the magnetic images are 12.8 km $\times$ 12.8 km.

8. The magnetic signatures of IOCG deposits, and their relationships to the gravity anomalies, depend on the geological history and are quite variable. Overall the magnetic sources of anomalies associated with IOCG deposits tend be deeper and more laterally extensive than the gravity sources.
9. Magnetite, formed under relatively reducing conditions, has very high susceptibility compared to hematite. Hematite has low susceptibility and fairly weak remanence, unless it has formed at, or been taken to, very high temperatures. High grade regional or contact metamorphism of hematite-rich zones can impart an intense thermoremanence to the hematite, which can cause large magnetic anomalies. This appears to explain the strong magnetic anomalies exhibited by massive hematite bodies of the Mount Woods Inlier that have been contact metamorphosed (Schmidt et al., 2007), whereas similar unmetamorphosed massive hematite at the nearby Prominent Hill IOCG deposit produces no discernible magnetic anomaly (Belperio et al., 2007).
10. Monoclinic pyrrhotite, formed under reducing conditions with moderate sulfur fugacity, has moderate susceptibility, but tends to carry intense remanence. The oxidation state of the host sequence appears to influence the oxidation state of IOCG deposits, as well as the redox state of the source (e.g. magmatic fluids) and the palaeodepth (more oxidised at shallow depths).
11. The predictive models illustrate a crucial point: namely that signatures of porphyhry copper and IOCG deposits are very sensitive to local geological setting. In particular, within a given metallogenic province local anomaly patterns that may indicate a mineralised system must be interpreted appropriately, by taking into account geological factors such as country rock composition, geomorphological history that controls present level of exposure of the systems of interest, local tectonic rotations and displacements along faults, and asymmetric zoning patterns for systems occurring along contacts between contrasting lithologies. For example, tilting of a vertically zoned IOCG system, or upfaulting of the deeper magnetite-rich portion, may juxtapose the magnetite and hematite zones, producing juxtaposed, rather than “coincident” gravity and magnetic anomalies. Identification of prospective systems therefore requires a sophisticated use of all available geological and geophysical data, rather than simply searching for “look-alike” signatures of a known deposit. When these factors are considered appropriately, however, signatures are much more predictable and exploration is more likely to be successful.

Clark et al. (2004) developed some general guidelines for exploration, applicable at regional to prospect scales, based on the predictive exploration models and magnetic petrological principles. That work provides criteria for recognition of favourable tectonic settings; structures that represent pathways for magmas and mineralising fluids, signatures of magmatic suites that have undergone substantial fractional crystallisation (which is a prerequisite for high-temperature for concentration of ore metals to economic grades), and signatures of melt-rich magmas that are capable of undergoing substantial fractional crystallisation and generating large hydrothermal systems. Details of these criteria are beyond the scope of this paper, but can be found in Clark et al. (2004).

Acknowledgements

This review incorporates findings of AMIRA International project P700, "Predictive magnetic exploration models for porphyry, epithermal and iron oxide Cu-Au deposits" (Clark et al., 2004), which was sponsored by Anglo American Prospecting Services Pty Ltd, AngloGold Ashanti Limited, BHP Billiton Exploration Australia Pty Ltd, Companhia Vale do Rio Doce, Phelps Dodge Australasia Inc, Rio Tinto Exploration Pty Limited and WMC Exploration. Terry Hoschke provided the RTP magnetic image for the Bajo de la Alumbrera deposit. I thank James Austin for helpful comments that improved the manuscript. This paper represents a contribution towards a Ph.D. in the Department of Earth and Planetary Sciences at Macquarie University, under the supervision of Drs Mark Lackie and Richard Flood.

Table 11. Typical magnetic properties and densities of IOCG-style alteration systems (low metamorphic grade)

ZONE	Vol. % magnetite	Vol. % hematite	Calculated susceptibility* (10^{-3} SI)	Calculated Density (kg/m^3)
Felsic Host	0.15	0	5.2	2650
Outer hematite halo - upper (HSCC) zone	0.2	2	7.7	2710
Inner hematite halo - upper (HSCC) zone	2	4	72	2800
Hematite breccia - upper (HSCC) zone	1	36	49	3590
Hematite-quartz breccia - upper (HSCC) zone	0	37	15	3590
Massive hematite lens	0	60	24	4180
Potassic/Potassic-calcic/sodic/sodic-calcic deep zones	3.5	0	124	2740
Massive magnetite lens	60	0	4110	4180
Mt-rich Mafic Host	5.2	0	187	3000
Outer hematite halo - upper (HSCC) zone	2	5	72	3040
Inner hematite halo - upper (HSCC) zone	2	9	74	3140
Hematite breccia - upper (HSCC) zone	1	41	51	3810 (ρ_G = 2800)
Hematite-quartz breccia - upper (HSCC) zone	0	42	17	3810 (ρ_G = 2800)
Massive hematite lens	0	60	24	4240 (ρ_G = 2800)
Potassic/Potassic-calcic/sodic/sodic-calcic deep zones	8.5	0	315	3080
Massive magnetite lens	60	0	4110	4270

* Susceptibility calculated from magnetite and hematite contents, using equation (3).
ρ_G = assumed gangue density (2650 kg/m^3 for felsic host; 2880 kg/m^3 for mafic host, except where sericitic alteration is dominant). Density is calculated as
$\rho = \rho_{GANGUE} + (\rho_{OXIDES} - \rho_{GANGUE})(f_{MT} + f_{HM})$, where ρ_{OXIDES} = 5200 kg/m^3.

References

Airo, M. L., 2002. Aeromagnetic and aeroradiometric response to hydrothermal alteration. Surveys in Geophysics, 23(4), 273-302.

Allis, R.G., 1990. Geophysical anomalies over epithermal systems. J. Geochem. Explor., 36, 339-374.

Astudillo, N., Roperch, P., Townley, B., Arriagada, C., Chauvin, A. (2010). Magnetic polarity zonation within the El Teniente copper–molybdenum porphyry deposit, central Chile. Mineralium Deposita, 45(1), 23-41.

Austin, J., Foss C., 2012. Rich, attractive and extremely dense: A geophysical review of Australian IOCGs. *Australian Society of Exploration Geophysicists Conference and Exhibition, Extended Abstracts*, http://dx.doi.org/10.1071/ASEG2012ab278.

Austin, J., Geuna, S., Hillan, D., Clark, D., 2012. Modelling Iron-Oxide Copper Gold deposits from Candelaria district, Chile and the Cloncurry district, Australia: The Influence of Remanent Magnetism and Self-demagnetisation (Poster). Society of Economic Geologists Conference, Lima.

Austin, J. R., Schmidt, P. W., Foss, C. A., 2013. Magnetic modeling of iron oxide copper-gold mineralization constrained by 3D multiscale integration of petrophysical and geochemical data: Cloncurry District, Australia. Interpretation, 1(1), T63-T84.

Barton, M. D., Johnson, D. A., 2000. Alternative brine sources for Fe-oxide (-Cu-Au) systems: Implications for hydrothermal alteration and metals, in: Porter, T.M. (Ed.), Hydrothermal Iron Oxide Copper-gold & Related Deposits: A Global Perspective, Australian Mineral Foundation, Adelaide, 43-60.

Beane, R.E., 1994. A graphic view of hydrothermal mineral stability relations, in: Lentz, D.R. (Ed.), Alteration and Alteration Processes Associated with Ore-forming Systems. Geological Association of Canada Short Course Notes, 11, pp.1-30.

Belperio, A., Flint, R., Freeman, H., 2007. Prominent Hill: A Hematite-Dominated, Iron Oxide Copper-Gold System. Economic Geology, 102, 1499-1510.

Blakely, R.J., 1996. Potential Theory in Gravity and Magnetic Applications, Cambridge University Press.

Blevin, P.L., Chappell, B.W., 1992. The role of magma sources, oxidation states and fractionation in determining the granite metallogeny of eastern Australia: Trans. Roy. Soc. Edinburgh, Earth Sciences, 83, 305-316.

Burnham, C.W., 1997. Magmas and hydrothermal fluids. *In*: Barnes, H.L. (Ed), Geochemistry of Hydrothermal Ore Deposits, Third Edition. Wiley, New York, 63-123.

Champion, D.C., Heinemann, M.A., 1994. Igneous rocks of northern Queensland: 1:500,000 map and GIS explanatory notes. AGSO Record 1994/11.

Clark, A.H., Arancibia, O.N., 1995. The occurrence, paragenesis and implications of magnetite-rich alteration-mineralization in calc-alkaline porphyry copper deposits., in: Clark, A.H. (Ed.), Giant Ore Deposits - II, Controls on the Scale of Orogenic Magmatic-Hydrothermal Mineralization (Proceedings of the Second Giant Ore Deposits Workshop, Kingston, Ontario, Canada, April 25-27, 1995), pp. 583-640.

Clark, D.A., Tonkin, C., 1987. Magnetic properties of ironstones and host rocks from the Tennant Creek area. CSIRO Division of Mineral Physics and Mineralogy Restricted Investigation Report 1691R, 124pp
https://wiki.csiro.au/confluence/download/attachments/457769088/Clark%26Tonkin+1987+CSIRO+1691R.pdf

Clark, D.A., 1988a. Magnetic properties and magnetic signatures of the Trough Tank and Starra copper-gold deposits, Eastern Mt Isa Block. CSIRO Division of Exploration Geoscience, Restricted Investigation Report 1745R, 50p.
https://wiki.csiro.au/confluence/download/attachments/457769088/Clark+1988+CSIRO+1745R.pdf

Clark, D.A., 1988b. Catalogue of magnetic properties of Australasian rocks III. CSIRO Division of Exploration Geoscience, Restricted Investigation Report 1746R.

Clark, D.A., French, D.H., Lackie, M.A., Schmidt, P.W., 1992. Magnetic petrology: application of integrated rock magnetic and petrological techniques to geological interpretation of magnetic surveys. Exploration Geophysics, 23, 65-68.

Clark, D.A., 1994. Magnetic properties and magnetite contents of ores from the Ernest Henry deposit, eastern Mount Isa Inlier. CSIRO Division of Exploration and Mining Report 23C, 79p.

Clark, D.A., 1997. Magnetic petrophysics and magnetic petrology: aids to geological interpretation of magnetic surveys. AGSO Journal of Australian Geology and Geophysics, 17, 83-103.

Clark, D.A., 1999. Magnetic petrology of igneous intrusions: implications for exploration and magnetic interpretation. Exploration Geophysics, 30, 5-26.

Clark, D.A., 2000. Self-demagnetisation in practice: the Osborne Cu-Au deposit. Preview, 85, 31-36.

Clark, D. A., Schmidt, P. W., 2001. Petrophysical properties of the Goonumbla Volcanic Complex, NSW: Implications for magnetic and gravity signatures of porphyry Cu-Au mineralisation. Exploration Geophysics, 32, 171-175.

Clark, D.A., Lackie, M.A., 2003. Palaeomagnetism of the Early Permian Mount Leyshon Intrusive Complex and Tuckers Igneous Complex, North Queensland, Australia. Geophys. J. Int., 153, 523-547.

Clark, D.A., Geuna, S.E., Schmidt, P.W., 2004. Predictive magnetic exploration models for porphyry, epithermal and iron oxide Cu-Au deposits. P700 Final Report, 398 p. + CD Atlas of Geophysical Signatures + Relational Database of Porphyry, Epithermal and Iron Oxide Cu-Au Deposits, AMIRA International (Report can be downloaded from:

https://wiki.csiro.au/confluence/download/attachments/457769088/Clark+etal+2004+P700+CSIRO+1073Rs.pdf)

Corbett, G. J., Leach, T. M., 1998. Southwest Pacific Rim Gold-copper Systems: Structure, Alteration, and Mineralization, Special Publication 6, Society of Economic Geologists.

Corriveau, L., 2007. Fe oxide copper-gold deposits: a Canadian perspective, in: Goodfellow, W.D. (Ed.), Mineral Deposits of Canada: a Synthesis of Major Deposit-types, District Metallogeny, the Evolution of Geological Provinces, and Exploration Methods, Geological Association of Canada, Mineral Deposits Division, Special Publication 5, pp. 307–328.

Criss, R.E., Champion, D.E., 1984. Magnetic properties of rocks from the southern half of the Idaho Batholith: influences of hydrothermal alteration and implications for aeromagnetic interpretation: J. Geophys. Res., 89, 7061-7076.

Criss, R.E., Champion, D.E. and McIntyre, D.H., 1985. Oxygen isotope, aeromagnetic, and gravity anomalies associated with hydrothermally altered zones in the Yankee Fork mining district, Custer County, Idaho. Econ. Geol., 80, 1277-1296.

Direen, N. G., Lyons, P., 2007. Regional crustal setting of iron oxide Cu-Au mineral systems of the Olympic Dam region, South Australia: Insights from potential-field modeling. Economic Geology, 102, 1397-1414.

Drummond, B., Lyons, P., Goleby, B., Jones, L., 2006. Constraining models of the tectonic setting of the giant Olympic Dam iron oxide–copper–gold deposit, South Australia, using deep seismic reflection data. Tectonophysics, 420, 91-103.

Dunlop, D.J., Özdemir, Ö., 1997. Rock Magnetism: Fundamentals and Frontiers. Cambridge University Press.

Dunlop, D.J., Kletetschka, G., 2001. Multidomain hematite: a source of planetary magnetic anomalies? Geophysical Research Letters, 28 (17), 3345-3348.

Einaudi, M.T., 1982. Description of skarns associated with porphyry copper plutons: southwestern North America, in: Titley, S.R., (Ed.), Advances in Geology of the Porphyry Copper Deposits, Southwestern North America. University of Arizona Press, Tucson, 139-183.

Einaudi, M.T., Meinert, L.D. and Newberry, R.J., 1981. Skarn deposits, Econ. Geol., 75th Anniversary Volume, 317-391.

Esdale D., Pridmore, D.F., Fritz, F., Muir, P., Williams P., Coggon J., 2003. The Olympic Dam copper-uranium-gold-silver-rare earth element deposit, South Australia: A geophysical case history. *ASEG Extended Abstracts*, 147–168, doi:10.1071/ASEGSpec12_13.

Ferneyhough, A. B., Qarana, I. A., 1996. Case history study over the Batu Hijau copper-gold porphyry in SW Sumbawa, Indonesia. SEG Technical Program Expanded Abstracts 1996: pp. 1159-1162, doi: 10.1190/1.1826299.

Finn, C.A., Sisson, T.W., Deszcz-Pan, M., 2001. Aerogeophysical measurements of collapse-prone hydrothermally altered zones at Mount Rainier volcano. Nature, 409, 600-603.

Finn, C.A., Morgan, L.A., 2002. High-resolution aeromagnetic mapping of volcanic terrain, Yellowstone National Park. Journal of Volcanology and Geothermal Research, 115, 207-231.

Finn, C.A., Deszcz-Pan, M., Anderson, E.D., John, D.A., 2007. Three-dimensional geophysical mapping of rock alteration and water content at Mount Adams, Washington: Implications for lahar hazards. Jour. Geophys. Res., 112, B10204.

Force, E.R., Dickinson, W.R., Hagstrum, J.T., 1995. Tilting history of the San Manuel-Kalamazoo porphyry system, southeastern Arizona. Econ. Geol., 90, 67-80.

Frost, B.R., 1991a. Magnetic petrology: factors that control the occurrence of magnetite in crustal rocks, in: Lindsley, D.H., (Ed.), Oxide minerals: Petrologic and Magnetic Significance: Rev. Mineral., 25, 489-509.

Frost, B.R., 1991b. Introduction to oxidation fugacity and its petrologic importance. in: Lindsley, D.H., (Ed.), Oxide minerals: Petrologic and Magnetic Significance: Rev. Mineral., 25, 1-10.

Geissman, J.W., Van der Voo, R., Howard, K.L., 1982. A paleomagnetic study of the structural deformation in the Yerington district, Nevada. Am. J. Sci., 282, 1042-1109.

Grant, F.S., 1985a. Aeromagnetics, geology and ore environments, I. Magnetite in igneous, sedimentary and metamorphic rocks: an overview. Geoexploration, 23, 303-333.

Grant, F.S., 1985b. Aeromagnetics, geology and ore environments, II. Magnetite and ore environments. Geoexploration, 23, 335-362.

Groves, D. I., Bierlein, F. P., Meinert, L. D., Hitzman, M. W., 2010. Iron oxide copper-gold (IOCG) deposits through earth history: implications for origin, lithospheric setting, and distinction from other epigenetic iron oxide deposits. Economic Geology, 105, 641-654.

Guilbert, J.M., 1995. Geology, alteration, mineralization, and genesis of the Bajo de la Alumbrera porphyry copper-gold deposit, Catamarca Province, Argentina, in: Pierce, F.W, Bolm, J.G. (Eds.), Porphyry Copper Deposits of the American Cordillera. Arizona Geological Society Digest, 20, 646-656.

Guilbert, J.M., Lowell, J.D., 1995. Tilting history of the San Manuel-Kalamazoo porphyry system, southeastern Arizona - a discussion. Econ. Geol., 90, 2094-2096.

Guilbert, J.M., Park, C.F., 1986. The Geology of Ore Deposits. Freeman, New York.

Hanneson, J.E., 2003. On the use of magnetics and gravity to discriminate between gabbro and iron-rich ore-forming systems. *Exploration Geophysics*, 34 , 110–113, doi:10.1071/EG03110.

Harris, A. C., Golding, S. D., 2002. New evidence of magmatic-fluid–related phyllic alteration: Implications for the genesis of porphyry Cu deposits. Geology, 30, 335-338.

Haynes, D. W. (2000). Iron oxide copper (-gold) deposits: Their position in the ore deposit spectrum and modes of origin, in: Porter, T.M. (Ed.) Hydrothermal Iron Oxide Copper-gold & Related Deposits: A Global Perspective, Australian Mineral Foundation, Adelaide, 71-90.

Hayward, N., Enkin, R. J., Corriveau, L., Montreuil, J. F., Kerswill, J., 2013. The application of rapid potential field methods for the targeting of IOCG mineralisation based on physical property data, Great Bear magmatic zone, Canada. Journal of Applied Geophysics, 94, 42-58.

Heinson, G. S., Direen, N. G., Gill, R. M., 2006. Magnetotelluric evidence for a deep-crustal mineralizing system beneath the Olympic Dam iron oxide copper-gold deposit, southern Australia. Geology, 34, 573-576.

Henkel, H., 1991. Petrophysical properties (density and magnetization) of rocks from the northern part of the Baltic Shield. Tectonophysics, 192, 1-19.

Henkel, H., 1994. Standard diagrams of magnetic properties and density - a tool for understanding magnetic petrology. J. Appl. Geophys., 32, 43-53.

Hitzman, M.W., 2000. Iron oxide-Cu-Au deposits: What, where, when, and why, in: Porter, T.M. (Ed.) Hydrothermal Iron Oxide Copper-gold & Related Deposits: A Global Perspective, Australian Mineral Foundation, Adelaide, 9-25.

Holden, E-J, Fu S-C, Kovesi, P., Dentith, M., Hope, M., Bourne, B., 2010. Automated identification of magnetic responses from porphyry systems. *ASEG Extended Abstracts* 2010, doi:10.1071/ASEG2010ab111.

Holden, E-J, Fu S-C, Kovesi, P., Dentith, M., Hope, M. and Bourne, B., 2011. Automated detection of responses from porphyry-style mineralisation within magnetic data. In Li, X., Li, Y., Meng, X. (Eds.), GEM Beijing 2011: International Workshop on Gravity, Electrical & Magnetic Methods and Their Applications Beijing, China. October 10-13, 2011, Society of Exploration Geophysicists and Chinese Geophysical Society, doi: 10.1190/1.3659070.

Hollister, V.F., 1975. An appraisal of the nature and source of porphyry copper deposits. Minerals Science and Engineering: 7, 225-233.

Hope, M., Bourne, B., Crosato, S., Howe, B., Holden, E-J, Fu, S.C., Kovesi, P., 2010. Application of automated detection techniques in magnetic data for identification of Cu-Au porphyries, ASEG Extended Abstracts *2010, doi:10.1071/ASEG2010ab137.*

Hoschke, T., 1991. Geophysical discovery and evaluation of the West Peko copper-gold deposit, Tennant Creek. Exploration Geophysics, 22, 485-495.

Hoschke, T., 2008, Geophysical signatures of copper-gold porphyry and epithermal gold deposits, in*:* Spencer, J.E., Titley, S.R., (Eds.), Ores and Orogenesis: Circum-Pacific tectonics, Geologic Evolution, and Ore Deposits: Arizona Geological Society Digest 22, pp. 85-100.

Hoschke, T., 2010. Geophysical signatures of copper-gold porphyry and epithermal gold deposits, and implications for exploration. M.Sc. thesis, University of Tasmania.

Hoschke, T., 2011. Geophysical signatures of copper-gold porphyry and epithermal gold deposits, and implications for exploration. ARC Centre of Excellence in Ore Deposits, University of Tasmania, 47p.

Hoschke, T., 2012. Geophysics of the Elang Cu-Au porphyry deposit, Indonesia, and comparison with other Cu-Au porphyry systems. Australian Society of Exploration Geophysicists 22nd International Geophysical Conference and Exhibition, 26-29 February 2012 - Brisbane, Australia, Extended Abstracts, doi:10.1071/ASEG2012ab178.

Hunt, J.P., 1991. Porphyry copper deposits, in: Hutchinson, R.W., Grauch, R.I. (Eds.), Historical Perspectives of Genetic Concepts and Case Histories of Famous Discoveries. Economic Geology Monograph 8, 192-206.

Irvine, R.J., Smith, M.J., 1990. Geophysical exploration for epithermal gold systems. J. Geochem. Explor., 36, 375-412.

Ishihara, S., Sawata, H., Arpornsuwan, S., Busaracome, P., Bungbrakearti, N., 1979. The magnetite-series and ilmenite-series granitoids and their bearing on tin mineralization, particularly of the Malay Peninsula region. Geol. Soc. Malaysia. Bull., 11, 103-110.

Jessell, M. W., Valenta, R. K., 1996. Structural geophysics: integrated structural and geophysical modelling. Computer Methods in the Geosciences, 15, 303-324.

John, D.A., Ayuso, R.A., Barton, M.D., Blakely, R.J., Bodnar, R.J., Dilles, J.H., Gray, Floyd, Graybeal, F.T., Mars, J.C., McPhee, D.K., Seal, R.R., Taylor, R.D., Vikre, P.G., 2010. Porphyry Copper Deposit Model, chap. B of Mineral deposit models for resource assessment: U.S. Geological Survey Scientific Investigations Report 2010–5070–B.

Kletetschka, G., Wasilewski, P.J., Taylor, P.T., 2000. Unique thermoremanent magnetization of multidomain sized hematite: implications for magnetic anomalies. Earth Planet. Sci. Lett., 176, 469-479.

Kwak, T.A.P., 1994. Hydrothermal alteration in carbonate-replacement deposits; oreskarns and distal equivalents, in Lentz, D.R. (Ed.), Alteration and Alteration Processes Associated with Ore-forming Systems. Geological Association of Canada Short Course Notes, 11, 69-99.

Lapointe, P., Morris, W. A., Harding, K. L., 1986. Interpretation of magnetic susceptibility: a new approach to geophysical evaluation of the degree of rock alteration. Canadian Journal of Earth Sciences, 23(3), 393-401.

Lentz, D.R., 1994. Exchange interactions in hydrothermally altered rocks: examples from biotite-bearing assemblages. *In*: D.R. Lentz (Editor), Alteration and Alteration Processes Associated with Ore-forming Systems. Geological Association of Canada Short Course Notes, v.11, 69-99.

Lowell, J. D., 1968. Geology of the Kalamazoo orebody, San Manuel district, Arizona. Econ. Geol., 63, 645-654.

Lowell, J. D., 1974. Regional characteristics of porphyry copper deposits of the southwest. Econ. Geol., 69, 601-617.

Lowell, J.D., Guilbert, J.M., 1970. Lateral and vertical alteration-mineralization zoning in porphyry copper deposits. Econ. Geol., 65, 373-408.

Lum, J.A., Clark, A.H., Coleman, P.J., 1991. Gold Potential of the Southwest Pacific: Papua New Guinea, Solomon Islands, Vanuatu, Fiji. Technical Report, Pacific Islands Development Program, East-West Center, Honolulu.

MacDonald, G.D., Arnold, L.C., 1994. Geological and geochemical zoning of the Grasberg Igneous Complex, Irian Jaya, Indonesia. J. Geochem. Explor., 50, 179-202.

McIntyre, J.I., 1980. Geological significance of magnetic patterns related to magnetite in sediments and metasediments - a review. Bull. Aust. Soc. Explor. Geophys., 11, 19-33.

McMillan,W.J., Panteleyev, A.J., 1995. Porphyry copper deposits of the Canadian Cordillera, in: Pierce, F.W., Bolm, J.G. (Eds.), Porphyry Copper Deposits of the American Cordillera. Arizona Geological Society Digest, 20, 203-218.

Meinert, L.D., 1992. Skarns and skarn deposits. Geosci. Canada, 19, 145-162.

Meinert, L.D., 1993. Igneous petrogenesis and skarn deposits. *In*: R.V. Kirkham, W.D. Sinclair, R.I. Thorpe and J.M. Duke (Eds), Mineral Deposit Modeling. Geological Association of Canada, Special Paper 40, 403-417.

Meinert, L.D., 1995. Compositional variation of igneous rocks asssociated with skarn deposits - chemical evidence for a genetic connection between petrogenesis and mineralization. *In*: J.F.H. Thompson (Editor), Magmas, Fluids and Ore Deposits. Mineralogical Association of Canada, Short Course Series, v. 23, 401-418.

Meyer, C. and Hemley, J., 1967. Wall rock alteration, in: Barnes, H.L. (Ed.), Geochemistry of Hydrothermal Ore Deposits, First Edition. Wiley-Interscience, New York, 166-235.

Ohmoto, H., 2003. Nonredox transformations of magnetite-hematite in hydrothermal systems. Econ. Geol., 98, 157-161.

Özdemir, Ö., Dunlop, D.J., 2002. Thermoremanence and stable memory of single-domain hematites. Geophysical Research Letters, 29 (18), 24-1 - 24-4.
doi:10.1029/2002GL015597.

Özdemir, Ö., Dunlop, D.J., 2005. Thermoremanent magnetization of multidomain hematite. J. Geophys. Res., 110, B09104, doi:10.1029/2005JB003820.

Padilla Garza, R. A., Titley, S. R., Pimentel, B. F., 2001. Geology of the Escondida porphyry copper deposit, Antofagasta region, Chile. Econ. Geol., 96, 307-324.

Parry, L.G., 1980. Shape related factors in the magnetization of immobilised magnetite particles. Phys. Earth Planet. Inter., 22, 144-154.

Pollard, P. J., 2006. An intrusion-related origin for Cu–Au mineralization in iron oxide–copper–gold (IOCG) provinces. Mineralium Deposita, 41, 179-187.

Porter, T.M. (Ed.), 2002. Hydrothermal Iron Oxide Copper-Gold & Related Deposits: A Global Perspective. PGC Publishing, Adelaide.

Potter, D.R., 1996. What makes Grasberg anomalous, implications for future exploration. *In*: Porphyry Related Copper and Gold deposits of the Asia Pacific Region (Conference Proceedings). Australian Mineral Foundation, 10.1-10.13.

Proffett, J.M., 2003. Geology of the Bajo de la Alumbrera porphyry copper-gold deposit, Argentina. Economic Geology, 98(8), 1535-1574.

Puranen, R., 1989. Susceptibilities, iron and magnetite content of Precambrian rocks from Finland. Geol. Surv. Finland Rep. Inv. 90, 45 pp.

Purucker, M., Clark, D.A., 2011. Mapping and interpretation of the lithospheric magnetic field, in: Mandea, M., Korte, M. (Eds.) Geomagnetic Observations and Models, IAGA Special Sopron Book Series 5, Springer, pp.311-337.

Reed, M.H., 1997. Hydrothermal alteration and its relationship to ore fluid composition. *In*: Barnes, H.L. (Ed), Geochemistry of Hydrothermal Ore Deposits, Third Edition. Wiley, New York, 303-365.

Rose, A.W., Burt, D.M, 1979. Hydrothermal alteration, in: Barnes, H.L. (Ed), Geochemistry of Hydrothermal Ore Deposits, Second Edition. Wiley-Interscience, New York, pp. 173-235.

Schmidt, P.W., Clark, D.A., Logan, K.J., 1997. Palaeomagnetism, magnetic petrophysics and magnetic signature of the Porgera Intrusive Complex, PNG. Explor. Geophys., 28, 276-280.

Schmidt, P.W., McEnroe, S.E., Clark, D.A., Robinson, P., 2007. Magnetic properties and potential field modeling of the Peculiar Knob metamorphosed iron formation, South Australia: An analog for the source of the intense Martian magnetic anomalies? J. Geophys. Res., 112, B03102, doi:10.1029/2006JB004495.

Shive, P.N., 1989. Can remanent magnetization in the deep crust contribute to long wavelength magnetic anomalies? Geophysical Research Letters, 16, 89-92.

Sillitoe, R.H., 1979. Some thoughts on gold-rich porphyry copper deposits. Mineral. Dep., 14, 161-1744.

Sillitoe, R.H., 1990. Gold-rich porphyry copper deposits of the circum-Pacific region - an updated overview. Pacific Rim 90 Congress Proceedings, 119-126.

Sillitoe, R.H., 1993. Gold-rich porphyry copper deposits: geological model and exploration implications, in: Whiting, B.H., Mason, R., Hodgson, C.J.(Eds.), Giant Ore Deposits, Society of Economic Geologists, Special Publication 2, pp. 305-362.

Sillitoe, R.H., 1996. Characteristics and controls of the largest porphyry copper-gold and epithermal gold deposits in the circum-Pacific region. Aust J. Earth Sci., 44, 373-388.

Smith, R.J., 2002. Geophysics of iron oxide copper-gold deposits, in: Porter, T.M. (Ed.) Hydrothermal Iron Oxide Copper-Gold & Related Deposits: A Global Perspective, Volume 2. PGC Publishing, Adelaide, 123-136.

Stacey, F.D., Banejee, S.K., 1974. The Physical Principles of Rock Magnetism. Elsevier, Amsterdam.

Stokking, L., Tauxe, L., 1990. Properties of chemical remanence in synthetic hematite: Testing theoretical predictions. J. Geophys. Res., 95, 12,639-12,652.

Studemeister, P.A., 1983. The redox state of iron: a powerful indicator of hydrothermal alteration. Geoscience Canada, 10, 189-194.

Wilkins, J., Heidrick, T.L., 1995. Post Laramide extension and rotation of porphyry copper deposits, southwestern United States, in: Pierce, F.W., Bolm, J.G., (Eds.), Porphyry Copper Deposits of the American Cordillera. Arizona Geological Society Digest, 20, 109-127.

Williams, S. A., Forrester, J. D., 1995. Characteristics of porphyry copper deposits, in: Pierce, F.W., Bolm, J.G. (Eds.), Porphyry Copper Deposits of the American Cordillera. Arizona Geological Society Digest, 20, pp. 20-34.

Wyborn, D., Sun, S-S., 1994. Sulphur-undersaturated magmatism - a key factor for generating magma-related copper-gold deposits. AGSO Research Newsletter, 21, 7-8.

Table 2. Characteristic Mineral Assemblages of the Main Alteration Types in Porphyry Systems

ALTERATION TYPE (synonym)	CHARACTERISTIC ASSEMBLAGE [magnetic effects]
Early magnetite ± amphibole ± plagioclase veins (M veins)	Quartz-magnetite ± amphibole ± plagioclase, sulfide-poor veins; Fe-metasomatism (Clark and Arancibia, 1995) [abundant multidomain magnetite created: high *k*, $Q < 1$]
Potassic (K-silicate)	K-feldspar and/or biotite, plus one or more of: sericite, chlorite and quartz (e.g. in the interior zone of porphyry copper deposits) [Usually magnetite-producing (increased *k*, $Q < 1$): up to 5 vol % in mafic/intermediate rocks (e.g. gold-rich porphyry copper deposits); minor magnetite addition in felsic rocks; often associated with early quartz-magnetite-(amphibole) veins. Sometimes magnetite-destructive in high sulphidation systems.]
Phyllic (Sericitic)	Quartz-sericite-pyrite-chlorite (e.g. in large halos around porphyry copper deposits) [Magnetite-destructive (pyrite + hematite produced); decreased *k*]
Intermediate Argillic	Smectite and kaolinite, commonly replacing plagioclase (e.g. variably developed zone outside sericitic zone in some porphyry coppers) [magnetite-destructive; decreased *k*]
Propylitic	Albite (or K-feldspar in potassic rocks), chlorite and epidote group minerals; with only minor change in bulk composition (e.g. outermost alteration zone of porphyry copper deposits) [strong: Partially to totally magnetite-destructive (Fe in pyrite, hematite, epidote, chlorite, actinolite), decreased *k*] [weak: magnetite stable, *k* unchanged]
Albitic	Na-rich plagioclase + epidote and other propylitic minerals; with substantial addition of Na [magnetite-destructive, decreased *k*]
Sodic-calcic	Sodic feldspar and epidote ± actinolite ± chlorite (e.g. adjacent to intrusion at depth, beneath certain porphyry copper deposits) [magnetite-destructive, decreased *k*]
Advanced Argillic	Quartz plus one or more of: kaolinite, dickite, pyrophyllite, diaspore, pyrite, alunite, zunyite, topaz (e.g. in epithermal systems that may overlie porphyry systems) [magnetite-destructive, decreased *k*]
Carbonate	Calcite, dolomite, ankerite, siderite plus sericite, pyrite and/or albite [partially magnetite-destructive, decreased *k*]
Skarn	Ca and Mg silicates (limestone protolith: andradite and grossular, wollastonite, epidote, idocrase, chlorite, actinolite; dolostone protolith: forsterite, serpentine, talc, brucite, tremolite, chlorite) [see Tables 3 and 4]
Supergene oxidation	Alunite, allophane, jarosite, Fe oxides, sulfates [magnetite- and pyrrhotite-destructive; hematite and goethite produced; decreased *k*]

Table 3. Typical magnetic properties of skarns

LITHOLOGY	Av. $k \pm$ SE (10^{-3} SI) [Range]	ΔB_z (nT)*	Average NRM ± SE [Range] (A/m) Average $Q \pm$ SE [Range]
Oxidised Magnetite Skarn†	650 ± 160 [120 - 2000]	16,250 ± 4000 [3000 - 50,000]	J = 50 ± 20 [0.3 – 210] Q = 1.4 ± 0.4 [0.05 – 4.5]
Reduced Pyrrhotite Skarn†	5 ± 2 [1 - 8]	125 ± 50 [25 – 200]	J = 14 ± 8 [1 – 34] Q = 16 ± 4 [8 – 25]
Reduced pyroxene ± garnet† skarn (mt rare or absent)	1.1 ± 0.2 [0.1 - 2]	28 ± 5 [2.5 – 50]	J < 0.02 Q << 1
Calcic Fe (Cu, Co, Au) skarn‡ (mafic intrusion; island arc or rifted continental margin)	2000 [1200 - 3500]	50,000 [30,000 – 175,000]	J : [5 – 300] Q ~ 1 [0.1 – 5]
Magnesian Fe (Cu, Zn) skarn‡ (felsic intrusion; continental margin)	2000 [1200 – 2700]	100,000 [60,000 – 87,500]	J : [5 – 220] Q ~ 1 [0.1 – 5]
Calcic Cu (Mo, W, Zn) skarn - proximal‡ (Grd-Qmz; continental margin)	[30 - 400]	[750 – 10,000]	J: [1 – 50] Q ~ 1.5 [0.1 – 5]
Magnesian Cu (Mo, W, Zn) skarn‡ (Grd-Qmz; continental margin)	[800 -1700]	[20,000 – 42,500]	J: [5 – 100] Q ~ 1.5 [0.1 – 5]

*ΔB_z is the maximum associated magnetic anomaly (steep field, non-magnetic country rocks, diameter >> depth below sensor, great depth extent), calculated from total magnetisation for case where remanence is parallel to induced magnetisation. The effective susceptibility is therefore taken to be $k(1+Q)$. †Averages from P700 Database and from CSIRO Catalogue of Magnetic Properties (Clark, 1988b). ‡Inferred values from data in Einaudi et al. (1981).

Table 4. Zonation of mineralogy and magnetic properties of a typical copper skarn (deep skarn, Carr Fork mine, Bingham Mining District, Utah)

ZONE	Distance from intrusive contact (m)	GANGUE	SULFIDES	Cu (wt %)	Magnetite (vol %)	k* (10^{-3} SI)
Bingham stock (potassic zone)	> 100	qtz, Kfsp, bio	cp, bn, py	0.65 (shallow) < 0.1 (deep)	0.1 –1	3.5 – 35
Endoskarn (Bingham stock)	< 100	act, ep	(0.5 vol %) mb > cp	< 0.1	~ 0.1	~ 3.5
Proximal exoskarn	0-50	and > di, cal, qtz,	(1-2 vol %) cp, (bn)	~0.2	1-2	35 - 70
Exoskarn	50 – 100	and	(2-5 vol %) cp > py	~ 0.6	2 - 5	70 - 180
Exoskarn	100 – 300	and >> di	(15 vol %) cp ≥ py	~ 8	5 – 10	180 - 380
Exoskarn	300 - 350	and ≥ di	(5 vol %) cp:py = 0.2	~ 0.5	2	70
Exoskarn	350 – 400	wo (gar, di)	(1 vol %) bn, cp, sph, (py)	~ 0.5	< 0.1	< 3.5
Distal exoskarn	400 - 600	wo-di-qtz; wo-cal; marble	(0.5 vol %) bn, cp, sph, gal	< 0.5	< 0.1	< 3.5
Marble, limestone	> 600	cal, marble	(< 0.1 vol %) (sph, gal, py)	0	0	0

Ore zone (~120-600 m from contact) average grades: ~2.3 % Cu, 0.6 g/t Au, 12 g/t Ag, 0.03 % Mo.
Mineralogical and chemical data from Einaudi (1982).
*Susceptibilities calculated using equation (3) from petrographically estimated modal magnetite contents.

Table 6. Characteristic Mineral Assemblages of the Main Alteration Types in IOCG Systems

ALTERATION TYPE (synonym)	CHARACTERISTIC ASSEMBLAGE [magnetic effects]
Sodic	extensive albitisation of host rocks, accompanied by magnetite ± scapolite ± chlorite ± actinolite ± hematite [abundant multidomain magnetite created: high *k*, $Q < 1$]
Sodic-calcic	plagioclase-magnetite-epidote-calcite-sphene ± scapolite ±chlorite ± actinolite ± garnet ± hematite [abundant multidomain magnetite created: high *k*, $Q < 1$]
Sodic-potassic	albite-K feldspar-magnetite-quartz ± sericite ± biotite ± hematite ± chlorite ± actinolite [abundant multidomain magnetite created: high *k*, $Q < 1$]
Potassic-calcic	K feldspar-biotite-magnetite-epidote-calcite-sphene ± chlorite ± actinolite ± garnet ± hematite [abundant multidomain magnetite created: high *k*, $Q < 1$]
Potassic	K feldspar-sericite-magnetite-quartz ± biotite ± hematite ± chlorite ± actinolite [abundant multidomain magnetite created: high *k*, $Q < 1$]
Sericite-hematite (HSCC, argillic, hydrolitic)	sericite-hematite-chlorite-carbonate ± quartz [abundant multidomain hematite created: low *k*; $Q < 1$, unless high-grade metamorphosed]

CHAPTER 10: CONCLUSIONS

Acquisition of magnetic gradient tensor data is anticipated to become routine in the near future. There is therefore a need to develop new methods that efficiently process gradient tensor data, exploit the extra information, and improve interpretability. In the meantime, modern ultrahigh resolution conventional magnetic data can be used, with certain important caveats, to calculate magnetic vector components and gradient tensor elements TMI or TMI gradient surveys.

New methods for inverting gradient tensor surveys to obtain source parameters have been developed for a number of elementary, but useful, models. These include point dipole (sphere), vertical line of dipoles (narrow vertical pipe), line of dipoles (horizontal cylinder), thin dipping sheet, and contact models. A key simplification is the use of eigenvalues and associated eigenvectors of the tensor. The normalised source strength (NSS), calculated from the eigenvalues, is a particularly useful rotational invariant that peaks directly over 3D compact sources, 2D compact sources, thin sheets and contacts, and is independent of magnetization direction. In combination the NSS and its vector gradient determine source locations uniquely. NSS analysis can be extended to other useful models, such as vertical pipes, by calculating eigenvalues of the vertical derivative of the gradient tensor.

Inversion based on the vector gradient of the NSS over the Tallawang magnetite deposit obtained good agreement between the inferred geometry of the tabular magnetite skarn body and drill hole intersections. Besides the geological applications, the algorithms for the dipole model are readily applicable to the detection, location and characterization (DLC) of magnetic objects, such as naval mines, unexploded ordnance, shipwrecks, archaeological artefacts and buried drums.

Some of these new methods have been applied to analysis of the magnetic signature of the Early Permian Mount Leyshon gold-mineralised system, Queensland. The Mount Leyshon magnetic anomaly is a prominent TMI low that is produced by rock units with strong reversed remanence acquired during the Late Palaeozoic Reverse Superchron. The inferred magnetic moment and direction of magnetisation for the source zone of the Mount Leyshon magnetic anomaly are consistent with petrophysical measurements and allow an estimate of the source volume and the depth extent of the magnetic zone.

The presence of a highly conductive medium around a measurement capsule influences electromagnetic measurements made in the ocean and fundamentally alters the structure of the magnetic gradient tensor, which is symmetric within the capsule, but asymmetric within the surrounding medium. Additional effects arise if seawater is flowing past the sensor package. For a spherical measurement capsule, the internal electric field is augmented by 50%, the external perturbation of the electric field around the cavity has the configuration of a dipole field and the external magnetic field due to the cavity is that of an elementary current dipole. An ellipsoidal cavity has an anisotropic response, except in the degenerate case where all axes are equal and the cavity is spherical. For a disk-like cavity the amplification of the applied electric field normal to the disk can be very large within the cavity. The anomalous magnetic field within an ellipsoidal cavity due to electric current flow around the cavity is nonuniform, but has a uniform gradient. At the center of the ellipsoidal cavity the magnetic field is equal to the field that existed at that point before insertion of the cavity. The *resultant* internal magnetic gradient tensor is symmetric and traceless, as required. Seawater motion past a sensor package produces easily detectable effects that can represent an important source of electromagnetic noise. These results have implications for marine controlled source electromagnetic surveys, magnetic gradient tensor measurements in the ocean, and marine magnetotellurics, as well as potential application to satellite measurements within the magnetosphere.

Assuming without evidence that magnetic sources are magnetised parallel to the geomagnetic field can seriously mislead interpretation and can result in drill holes missing their targets. Knowledge of total magnetisation is often critical for accurate determination of source geometry and position. Knowledge of magnetic properties such as magnetisation intensity and Koenigsberger ratio constrains the likely magnetic mineralogy (composition and grain size) of a source, which gives an indication of its geological nature. Determining the direction of a stable ancient remanence gives an indication of the age of magnetisation, which provides useful information about the geological history of the source and its environs. Several methods exist for estimating the magnetic moment vector of a source, without any knowledge of its shape. This yields directions of the resultant magnetisation (remanent plus induced), which is crucial for accurate modelling, and gives an indication of the size of the source, when plausible magnetisation intensities are assumed.

A new method that estimates the magnetic moment and location of a discrete source from integral moments of rotational invariants of the gradient tensor was developed and successfully applied to several remanence-dominated anomalies in northern New South Wales, yielding results that agreed well with detailed inversions of the magnetic survey data. Another new method for remote determination of *in situ* magnetic properties exploits local perturbation of natural geomagnetic variations by a magnetic source. This method yields estimates of the resultant magnetisation direction, the direction of remanence, and the Koenigsberger ratio of the source, without making any assumptions about its geometry. Furthermore, if the source is compact, this method gives a direct indication of direction to source, which can be exploited for drill targetting.

Magnetic anomaly patterns can be used as a tool for mapping lithology, metamorphic zones and hydrothermal alteration systems, as well as identifying structures that may control passage of magmas or hydrothermal fluids associated with mineralisation. Reliable geological interpretation of mineralised systems requires an understanding of the magmatic, metamorphic and hydrothermal processes that create, alter and destroy magnetic minerals in rocks. Predictive magnetic exploration models for porphyry copper and iron oxide copper-gold (IOCG) deposits can be derived from standard geological models by integrating magnetic petrological principles with petrophysical data, deposit descriptions, and modelling of observed magnetic signatures of these deposits.

Even within a particular geological province, the magnetic signatures of similar deposits may differ substantially, due to differences in the local geological setting. Searching for "look-alike" signatures of a known deposit is likely to be unrewarding unless pertinent geological factors are taken into account. These factors include the tectonic setting and magma type, composition and disposition of host rocks, depth of emplacement and post-emplacement erosion level, depth of burial beneath younger cover, post-emplacement faulting and tilting, remanence effects contingent on ages of intrusion and alteration, and metamorphism. Because the effects of these factors on magnetic signatures are reasonably well understood, theoretical magnetic signatures appropriate for the local geological environment can qualitatively guide exploration and make semiquantitative predictions of anomaly amplitudes and patterns. The predictive models also allow detectability of deposit signatures to be assessed, for example when deposits are buried beneath a

considerable thickness of nonmagnetic overburden, are covered by highly magnetic heterogeneous volcanic rocks, or there is a strong regional magnetic gradient.

Magnetic gradient tensor data potentially afford better source localisation, finer resolution of structural detail, and better determination of source magnetisations. Improved methods for exploiting the extra information contained in gradient tensor surveys can also add value to existing high quality conventional magnetic surveys, suitably reprocessed to produce gradient tensor grids. *Geological* interpretation of the improved solutions for source locations, geometries and magnetisations, obtainable from gradient tensor data, should be guided by magnetic petrological principles and constrained, wherever possible by petrophysical and palaeomagnetic data.

The theme of this thesis is that maximum benefit can be obtained from future developments in magnetics by adopting an *integrated* approach, whereby new technologies that generate information-rich, but complex multicomponent data, are efficiently processed to produce more interpretable parameters, which are used to generate source locations and inferred magnetisations that can then be interpreted geologically. Information on total magnetisation and remanence that is derived from analyses of these information-rich data sets can be used to constrain geometry, probable lithology, and geological history of sources. A final geological interpretation that is used to define exploration targets should incorporate insights from magnetic petrological principles and predictive exploration models.